University of Pisa

The MEG II Drift Chamber and the Search for Rare Muon Decays: Performance and Implications for Recent Experimental Results

Antoine Venturini

Department of Physics

Thesis submitted for the degree of

Doctor of Philosophy

Supervisor: Dr. Alessandro M. Baldini
Prof. Fabrizio Cei

XXXVIII PhD course, Academic Year 2025/26

Contents

Abstract

The MEG II experiment at the Paul Scherrer Institut searches for the charged Lepton Flavor Violating decay $\mu^+ \to e^+\gamma$, a golden channel to test the validity of the Standard Model and to explore possible signatures of New Physics.

In this thesis, we report the results of the MEG II analysis of the dataset collected during the 2021–2022 physics runs, achieving the highest sensitivity to date on the $\mu^+ \to e^+\gamma$ branching ratio, $\mathcal{S} = 2.2 \times 10^{-13}$. No evidence for the $\mu^+ \to e^+\gamma$ decay was observed, and a new upper limit on the branching ratio was established:

$$\mathrm{BR}(\mu^+ \to e^+\gamma) \leq 1.5 \times 10^{-13} \text{ (90\% C. L.)}$$

which is twice as stringent as the previous limit.

A central contribution to this achievement was the calibration of the experiment's tracking detector—a single-volume cylindrical drift chamber—using 2022 data, along with the optimization of its performance through updates to the positron reconstruction algorithms, leading to a 10% improvement in resolution. Systematic uncertainties related to tracker alignment were also significantly reduced thanks to a novel tracking algorithm for cosmic ray events. This thesis details the candidate's work on these developments and their impact on the final analysis.

Introduction

> The [...] punchline, "There is a muon", may have caused laughter in the heavens, but man was, and still is, ignorant of the joke. What else was the muon good for other than being the pion's favorite decay product? [...] Now, forty years later, the divine laughter continues unabated.

Now, forty years later the publication of A. Pais memories [1], humanity still hasn't taken part to this joke.

The first observation in a cosmic ray experiment of "a particle with unit charge, a mass greater than that of a free electron, and much smaller than that of a proton [...]"[2], which would later be known as the *muon* (μ) [3], dates back to 1937.

With its mass of about 100 MeV (first measured in [4]), the muon was the natural candidate to be the mediator of the strong interaction according to Yukawa's theory. However, in 1947 Conversi, Pancini, and Piccioni [5] showed that the muon did not interact with matter as expected for a particle mediating the strong interaction, but rather resembled the electron—initially considered an excited state of it. This idea motivated the first experimental search for the electromagnetic decay $\mu \to e\gamma$ [6].

The negative results in searches for this process pushed forward the idea that the muon was a "twin" of the electron. The experimental confirmation of the existence of two distinct *families* of leptonic particles came in 1962, from neutrino experiments [7]. In 1975, the existence of a third family of leptons was discovered, the τ lepton, with mass $m_\tau \gg m_\mu \gg m_e$.

Meanwhile, roughly in parallel, in hadronic physics the discovery of new particles (kaons in the 1950s, the J/ψ in 1974, the Y meson in 1977 and finally the top quark in 1995) led to the formulation of the quark model, with again three families of quarks displaying the same pattern of mass ordering found in the lepton sector: $m_t \gg m_c \gg m_u$.

This concept of *flavor*, i.e. the organization of leptons and quarks into three groups carrying a quantum number which determines the mixing probability of particles and seems related to their mass, is a cornerstone of the Standard Model of Fundamental Interactions. Yet, the essence of *flavor* continues to be a mystery intriguing the community of particle physicists. Beyond the question: "Why are there three copies of the fundamental matter fields?" may lay a new, more comprehensive theory of Nature.

Since the first tiles of the *flavor puzzle* manifested themselves in the 1940s, the search for charged Lepton Flavor Violating processes has been a very fruitful experimental effort, capable of shedding light onto new theories, which eventually converged to the formulation of the Standard Model. Today, as will be discussed in Chapter 1, these very same searches could test the existence of New Physics beyond the Standard Model.

The MEG II experiment at the Paul Scherrer Institut is one of the main actors in this field of research (Chapter 2). Designed to detect the $\mu^+ \to e^+\gamma$ decay with a record sensitivity to $\mathrm{BR}(\mu^+ \to e^+\gamma) \leq 6 \times 10^{-14}$ (90% C.L.), the experiment has been taking data continuously since 2021 and has already published an updated lower limit on the branching ratio:

$$\mathrm{BR}(\mu^+ \to e^+\gamma) \leq 3.1 \times 10^{-13} \text{ (90\% C. L.)}$$

based on the analysis of the first-year dataset [8] and combined with previous MEG results [9].

In this thesis, the result of MEG II on $\mathrm{BR}(\mu^+ \to e^+\gamma)$ with the full 2021+'22 dataset will be reported. With a sample of data five times larger than the 2021 dataset alone, the sensitivity is boosted to $2.2 \times$

10^{-13}, almost three times better than MEG; therefore this is the most sensitive search for the $\mu \to e\gamma$ decay ever performed yet.

The candidate contributed to this result through his work on the experiment's tracker, the cylindrical drift chamber (CDCH). The principal aspects of the detector are outlined in Chapter 3. Chapter 4 discusses the results of the detector calibration performed on the 2022 data, using mainly positron tracks. Chapter 5 presents the optimization of the reconstruction algorithms for cosmic rays, which made it possible to reduce systematic uncertainties on the detector alignment that limited the experiment's sensitivity. There, we report also about the investigation on a new software alignment algorithm for the CDCH using the so-called "Millepede" strategy. The efforts described in Chapters 4 and 5 converge in the Positron Analysis presented in Chapter 6, where the parameters for the final likelihood analysis are determined. The MEG II final results on the 2021+'22 dataset are finally presented in Chapter 7.

Future prospects of the $\mu \to e\gamma$ search with MEG II are outlined in the concluding Chapter 8.

Part I

The search for charged Lepton Flavor Violation and the MEG II experiment

Chapter 1

Motivations for the MEG II experiment: a theoretical overview

This first Chapter introduces the reader to the field of research in *charged Lepton Flavor Violating* (cLFV) processes, illustrating the motivations which have led scientists to build complex experiments, such as MEG and MEG II to search for the $\mu \to e\gamma$ decay for instance. More about this topic can be found in [10, 11].

In Section 1.1, we briefly introduce the flavor sector of the Standard Model and explain why it remains an active area of research for probing physics beyond it. Section 1.2 focuses on the role of cLFV processes in testing a specific New Physics scenario within the framework of supersymmetry, while Section 1.3 presents a model-independent approach.

1.1 Flavor in the Standard Model of Particle Physics

The Standard Model of Particle Physics (SM) is the most comprehensive theory developed so far to describe the nature of matter and the fundamental interactions. Its main components are schematically illustrated in Figure 1.1.

The SM describes elementary matter particles as fermionic fields, divided into two classes: *quarks*, which participate in the strong interaction, and *leptons*, which do not. Fermions interact through particles that act as "force carriers," represented by bosonic fields. Electromagnetic (EM) interactions are mediated by the *photon*, weak interactions by the $W^{\pm}$ and Z^0 bosons, and strong interactions by the *gluons*. These interactions are fully described within the SM by the three gauge symmetries and their relative couplings:

$$\mathrm{SU}(3)_{strong} \times \mathrm{SU}(2)_{weak} \times \mathrm{U}(1)_{EM}$$

The twelve fundamental fermions of the SM appear to be naturally divided into three families (or generations), depending on their masses and on the mixing probability between members of a different generation. The quantum number that characterizes each family is called *flavor*. The parameters governing the flavor sector of the SM

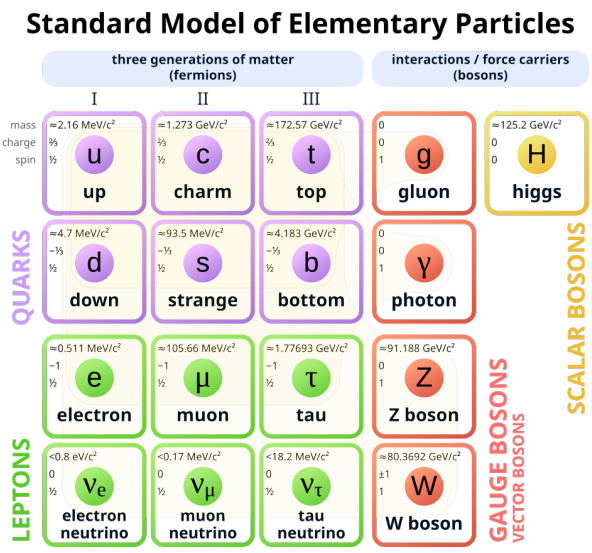

Figure 1.1: The "periodic table" of the Standard Model. Credits to Wikipedia.

originate from the Yukawa couplings between the fermion fields and the Higgs field:

$$-\mathcal{L}_{Yukawa} = (Y_u)_{ij}\,\overline{Q}_{Li} u_{Rj}\tilde{\Phi} + (Y_d)_{ij}\,\overline{Q}_{Li} d_{Rj}\tilde{\Phi} + (Y_e)_{ij}\,\overline{L}_{Li} e_{Rj}\Phi + h.c. \tag{1.1}$$

where $Y_{u,\,d,\,e}$ are complex 3×3 matrices encoding the couplings between fermions of the i-th and j-th families (u for up quarks, d for down quarks, e for charged leptons), Φ is the Higgs scalar field, $Q_{Li} = \begin{pmatrix} u_i \\ d_i \end{pmatrix}_L$ and $L_{Li} = \begin{pmatrix} \nu_i \\ l_i^- \end{pmatrix}_L$ are respectively the left-handed quarks and leptons doublets, while d_{Ri}, u_{Ri}, e_{Ri} are the right-handed singlets.

Fermion masses arise from the spontaneous breaking of the electroweak symmetry $\mathrm{SU}(2)L \times \mathrm{U}(1)Y$ via the Higgs mechanism into the gauge groups $\mathrm{SU}(2)_{weak} \times \mathrm{U}(1)_{EM}$:

$$\left(m_f\right) ij = \frac{v}{\sqrt{2}} \left(Y_f\right) ij, \quad f = u, d, e, \tag{1.2}$$

where $\frac{v}{\sqrt{2}} \approx 174$ GeV is the Higgs vacuum expectation value. Notably, a right handed neutrino term is absent in Equation 1.1. Although neutrinos are now known to be massive, as demonstrated by the observation of neutrino oscillations, it remains unknown whether they are Dirac or Majorana fermions. Their mass generation can therefore be incorporated into the SM in two possible ways:

- if neutrinos were Dirac's fermions, right-handed singlets ν_R can be introduced, in perfect analogy with the other fundamental fermions:

  $$\mathcal{L}_Y \supset -(Y_\nu)_{ij}\,\overline{\nu}_{Ri}\tilde{\Phi}^\dagger L_{Lj} + h.c. \tag{1.3}$$

  The neutrino masses in this case are calculated as in Equation 1.2, and their smallness depends on the couplings Y_ν being very tiny $\approx 10^{-12}$;

- in the case that neutrinos were Majorana fermions, i. e. the neutrino is its own antiparticle, mass terms different to those in Equation 1.3 can arise. Without the need of adding a right-handed neutrino, the following non-renormalisable operator can be included in the Yukawa lagrangian:

  $$\mathcal{L}_Y \supset \frac{C_{ij}}{\Lambda} \left(\overline{L_{Li}^C}\sigma_2\Phi\right) \left(\Phi^T \sigma_2 L_{Lj}\right) + h.c. \tag{1.4}$$

  where σ_2 is the Pauli matrix, and $\Lambda \gg v$ corresponds to the energy scale at which an underlying theory, including the SM as a low-energy approximation, undergoes the phenomenon of symmetry breaking. The neutrino masses in this case are:

  $$(m_\nu)_{ij} = C_{ij}\frac{v^2}{\Lambda} \tag{1.5}$$

  and their smallness is linked to the high value of the energy scale Λ.

  In another scenario, we could add a right-handed Majorana neutrino ν_R with mass M_R[i], which would extend the SM lagrangian with the following operators:

  $$\mathcal{L} \supset -\left(Y_\nu\,\overline{\nu_R}\tilde{\Phi}L_L + \frac{1}{2}M_R\overline{\nu_R}\nu_R^C\right) + h.c. \tag{1.6}$$

  This SM extension is responsible for the so called *seesaw* mechanism [12]: the mass matrix will have mixed Dirac ($\mathbf{m}_D$) and Majorana ($\mathbf{M}_R$) terms

  $$\begin{pmatrix} \mathbf{0} & \mathbf{m}_D \\ \mathbf{m}_D & \mathbf{M}_R \end{pmatrix}$$

[i] Majorana masses for right-handed neutrinos are not forbidden since they are singlets of the SM gauge symmetries.

which, in the limit $m_D \ll M_R$, gives the following masses for left-handed and right-handed neutrinos:

$$m_{\nu_L} \approx \frac{m_D^2}{M_R}, \quad m_{\nu_R} \approx M_R \tag{1.7}$$

Again, the smallness of left-handed neutrino masses is naturally explained in this extension of the SM. More about this topic can be found [13].

The mixing between fermion families arises when the fermion fields are rotated to diagonalize the fermion mass matrices, since in principle the Y_f, $f = u, d, e$ are diagonalized through different sets of rotations. Charged current interactions mediated by the W bosons allow flavor violating processes through the lagrangian term:

$$\mathcal{L}_{cc} = \frac{g}{\sqrt{2}} \left[\overline{u}_L \gamma^\mu \left(V_u^\dagger V_d \right) d_L + \overline{\nu}_L \gamma^\mu \left(V_\nu^\dagger V_e \right) e_L \right] W_\mu^+ + h.c. \tag{1.8}$$

where V_f, $f = u, d, e$ are the unitary matrices diagonalizing the mass matrices. In Equation 1.8 we notice that the flavor mixing in the quark sector is described by the matrix $V_{CKM} \equiv V_u^\dagger V_d$, known as the Cabibbo - Kobayashi - Maskawa matrix, while the mixing in the lepton sector depends on the matrix $V_{PMNS} \equiv V_\nu^\dagger V_e$, the Pontecorvo-Maki-Nakagawa-Sakata matrix [14, 15].

1.1.1 Open questions beyond the Standard Model

The SM is generally regarded as a low-energy approximation (valid at energy scales $\lesssim 1$ TeV) of a more general theory, capable of explaining phenomena which are not included at all in the SM.

The main fundamental questions which remain unanswered by the SM are:

- *what is the nature Dark Matter?* Compelling astronomical and cosmological observations show that we are ignorant about what most of our Universe is made of. In the framework of Particle Physics, many proposed new theories predict new particles which, if discovered, could be plausible Dark Matter candidates;
- *what is at the origin of the observed matter-antimatter asymmetry?* We live in a matter-dominated Universe because of an unbalance between matter and antimatter at an early stage of the evolution of the Universe (according to the theory of Big Bang). Matter-antimatter asymmetries arise in the context of the SM when the CP symmetry is violated, but the observed asymmetries are not enough to account for the huge primordial discrepancy observed;
- *what is the nature of neutrinos?* As already mentioned in Section 1.1, it is unknown whether neutrinos are Dirac or Majorana fermions.

In the current theoretical framework there are also other puzzles which motivate theoreticians, and experimentalists, to search for new theories, and evidence of them:

- *Grand Unification* - the running gauge couplings in the SM have approximately equal strength at an energy scale of $\Lambda_{GUT} \simeq 10^{14}$ GeV. Since the 1970s, this observation has motivated the formulation of so-called Grand Unification Theories (GUT) which encapsulate the $SU(3)_{strong} \times SU(2)_L \times U(1)_Y$ groups into a larger symmetry group (like SU(5) [16]) broken at the scale Λ_{GUT}. Based on Grand Unified Theories (GUTs) that combine the strong, weak, and electromagnetic forces, Theory of Everything frameworks such as *supersymmetry* (SUSY) aim to include gravity as well;
- *the naturalness puzzle* - the Higgs boson mass is measured to be $m_H \sim 125$ GeV/c^2 [17], a very small value when considering that m_H receives quantum corrections from the interaction of the Higgs field with the other fields through loop diagrams which scales as $\Delta m_H \propto m^2$. In particular, it should be expected that the Higgs field would interact with "something" at the Planck energy

scale $M_{Pl} \approx 10^{19}$ GeV/c^2, where gravitational effects are comparable in size to those of the other fundamental interactions. To keep the Higgs light, these huge corrections must be dumped by a proper, very small, coupling constant between the Higgs field and the New Physics appearing at the Planck scale. New theories may account for this fact with a more *natural* explanation, which doesn't need fine-tuned parameters;

- *the strong-CP puzzle* - the SM allows strong interactions to violate CP symmetry, as weak interactions do. The θ_{CP} phase that encodes CP violation in the strong sector has not yet been measured, but it has a very small experimental upper limit: $|\theta_{CP}| < 10^{-9}$. Again, the question arises if it is possible to comprehend this infinitesimal parameter as the manifestation of a more fundamental phenomenon (more about this in Chapter 2, Section2.3);

- *the origin of flavor* - the SM doesn't provide any *a priori* explanation for the existence of three fermion families nor for the differences between them: masses and mixing terms are unconstrained by the theory and can only be determined experimentally. This large number of free parameters, over twenty in total, stands in sharp contrast with the simplicity of the gauge sector, which is characterized by only three coupling constants.

The above list gives only an overview of some short-comings of the SM; a more extensive discussion about the existing line of research in Particle Physics can be found in [18].

In the next Section we will see how and why the flavor sector is privileged by both experimentalists and theoreticians to scout New Physics beyond the Standard Model.

1.1.2 Charged Lepton Flavor Violating processes

The evidence of flavor-changing processes in the lepton sector has eluded physicists for many years. In the 1950s, the very absence of signals in searches for $\mu \to e\gamma$, $\mu \to eee$, and for the nuclear capture process $\mu N \to eN$ suggested the existence of a conserved quantum number, i.e. the *flavor* [19]. The discovery of charged currents interactions in the quark sector brought physicists to interpret the conservation of lepton family number as an accidental symmetry of the SM due to neutrinos having mass $m_\nu = 0$.

Although nowadays we have observed neutrino oscillations, no evidence of charged flavor violating processes has been collected yet; actually, within the present formulation of the SM with non-zero neutrino masses, such processes are expected to elude experimentalists for many years to come. We will illustrate why through the case study of the $\mu \to e\gamma$ process, which is central in this thesis work.

The SM allows the $\mu \to e\gamma$ decay through loop diagrams like the one drawn in Figure 1.2. The branching ratio of this process, normalized to the Michel muon decay $\mu \to e\nu\overline{\nu}$, is [20, 21]:

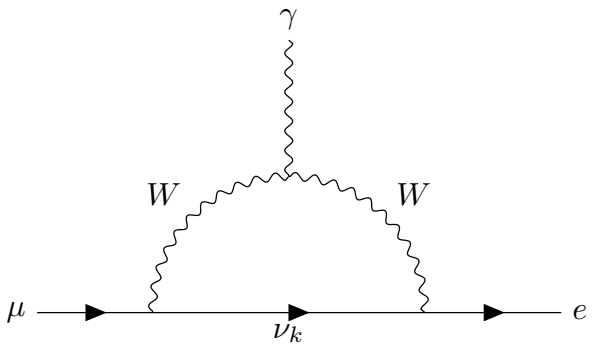

Figure 1.2: Feynman diagram contributing to the amplitude of the $\mu \to e\gamma$ process within the SM.

$$\mathrm{BR}(\mu \to e\gamma) \simeq \frac{\Gamma(\mu \to e\gamma)}{\Gamma(\mu \to e\nu\overline{\nu})} = \frac{3\alpha}{32\pi}\left|\sum_{k=1,3} V_{\mu k} V_{ek}^{*} \frac{m_{\nu_k}^2}{m_W^2}\right|^2 \propto \left(\frac{\Delta m_{31}^2 + \Delta m_{21}^2}{m_W^2}\right)^2 \tag{1.9}$$

where $V_{\mu k}$, V_{ek} are elements of the V_{PMNS} mixing matrix, $m_{\nu_k}, k = 1, 3$ are the masses of the first and third neutrinos (mass eigenstates) and m_W is the W boson mass. The decay probability is heavily suppressed because of the smallness of the $\left(\frac{\Delta m}{m_W}\right)^4$ ratio. Taking into account the uncertainty on the values for neutrino parameters entering in Equation 1.9, the expected value for $\mathrm{BR}(\mu \to e\gamma)$ is of the order of $10^{-55} - 10^{-54}$.

The same considerations hold also for the other cLFV processes. For a broader overview on this, see [10, 11]. Since the SM predicts negligible rates for cLFV processes, any evidence of a similar event implies the discovery of New Physics phenomena. For this reason, cLFV processes as $\mu \to e\gamma$ are considered as golden channels to investigate the existence of Physics beyond the SM.

1.2 Supersymmetry: a case study of beyond Standard Model theories

Among the various Grand Unified Theories proposed to unify the fundamental interactions within a single gauge framework, SUSY stands out as one of the most influential extensions of the Standard Model. It has provided strong theoretical motivation for the search for cLFV processes. A general introduction to SUSY can be found in [22].

In SUSY theories, each Standard Model particle is paired with a *supersymmetric* partner having opposite spin statistics: each boson is associated with a fermionic partner, and each fermion with a bosonic one. In this way, the "naturalness problem" of the Higgs boson mass is resolved: in calculating higher-order corrections to the Higgs boson mass, loop diagrams with bosons or fermions contribute equally but with opposite sign, thus allowing an exact cancellation of divergences naturally within this theory, without requiring the fine-tuning of parameters.

SUSY are attractive not only because they solve this specific puzzle, but also because of the plethora of hypotheses which can be experimentally tested in past, present and future facilities. Indeed, the simplest formulations of SUSY theories, the Minimal Supersimmetric Standard Model (MSSM), requires the mass scale of SUSY particles to lie at around $m_{SUSY} \lesssim 1$ TeV/c^2 to explain a Higgs boson so light, an energy scale accessible in a direct production mechanism at Tevatron, LEP and LHC.

Table 1.1: Supersymmetric partners of SM particles which are relevant in cLFV processes in the MSSM model.

Gauge eigenstates	Mass eigenstates	Spin	SM partner
$\tilde{B}$, $\tilde{W}^0$, $\tilde{H}_u^0$, $\tilde{H}_u^0$ Bino, n. Wino, n. Higgsinos	$\tilde{\chi}_i^0$, i = 1, ... , 4 neutralinos	$\frac{1}{2}$	γ, Z, h
$\tilde{W}^{\pm}$, $\tilde{H}_u^+$, $\tilde{H}_u^-$ c. Wino, c. Higgsinos	$\tilde{\chi}_i^{\pm}$, i = 1, 2 charginos	$\frac{1}{2}$	$W^{\pm}$
$\tilde{e}_R^{\pm}$, $\tilde{e}_L^{\pm}$, $\tilde{\nu}_e$ $\tilde{\mu}_R^{\pm}$, $\tilde{\mu}_L^{\pm}$, $\tilde{\nu}_\mu$ R/L selectron, smuon, stau	$\tilde{l}_i^{\pm}$, i = 1,..., 6 $\tilde{\nu}_i$, i = 1, 2, 3 sleptons, sneutrinos	0	$e^{\pm}$, $\mu^{\pm}$, $\tau^{\pm}$ ν_e, ν_μ, ν_τ

Direct searches at the LHC with collisions at $\sqrt{s} = 8$–13 TeV have extensively explored the mass range 1–2 TeV/c^2 with negative results [24, 25]. Nevertheless, theories with mass scales in the range 2–10^4 TeV/c^2 remain consistent with current experimental results [26–28]. The best constraints on these models come from indirect searches, like those for cLFV processes.

The sensitivity of processes such as $\mu \to e\gamma$ and $\mu \to eee$ to the SUSY parameters has been well known since the early days of the theory [29]. CLFV arises naturally from the interaction between Standard Model particles and their supersymmetric partners, whose mass matrices are in general not diagonal in the flavor basis (a mechanism similar to that of neutrino-induced cLFV).

For instance, we will briefly illustrate how this works for the $\mu \to e\gamma$ decay in a MSSM with right-handed (RH) Majorana neutrinos, a scenario which predicts branching ratios for $\mu \to e\gamma$ at the edge of present experimental sensitivity [12, 23].

The particle content of the MSSM model is listed in Table 1.1, to which we must add right-handed neutrinos.

Examples of loop diagrams contributing to the $\mu \to e\gamma$ decay amplitude in this scenario are shown

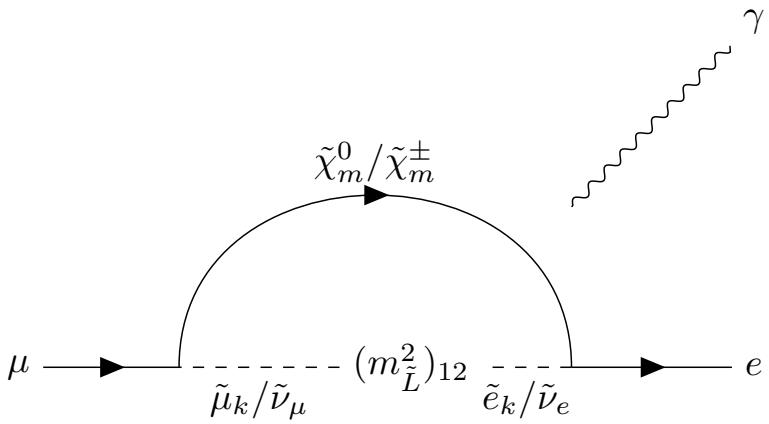

Figure 1.3: Supersymmetric contributions to the $\mu \to e\gamma$ decay in a MSSM model with right-handed neutrinos. In the above diagram, the photon vertex can be attached either to fermion or scalar lines, depending on which field is charged. From [10, 23].

in Figure 1.3. The approximate formula for BR($\mu \to e\gamma$) derived in this framework is [23]:

$$\mathrm{BR}(\mu \to e\gamma) \simeq \alpha^3 \tan^2\beta \frac{\left|m^2_{\tilde{L}}(LL)_{\mu e}\right|^2}{G_F^2 m^8_{SUSY}} \tag{1.10}$$

where:

- α and G_F are respectively the EM and Fermi coupling constants;
- β is a parameter of the specific SUSY model, like $m^2_{\tilde{L}}(LL)_{\mu e}$. It is defined as

$$\beta \equiv \frac{v_u}{v_d}, \quad v \equiv \sqrt{v_u^2 + v_d^2} \simeq 246 \text{ GeV} \tag{1.11}$$

  where v_u and v_d are the two vacuum expectation values developed by the MSSM superpotential involving two Higgs supermultiplets, required to give mass to all fermions present in this model;
- $m^2_{\tilde{L}}(LL)_{\mu e}$ is an element of the slepton mass matrix, which in general is not diagonal in the lepton mass basis and has therefore off-diagonal terms. In this proposed framework, this term can be expressed as a function of relevant parameters like M_N, m_{GUT} (the energy scale of Grand Unification), and the three parameters characteristics of the symmetry breaking mechanism of the model m_0, m_{H_u}, A_0 [22]:

$$m^2_{\tilde{L}}(LL)_{\mu e} \propto \left(2m_0^2 + m_{H_u}^2 + A_0^2\right) \log \frac{m_{GUT}}{M_N} \tag{1.12}$$

- m_{SUSY} is the typical mass scale of sparticles.

The predicted value for BR($\mu \to e\gamma$) will depend on the choice of the (many) unknown parameters of the theory, which however are bounded by many experimental measurements, like limits on neutrino masses, electro-weak parameters and past searches for SUSY.

As clearly shown in Figure 1.4, where each scatter point corresponds to a different set of parameters of this SUSY model, in the case that the sneutrino mass hierarchy is inverted[ii], the parameter space of the theory is still unexplored by past experiments, and the future generation of searches on cLFV processes may fill this gap.

[ii] $m_{\tilde{\nu}_{\tilde{u}_1}} \simeq m_{\tilde{\nu}_2} > m_{\tilde{\nu}_3}$

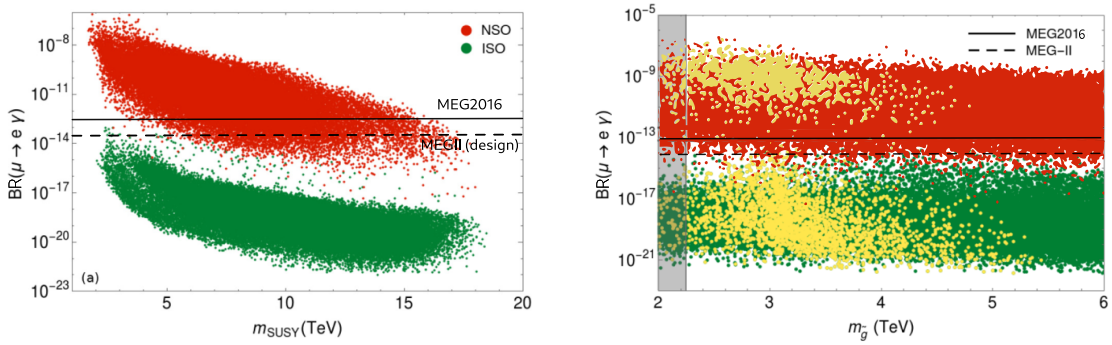

(a) BR($\mu \to e\gamma$) as a function of the SUSY mass scale m_{SUSY}.

(b) BR($\mu \to e\gamma$) as a function of the gluino mass. The grey area is excluded by LHC run 2 searches[30]. In yellow are predictions with SUSY parameters satisfying electroweak naturalness constraints [31].

Figure 1.4: Predictions on BR($\mu \to e\gamma$) calculated in the MSSM model with RH neutrinos described in the text. In red are calculations in the normal sneutrino mass ordering (NSO), in green for the inverted mass ordering (ISO). The past results obtained by the MEG experiment [9] are indicated with a continuous line, while the MEG II expected sensitivity (see Chapter 2) is indicated with a dashed line. Modified from [23].

1.3 A model independent approach

Whatever the specific model for New Physics may be, at low energies it is possible to express them in a model-independent way through effective field theories (EFT): in the low-energy limit, the SM can be extended recurring to non-renormalisable, gauge-invariant operators to build an effective interaction Lagrangian:

$$\mathcal{L} = \mathcal{L}_{SM} + \frac{1}{\Lambda}\sum_a C_a^{(5)} Q_a^{(5)} + \frac{1}{\Lambda^2}\sum_a C_a^{(6)} Q_a^{(6)} + h.c. \tag{1.13}$$

where $\Lambda \gg v = 246$ GeV is the energy scale of New Physics, and $Q_a^{(D)}$ are the dimension-D operators that mediate new phenomena.

CLFV processes are known to be extremely sensitive to New Physics operators also at very high energy scales Λ, allowing to probe regions forbidden to other precision experiments. See Figure 1.5 for a comparison of the search reach on New Physics scale attainable in the near future through many observables.

If the dominant term for flavor symmetry breaking is, for example, a dimension $D = 6$ operator, then the effective interaction Lagrangian can be written in terms of two parameters k and Λ:

$$\mathcal{L}_{eff}^{CLFV} = \frac{m_\mu}{(k+1)\Lambda^2}\overline{\mu}_R \sigma_{\mu\nu} e_L F^{\mu\nu} + \frac{k}{(k+1)\Lambda^2}\overline{\mu}\gamma_\mu e \sum_q \overline{q}\gamma^\mu q + h.c. \tag{1.14}$$

where the first term describes a dipole interaction, while the second describes a four-fermion interaction. A graphical representation of how these operators mediate the processes $\mu \to e\gamma$, $\mu \to eee$, and muon-to-electron conversion in the nuclear field is shown in Figure 1.6. For example, the operator with SUSY particles in Figure 1.3 induces a dipole transition. From the Feynman diagram, one can see that in the presence of a dominant dipole operator, $\mu \to e\gamma$ is favored by a factor α^{-1} compared to the others [10]:

$$\mathrm{BR}(\mu \to eee) \approx \frac{\alpha}{3\pi}\left(2\ln\frac{m_\mu}{m_e} - 3\right) \times \mathrm{BR}(\mu \to e\gamma) \tag{1.15}$$

$$\mathrm{CR}(\mu + N \to e + N) \approx \alpha \times \mathrm{BR}(\mu \to e\gamma) \tag{1.16}$$

where CR stands for "conversion rate". This is the case for example of the SUSY model described in Section 1.2. Conversely, if the dominant operator were the four-fermion one, then $\mu \to e\gamma$ would be

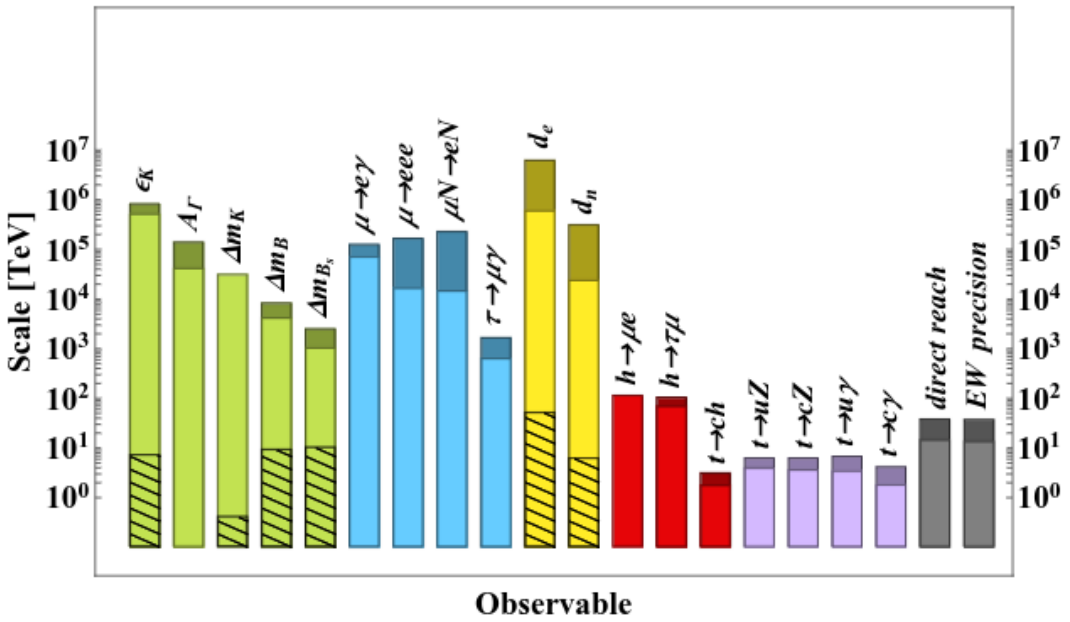

Figure 1.5: Reach in new physics scale of present (light colors) and future (darker colors) facilities, from generic dimension six operators $\mathcal{Q}_a^{(6)}$. Color coding of observables is: green for observables involving K or B mesons, blue for leptons, yellow for Electric Dipole Moments, red for Higgs flavored couplings and purple for the top quark, grey for direct flavor-blind searches and EW precision measurements. Shaded areas represent the reach when flavor violating operators are suppressed. From [18].

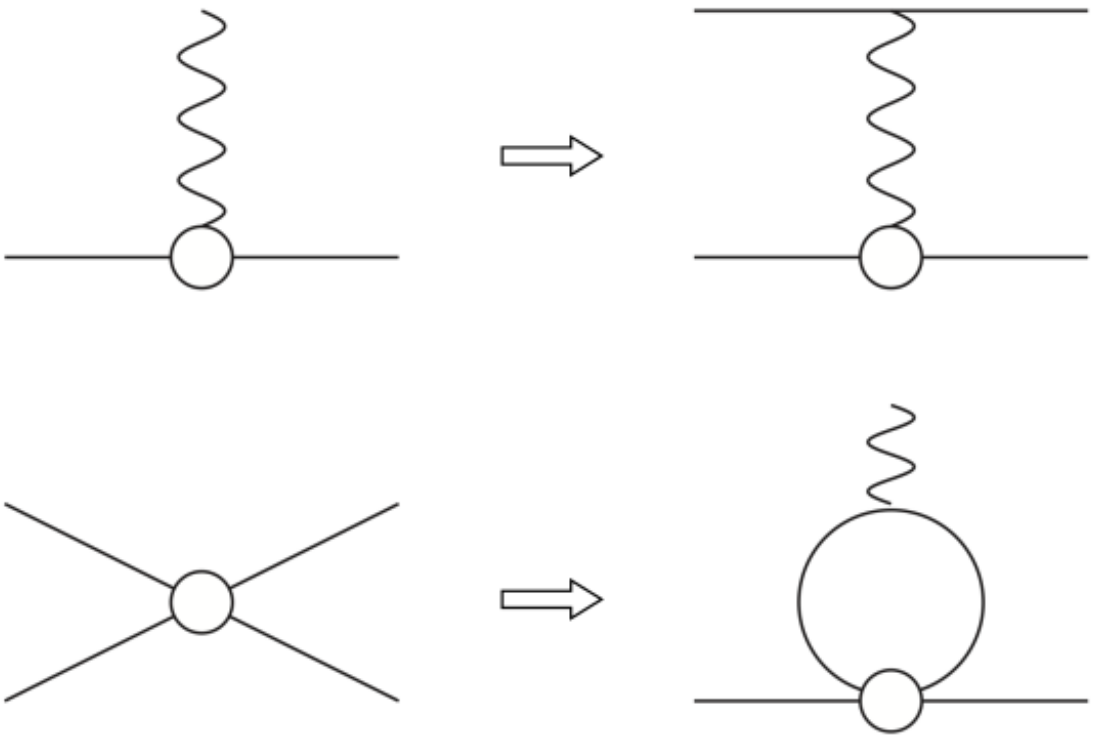

Figure 1.6: Schematic representation of the contribution of a dipole operator to the processes $\mu \to e\gamma$ and $\mu + N \to e + N$ (and also $\mu \to eee$), and of a four-fermion operator to $\mu \to eee$ and $\mu \to e\gamma$ (loop). From [10].

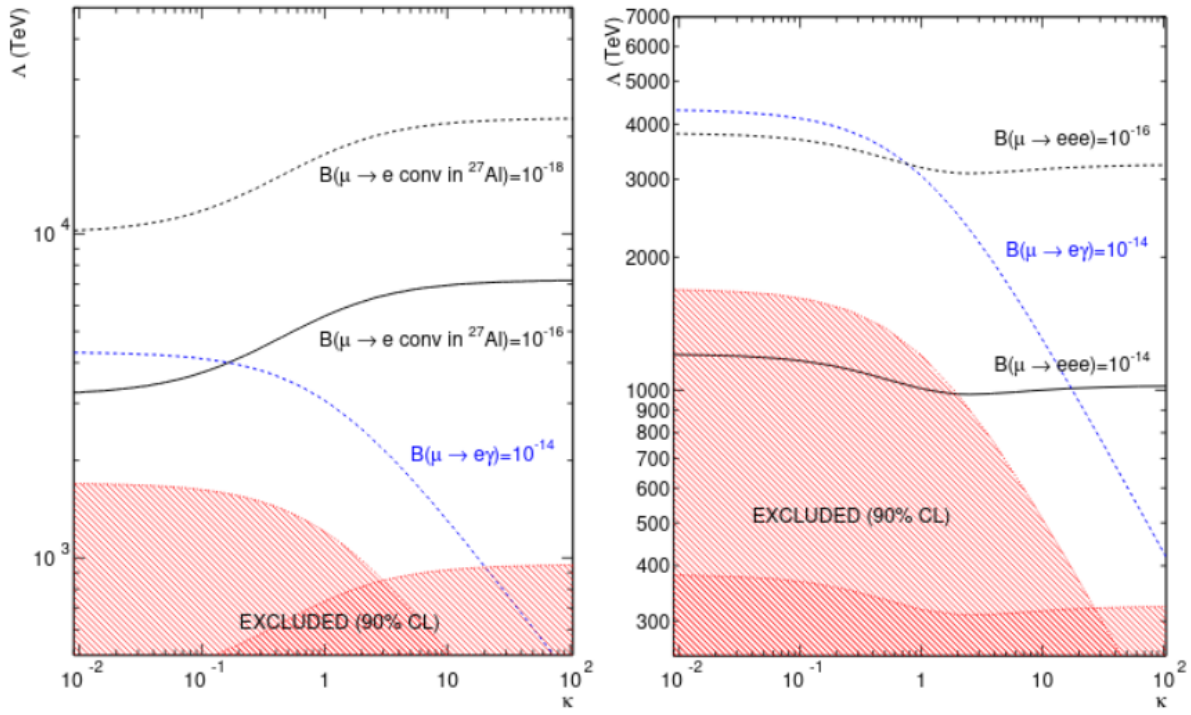

Figure 1.7: Exclusion plot of the parameters k and Λ of an effective Standard Model theory. The constraints come from the results of cLFV searches conducted up to now. The areas that would be excluded by a null result from next-generation experiments such as MEG II, Mu3e, Mu2e, and COMET are enclosed by the respective lines of the searched process. Updated from [32].

suppressed by a factor α. From these observations and from relations 1.15 and 1.16, it follows that the searches for all these processes are complementary and synergistic.

An exclusion plot of the parameters k and Λ of Equation 1.14 is shown in Figure 1.7, where the new constraints that future cLFV experiments may establish are also highlighted: MEG II for the decay $\mu^+ \to e^+\gamma$, Mu3e for $\mu^+ \to e^+e^-e^+$ [33], and Mu2e [34] and COMET [35] for the muon-to-electron conversion process on aluminum nuclei $\mu^-\text{Al} \to e^-\text{Al}$.

Chapter 2

The search for New Physics with the MEG II experiment

The candidate is an active member of the MEG II Collaboration, who participated in all data-taking campaigns since July 2022 as a shifter.

This Chapter focuses on the experimental methods peculiar to the search for the $\mu \to e\gamma$ decay (Section 2.1), with most of the space dedicated to the explanation of the detectors' system of the MEG II experiment (Section 2.2).

The description of the MEG II tracker detector, the Cylindrical Drift Chamber (CDCH), is left for the next Chapter 3 because of the relevance of this item for the discussion within this thesis.

In the last Section 2.3 we explain briefly how other measurements looking for New Physics observables are being investigated within the MEG II experiment: the search for an axion-like particle (ALP) in the decay $\mu \to ea\gamma$ and the search for the X17 boson.

2.1 Searching for $\mu \to e\gamma$

The success of a search experiment depends on the *accumulated statistics*, i.e. the number of total events among which looking for the rare, if even existing, process, and on the capacity of the instrumentation to *distinguish signal from background*.

In the history of experiments working on cLFV searches in the muon sector, any advancement in accelerator facilities marks a jump in the achieved sensitivity, reflecting the large increase of statistics that an experiment can cumulate thanks to that specific innovation (Figure 2.1). The first pioneering works by Hinks and Pontecorvo in 1947 [36] used cosmic rays as a source of muons. Since the 1950s, accelerator facilities allow to collect significantly larger samples of data: stopped pion beams were employed until the 1970s, when muon beams took over. Today, the innovations in the sector of muon beamlines, such as the HiMB upgrade at Paul Scherrer Institut (PSI) [37, 38], continue to open new possibilities in this field of Particle Physics for future projects [39, 40].

Modern experiments searching for the $\mu \to e\gamma$ or $\mu \to eee$ decay exploit positive muon beams[i], which offer a two-fold advantage: first, μ^+ beams can attain higher intensity with respect to μ^- beams (see next Section); second, positively charged muons don't undergo nuclear capture in the stopping target.

Indeed, it is experimentally desirable to observe the decay of the muon at rest, because of the clear signature of the signal which can help discriminating the background. The $\mu \to e\gamma$ decay is a two-body

[i] For this reason in the text we will always refer to the process $\mu^+ \to e^+\gamma$.

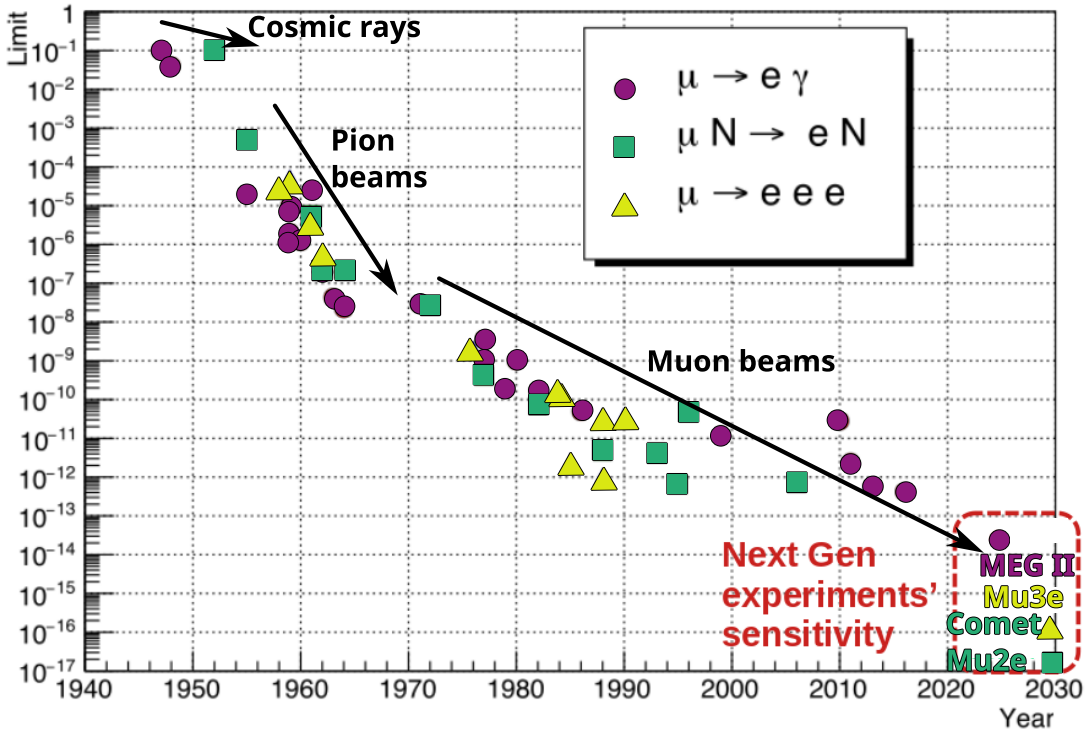

Figure 2.1: Progression over the years of the limits on cLFV processes with muons. Modified from [10].

process, therefore in the muon rest frame the decay products' kinematic is fixed:

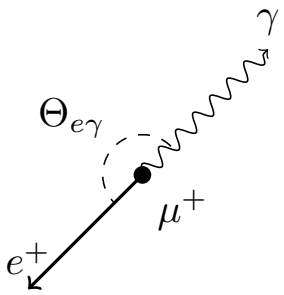

- Monochromatic energies: $\begin{cases} E_e = \frac{m_\mu^2+m_e^2}{2m_\mu} \approx 52.83 \text{ MeV} \\ E_\gamma = \frac{m_\mu^2-m_e^2}{2m_\mu} \approx 52.83 \text{ MeV} \end{cases}$
- Back-to-back emission: $\vec{p_e} = -\vec{p_\gamma} \rightarrow$ angle between direction of flight $\Theta_{e\gamma} = \pi$
- Coincident emission time: $t_e - t_\gamma \equiv t_{e\gamma} = 0$

These signal characteristics can be mimicked by background events, which arise from the following processes [41]: *radiative muon decay* events (RMD) and *accidental coincidences.*

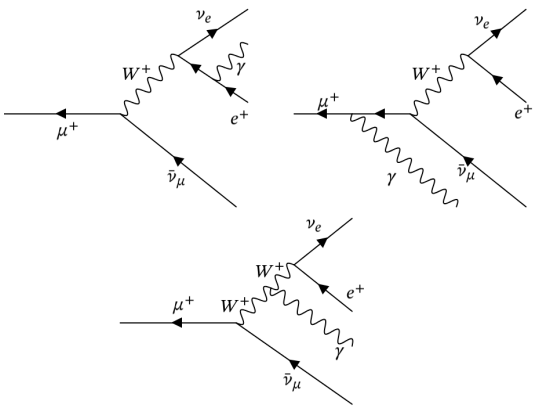

Figure 2.3: Feynman diagrams for the RMD.

Radiative Muon Decay Apart from the common $\mu \rightarrow e\nu\overline{\nu}$ decay (BR $\approx$ 100 % [17]), the $\mu \rightarrow e\nu\overline{\nu}\gamma$ decay is possible (BR = $(6.0 \pm 0.5) \times 10^{-8}$ for $E_\gamma > 40$ MeV and $E_e > 45$ MeV [17]) with the internal state radiation of a photon (Feynman diagrams in Figure 2.3). The positron and photon are emitted simultaneously, and in the condition of them flying in almost opposite directions, with the two neutrinos carrying very few energy, an RMD can mimic a $\mu \rightarrow e\gamma$ decay.

The effective RMD branching ratio (i. e. normalized to BR($\mu \rightarrow e\nu\overline{\nu}$)) around a signal region of size $\delta x \delta y \delta z$, with $\delta x \equiv \frac{2\delta E_e}{m_\mu}$, $\delta y \equiv \frac{2\delta E_\gamma}{m_\mu}$, $\delta z \equiv \pi - \delta\Theta_{e\gamma}$ being the experimental resolutions on the kinematic

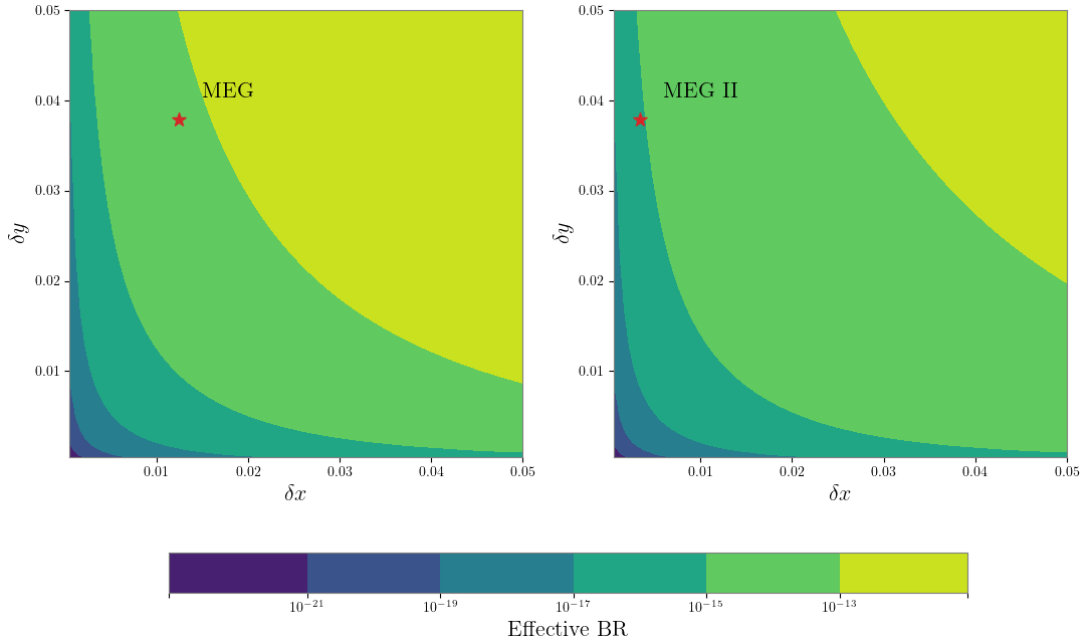

Figure 2.2: Effective branching ratio of the RMD decay as a function of resolution δx and δy. On the left with MEG angular resolution, on the right for MEG II. Calculated from Equation 2.1.

variables, is calculated from [41]:

$$\mathrm{BR}(\mu \to e\nu\overline{\nu}\gamma) = \frac{1}{\Gamma(\mu \to e\nu\overline{\nu})} \int_{1-\delta x}^{1} dx \int_{1-\delta y}^{1} dy \int_{0}^{\delta z} dz \frac{d\Gamma}{dx dy dz} \tag{2.1}$$

The values of the effective branching ratio for a set of experimental resolutions are depicted in Figure 2.2, with the MEG and MEG II experiment conditions highlighted: in MEG II the background level from RMD is below 10^{-15}, improving the MEG rejection capabilities, where the effective RMD branching ratio, i. e. the probability of observing RMD decays in the signal region, was $\approx 10^{-14}$ [9].

Accidental coincidences The main source of background in MEG and MEG II experiments, accounting for more than 90% of the background events in the signal region, is the accidental coincidence of in-time and anti-parallel high-energy positrons and photons produced in independent processes (bremsstrahlung, annihilation-in-flight, muon decays).

The number of accidental background events, N_{acc}, expected in the signal region depends both on the detectors resolutions ($\approx \delta q$) and on the peculiarities of each experiment, which may favor a specific process as a source of high-energy particles. For example, in lighter detectors annihilation-in-flight (AIF) of positrons or bremsstrahlung are less likely. This is why in MEG and MEG II experiments the detector apparatus are designed to have the lowest affordable material budget. When AIF or bremsstrahlung are suppressed, only muon decay processes remain as the most relevant source for accidental coincidences and the following expression for N_{acc} can be derived [9, 41]:

$$N_{acc} \propto R_{\mu}^2 \cdot \delta t_{e\gamma} \cdot \delta E_{\gamma}^2 \cdot \delta E_e \cdot \delta \Theta_{e\gamma}^2 \tag{2.2}$$

The quadratic dependence on the beam intensity R_μ implies the necessity for experiments involved in the $\mu \to e\gamma$ search to use continuous muon beams instead of pulsed muon beams for the lower instantaneous luminosity.

2.2 The MEG II experiment

The MEG II collaboration is searching for the $\mu^+ \to e^+\gamma$ decay at the Paul Scherrer Institut (PSI) muon beam facility. The MEG II experiment has been fully commissioned during the year 2021; physics data

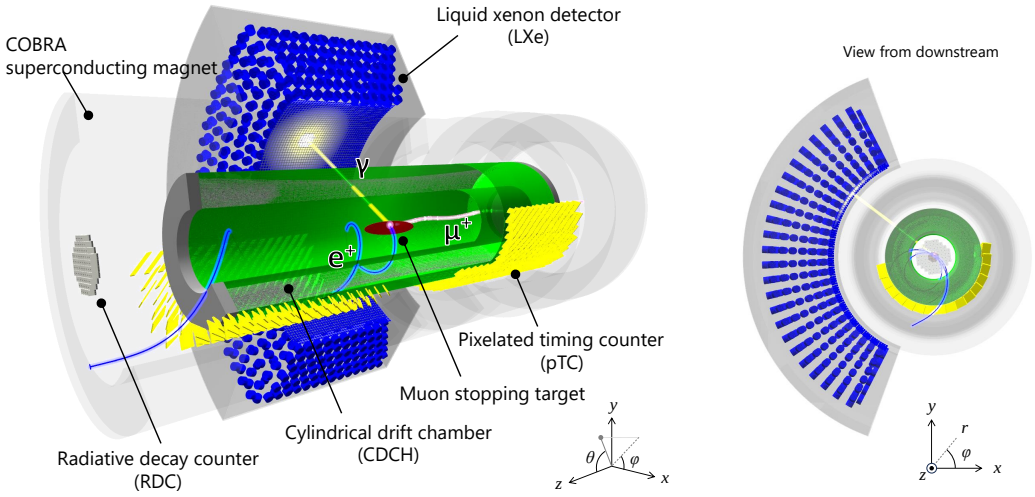

Figure 2.4: MEG II detectors scheme and global reference frame.

taking started right after and is scheduled to end in 2026, when the PSI muon facility will be closed for the HiMB upgrade. By that date, MEG II goal is to refine the sensitivity of the branching ratio for this decay to $\mathcal{B}(\mu^+ \to e^+\gamma) < 6 \times 10^{-14}$ (90% CL). This would mark a significant improvement, achieving an order of magnitude greater precision compared to the limit set by the MEG experiment $\mathcal{B}(\mu^+ \to e^+\gamma) < 4.2 \times 10^{-13}$ (90% CL) [9].

To pursue this objective, the MEG II apparatus has been designed [42] to improve significantly the detector system of the precursor MEG experiment, although the underlying idea of the experiment has remained almost unchanged. A schematic view of the detector with its main components highlighted is drawn in Figure 2.4. The detector is located downstream the πE5 beamline in the high-intensity proton accelerator facility at PSI, where the world's most intense continuous positive muon beam is located. Muons are stopped on a thin plastic target at the center of the apparatus to measure the decay products (see Section 2.2.2). In brief, the apparatus consists of a Liquid Xenon photon detector (LXe, Section 2.2.4) and a magnetic spectrometer (Section 2.2.3 and Chapter 3) composed of the non-solenoidal superconducting magnet COBRA, the Cylindrical Drift Chamber tracker (CDCH) and a timing detector made of scintillating tiles (pTC). An auxiliary detector, the Radiative Decay Counter (RDC), allows the mitigation of the accidental background (Section 2.2.5). More details about the apparatus can be found in [43] and references therein.

The equipment to run the MEG II experiment is composed also of many others detectors and items necessary to perform a full calibration of the system. The list of calibration methods used is given in Table 2.1. More details about calibration techniques follow in the next sections or in the dedicated chapters for the case of the CDCH. An exhaustive discussion can be found in [43, 44].

2.2.1 MEG II's coordinate system

The global reference frame of the MEG II experiment, in both cylindrical and Cartesian coordinates, is shown in Figure 2.4. The z-axis is aligned with the COBRA axis in the direction of the muon beam; the y-axis points upward, and the x-axis is therefore defined to point in the opposite direction with respect to the LXe detector. The azimuthal angle ϕ is zero along the x-axis and increases counterclockwise. The polar angle θ is measured with respect to the z-axis. We refer to the region with $z < 0$ (closer to the beam entrance) as upstream (US), and to the opposite side as downstream (DS).

The origin of the reference frame is the geometrical center of the CDCH. All other detectors are aligned relative to it, as discussed in Section 2.2.6.

Table 2.1: The ensemble of calibration procedures for MEG II.

Processes		Energy	Goal	Frequency
Cosmic rays	atmospheric $\mu^{\pm}$	Wide energy range ($\mathcal{O}$(GeV))	CDCH-XEC alignment CDCH wire-by-wire alignment XEC purity & energy scale	annually annually weekly
Charge Exchange (CEX)	$\pi^- p \to n\pi^0(\gamma\gamma)$	55 and 83 MeV γs	XEC energy calibration	annually
Cockroft-Walton proton accelerator	^{7}Li(p,γ)^{8}Be	14.8, 17.6 MeV γs	XEC energy calibration	weekly
Radioactive sources	^{241}Am(α, γ)^{237}Np	5.6 MeV αs	XEC MPPCs calibration (PDE)	continuous
Neutron generator	^{58}Ni(n, γ)^{59}Ni	9 MeV γs	XEC energy calibration	weekly
LED		UV light	XEC photosensors calibration (gain)	continuous (1 Hz)
pTC Laser system		λ = 401 nm, FWHM = 60 ps	pTC time offset calibration	weekly
RMD	$\mu \to e\nu\overline{\nu}\gamma$	$\gamma > 40$ MeV; $e^+ > 45$ MeV	pTC-XEC time calibration	continuous
Michel decay	$\mu \to e\nu\overline{\nu}$	$e^+ > 45$ MeV	CDCH calibration Target alignment pTC time offset calibration	continuous

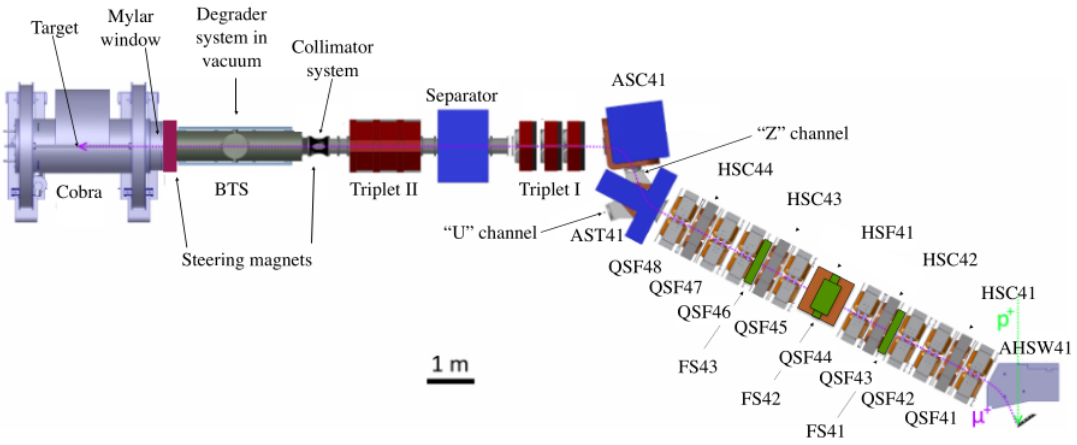

Figure 2.5: πE5 beamline section connected to the MEG II experiment.

2.2.2 Beamline and target

Beam characteristics The PSI muon beam is produced sending 590 MeV protons, accelerated by the PSI Ring Cylcotron, onto a rotating carbon target. Muons are produced from pion decay resulting from the interaction of protons with the target's nuclei [45]. The πE5 beamline delivers the most intense continuous μ^+ beam in the world, up to 10^8 μ^+/s, transporting *surface muons* from pions decay near the production target edges. Surface muons have a typical momentum of 28 MeV/c, with a small momentum bite of 5-7%.

The muon beam is accurately tuned thanks to various beamline elements, represented in Figure 2.5, to deliver a beam with the characteristics needed for the MEG II experiment:

- a slit system (FS41-42-42) reduces the beam intensity to a level manageable by the detectors: in MEG II physics runs between 2021 and 2024 the beam intensity was varied between 2–5×10^7 μ^+/s;
- A Wien filter separator allows to purify the muon beam removing pions and positrons contamination. The πE5 beamline is suited to deliver also a pure π^- or e^+ beam;
- The Beam Transport Solenoid (BTS) links the beamline magnetic field to COBRA's one, allowing muons to reach the center of the apparatus with minimum deflections.

The beam profile and beam intensity at the center of MEG II experiment is measured at the beginning of each data-taking period using a scintillating tile coupled to an avalanche photodiode [42]. Measurements of the beam intensities after beam tuning are compatible to the goal values $2 - 5 \times 10^7$ μ^+/s within 5% each year. The measured beam profile (year 2021) is shown for reference in Figure 2.6 (a). The typical beam spot width is $\sigma_x \approx \sigma_y \approx 10$ mm, while the beam spot position can shift every year up to a few millimeters. All beam parameters are very stable during data taking.

Target MEG II's target (Figure 2.6 (b)) is an elliptical foil of dimensions: length = 270 mm, width = 66 mm, thickness = (174 ± 20) µm (the error being the maximum deviation from the central value) made of a plastic scintillator material, BC400. Material and thickness were chosen to optimize the trade-off between stopping efficiency and material budget [46]. It is positioned at the center of the apparatus, slanted of an angle of 15° with respect to the beam direction z. This setup augments muons path inside the target, increasing the stopping efficiency which is measured with Monte Carlo simulations to be 89%, while simultaneously reducing the material encountered by the decay products.

Precise knowledge of the target position is essential to properly identify $\mu^+ \to e^+\gamma$ candidates events based on the opening angle between the two particles: the positron trajectory is back-propagated to the target surface where the emission angles (ϕ_e, θ_e) are measured as well as its origin (x_e, y_e, z_e) and

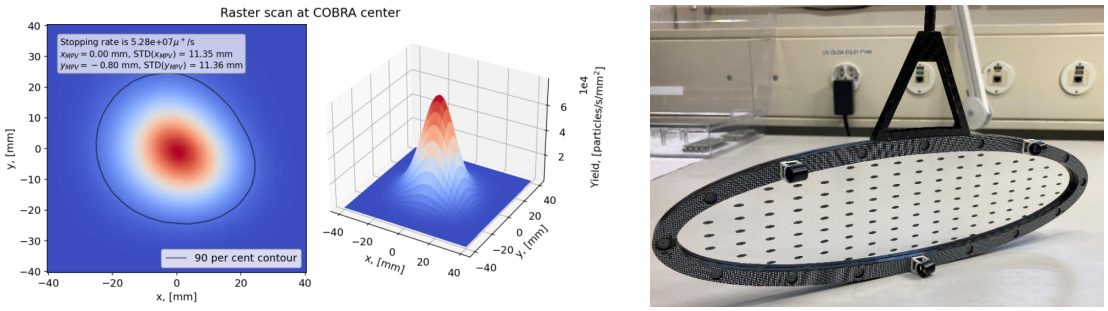

(a) (b)

Figure 2.6: (a) Beam profile measured at COBRA center for a stopped muon rate $R_\mu = 5.3 \times 10^7$ μ^+/s; (b) MEG II target.

these measurements are combined with the measurement of the photon interaction point in the LXe detector (x_γ, y_γ, z_γ) to evaluate the opening stereo angle between the two particles $\Theta_{e\gamma}$. The position of the target and its planarity need to be carefully measured during the whole data taking period to avoid systematic effects on the measurement of $\Theta_{e\gamma}$: the uncertainty in target position and planarity was the leading systematic uncertainty in MEG experiment [9].

The target position and planarity is measured exploiting dots and holes drawn and pierced on the target surface, as visible in Figure 2.6 (b). Two CMOS photo cameras installed at the entrance of the COBRA magnet take pictures of the target with a few minutes interval [47, 48]. The imaging of the dots on the pictures allows a precise determination of the target center position, with an uncertainty of 12 µm in the direction perpendicular to and 30 µm in that parallel to the target plane, as well as a control of its deformations with a sensitivity below 50 µm. Holes in the target are used to align the target with respect to the CDCH. Since muons fly through the holes, the distribution of decay vertex in the target plane reconstructed from the positron tracks allows to measure the holes positions. This method is detailed in Chapter 4 Section 4.4. This measurement can be combined with the photo cameras measurements to assess the relative positioning of the CDCH and the target.

2.2.3 The spectrometer

Table 2.2: Performances of the MEG II spectrometer measured for the 2021 analysis (efficiency and kinematical variables resolutions) are compared with those reached in MEG and those predicted by the Monte Carlo simulations for the system upgrade. We quote the performances for signal-like events at 3×10^7 μ^+/s beam intensity.

Observable	MEG II (2021)	MEG II design	MEG
ε_{e^+}	0.74	0.78	0.30
$\sigma_{\theta_{e^+}}$	7.2 mrad	6.7 mrad	9.4 mrad
$\sigma_{\phi_{e^+}}$	4.2 mrad	3.7 mrad	8.7 mrad
$\sigma_{p_{e^+}}$	89 keV	130 keV	360 keV
$\sigma_{t_{e^+}}$	43 ps	30 ps	70 ps

The spectrometer is the detector system devoted to measuring positron kinematic variables. MEG II spectrometer is composed by two subdetectors immersed in the magnetic field generated by the superconducting magnet COBRA:

- the pixelated Timing Counter (pTC) is a timing layer made of scintillating tiles;
- the Cylindrical Drift Chamber (CDCH) is the tracker.

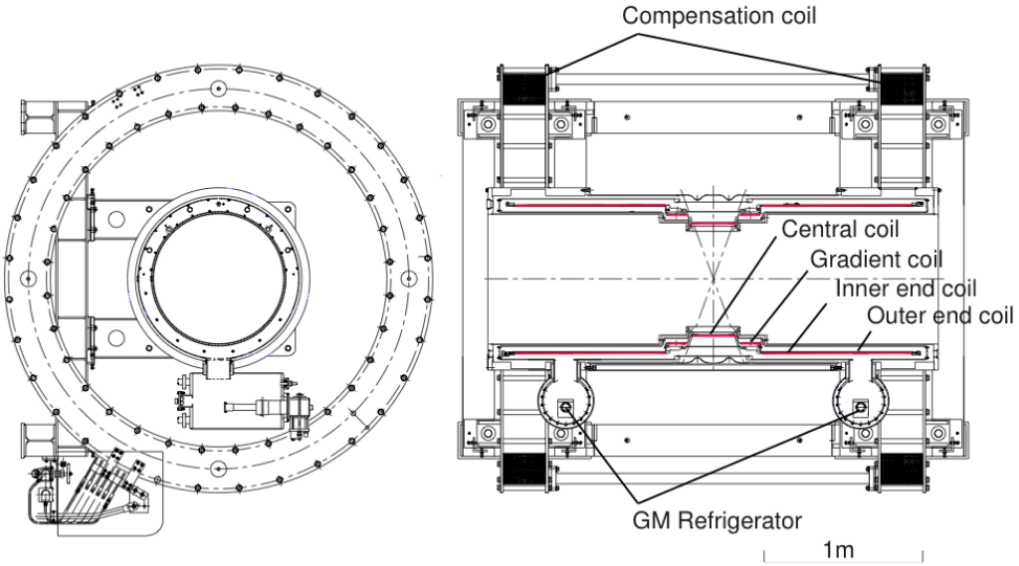

(a) COBRA magnet technical drawing, frontal and lateral view.

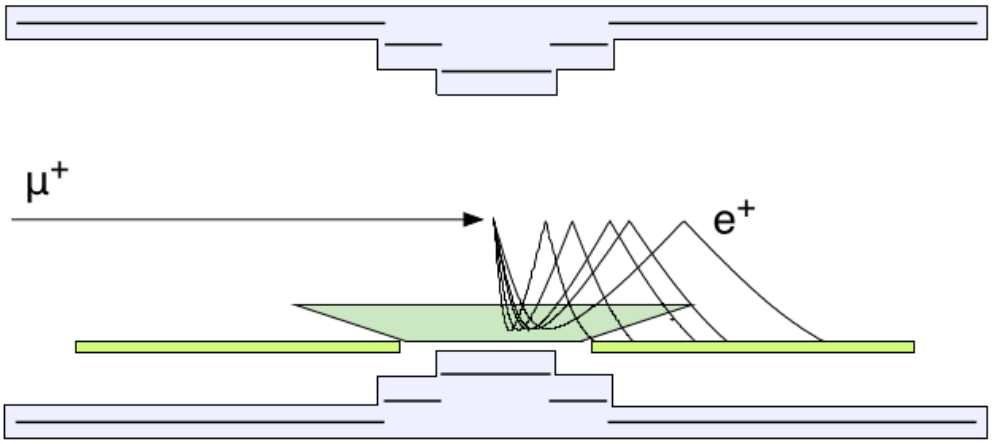

(b) Lateral view of various positron trajectories inside the MEG spectrometer. The positrons have equal momentum but different exit angles from the target, although for effect of the COBRA field they have almost equal bending radii.

Figure 2.7: The COBRA magnet.

The upgrade project aimed at improving significantly the tracking efficiency and resolutions on all relevant kinematic variables: time, angles, momentum, position at the target. As reported in Table 2.2, these goals have been fully achieved.

COBRA superconducting magnet In MEG and MEG II the spectrometer doesn't use a solenoidal magnetic field to bend charged particles, but a superconducting magnet generating a gradient magnetic field of intensity $0.1\ \mathrm{T} < |\vec{B}| < 1.27\ \mathrm{T}$, with maximum intensity at $z = 0$. The technical drawing of the magnet is depicted in Figure 2.7 (a). Because of its peculiar effects on positrons trajectories, the magnet is denominated COBRA, i.e. COnstant Bending RAdius [49].

The peculiar properties of this gradient magnetic field allow to have a curvature radius in the transverse plane (almost) independent of the emission angle, therefore it is possible to find a tracker geometry with full acceptance only for particles above a certain absolute momentum, minimizing the occupancy of the detector for low momentum particles. A second advantage of this design is that particles are swept away faster, with the "helix" path increasing at every step in $|z|$ towards the outside

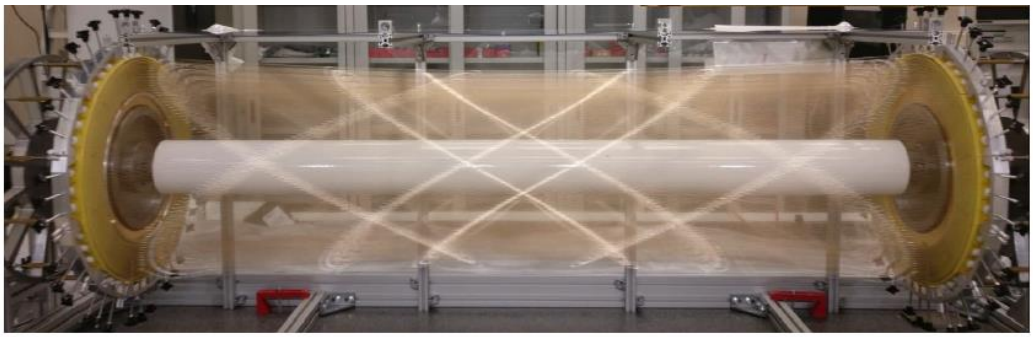

Figure 2.8: The MEG II Cylindrical Drift Chamber fully wired.

of the tracker. These effects are illustrated in Figure 2.7 (b).

The Cylindrical Dirft Chamber, CDCH The tracking detector for the MEG II experiment is an ultra-light single-volume cylindrical drift chamber [50], referred to as CDCH.

Already in MEG the tracking system was composed of 16 planar drift chambers [44]: because the main source of uncertainty in position measurements for low momentum particles ($p_e \lesssim 50$ MeV/c) is the multiple scattering, a light detector, like a drift chamber, is a sensitive solution. Keeping the tracking detector as thin as possible has also the advantage of reducing possible sources of high-energy photons which would increase the combinatorial background.

The upgraded tracker design has been sensibly improved in MEG II with respect to MEG, to achieve much higher detection efficiency and at least a factor two improvements in resolution.

The individual drift chambers of MEG have been replaced with a single-volume detector ≈ 1.93 m long with a cylindrical symmetry around the beam axis z with full acceptance for signal positrons, covering the area in the $x - y$ plane between a radius of 19.6 and 28.5 cm.

The detector is divided in 9 detection planes with a stereo configuration to improve the resolution on the longitudinal coordinate z: the stereo angle is $\pm 7.5^{\circ}$, depending if the plane number is even or odd. The stereo geometry is well visible in the CDCH envelope shape in Figure 2.8, where the fully wired detector is illustrated. To cope with the very intense radiation environment, the CDCH is heavily segmented: the active volume is divided in 1728 square cells (192 per plane) with small sides between 5.8 and 8.7 mm, depending on the plane and on the position along z.

In order to keep the material budget as low as possible:

- an open-cell geometry is adopted, where the drifting electric field is shaped by eight cathode wires arranged in a square shape around the anode wire. In total, ≈11000 wires compose the detector, including two layers of guard wires at the innermost and outermost radii;
- therefore, extremely thin silver-plated aluminum (Al/Ag) cathode wires are used, with diameters of 40 and 50 µm (to be compared with 80 µm diameters commonly used, e. g. the drift chamber of the KLOE experiment [51]). The anodes (20 µm diameters) are made of gold-plated tungsten;
- the gas mixture used is also very light: 90:10 Helium - isobutane + additives (1.5% isopropanol + 0.5% O_2) for stability.

(a) Downstream module of the pTC.

(b) An event in the pTC.

Figure 2.9: The pixelated Timing Counter detector scheme.

The total material budget typically traversed by a signal positron of 52.83 MeV corresponds to 1.6×10^{-3} X_0 per turn.

All details on its construction, operations and performances are left to Chapter 3 and can be found in great detail in [50].

The pixelated Timing Counter, pTC The pixelated Timing Counter (pTC) is the timing layer of the MEG II spectrometer, providing precise measurement of the positron arrival time t_e. It is composed of 512 tiles of plastic scintillator with dimensions $120 \times (40 \text{ or } 50) \times 5$ mm^3 each read by an array of six SiPMs of 3×3 mm^2 area. The 512 tiles are arranged in two identical modules, one upstream and one downstream, covering the regions 23.0 cm $\leq |z| \leq$ 116.7 cm and $-165.8^\circ \leq \phi \leq +5.2^\circ$ (Figure 2.9). The entire setup, optimized with Monte Carlo studies, guarantees full acceptance for positrons coming from the $\mu \to e\gamma$ decay [42, 52].

The position of each tile in the pTC is measured with a FARO 3D scan with an error on the position smaller than 1 mm. The impact of such a small uncertainty on the tile position translates to an error on the positron's time-of-flight measurement around 1-5 ps.

The pTC is protected against air humidity to avoid fast deterioration of the scintillator material and SiPMs are cooled down to $\approx 15^\circ$ C with a water cooling system to reduce the dark count rates. Since 2022, tiles and SiPMs which have suffered from too much radiation damage are substituted annually to maintain the detector performances.

The pTC timing performances depend on the number of tiles N_{hit} hit by the incoming positron:

$$\sigma_{t_{e^+}}(N_{hit}) = \frac{\sigma t_{e^+}^{single}}{\sqrt{N_{hit}}} = \frac{\sigma t_{e^+}^{counter} \oplus \sigma t_{e^+}^{off} \oplus \sigma t_{e^+}^{elec}}{\sqrt{N_{hit}}} \tag{2.3}$$

where $\sigma t_{e^+}^{counter}$ is the intrinsic counter resolution, $\sigma t_{e^+}^{off}$ is the uncertainty on time offset between counters and $\sigma t_{e^+}^{elec}$ is the uncertainty on the electronic transient time.

The relative time offset between counters is calibrated using both a laser system [53] and a procedure involving reconstructed positron tracks inside the pTC [43]: another advantage of having a segmented timing layer is that it can reconstruct tracks in a coarse way. The two methods allow to keep σt_e^{off} below the level of 20 ps.

2.2.4 The Liquid Xenon photon detector, XEC

The measurement of the photon energy, timing and flight direction is performed with a homogeneous photon detector filled with $\approx$ 900 liters of Liquid Xenon (LXe), called XEC.

The MEG experiment has been a precursor in the development of large LXe detectors, holding the record for the largest one until the commissioning of the XENONnT experiment. Liquid Xenon indeed is an appealing scintillator meeting all requirements for the MEG and MEG II experiments:

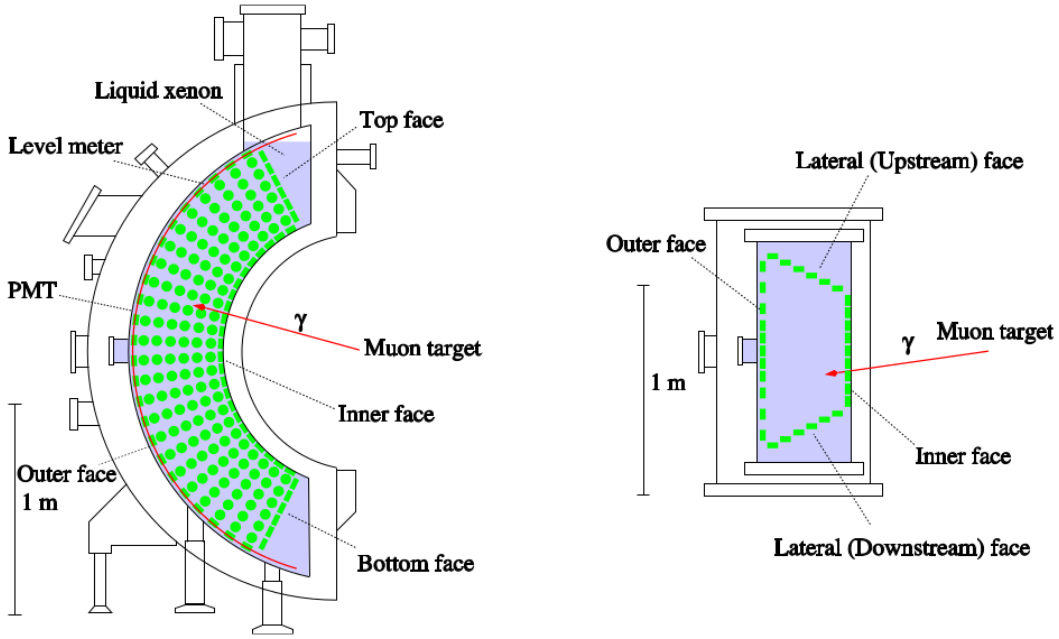

Figure 2.10: Design of the MEG and MEG II XEC detector. In green, PMTs are highlighted. In MEG II the inner face PMTs are replaced with MPPCs.

- scintillation light is emitted according to one of these two processes of excitation or ionization of the Xenon atoms or Xe_2 dymers [54]:

$$Xe^* + Xe \rightarrow Xe_2^* \rightarrow 2Xe + light$$

and

$$\begin{aligned} Xe^+ + Xe &\rightarrow Xe_2^+ \\ Xe_2^+ + e &\rightarrow Xe + Xe^{**} \\ Xe^{**} &\rightarrow Xe^* + heat \\ Xe^* + Xe &\rightarrow Xe_2^* \rightarrow 2Xe + light \end{aligned}$$

The characteristic time of the two processes are respectively 4 ns and 20 ns: such fast responses are ideal for building a photon detector sustaining high interaction rates and not being overwhelmed by *pile-up*;

- Xenon is transparent to its own scintillation light, which has a wavelength of $\lambda = 175 \pm 5$ nmm in the VUV range, and can be easily purified to remove contaminating elements: attenuation effects are so small that it is possible to build a homogeneous detector several radiation length long;

- the large atomic number of Xenon ($Z = 54$, $A = 131$), larger than any other noble gas used in detectors technologies, implies a small radiation length X_0 and therefore a compact detector can contain most of the electro-magnetic shower. In MEG II (and MEG) the LXe detector has a depth of ≈ 38.5 cm $\approx 14\ X_0$;

- a very good energy resolution is attainable thanks to the very high Light Yield, which is almost 40k photons/MeV, comparable with the NaI Light Yield (46k photons/MeV).

MEG II reused the old detector metal vessel and cryostat, which cools the Xenon down to $\sim$ 165 K. It is "C" shaped, as is illustrated in Figure 2.10, and has a limited angular acceptance of $\approx$11% for photons emitted from the target. In MEG, the detector cryostat was instrumented with 864 2-inch

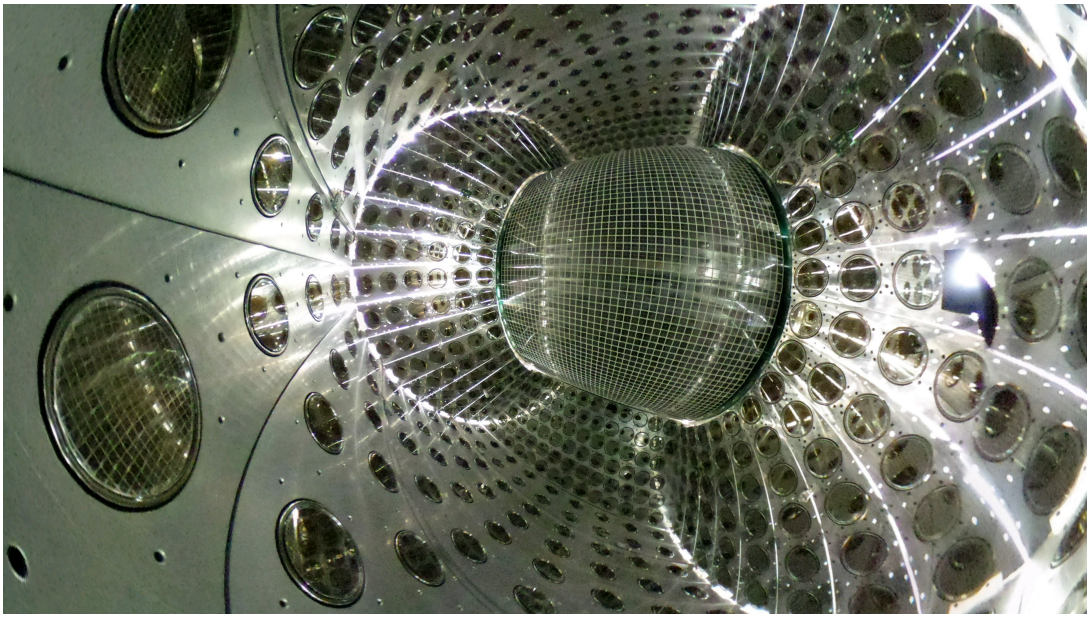

Figure 2.11: View of the inside of the XEC detector with MPPCs on the inner face PMTs all around.

photomultipliers (PMTs) arranged on all six detector faces. A part of these PMTs has been reused in MEG II for the back and lateral faces. Instead, the ≈ 200 PMTs covering the inner face have been replaced with 4096 Multi-Pixel Photon Counters (MPPCs) of 15×15 mm^2 area. Both PMTs[ii] and MPPCs result from an intense R&D with the Hamamatsu company to develop UV-sensitive photo detectors. A view of the inside of the detector with all photosensors allocated is shown in Figure 2.11. In the upgrade design [42], the use of MPPCs on the photon entrance window of the detector was intended to achieve a better energy and spatial resolution and increased pile-up identification capabilities thanks to the more segmented and denser coverage of the detector volume.

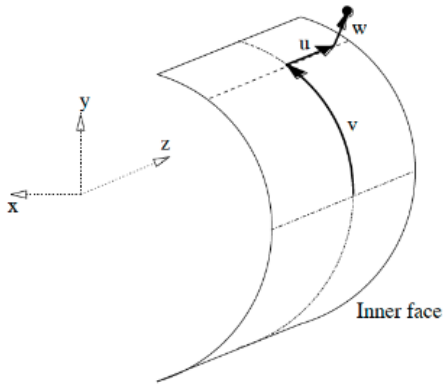

Figure 2.12: LXe local coordinate system.

The local coordinate system (u, v, w) for the LXe detector is defined as in Figure 2.12: the u-axis is parallel to the beam axis and has its origin at COBRA center; the v-axis is tangent to the surface of the entrance face and has its origin at the height of COBRA center; the w coordinate measures the conversion depth of the photon, with the w-axis defined as the direction perpendicular to the detector's inner face and the axis origin starting at the MPPC plane.

The kinematics of the incident photon is reconstructed from the charges Q and timings of the photosensors signals caused by the scintillation light of the LXe. All details about the photon analysis can be found in [43, 55].

The number of scintillation photons N_{pho} impinging on each photosensor is computed as:

$$N_{pho} = \frac{Q}{e \cdot G \cdot F_{EC} \cdot \mathcal{E}} \tag{2.4}$$

where e is the elementary charge, G is the photosensor's gain, F_{EC} is the photosensor's excess charge factor, $\mathcal{E}$ is the quantum efficiency, for PMTs, or the photon detection efficiency (PDE) for MPPCs. The first conversion position of the incident photon and its energy are reconstructed starting from N_{pho}.

[ii] Model Hamamatsu R9869.

The position reconstruction is obtained through the minimization of the quantity:

$$\chi^2_{pos}(\vec{x}_{LXe}) = \sum_i \left(\frac{N_{pho,i} - C \times \Omega_i(\vec{x}_{LXe})}{\sigma_{N_{pho}}} \right)^2 \tag{2.5}$$

where C is the light-yield, $\Omega_i(\vec{x}_{LXe})$ is the solid angle at position $\vec{x}_{LXe}$ subtended by the photosensor and $\sigma_{N_{pho}} = \sqrt{N_{pho} \times \mathcal{E}}$ is uncertainty on N_{pho}. For this calculation only MPPCs are considered as they give the best spatial resolution. The sum runs over all MPPCs in a region around the MPPC which has detected the most scintillation photons.

The photon energy E_γ is reconstructed using the following equation:

$$E_\gamma = S_E \times T(t) \times F(u,v,w) \times \left[\sum_i w_i(u,v,t) \times N_{pho,i} \right] \tag{2.6}$$

where S is the energy scale to convert N_{pho} in an energy measurement, the rest are correction factors determined through dedicated calibration procedures as detailed in [55]: $T(t)$ accounts for temporal variations of the energy scale; $F(u,v,w)$, is a position dependent correction of the energy response of the LXe detector; $w_i(u,v,t)$ is a correction term for the light observed by each photosensor which takes into account dead channels around the sensors, their spatial coverage as a function of the photon conversion point, the time evolution of the light yield.

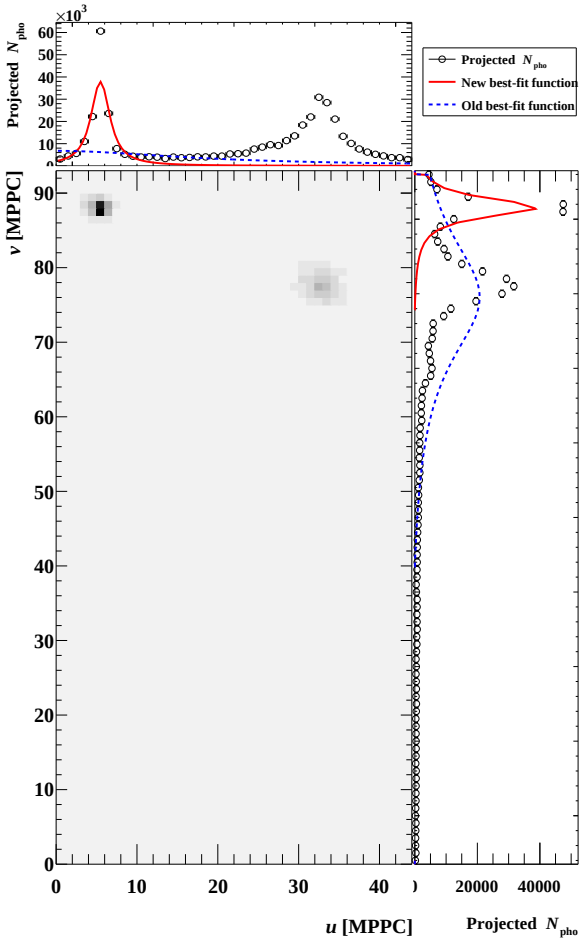

Figure 2.13: Reconstructed positions of two photons in an pile-up event. In the bi-dimensional view, the distribution of N_{pho} for all MPPCs is shown. The one-dimensional projections show N_{pho} projection over u or v. The best fit function (red), used to extract the conversion point position, is superimposed.

The time of the photon first interaction in the LXe detector is reconstructed using the timing of each photosensor, calculated from the waveform shape.

Both PMTs gain and MPPCs PDE deteriorate during the data taking period in the high-rate environment: the first is degraded by the large photoelectric current induced by scintillation photons, the latter by radiation damages. In Figure 2.14 (a) the temporal evolution of the PMTs' gain is shown. Jumps in the gain correspond to HV tuning to compensate the observed loss. The MPPCs' gain is quite stable during the runs, with a fluctuation of $\approx 2\%$ in 2021 because of temperature variations inside the detector. MPPCs' PDE temporal degradation is caused by radiation damages. The trend is shown in Figure 2.14 (b). To recover the PDE, after each year of data taking, an annealing procedure on MPPCs is conducted: between 2021 and 2022 the average PDE recovery was 9.4%, from 6.0% to 15.4% PDE; a similar result was obtained before the 2023 run, while the annealing procedure carried out after 2023 and 2024 runs however didn't manage to increase the PDE, which is now at an average value of 9%. The reason is currently under investigation.

Various types of calibration data (outlined in Table 2.1) are collected at regular intervals during the physics run to monitor the time evolution and uniformity of the detector response, which are essential to maintain optimal trigger conditions on the photon energy and for the offline detector calibration towards the physics analysis (see Section 2.2.7):

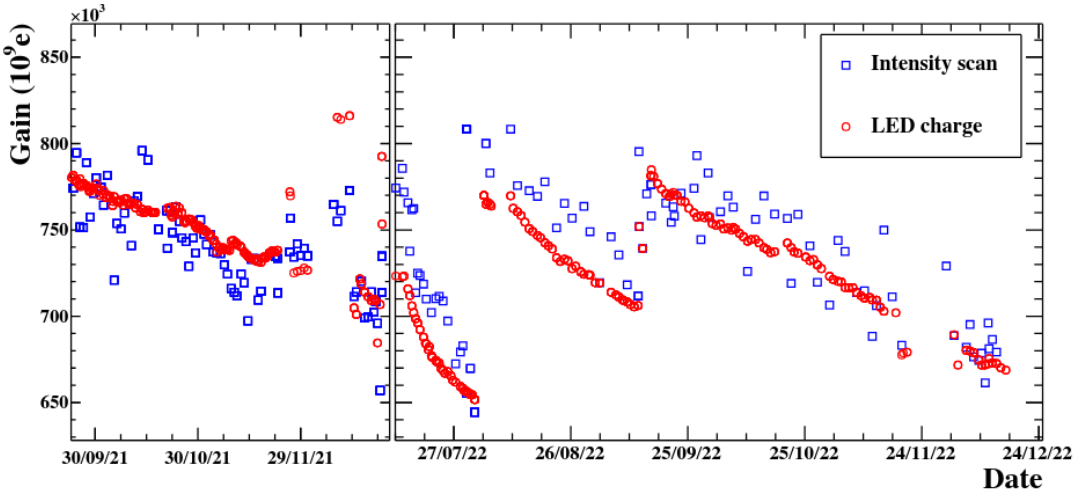

(a) Temporal evolution of a representative PMT's gain in 2021 and 2022. Blue markers indicate measurements of the gain obtained scanning the PMT's collected charge for different intensities of the LED light; red markers are measurements of the charge from LED light of fixed intensity normalized to the charge collected at the beginning of the run. More details in [55].

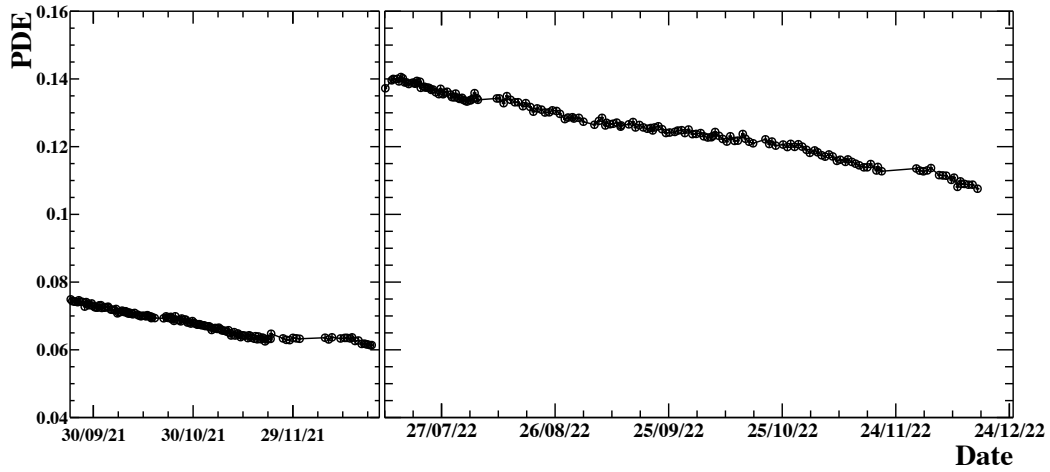

(b) Temporal evolution of a representative MPPC's PDE.

Figure 2.14: Temporal evolution of PMTs' gain and MPPCs' PDE during data taking between 2021 and 2022.

LED UV-light Blue LEDs ($\lambda \approx 460$ nm) installed in the LXe detector volume are flashed at different intensities to measure the photodetectors gain.

α particles Twenty-five ^{241}Am sources, deposited on thin tungsten wires suspended in the detector volume, emit α particles of known kinetic energy from well-measured positions. Using Monte Carlo simulations to estimate the expected number of photons arriving at each photosensors, it is possible to measure MPPCs PDE and PMTs Quantum Efficiency (QE) in the detector's operating conditions.

$\mathcal{O}$(10) MeV γs A 1 MeV Cockroft-Walton (CW) proton accelerator allows to produce 14 MeV and 17.6 MeV photons from the ^{7}Li(p, γ)^{8}Be reaction. From the reconstructed energy spectrum the uniformity of the detector response and the energy scale variations can be monitored.

This set of weekly calibration procedures required 7-8 % of beam time during 2021 and 5% in 2022.

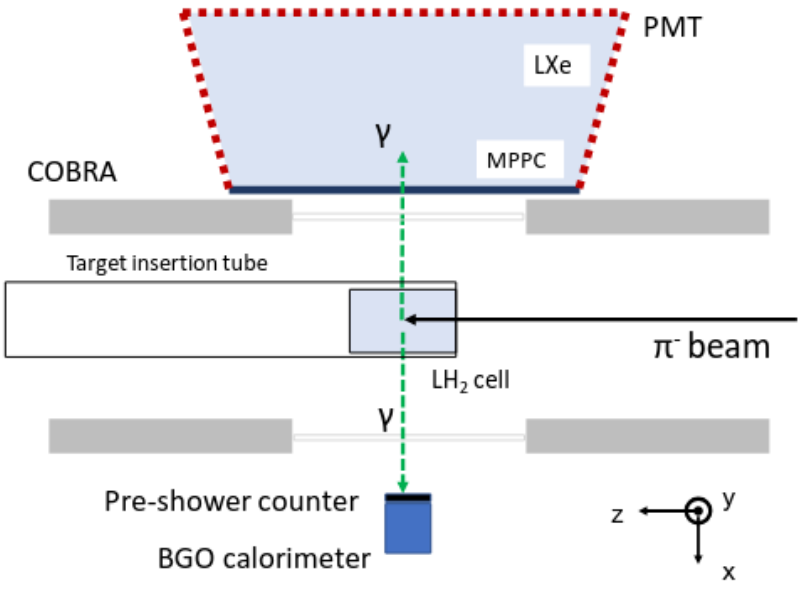

Figure 2.15: Setup for the CEX reaction.

CEX Once per year, the MEG II beamline is modified to transport a π^- beam onto a liquid hydrogen (LH_2) target [56] to perform a dedicated calibration procedure using the Charge Exchange (CEX) reaction:

$$\pi^- p \to \pi^0 n \tag{2.7}$$

The setup for this measurement is shown in Figure 2.15. Employing an auxiliary calorimeter made of BGO crystals positioned in front of the LXe detector, in opposite directions with respect to the LH_2 target, data of back to back photons can be acquired. This allows to measure the detector response in energy and time for 55 MeV and 83 MeV photons, close to the signal region ($E_\gamma \approx 52.83$ MeV). See Figure 2.16 for the photon spectra from CEX reaction recorded in 2021 and 2022.

The interactions of pions with the LH_2 target produces also 129 MeV photons from the radiative capture:

$$\pi^- p \to \gamma n \tag{2.8}$$

which are used to check the LXe detector linearity (Chapter 7, Section 7.1.1).

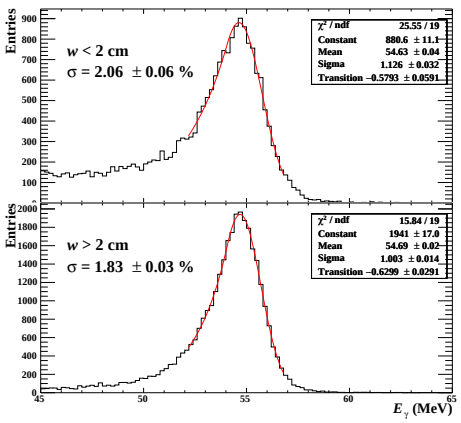

(a) Year 2021.

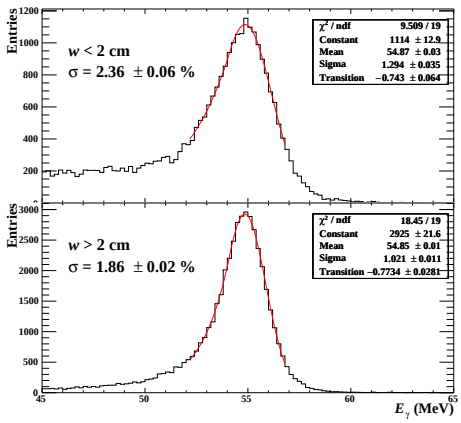

(b) Year 2022.

Figure 2.16: Photon energy spectrum of the 55 MeV line from the CEX reaction.

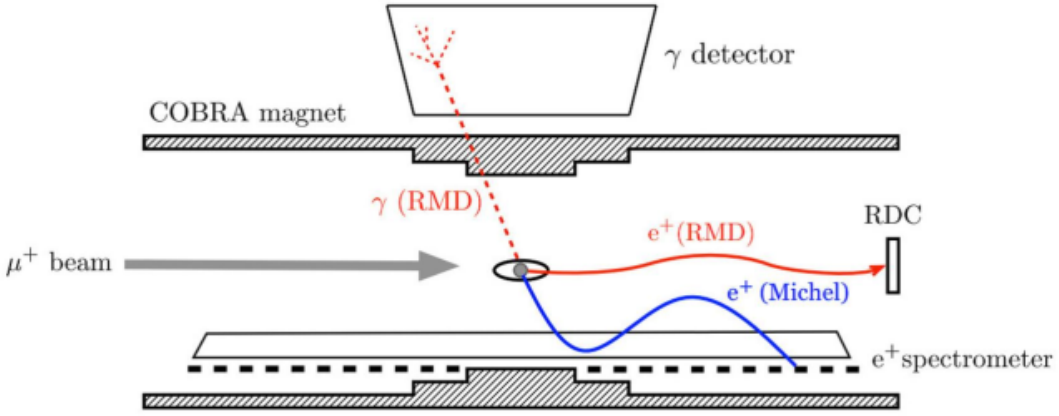

(a) How the RDC works as a detector for low energy positrons from RMD.

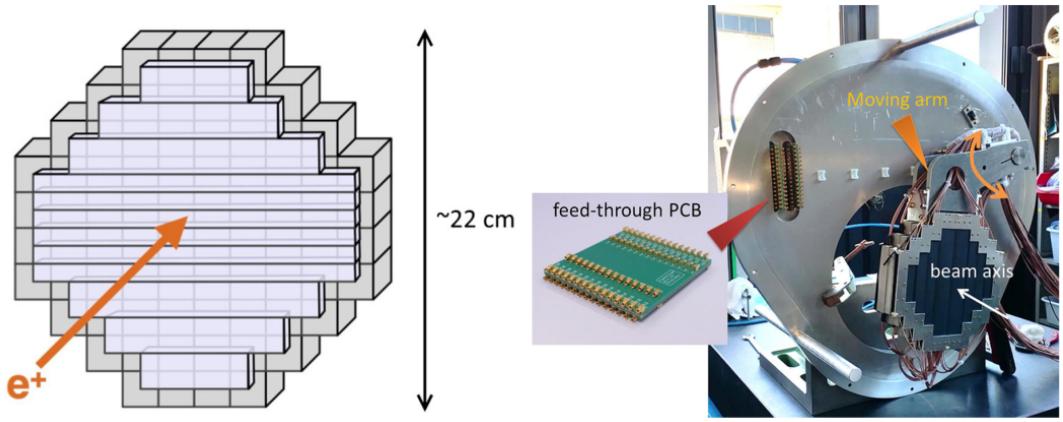

(b) RDC detector scheme and realization.

Figure 2.17: The RDC detector.

2.2.5 The Radiative Decay Counter, RDC

MEG II ultra-light spectrometer reduces the probability of positrons annihilation-in-flight, mitigating a source of high-energy photons contributing to the accidental background. The major source of high-energy photons are RMD decays. The Radiative Decay Counter detector has been developed to tag RMD events, in cooperation with the LXe detector. As illustrated in Figure 2.17 (a), RMD decays with an high-energy photon emit low-energy positrons which spiral inside the COBRA magnet towards the upstream or downstream side of the experiment with a small curvature radius. The RDC detects such positrons and this allows to identify RMD events requiring a time coincidence with a photon detection in the LXe detector.

The RDC (Figure 2.17 (b)) is composed of 12 bars of plastic scintillator and of an array of 76 LYSO crystals of volume $2 \times 2 \times 2$ cm^3 for precise timing and energy measurements. Every element is readout by SiPMs.

At the moment, only one RDC module is installed downstream the muon beam. Studies for the realization of an upstream RDC detector, based on the Diamond-Like Carbon Resistive Plate Chamber (DLC RPC) technology, are ongoing [57]. Since the upstream RDC would interact with the muon beam before muons reach the MEG II's target, its development is a challenging project which requires to realize a ultra-light, radiation hard, fast detector.

Table 2.3: Summary of the methods used to determine the alignment of each detector with respect to each other. The expression "GLB survey" indicates the optical survey measurement with a theodolite.

	CDCH	**COBRA**	**Target**	**pTC**	**LXe**
CDCH		GLB survey & Michel fit analysis	Hole analysis	Time offset calib.	Align. with cosmic rays
COBRA			GLB survey	GLB survey	GLB survey
Target				×	×
pTC					Time offset calib.
LXe					

2.2.6 The alignment of detectors

The alignment of detectors with respect to the MEG II reference frame is carried out using both direct measurements of the position of markers located on them, and indirect measurements which use collected data to determine the relative position of a detector with respect to another. The Table 2.3 summarizes the employed methods for the alignment of each system. In the following, we will describe briefly the techniques to determine the relative alignment of detectors. How the sensors' position in each detector is determined is described in the Section devoted to that element.

The absolute position of each system with respect to the COBRA cryostat is measured at the beginning of each data taking year through an optical survey campaign using a theodolite and a laser tracker system to locate the position of cross hair marks on the detectors' bodies or corner cube reflectors. The resolution of the laser method is $\approx$ 0.2 mm. The relative alignment between the CDCH and the other systems are detailed in: Chapter 4 Section 4.3 for the CDCH - magnetic field alignment; Chapter 4 Section 4.4 for the CDCH - target alignment; Chapter 5 Section 5.2 for the CDCH - LXe detector alignment. The pTC time alignment with respect to the LXe detector is described in Chapter 7 Section 7.1, while the alignment of the tiles' positions with respect to the CDCH is done using fitted tracks and is briefly described in Section 2.2.3 and in [43].

Since the MEG II reference frame has its origin fixed at the center of the CDCH, any shift between the CDCH and COBRA discovered through the alignment procedure must be applied to the measurements through the optical survey of each detector's location to determine its position in the MEG II reference system.

2.2.7 The Trigger and Data Acquisition system

MEG II's trigger and data acquisition system, called *WaveDAQ* [58, 59], solved the experiment requirements for a compact system capable of handling up to $10k$ channels and integrating a trigger system based on FPGAs for complex event reconstruction tasks. The central elements of the WaveDAQ system are the following three electronic boards, disposed in a custom crate as in Figure 2.18 (a):

- the *WaveDream* board (WDB), in Figure 2.18 (b) on the left, is the cornerstone of the WaveDAQ. Up to 16 input channels per board are digitized by the Domino Ring Sampler DRS4 chip with a speed up to 5 GSPS [60]. Each waveform of each detector channel in a triggered event is written on disk for the offline analysis. In parallel to the digitization process, the input signals are sampled at 80 MSPS for trigger processing. A low-noise onboard power supply can power SiPMs arrays with voltage up to 240 V, a feature exploited by the LXe and pTC detectors;

- in a single crate, each WDB is connected through a 5.12 Gbit/s serial connection to the Trigger Concentration Board (TCB), in Figure 2.18 on the right. The TCB collects data from the WDBs and processes them on an FPGA to perform the trigger decision. In a large system as MEG II's

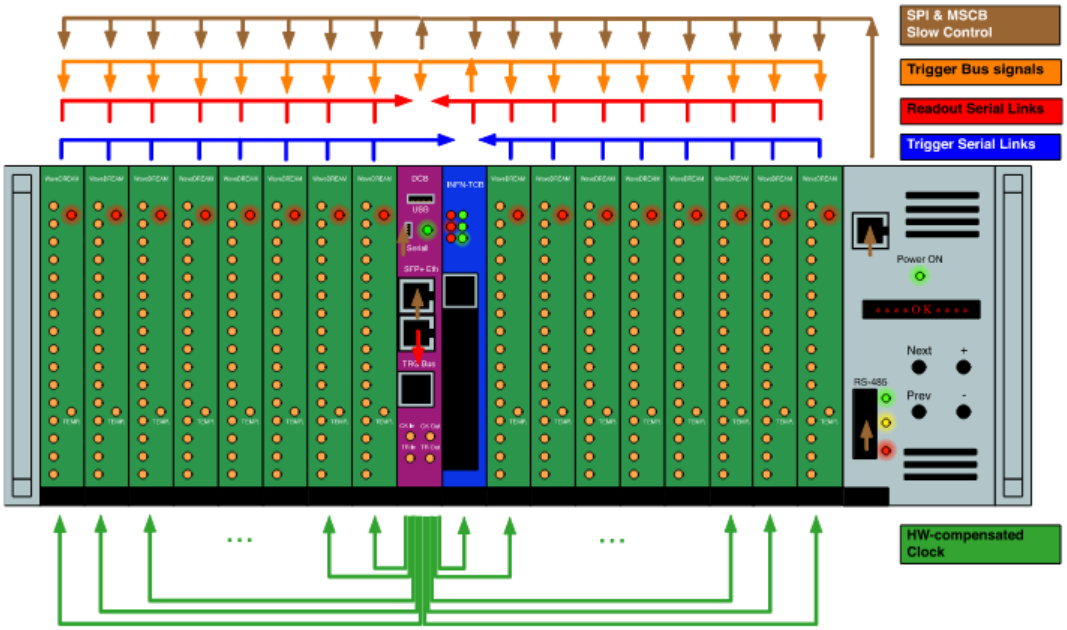

(a) Sketch of a create of the WaveDAQ system, The 16 green boards are WDBs, the blue board is the TCB and in magenta is the DCB. Green arrows indicate the clock distribution to the WDBs and the TCB; blue and red arrows represent serial links from the WDBs to the TCB and from them to the DCB, respectively; the trigger bus and the slow-control are shown in orange and brown.

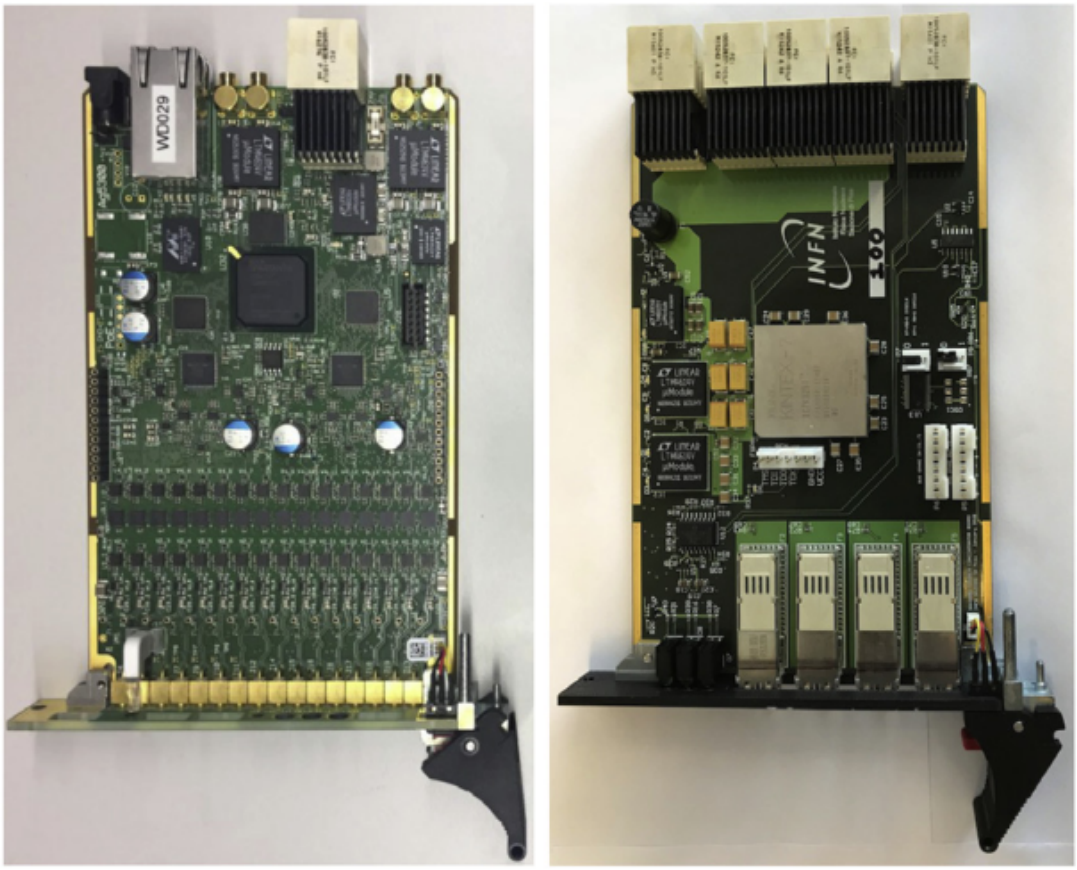

(b) Left: the WaveDREAM board. Right: the Trigger Concentration Board.

Figure 2.18: Crate scheme and boards composing the WaveDAQ.

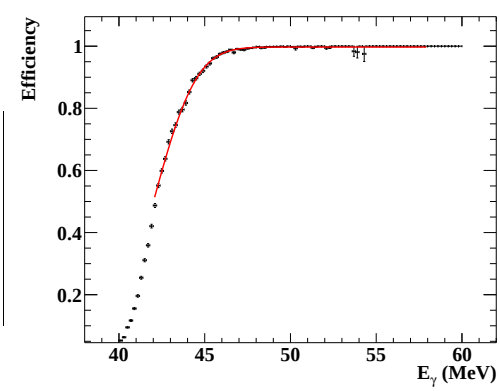

(a) E_γ trigger cut efficiency as a function of E_γ.

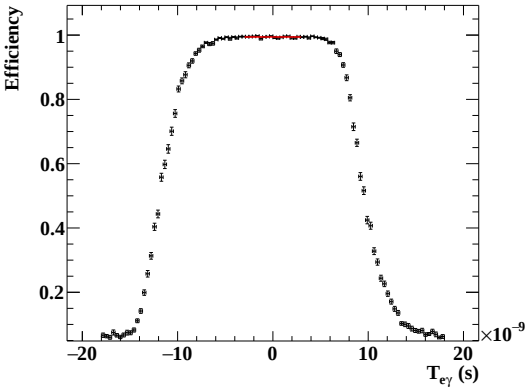

(b) $\Delta t_{e\gamma}$ trigger cut efficiency.

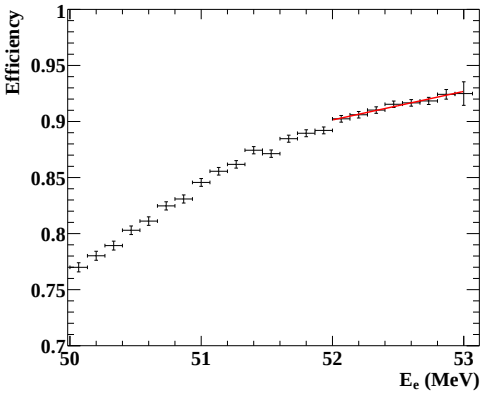

(c) Direction match selection efficiency.

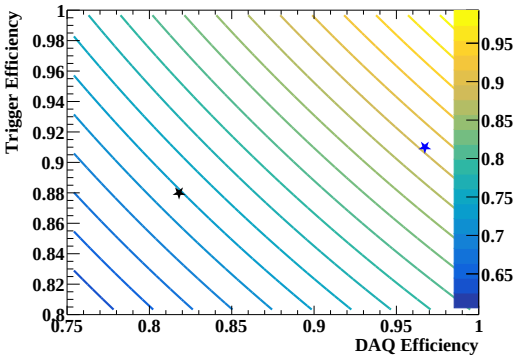

(d) Contour lines for fixed TDAQ efficiency (DAQ efficiency × trigger efficiency), with the two working points for the 2021 (black) and 2022 (blue star) data taking periods.

Figure 2.19: Trigger efficiencies measured on 2022 data.

WaveDAQ, where up to 32 crates for signal readout are mounted together, a special trigger concentrator crate hosting only TCBs is needed. Each crate's TCB forwards the trigger information towards the trigger concentrator, where the trigger decision is made and later sent back to all crates;

- when an event of interest is identified, the Data Condensation Board (DCB) collects the data from all WDBs and sends the digitised waveforms to the readout computer to be stored.

The trigger decision is taken within $\sim$ 600 ns, a constraint imposed by the DRS4 buffer length when operating at 1.4 GSPS. This small latency time doesn't allow to use CDCH data at the trigger level because of the large time needed for signal formation (up to $\sim$ 250 ns) and Pattern Recognition tasks. Therefore, only signals from the LXe and pTC detectors are used at the trigger level to identify a candidate $\mu \to e\gamma$ event.

The MEG II trigger logic implements the following criteria to identify signal events over background ones:

E_γ selection candidate events have high energetic photons: $E_\gamma > 40$ MeV is required. At the online level, the photon energy is estimated as a weighted sum over photo sensors signal amplitude $E_\gamma = \sum_i c_i \cdot \text{ampl}_i$, with the weights c_i calculated from calibration runs using the Li$p \to$ Beγ(17.6 MeV)

reaction with the Cockroft-Wolton proton accelerator. The online energy resolution is around 4% at 55 MeV.

The efficiency of the energy cut is measured on data acquired with a loose cut, comparing the number of triggered events with that of events which would pass the tight selection criteria. This efficiency is measured to be $\approx$ 96% in 2021 and $\approx$ 99% in 2022 for a photon of energy above 48 MeV (see Figure 2.19(a)).

$\Delta t_{e\gamma}$ selection Photon and positron should be emitted in time coincidence: -2.5 ns $< t_\gamma^{LXe} - t_e^{pTC} <$ 1.5 ns. An event passes the time selection cut if the relative time of LXe and pTC sensors with over-threshold signals, corrected for the particles time of flight, falls within this range. The range is asymmetric because the positron path in the spectrometer before interaction with the pTC can be longer than the maximum distance between the target and the LXe detector. As for the energy cut, the efficiency of the trigger is measured on data acquired loosening the time coincidence requirement, counting the number of RMD events that would pass the more stringent cut. The attained efficiency is $\approx$ 95% in 2021 and $\approx$ 99% in 2022 (see Figure 2.19(b))

Direction match A direction-match cut is implemented to identify back-to-back candidate events. A look-up table of possible LXe detector patches - pTC tiles couples hit in the case of back-to-back emission is built, using a Monte Carlo simulation of $\mu \to e\gamma$ events. Only events where the LXe-pTC patches belong to the table are selected. The direction match efficiency was $\approx$95% 2021 and $\approx$ 92% in 2022. See Figure 2.19(c) for the $\epsilon_{DM} - E_e$ correlation verified on Michel positrons' data.

The maximum sustainable data throughput of the system is 50 Hz, with the trigger live time dropping below 100% at rates higher than 40 Hz. The trigger rate was around 14-20 Hz during 2021 and 2022 data taking periods.

The total trigger efficiency for 2021 and 2022 was 88% and 90% respectively, with a DAQ efficiency boosted from around 81% to above 95% following a system upgrade. In Figure 2.19 (d) we show the TDAQ working points in 2021 and 2022.

2.2.8 Data taking operations since 2021

The total estimated number of muons stopped on MEG II's target in four years of data taking is $N_\mu^{stop} \approx 1.1 \times 10^{15}$. The detail of the accumulated statistics in each year of data taking is shown in Figure 2.20.

MEG II is scheduled to run for two more years before its shutdown in coincidence with PSI renewal works on the muon beam lines. The total allocated beam time for 2025 is 25 weeks, while it will be decided in February '26 for the year 2026. The projected sensitivity of the experiment to the $\mu \to e\gamma$ decay as a function of the total DAQ time is shown in Figure 2.21: based on the results obtained on the analysis of 2021 data and Monte Carlo simulations, we see that MEG II experiment is expected to reach its goal for a final sensitivity of $\mathcal{S}_{90}(\mu \to e\gamma) \leq 6 \times 10^{-14}$ in 2026. Already with the analysis of the 2021 dataset alone, combined with the MEG past result, the MEG II experiment set a new limit on this process [8]:

$$\mathrm{BR}(\mu^+ \to e^+\gamma) \leq 3.1 \times 10^{-13} \text{ @90\% C.L.} \tag{2.9}$$

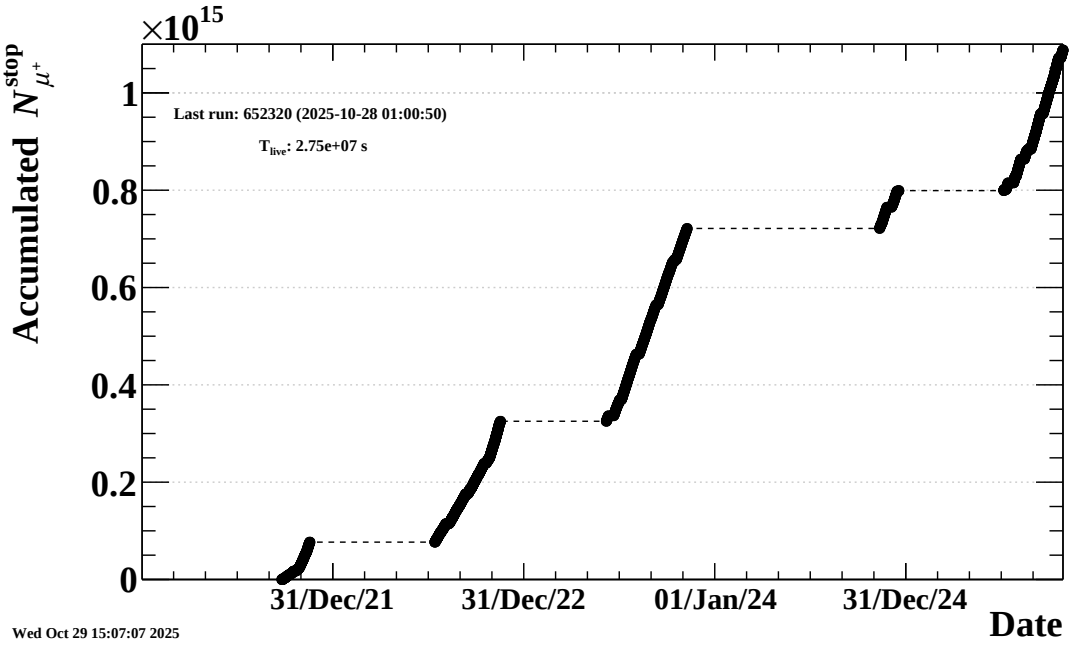

Figure 2.20: Number of delivered μ^+ by the πE5 beamline which have been stopped on MEG II target between 2021 and 2025 (ongoing) data taking periods.

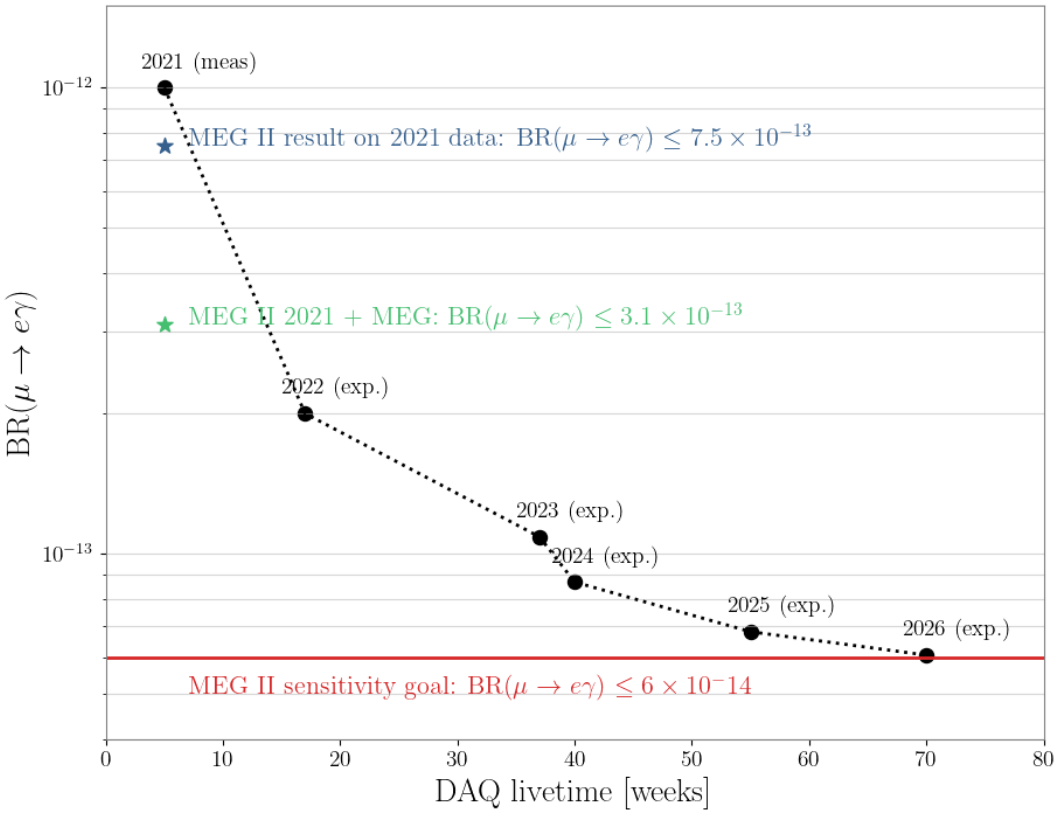

Figure 2.21: MEG II projected sensitivity based on Monte Carlo simulations with inputs from the first analysis results of 2021 [8].

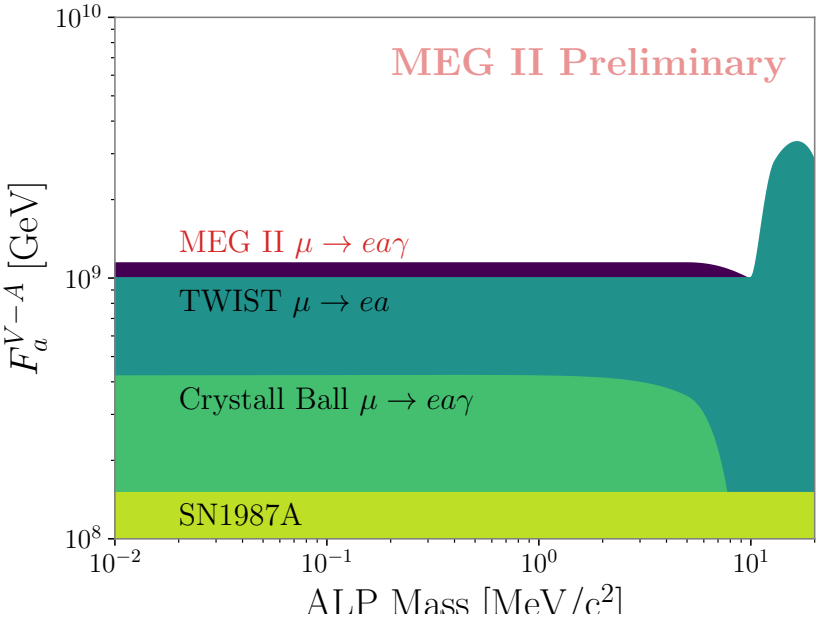

Figure 2.22: Exclusion plot for ALPs coupling parameters $F_a^{V-A} \equiv \frac{\sqrt{2}f_a}{C_{\mu e}^{V-A}}$ in the case of left handed couplings ($C_{\mu e}^V = -C_{\mu e}^A \equiv C_{\mu e}^{V-A}$), for ALPs with mass in the range [0, 10] MeV/c^2. Modified from [61].

2.3 Other searches in MEG II

In the following sections we describe the experimental effort within the MEG II Collaboration to use the apparatus to perform other searches for New Physics signals.

2.3.1 The search for $\mu \to ea\gamma$ in MEG II

In 1977, R. Peccei and H. Quinn proposed an extension of the Standard Model including a new pseudoscalar particle to solve one of Standard Model mysteries, namely the "strong-CP problem": the *axion* [62].

Although Peccei-Quinn axion has not been observed yet, their idea was very fruitful for the development of new lines of research between the community of theoreticians. Axion-like particles (ALPs) are pseudo Nambu-Goldstone bosons arising from spontaneous breaking mechanisms of a global symmetry at an energy scale f_a. ALPs are today a family of hypothetical particles predicted by many BSM theories, providing solutions to many problems like dark matter, fermion mass hierarchy and more [63]. Their parameters cover a wide spectrum of mass range, between $< 10^{-20}$ eV/c^2 and ≈ 10 GeV/c^2, and couplings to Standard Model particles.

Extending the SM with an ALP interaction term to SM fermions like the following:

$$\mathcal{L} \supset \frac{\partial_\mu a}{2f_a} \overline{\psi}_i \gamma^\mu \left(C_{ij}^V + C_{ij}^A \gamma^5 \right) \overline{\psi}_j + \text{h.c.} \tag{2.10}$$

where $C_{ij}^{V(A)}$ are the vector (axial) couplings between fermions i and j and the ALP particle, implicates the possibility of Lepton Flavor Violating processes like $\mu \to ea$, $\mu \to ea\gamma$. Indeed, the highest constraints to ALP parameters in the mass range $\lesssim 10$ MeV/c^2 come from high intensity experiments with muons, like MEG II.

The MEG experiment has searched for the $\mu \to e\gamma\gamma$ decay, a possible signature of an axion decay into two photons [64], and explored the feasibility of investigating the $\mu \to ea$ decay, with a long-lived axion [65]. A recent publication [66] highlighted the competitiveness of the MEG II experiment to search for the radiative process $\mu \to ea\gamma$, thanks to its apparatus optimized for the detection of both photons and positrons. Feasibility studies conducted within the MEG II Collaboration, based on Monte Carlo simulations and data collected in 2021 and 2022, show that the statistics collected in few weeks

at lower beam intensity $\mathcal{O}(10^6\ \mu^+/\mathrm{s})$ is enough to reach a record sensitivity[61], surpassing past results [67]. Preliminary results of the MEG II sensitivity to $\mu \to eay$ in the mass range $m_a \in [0; 10\ \mathrm{MeV/c^2}]$ are shown in Figure 2.22.

2.3.2 Searching for the X17 anomaly with the MEG II apparatus

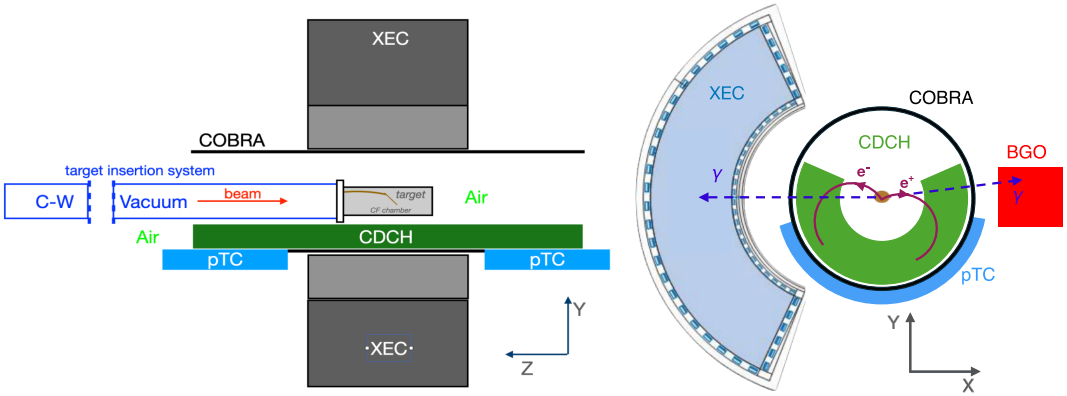

Figure 2.23: MEG II apparatus modified for the search of the X17 particle. From [68].

In 2016, an experiment at the ATOMKI Laboratory in Debrecen (Hungary) studying the nuclear process $^7\mathrm{Li}(p, e^+e^-)^8\mathrm{Be}$ observed an unexpected resonance in the energy and angular distribution of e^+e^- pairs [69]. Similar excesses have been measured also in subsequent experiments conducted at ATOMKI laboratory in nuclear reactions with ^{12}C[70] and ^{4}He nuclei[71]. In 2024, an experiment conducted at VNU-University of Science (Vietnam) confirmed the observations on ^{8}Be [72]. All these results are compatible with the hypothesis of a signal from a new light particle of mass (16.97 ± 0.22) MeV/c^2[iii], named X17 [73, 74].

Many ongoing (PADME at Frascati, Italy [75]) or planned (at Legnaro National Laboratories, Italy [76], MAGIX@MESA in Mainz, Germany [77], at Montreàl, Canada [78]) experiments world-wide aim at cross-checking these claims. Recently, PADME published the results of the analysis of the dataset from their Run III: they observed a resonance with a $(1.77 \pm 0.15)\ \sigma$ global significance for an X17 mass of 16.90 MeV/c^2 [79].

In MEG II, it has been possible to arrange an experimental setup to look for the X17 excess in the $^7\mathrm{Li}(p, e^+e^-)^8\mathrm{Be}$ process exploiting the Cockroft-Walton proton accelerator used for the weekly calibrations of the LXe detector. The setup is illustrated in Figure 2.23: the CW continuous beam of 1080 keV[iv] protons impinge on a Lithium-rich target with a current of 8-11 µA to produce photons from the $^8\mathrm{Be}^*$ decay; e^+e^- pairs from the photon conversion are tracked inside the MEG II spectrometer; auxiliary detectors, like a BGO calorimeter, monitor continuously the beam intensity. The trigger conditions require that the pTC gets a signal in correspondence to an event that generates up to 18 hits in the CDCH.

Instead of the ^{7}Li target used for MEG II energy calibrations, a new 7 µm-thick LiPON (lithium phosphorus oxynitride) target has been installed at the center of the apparatus: its design was optimized to reduce the material budget for a better measurement of the e^+e^- kinematics and to allow a better heat dissipation for long term operations. To allow the tracking of charged particles of momentum as low as ≈6 MeV/c, the COBRA magnetic field has been scaled to ×0.15 its nominal intensity.

After a first engineering run in 2022, in February 2023 a one month-long data-taking campaign was conducted during the PSI winter shutdown period. Because the CW proton beam was contaminated by H_2 with a 25% proportion, with the acquired dataset we could study the production mechanism of an

[iii] Average of the ATOMKI measurements on the three nuclei [69–71]. This value is used by the MEG II Collaboration to test the ATOMKI X17 hypothesis [68].

[iv] kinetic energy.

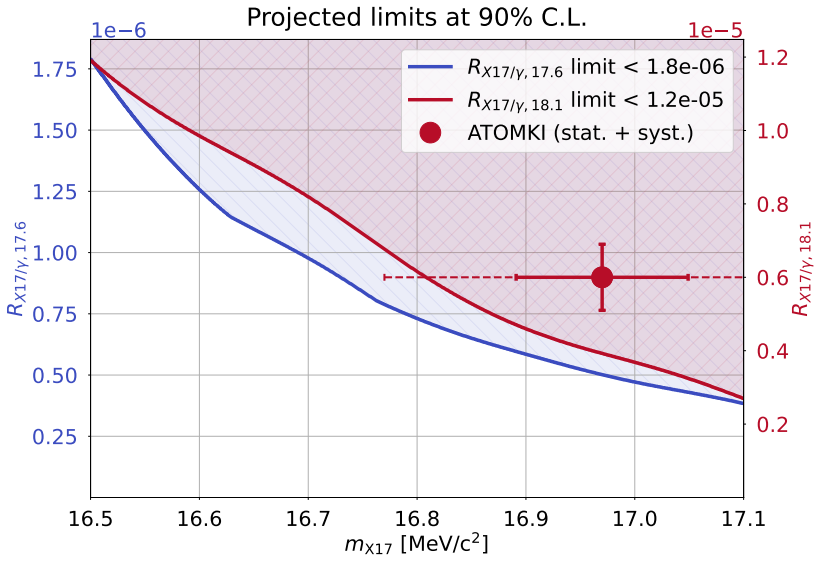

Figure 2.24: 90% C.L. limit projections of $R_{17.6}$ (blue) and $R_{18.1}$ (red) within the allowed mass range. The color filled area represents the excluded region. The red marker represents the X17 measurements at ATOMKI, averaged over all published results so far. From [68].

hypothetical X17 particle through the decay of the ^{8}Be* nucleus from the first (17.6 MeV) and second (18.1 MeV) excited states. The blind maximum likelihood analysis of the data yield no evidence of a signal in neither of these decay channels, with the following upper limits for the production rates R_{E_γ} being set:

$$\begin{cases} R_{17.6} \leq 1.8 \times 10^{-6} \\ R_{18.1} \leq 1.2 \times 10^{-5} \end{cases} \quad \text{for X17 masses in the range } [16.5; 17.1] \text{ MeV/c}^2 \tag{2.11}$$

The exclusion plot is shown in Figure 2.24. All details about the experiment and the data analysis are given in [68].

The MEG II best-fit results where tested against ATOMKI ones, yielding a p-value for the null hypothesis against the X17 hypothesis of 93.8% (1.5σ). A new data taking campaign is being prepared, with improved target and beamline configuration to eliminate the H_2 contamination, in order to increase the significance of these results.

Part II

The Cylindrical Drift Chamber

Chapter 3

The Cylindrical Drift Chamber

The candidate worked actively within the CDCH detector group, taking part in monitoring activities during data taking periods, in the maintenance works at PSI in 2022 and 2024, as well as being part of the Positron Analysis group working on the tracker's calibration and analysis. He also participated in the wiring and construction procedures of the CDCH2.

In this Chapter we focus on the description of the Cylindrical Drift Chamber design and operations (Section 3.1) and on the positron reconstruction algorithms, from the hit reconstruction to the track fitting (Section 3.2). In Section 3.3, the methods to assess the CDCH performances exploiting data of Michel positrons, which were developed and first employed at the time of the MEG experiment [44], are briefly described.

3.1 The characteristics of the CDCH

In this Section we describe the main features of the CDCH: its design, the gas mixture choice, the electric parameters and its electronics, the operation conditions during five years of data taking, from its commissioning in 2020/21 to 2024 data taking.

More details about the design can be found in [42, 80], while the detector commissioning is documented in [81, 82].

3.1.1 The assembly procedure

The CDCH was assembled using an innovative approach. Traditionally, wires are hanged passing the two ends through feed-through holes milled in the end-plates and clamped; instead, the CDCH assembly followed a modular scheme.

A "module" is a set of 32 wires soldered at both ends on two printed circuit boards (PCBs). The wiring and soldering procedure is performed using a semi-automatic robot [83], which winds in an helical path a single wire thread 32 times around a cylinder, depositing the wire onto two PCBs oriented at the correct stereo angle (Figure 3.1 (a)). The winding system, supervised by the machine operator with a digital camera, ensures a precision up to 20 μm in the wire positioning. The wire tension is controlled at a sub-gram level during the whole procedure. An infrared laser soldering system allows to fix the wire on the PCB pad.

At the end of the soldering procedure on a pair of PCBs, the wound layer is cut into 32 individual, parallel wires; it is then unrolled and ready to be installed onto the detector structure. The two PCBs of

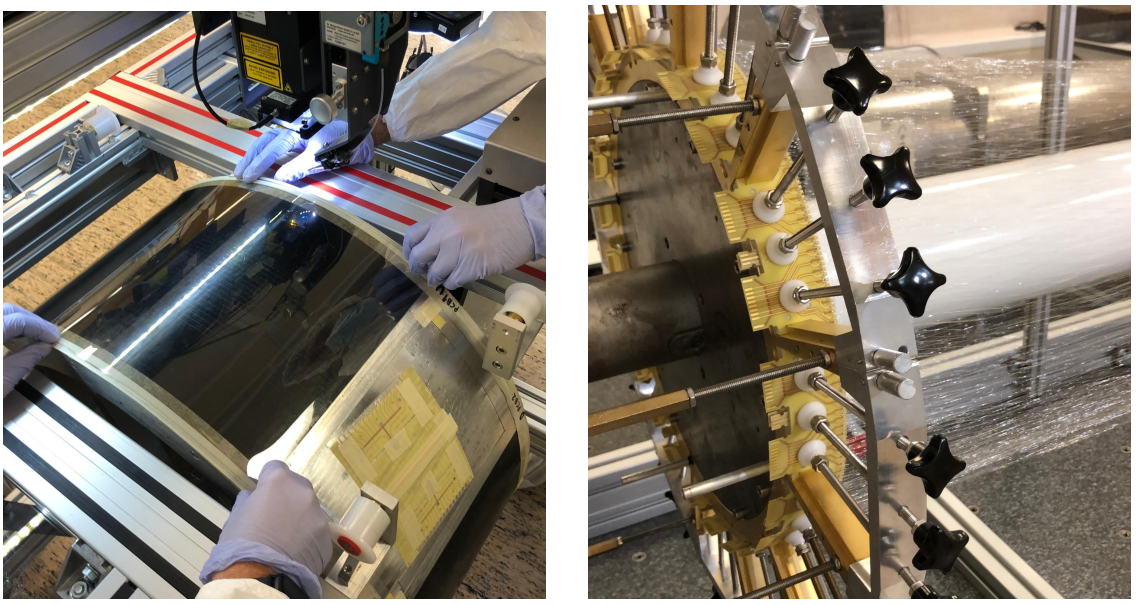

(a) (b)

Figure 3.1: (a) Detail of the semi-automatic wiring and soldering robot during the unwinding stage of a module; (b) a layer of multi-wire PCBs mounted on a CDCH end-plate.

a module are anchored on two wheel shaped end-caps kept at nominal longitudinal distance between each other (Figure 3.1 (b)). The wheels are divided into twelve sectors, one per module. Because of the stereo geometry, the wires extend from sector j to sector $j \pm 2$ depending on the stereo view. In order to form the open-cell geometry shown in Figure 3.2 (a), PCBs are stacked one on top of the other with the scheme shown in Figure 3.2 (b), alternating them with layers of PEEK[i] that ensures the right distance between anodes and cathodes to shape the drift cell.

At each step of the assembly, after a single layer of multi-wire PCBs is installed, the PCBs position (marked by three reference crosses on each) is measured using a coordinate measuring machine, a DEA Ghibli [84], which has a $\sim$ 20(40) µm accuracy in the horizontal (vertical) plane.

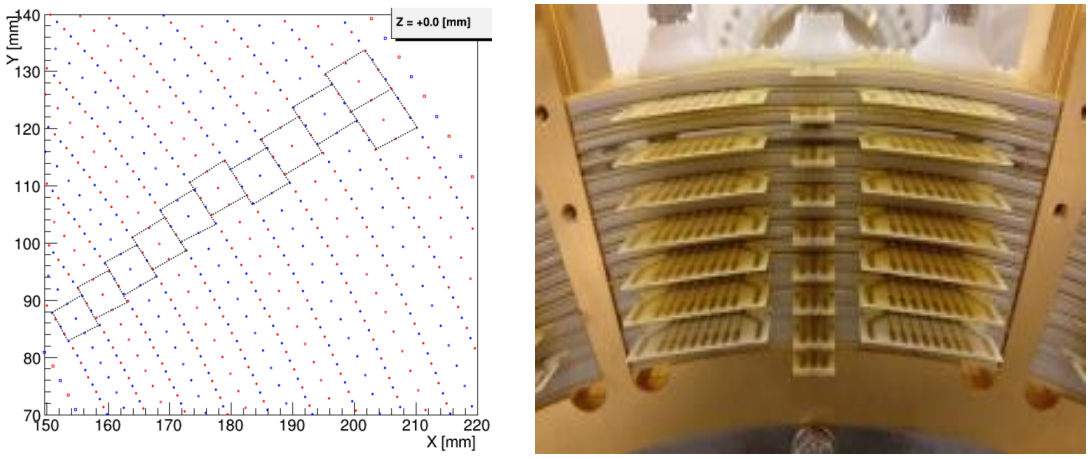

(a) Drift cells configuration at the center of the CDCH.

(b) End-cap detail of a CDCH sector with seven cells mounted.

Figure 3.2: The CDCH cell layout and construction.

[i] PolyEther Ether Ketone, a colorless organic thermoplastic polymer.

After the assembly of all layers, the detector volume is enclosed at the inner radius by a 20 μm Mylar foil, while a 100 μm aluminum field cage and a cylindrical carbon fiber structure mounted at the external radius ensure the ground connection of guard wires and mechanical rigidity. These choices minimize the interference of passive materials with the positron before entering or exiting the CDCH volume.

3.1.2 Geometrical parameters

Each CDCH wire position in space (with respect to the CDCH reference frame) is defined through 7 geometrical parameters, illustrated in Figure 3.3:

- position of wire's center $(x_0,\ y_0,\ z_0)$;
- spherical angles θ and ϕ defining the wire's vector orientation;
- since gravitational and electrical forces deform the wire, we approximate the deflection s along the wire with a parabolic function:

$$s(w) = s_0 \left[\left(\frac{2w}{L} \right)^2 - 1 \right]$$

  where w is the longitudinal coordinate along the wire ($w = 0$ at wire center) and L is the wire length. We call the s_0 parameter *sagitta*;
- an additional degree of freedom allows to describe the orientation in space of the wire deformation: the angle γ is the one between the sagitta vector $\vec{s}$ and the radial direction $\vec{r}$ from the CDCH center and the point $(x_0,\ y_0)$.

See [85] for a complete description of the CDCH wire geometry.

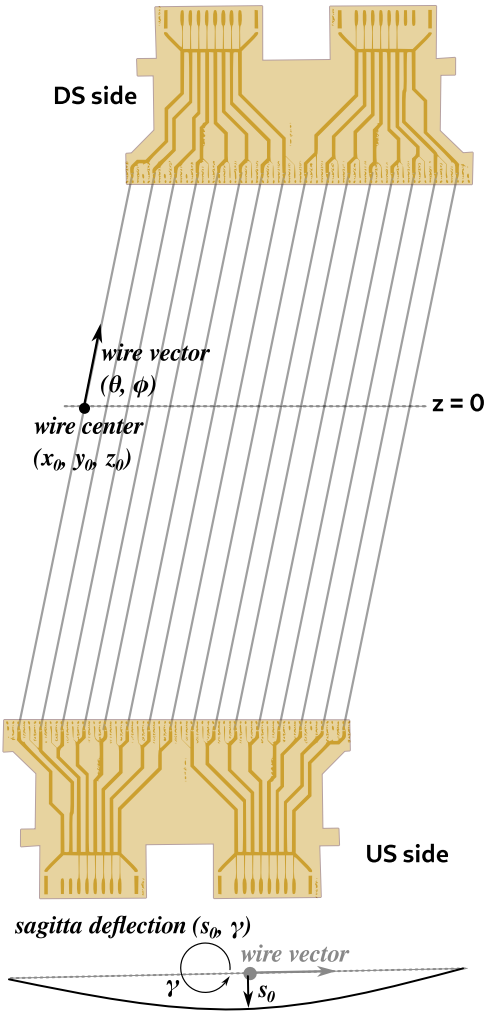

Figure 3.3: CDCH wire geometry.

3.1.3 Gas mixture

The CDCH uses a helium based gas mixture, continuously flowed through the detector by a dedicated gas system [86]. Because of its large radiation length ($X_0 \approx 5300$ m at STP), the choice of the helium ensures a small contribution to the multiple scattering. Furthermore, an helium based gas mixture, which has a fairly constant drift velocity, has a linear time–distance relation up to very close distances from the sense wire.

The high helium ionization potential of 24.6 eV is such that a crossing particle produces only a small number of primary electron–ion pairs: the average number of total clusters per cell is about 13 for a MIP (minimum ionizing particle) and the average number of ionization electrons per cluster is 1.3. The largest contribution to the spatial resolution uncertainty comes from the statistical fluctuation of primary ionization along the track.

A small amount (10%) of isobutane is required as a quencher to avoid self-sustained discharge. With this additive, the radiation length of the mixture is reduced to $X_0 \approx 1300$ m. On the other hand, the use of an organic quencher involves specific problems relating to exposure to high radiation fluxes,

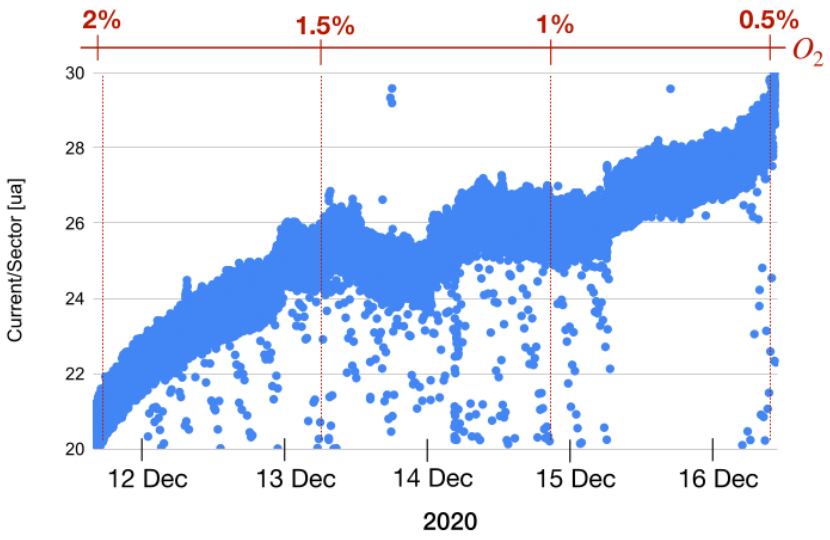

Figure 3.4: Current in a sector as the oxygen percentage is lowered from 2% to 0.5% with 0.5% steps. Dots outside the general trend are due to instabilities of the PSI particle beam.

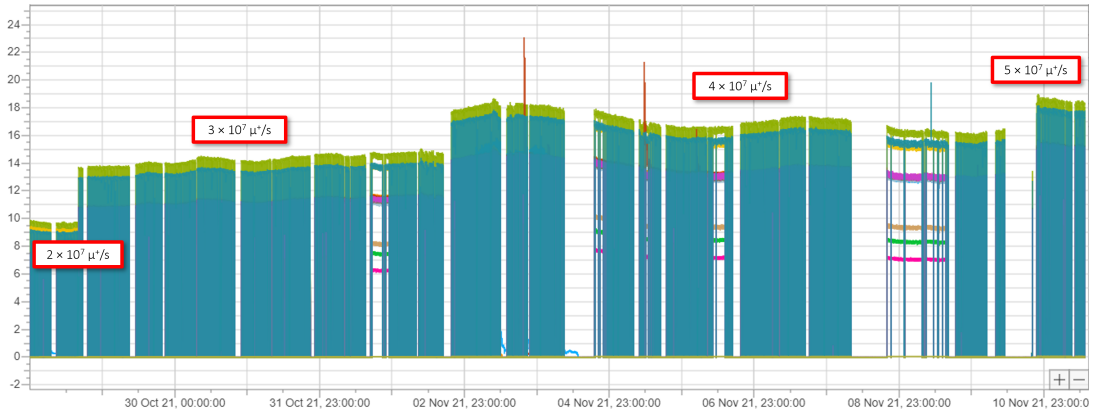

Figure 3.5: Beam induced currents on plane 9 of the CDCH. The data refer to a two-week period in 2021 during which the beam intensity was varied from 2×10^7 μ^+/s to 5×10^7 μ^+/s. The variation of the beam intensity is visible in the raise of the CDCH currents.

since the recombination of dissociated organic molecules leads to the formation of polymers which, by accumulating on the anodes and cathodes, contribute to the aging of the detector.

During commissioning, an abrupt increase in current up to 400 μA was observed in several cells of the chamber (standard levels are around 10–20 μA). A deep investigation revealed the formation of corona-like discharges in correspondence of some regions along some wires. The reduction of the high currents was achieved with an oxygen level up to 2%, then gradually lowered to minimize electron attachment effects. The effect of oxygen on the current per sector is shown in Figure 3.4; the lowering of the oxygen content is indicated by the red scale and vertical lines on the top of the figure; the current is lowered from oxygen capture and some loss of gas gain. In addition, a small percentage of isopropyl alcohol is added to guarantee stable operations: the alcohol acts as a quencher and reduces the deposit of insulating debris on the wires. The CDCH is now operated at the high-voltage (HV) working point in stable conditions at full MEG II beam intensity with the standard gas mixture + isopropyl alcohol (1.5%) + O_2 (0.5%).

The CDCH has been stably operated for data taking operations since 2021. The gas mixture with 1.5% isopropyl alcohol and 0.5% O_2 has ensured good stability of the detector throughout these years of data taking, as is visible in the flat profile of the wire currents in Figure 3.5. Fluctuations are caused by changes in the atmospheric pressure, which affects the gas gain [54].

The successful operation of the detector demonstrates that small percentages of oxygen can be added in the gas mixture to stabilize the detector without significative losses of performances, against

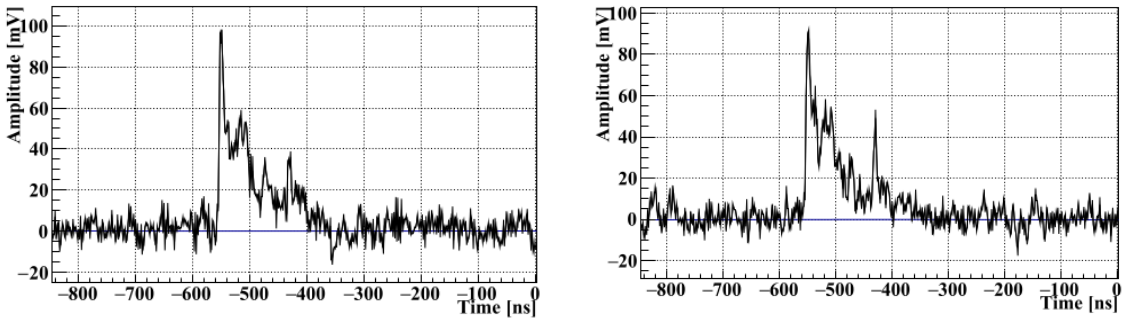

(a) Upstream side.

(b) Downstream side.

Figure 3.6: Signal measured at both ends of a drift cell.

a general reluctance in its employment motivated by the strong electronegativity of oxygen. This topic has been investigated inside the working group of the CDCH and is detailed in Appendix C.

3.1.4 Electric parameters

The CDCH HV working point has to be chosen balancing two opposite requirements: on one side, higher voltages augment the gain of the CDCH, with a better S/N ratio; on the other end, intense electric fields induce more easily electric discharges, compromising the stability of the operations; in addition, the HV set point is up-bounded by the wire tension and the cell size and has to be tuned to avoid wire attachments causing shorts. The working point ($\approx$ 1450 V) was chosen with the aid of simulation tools to monitor the electric stability and with measurements of the mechanical stability performed on a three-wire prototype.

To compensate for the variable dimensions of the CDCH drift cells, the HV bias of the anode wires is varied of 10V/layer, ranging from 1400V for the cells of the innermost layer, up to 1480V for the cells of the outermost layer. In this way, a uniform gas gain of about 2.5×10^5 is obtained, as measured by comparing the signal amplitude distributions in data and Monte Carlo simulations.

Aging effects [87], like build-up of radicals on the anode wires, can reduce the gas gain factor and the HV should be raised to compensate. No evidence of aging is observed on data so far and the HV working point hasn't been changed.

3.1.5 CDCH Front-end electronics

The CDCH signals are read out by custom two-stage front-end (FE) amplifier boards, each serving eight channels [88]. In addition to amplification, the same boards distribute the high-voltage bias to the anode wires, while providing decoupling and protection. The design ensures high linearity and stability, with a bandwidth matched to the spectral content of the CDCH signals.

A typical signal on an anode wire consists of a sequence of pulses produced by individual ionization clusters along the track (Figure 3.6). In the first design stage, the bandwidth was chosen to enable a *cluster counting* technique, enabling the detection of single ionization cluster few nanoseconds apart, which could improve spatial resolution by reducing the statistical fluctuations of primary ionization [89]. In practice, however, the front-end gain was increased to compensate for signal attenuation in the transmission lines, at the cost of a reduced bandwidth: from around 1 GHz to a little above 500 MHz.

The typical single ionization signal corresponds to an amplitude of about 20 mV at the wire end, with an average gain of ~30 dB. The electronic noise is below 2 mV (RMS) after transmission, resulting in an excellent signal-to-noise ratio. Cross-talk between adjacent channels is at the level of ~1% and negligible for further neighbors, ensuring reliable reconstruction performance.

A comprehensive description of the FE architecture and its characterization can be found in [88].

(a) The FE board for the CDCH signal readout and HV powering.

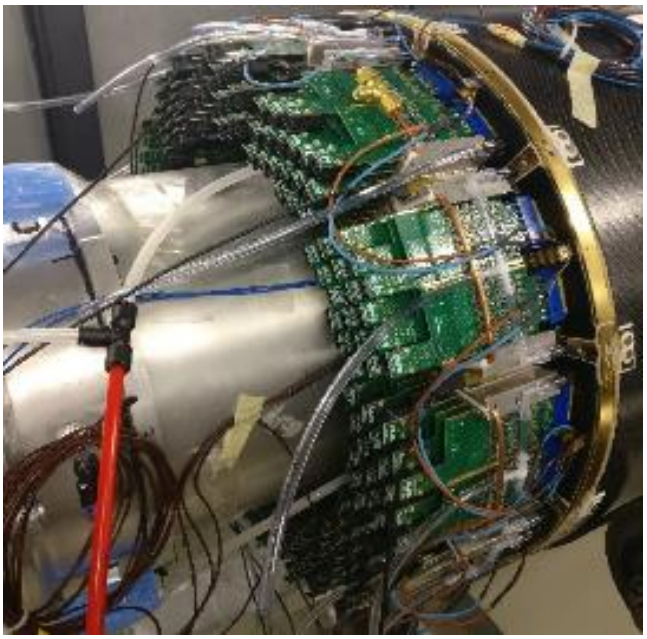

(b) CDCH downstream end-plate with all FE boards installed in the board holder and cooling and dry air tubes connected.

Figure 3.7: The FE electronics of the CDCH.

The current consumption for each channel of the front end board is 60 mA at a voltage supply of ±2.5 V, corresponding to a total power dissipation per end-cap of approximately 300 W. Therefore a dedicated cooling system based on a 1 kW chiller and a cold water distribution system with piping embedded in the front end board holders is used (Figure 3.7(b)). Moreover, a system of perforated pipes, glued to the external faces of the end-plates, flushing dry air is used to avoid water condensation and dangerous temperature gradients.

3.2 Tracking: from waveform analysis to track fitting

In this section we describe the analysis procedure for the track reconstruction inside the CDCH, starting from the waveform analysis for hit reconstruction and ending with the track fitting procedure. as detailed in the flow chart in Figure 5.1.

Each step of the analysis is performed in a hierarchical order by one or more `tasks` of the `MEGAnalyzer` software, indicated in the block diagram.

3.2.1 Waveform analysis

The analogue signals are digitized using a modified WaveDREAM board (Section 2.2.7) suited for the connection with the CDCH's multi-wire custom cables. Two cables (16 channels) are connected to each WaveDREAM board, with each cable digitized by one DRS4 chip. The waveforms saved on disks for the data analysis have 850 ns depth at an effective sampling speed 0.6 GSPS.

The first step in the event reconstruction procedure is the detection of hits in the waveform signals. Each wire is readout at both ends: an example of the waveforms forming at the two ends of a wire is given in Figure 3.6. A *hit* is defined as the group of ionization clusters produced by a single passage of a charged particle in the drift cell. Different clusters having different drift times produce multiple discrete pulses spanning over more than 400 ns. The goal of the waveform analysis is the identification of such pulses and the determination of their time of arrival, in particular of the earliest. In general,

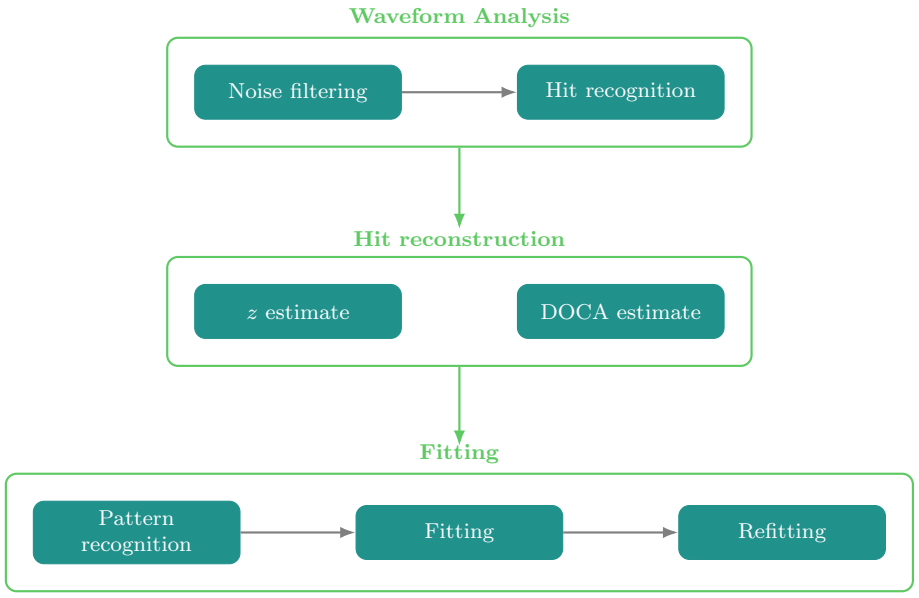

Figure 3.8: Flowchart of the track reconstruction procedure.

the detection of the first cluster is difficult because many hits from different events can overlap: in the innermost wires, the hit rate per cell can be up to 1.2 MHz at 5×10^7 μ^+/s.

Noise removal Before the hit detection procedure, noise is filtered out.

A low-frequency noise, common to all wires readout by the same WaveDREAM board, therefore called "coherent noise", was observed since 2021 data taking, later investigated, but could not be removed definitely: the πE5 area is an intrinsically noisy environment with many possible sources not controllable nor testable. A filtering procedure was developed [50, 90] and proved to be very effective in strongly reducing the low-frequency noise peaks observed at $\sim$ 50 and $\sim$ 150 MHz: the strategy adopted is to subtract bin-by-bin the mean amplitude of the waveforms sharing the same DRS4 chip (8 channels).

Some tens of wires instead are affected by a low-frequency noise non-common to others, probably linked to missing electrical components on the FE board. In this case, the noise is subtracted with a moving average filter.

Once the low-frequency noise is filtered out on all wires, a discrete Fourier transform (DFT) high-frequency cut off at 225 MHz is applied: the waveform is transformed with a DFT in the frequency domain, the power of all frequencies above the threshold are set to zero, the waveform is then transformed back to time domain.

Hit detection Two algorithms perform the hit detection task.

The first algorithm uses a conventional "pass-or-fail" strategy. Since the hit signal propagates through the wire to its two ends, the hit detection procedure is applied on the sum of the two waveforms (correcting for time misalignment). Selection cuts are based on studies of typical signal pulse shapes, as shown in Figure 3.9 for different drift times. At the CDCH working point, the average amplitude of a single cluster pulse is 35 mV. The rise time is usually very steep (< 2 ns), with a longer fall time of 20 ns. The following cuts are applied:

- a fixed threshold on the amplitude (in Volt) on two adjacent bins is applied to identify the rising edge;
- a fixed threshold on the pulse shape integrating over 20 ns after the two first bins is implemented.

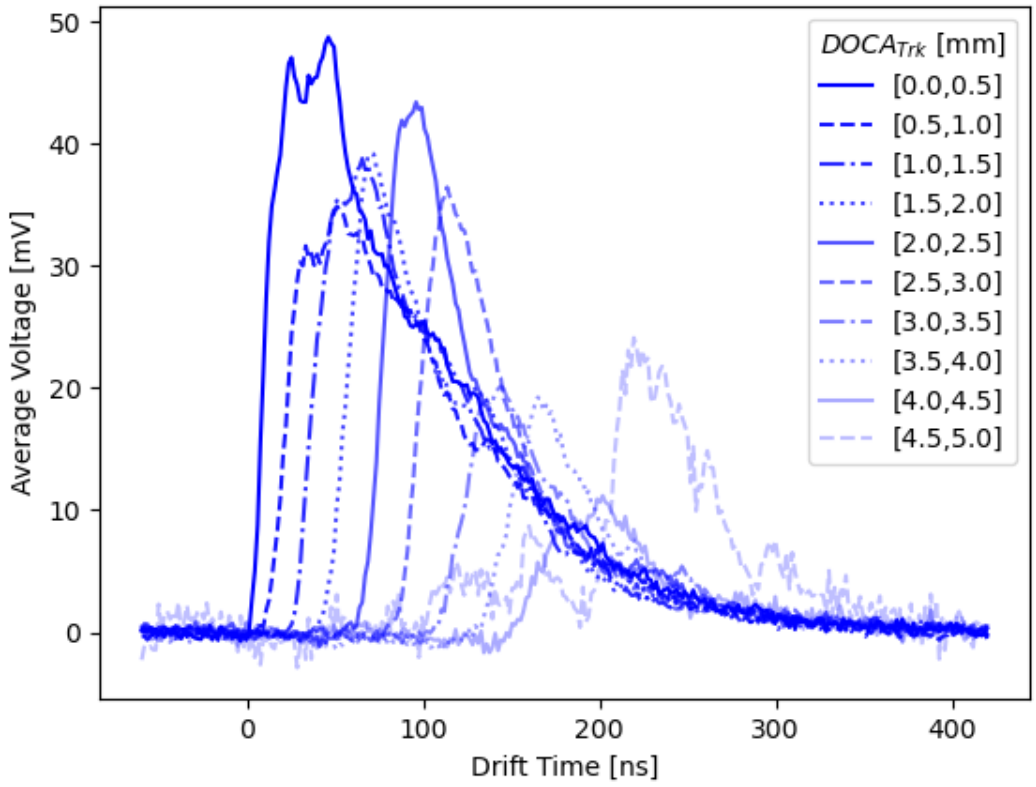

Figure 3.9: Hits waveform shapes for different *DOCA*/drift times, averaged over many events.

The time of arrival of the hit is determined with a linear interpolation between the time of the first two bins above threshold.

A second algorithm uses a deep-learning approach instead, based on a convolutional neural network (CNN). Every set of sixteen unfiltered waveform data (sampled amplitudes) from eight adjacent wires (both ends are considered) are input to the net, and the output is, for each time bin, the probability that the first cluster is found in that bin for that wire waveform. This automatically returns also the estimate of the cluster time of arrival. The architecture of the model consists of a cascade of two auto-encoders, with the first stage performing noise estimation and removal, while the second stage performs the hit detection task based on the former part output. The neural network algorithm was trained on simulated waveform data superimposed on pedestal data taken without beam to realistically represent the noise. Hits are randomly distributed in time replicating the occupancy for a nominal beam rate of 3×10^7 μ^+/s.

Instead of merging the two lists of candidate hits applying both hit detection algorithms independently, which would increase the fake hit rate and generates duplicates, the analysis routine is carried out in two separate stages, combining the results only after the track reconstruction is completed. In the first stage, the full analysis chain is ran using only hits found by the conventional hit detection algorithm; later, the analysis uses hits found by both algorithms. The track reconstructed in these two passages are then mixed and sorted by a fine-tuned track selection algorithm (described below). This technique for combining the results of the two hit recognition tasks resulted in an improvement of 10% of the global tracking efficiency of the spectrometer.

3.2.2 *DOCA* estimate

The arrival time measurement t of the first cluster, which usually corresponds to the cluster generated closest to the anode by the impinging particle, is composed of the cluster's drift time (up to ~ 400 ns) and

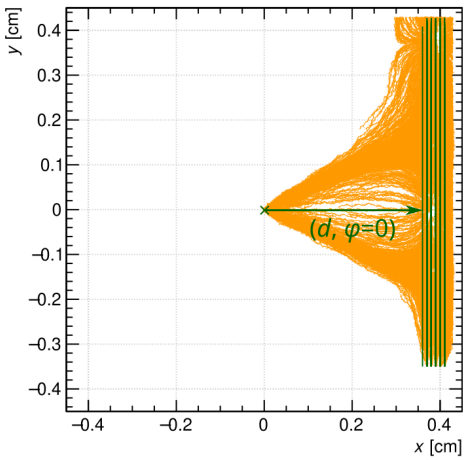

(a) *Garfield++* simulation of the drift of ionized electrons from tracks at different d inside a drift cell using the `AvalancheMC` method to include also dispersion effects.

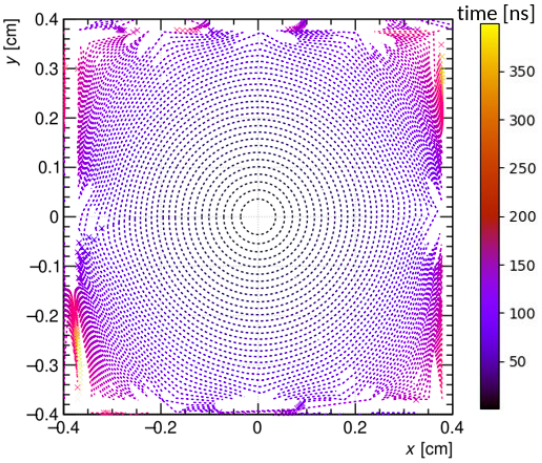

(b) Isochrone curves for a drift cell in the first CDCH layer.

Figure 3.10: *Garfield++* simulation of the $t \rightarrow DOCA$ relationship.

the track time T_0 at which the cell is crossed, given by the pTC detector with a ≈ 40 ps resolution and the estimate of the time-of-flight of the ionizing particle. This measurement of t has to be transformed into a measurement of the distance of closest approach, *DOCA*, between the particle and the wire. No direction information is available from the time measurement to locate the ionization process inside the drift: only the absolute distance can be determined at first. Yet, the coordinates of the hit can be later inferred from the tracking procedure.

Two methods were developed to determine the $t \rightarrow DOCA$ relationship, which is not analytical because of the complex dependence of the drift velocity on the electric field in each point of the squared cells and magnetic field effects deforming the trajectory of the drift electrons. For a complete discussion on this topic see [54], Chapter 4 and 7.

The first implemented method is based on *Garfield++*[91] simulations: the plane of a drift cell is sampled in pairs of $d - \phi$ values (d = distance to the anode; ϕ = angle in the drift cell plane)[ii]; for each given parameter impact d and incident angle $\phi + \pi/2$, 1000 tracks crossing the drift cell are simulated; for every track, each ionization cluster is propagated towards the anode. A simulation of the drift process for a set of tracks with different values of d is shown in Figure 3.10 (a). For a single simulated track, the closest ionized cluster to the anode, originating at a distance d', has a drift time t'_{drift}: the best estimate for the drift time $\hat{t}_{drift}$ of first ionization clusters originating from a particle with $DOCA = d$ is taken to be the average of the drift times:

$$\hat{t}_{drift} = \frac{1}{N} \sum_{i=1}^{N=1000} t'_{drift} \tag{3.1}$$

The tables (called *TXY* tables) formed by the values $\{d, \phi, \overline{t}_{drift}\}$ are then used to infer the $DOCA$ from t_{drift} measurements in data. When no information on the impinging direction is available, average (over ϕ) tables are used instead, and the estimate is later refined during the fit procedure. See Figure 3.10 (b) to visualize the time-distance relationship inside a drift cell. Since the drift cells size changes along the wire z coordinate and augments from the inner to the outer layers, we use different table for each detector plane in segments of z (10 cm steps).

[ii] Sampling the drift cell plane is necessary to correctly estimate the effects on the electrons' motion of the cell shape and of the magnetic field.

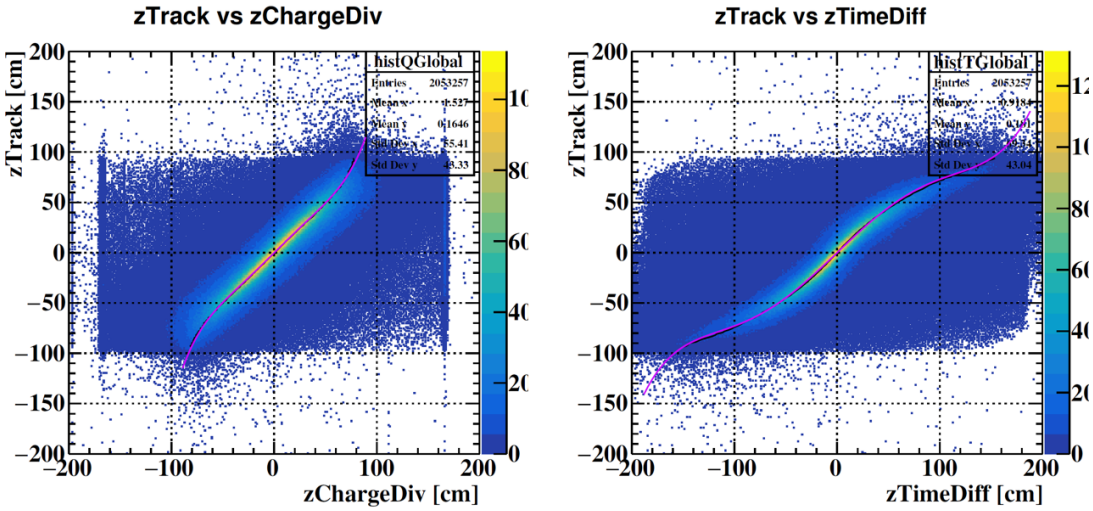

Figure 3.11: Correlation between the z hit position estimate from tracking and from the charge division (left) and the arrival time difference (right) methods after inter-calibration of the wire ends.

The error σ_{DOCA} on the estimated $DOCA$ value from the measurement of t_{drift} is computed as the 68-percentile of the residuals distribution $d' - d$, where d' is the distance between the closest ionization cluster and the anode wire, and d is the true value. The estimate of σ_{DOCA} for each point also enters the *TXY* tables.

A second method using a neural network approach was developed [92] to create an improved $DOCA$ estimator, tuned on data, that overcomes the conventional approach when this latter is not fully calibrated. A convolutional neural network (CNN) architecture is used. The input to the network are wire waveforms and a series of variables (hit arrival time, T0 , layer, z, etc.), trained to create a model that maps the hit properties to a final $DOCA$ estimate. The advantage of this procedure which makes use of the full waveform is the capability of using information also of other ionization clusters to derive an unbiased $DOCA$ estimate, in a fashion similar to the "cluster counting technique". The neural network algorithm is trained on fitted tracks recorded at low beam intensity (10^6 μ^+/s), where the conventional *TXY* tables were used. Training on experimental data, the network learns the bias due to the ionization statistics.

This neural network technique has been verified using data-driven kinematic resolution estimating techniques to improve all kinematic resolutions by ~ 5-13%.

The CNN model was trained using 2021 data first for the 2021 analysis, and has been retrained in view of the analysis of the 2021+'22 dataset, but no difference between the two models has been observed: this is expected, since the gas mixture and HV settings of the CDCH were the same in both years.

3.2.3 z estimate of the hit position

The difference in arrival times and the ratio between the total charges collected on the two ends of the cell sense wire allow a preliminary determination of the longitudinal (z) coordinate of the hit. The w coordinate along the wire is calculated as:

- using the time difference:

$$w = \frac{v}{2}(t_0 - t_1 - \delta t) \tag{3.2}$$

  where v is the signal propagation velocity inside the wire, t_0 and t_1 are the arrival time on the two wire ends and δt is the calibrated time offset between the two wire ends;

- using the charges:

$$w = L_{wire}\left(\frac{R_G \cdot q_1 - q_0}{R_G \cdot q_1 + q_0}\right) \tag{3.3}$$

where L_{wire} is the wire length, q_1 and q_0 the charges and R_G is the calibrated ratio of the gains at the two wire ends.

w is then transformed to a measurement of z in the MEG II coordinate system using the individual wire position and direction within the CDCH. The parameters δt and R_G for all wires are obtained by calibration procedures using positron and cosmic tracks and iteratively optimized to get the best single hit resolution (Figure 3.11). The precision of this measurement of z is roughly 9 cm with both methods, which can be combined to obtain a 7.5 cm resolution before tracking.

3.2.4 Track finding and fitting

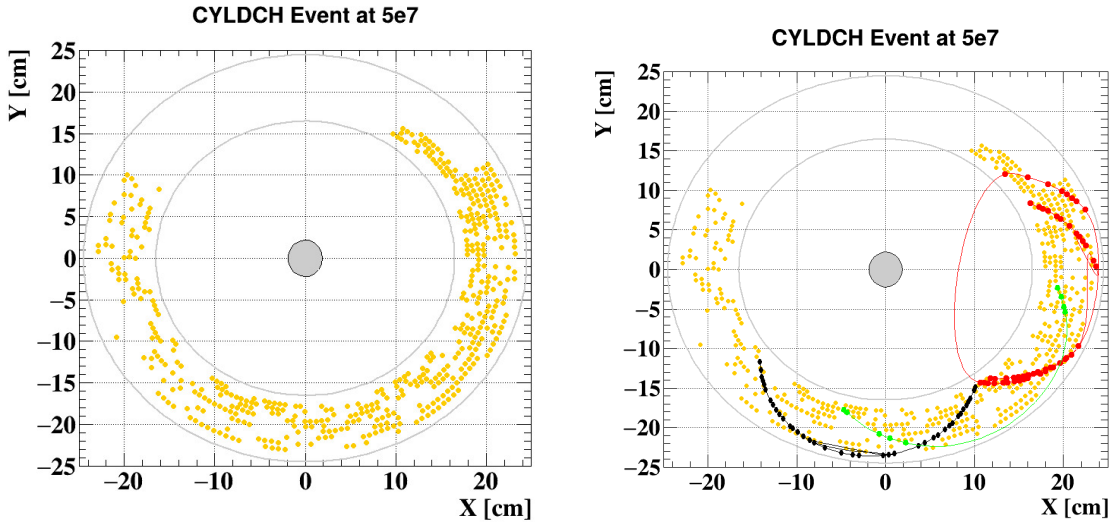

(a) (b)

Figure 3.12: CDCH event at 5×10^7 μ^+/s. In yellow, all reconstructed hits within 400 ns (a); three fitted tracks (black, red and green) are identified after the track finding and fitting procedure (b).

Once all hits in a CDCH event have been reconstructed, the positron track reconstruction begins: first, a track finding algorithm groups hits into segments of candidate tracks; then, the tracks are fitted to extract the best estimate of the positron's kinematics at the target.

Track finding The positron reconstruction is a challenging task because the CDCH operates in a high-rate environment, with an average cell occupancy of 15-25% per event in a 400 ns (maximum drift time) time window. The pattern recognition task of distinguishing individual tracks in a crowded (and noisy) detector is further complicated by the small number of layers (for instance, Belle II CDC[93] has 56 layers while the CDCH only nine) and the full-stereo geometry.

The track finding algorithm uses a "local" approach based on the track following with the Kalman filter method [94]. Starting from the most external and less busy layers of the detector, hits are combined in group of two or three into many track "seeds": they are grouped based on the relative time difference, geometrical proximity and z measurement. To evaluate the hits' $DOCA$, a reference T_0 is needed: for three hits seeds, T_0 can be self determined by the hits time, while for two hits seeds all pTC clusters within 50 ns of the trigger time are considered: for each pTC cluster a different seed with the same hits but different drift times is created.

The seeds are matched with others in the next layer, with opposite stereo view, if they are compatible within error with the estimate of z and transversal direction. At this point of the procedure the

(short) track has all its kinematics fully defined and its trajectory can be propagated back and forth to contiguous layers and wires, according to the expected motion in the magnetic field. Energy loss is included in the estimate of the trajectory in addition to the motion in the magnetic field. The uncertainties of track parameters in the propagation stage takes into account both energy loss fluctuations and multiple scattering effects. Hits are added to the track if they are consistent with the trajectory hypothesis (χ^2 test), and in that case the track parameters are updated. The procedure stops when the innermost layers are reached or when a track hypothesis fails quality checks, monitoring the number and density of merged hits or its χ^2, at intermediate steps.

After track candidates are formed starting from seeds in the outermost layers and propagating to the innermost ones, the seeding procedure continues iteratively starting from the next layer with hits not previously matched to a track segment. This procedure doesn't prevent the algorithm from finding strongly overlapping tracks, with many hits in common. Therefore, track candidates are sorted according to a quality factor, which includes track length, hits density and track χ^2, and only the best candidate among similar tracks is selected.

After track finding, track segments of single or half turns inside the CDCH (intersecting the CDCH nine layers twice or once, respectively) are passed to the fitting stage, which will also merge those segments belonging to the same particle making multiple turns inside the CDCH: 85% of tracks do three full crossings of the CDCH layers (1.5 turns), with the rest making 2.5 or even 3.5 turns before reaching and stopping in the pTC.

A novel track-finding algorithm based on Deep Neural Network models, designed to mitigate the pile-up limitations inherent to the iterative approach, is described in detail in Appendix F. Although this Pattern Recognition algorithm was not yet deployed in the 2021+'22 analysis, it is expected to provide a significant improvement in tracking performance for future searches in MEG II.

Track fitting The track fit algorithm is developed with the GenFit toolkit [95], which comes with its own Kalman Filter implementation and allows to include an optimal treatment of the material effects (energy loss and multiple scattering). The CDCH is modeled as a uniform volume of gas, since considering individual wires makes the fit procedure susceptible of instability when small trajectory changes imply hitting a wire. A possible alternative to neglecting the wire material completely is to consider an "average" medium, with gas and wire material in the correct proportion. This method was also tested, but it had poorer tracking performances compared to the model with gas only: a possible reason it that only 20% of particles are estimated to cross a wire along the trajectory, therefore in most cases wire effects are not relevant at all. The $DOCA$ and longitudinal position z of the hits are the measurements entering the χ^2 function minimized with the Kalman algorithm. The z measurement is statistically irrelevant to the fit result because of the good z estimate provided by the wires stereo angles, but it is important to stabilize the procedure numerically. The Kalman filter is complemented with a deterministic annealing filter [96] to identify and reject *pile-up* and noise hits, and to improve the resolution of the left–right ambiguities.

First, the track segments obtained by the track finder are fitted. These segments are later merged with others to get the full, multi-turn trajectory of the positron. This is done by propagating the first and last hit of each segment to the point of closest approach to the z axis, and comparing two by two the resulting positions and directions looking for a good match (quantified by a χ^2 based on the Kalman covariance matrix).

Once the track segment merge has been tried, the fitted tracks are propagated through the CDCH for their full trajectory from the target to the pTC, and a "refit" procedure searches for missing hits that the track finder, with its lower accuracy, was unable to associate to the track. Frequently, the final half turn output from the track finder results in a low quality fit due to a low number of hits and thus it is difficult to merge without this dedicated procedure. Adding hits of the final half turn to single full turns results in improved momentum resolution. The refit procedure has a large impact, increasing by ≈30% the number of hits per track, with an improvement of about 14% in the core momentum resolution (see Section 3.3).

The last fitting step consists in the propagation towards

- the pTC: at this stage the correctness of the pTC cluster association to the track is checked and the optimal track time is estimated. Updating the track time implies another correction of t_{drift} for all hits and another, more precise, estimate of the track parameters;

- the target: this provides the best estimate of the muon decay point and time, and of the positron kinematics at production, including an estimate of the full covariance matrix for the kinematics observables.

Track selection Numerous quality requirements and cleanup procedures are imposed or applied on track candidates during the track finding and fitting procedure. Yet, a certain number of poor quality tracks and duplicated tracks of a single positron, called "ghost tracks", can't be avoided. A track selection procedure has been developed to efficiently identify the best positron candidate:

1. quality cuts on fit results and geometrical properties are applied. This procedure eliminates tracks with large errors on kinematics ($> 4\sigma$ away from the core resolution), large χ^2, few hits (less than one full turn), non congruent propagation to the target or the pTC. The list of all selection criteria is in [50];

2. a neural network classifier allows to apply efficiently stricter cuts. The model is trained on labeled data, sorted with very stringent/loose quality cuts described above. The classifier outputs the probability of a track being mismeasured based on track observables like the number of hits per turn, number of turns, fit uncertainty, χ^2, hit density. This procedure reduced significantly the number of mismeasured tracks in the signal region, with a selection efficiency larger than 90%.

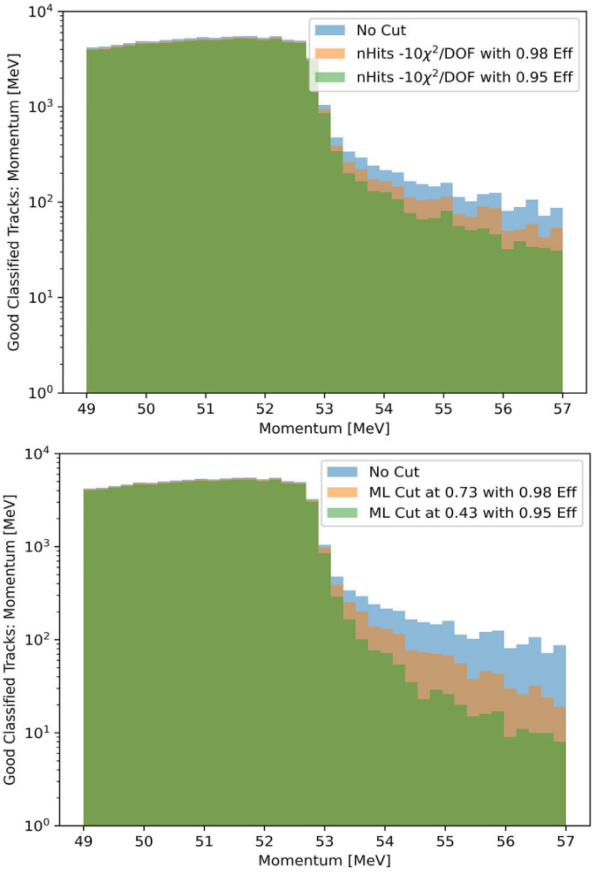

Figure 3.13: Reconstructed momentum for tracks with the application of quality cuts on N_{hits} and χ^2/DOF (top) or on the neural network classifier (bottom).

These selection criteria are used to cut misreconstructed tracks and to define a quantity, called R_{ghost}, to rank ghost tracks and choose the best one of the many duplicates:

$$R_{ghost} = -O_{NN} + 2 \times N_{turn} - B_{hit} \tag{3.4}$$

where O_{NN} is the neural network output, N_{turn} is the number of turns per track, $B_{hit} = 0$ if hits are reconstructed with the traditional hit detection algorithm, 1 if the CNN algorithm is used (the deep learning algorithm has a higher fake hits ratio, resulting in tracks of poorer quality).

The track with largest R_{ghost} is selected for each positron.

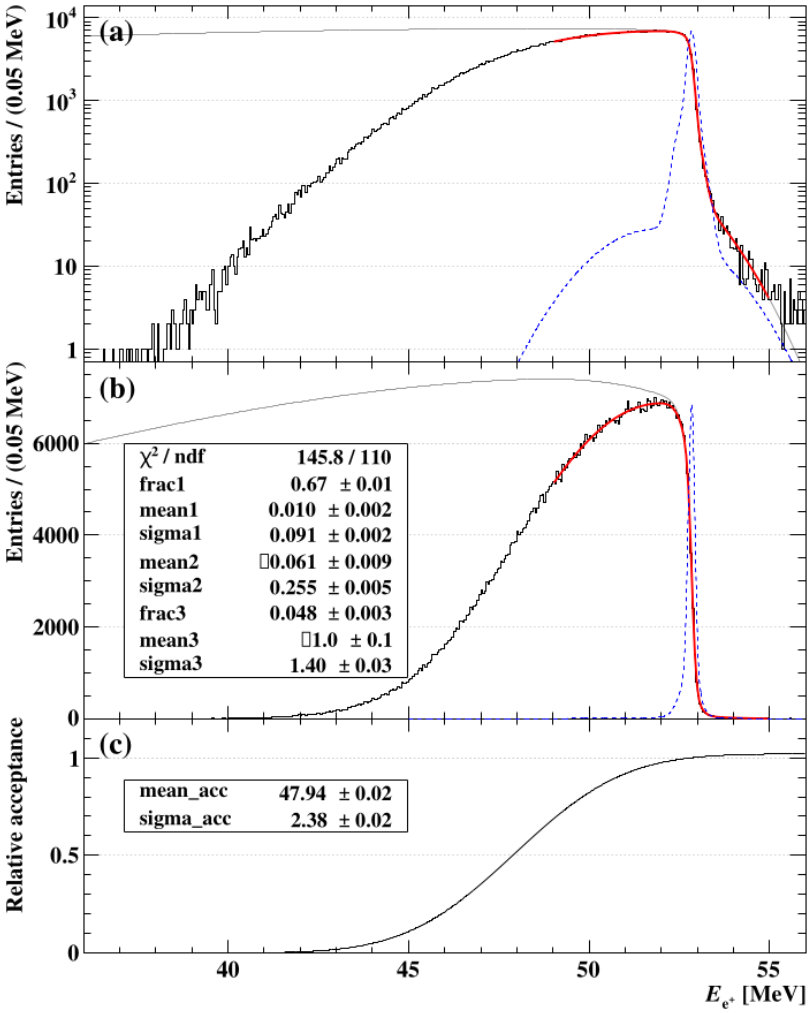

Figure 3.14: Fit to the positron's Michel decay $\mu \to e\nu\overline{\nu}$ spectrum on 2022 data: (a) in semi-logarithmic scale, (b) in linear scale. On the bottom, the fitted acceptance function.

3.3 Methods to assess performances with e^+ data

The positron kinematic variables relevant for building the $\mu \to e\gamma$ observables are: the positron momentum $\vec{p}$ at the decay point on target, described by the magnitude p and the two angles ϕ and θ, and the y and z decay position on the target[iii].

- Momentum resolution σ_p is measured from a fit to the observed Michel spectrum in $\mu \to e\nu\overline{\nu}$ events, as described in Section 3.3.1;
- the resolutions on the other variables, as well as correlations between them, is obtained through the *double turn* (DT) method, detailed in Section 3.3.2

3.3.1 Michel spectrum Fit

The energy resolution of the spectrometer is measured by fitting the positrons Michel's spectrum measured on data with the function [44]:

$$\frac{d\Gamma}{dE_e}(E_e^{meas}) = \left(\frac{d\Gamma}{dE_e}|_{th.} \times \mathcal{A} \right)(E_e^{true}) * \mathcal{R} \tag{3.5}$$

[iii] Refer to Fig. 2.4 for the definition of the variables in MEG II coordinate system.

where:

$$\begin{cases} \frac{d\Gamma}{dE_e}|_{th.} = \text{theoretical Michel spectrum @NNLO for polarized muons [85]} \\ \mathcal{A} = \text{Acceptance function of the spectrometer} = \frac{1+\text{erf}\left(\frac{E_e^{true}-\mu_{\mathcal{A}}}{\sqrt{\sigma_{\mathcal{A}}}}\right)}{2} \\ \mathcal{R} = \text{resolution function = sum of three Gaussians PDFs} \end{cases}$$

The functional forms for the acceptance $\mathcal{A}$ and resolutions $\mathcal{R}$ terms are based on Monte Carlo simulations. The detector resolution for signal-like events is well described by the Gaussian shape accounting for the largest fraction of the resolution curve integral, called the "core".

Apart from measuring the energy resolution of the spectrometer, the Michel fit allows to calibrate the magnetic field intensity and the relative alignment between the COBRA magnet and the CDCH:

- the resolution function is centered on the spectrum edge ($E_e = 52.83$ MeV). A bias in the measured energy $E_e^{meas} - E_{true}$ causes the edge position to be shifted, with the mean of the central gaussian function that is significantly ($\mathcal{O}(100)$ keV) different from zero. The magnetic field intensity is eventually rescaled to set this bias to zero again;
- CDCH and B field misalignment is visible as a non constant bias of the Michel edge as a function of the positron emission angles θ_e and ϕ_e.

3.3.2 Double Turn Analysis

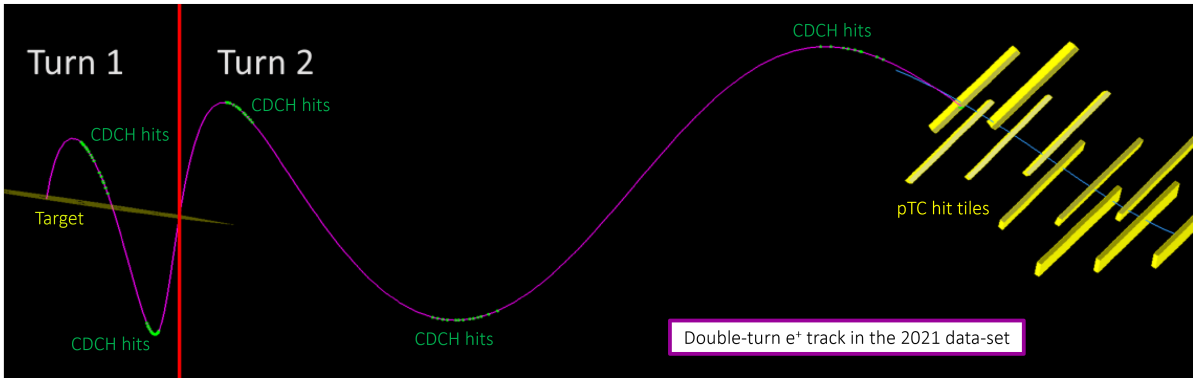

Figure 3.15: Event display of a track making two full turns inside the spectrometer.

Many positron tracks traverse the spectrometer making more than two turns, as exemplified in Figure 3.15. These "double turn" events [44, 90] are exploited to extract from data the resolution of kinematic variables: the two fitted segments of a track to each turn are propagated independently to the midpoint between the two turns, called the "vertex"; from a fit to the distribution of $q_1 - q_2$, the difference in the estimated observable q, we can estimate the detector resolution of the variable q. The fit function used is the convolution of two gaussians, one describing the resolution of the first turn, one that of the second turn:

$$A_1^2 \cdot \left[exp\left(-\frac{(x-2\mu_1)^2}{2\sigma_{core}^2} \right) + \left(\frac{A_2}{A_1} \right)^2 exp\left(-\frac{(x-2\mu_2)^2}{2\sigma_{tail}^2} \right) + 2\frac{A_2}{A_1} exp\left(-\frac{(x-\mu_1-\mu_2)^2}{2(\sigma_{core}^2+\sigma_{tail}^2)} \right) \right] \tag{3.6}$$

In Figure 3.16 the Double Turn distribution for the y_e variable is plotted as an example.

3.3.3 Positron efficiency

The positron efficiency ϵ_e is defined as the ratio of the number of reconstructed positrons[iv] in the signal energy region to the number of emitted positrons in the direction opposite to the LXe acceptance

[iv] Reconstructed positron ≡ positron's track correctly fitted from the target to the pTC tile firing the trigger.

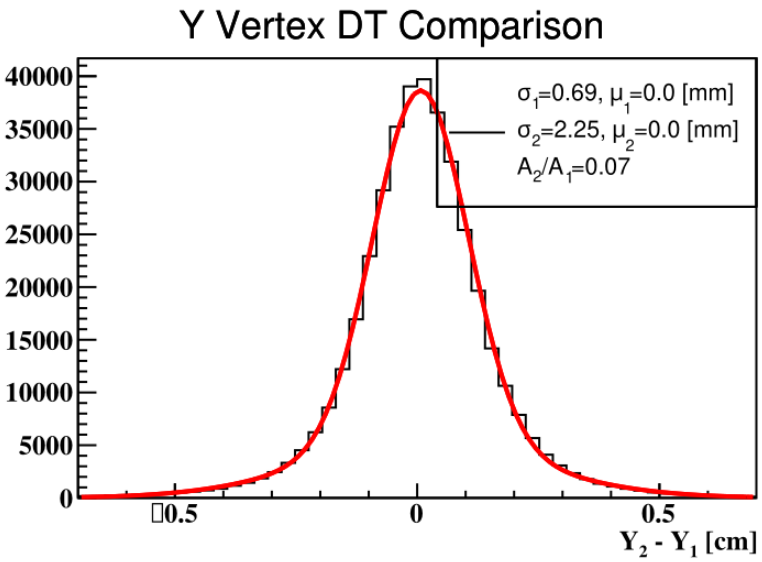

Figure 3.16: Double turn residual distribution of the y reconstructed position of the track on the target. The fit function is given in (3.6).

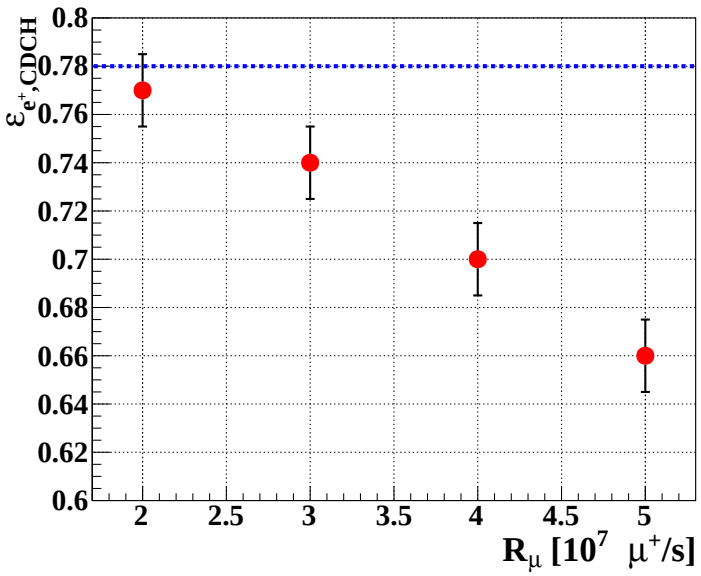

Figure 3.17: CDCH efficiency measured on 2021 data at various beam intensities. The tracking efficiency worsens because the tracking algorithm struggles with increasing pile-up levels.

region. The positron efficiency ϵ_e is the product of the CDCH and pTC efficiencies. The pTC efficiency is very high: for signal positrons it's $\epsilon_{e,\,\mathrm{pTC}} = (91 \pm 2)\%$ (value extracted from Monte Carlo simulations).

The efficiency of the CDCH $\epsilon_{e,\mathrm{CDCH}}$ is measured using data taken through a minimum bias trigger developed to select Michel events. The trigger requires only one hit on the pTC to select an event. Monte Carlo simulations are used to correct for muon decays out of the target[v] and to extrapolate the efficiency to the energy region of the signal [43, 85]. In Figure 3.17 the trend of $\epsilon_{e,\mathrm{CDCH}}$ as a function of the beam intensity is shown. While the pTC efficiency is almost independent of the beam intensity, the CDCH tracking efficiency decreases when R_μ increases. This is expected, since when the pile-up augments, the track finder algorithm is less effective at identifying hits belonging to individual tracks.

As discussed in Appendix F, novel track finder algorithms based on Deep Neural Networks architectures are being developed inside the MEG II Collaboration to overcome this decrease of the tracking efficiency in high pile-up conditions.

3.4 The Cylindrical Drift Chamber 2

The successful construction of the CDCH was seriously threatened by an issue that occurred to the ultra-thin 40 µm silver plated aluminum cathode wires. About 100 of these wires (out of 1728) broke during the construction stage because of chemical corrosion taking place at the aluminum-silver interface in presence of water (air humidity) [97]. This problem didn't affect the 50 µm cathodes because they are machined with a different technique by the manufacturer[vi], and the surface of these bigger wires doesn't present the same amount of imperfections in the silver coating.

The problem was finally solved removing all broken wires, and since then the CDCH's volume is fluxed with water-free gas mixtures also when MEG II data taking stops to prevent other wires from breaking. A new accident would be probably fatal for the operations of the CDCH: for this reason, a second drift chamber, the CDCH2, has been built in the INFN laboratories in Pisa [98].

The design of the CDCH2 is identical to the CDCH's one, excepting:

- both the 40 µm and 50 µm Al/Ag cathode wires have been replaced with 50 µ Al wires. New tests on California Fine Wires samples showed that also the 50 µm Al/Ag wires were subject to corrosion, therefore pure aluminum wires where chosen;
- a tenth layer, at the outermost radius, has been added: this layer fits the mechanical constraints and was actually already planned for the CDCH also, but never built.

The choice of pure aluminum cathode wires requires a new strategy to solder them to the PCB: indeed, the infrared laser mounted on the wiring machine can not properly solder them, and wires slip through the tin drop deposited during the soldering procedure.

To keep the wires in position, after the soldering, a drop of bi-component DP100[vii] epoxy glue is deposited with an air-powered dispenser integrated in the wiring machine. The gluing system is shown in Figure 3.18. The glue takes $\approx$ 20 minutes to dry, and after this time the wires are anchored to their position.

The wiring and assembly procedures were completed in $\approx$ 3 years (2022-2025), and carried out entirely in the clean room of the INFN laboratories in Pisa. The detector fully wired is shown in Figure 3.19. The detector will now (2025) be moved to PSI for the installation of the internal Mylar foil and the sealing with the carbon fiber structure, as for the CDCH. There, it will remain as a backup solution in cases of unrecoverable problems with the CDCH in the last year of data taking (2026).

[v] These events would produce a signal in the pTC that can not be matched with a track originating from the target.
[vi] California Fine Wires https://calfinewire.com/.
[vii] https://www.3mitalia.it/3M/it_IT/p/d/b40066435/

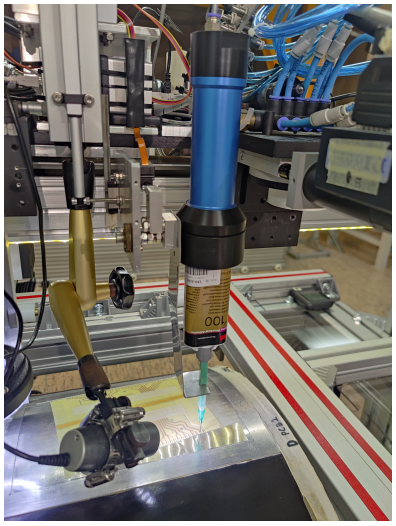

(a) The glue dispenser mounted on the wiring machine.

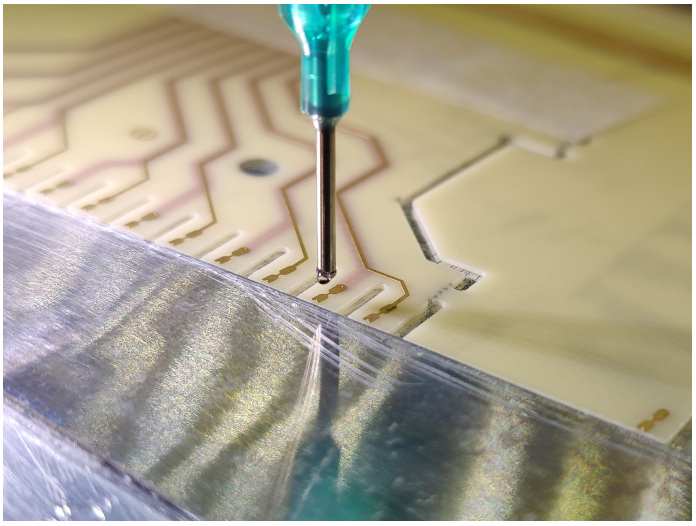

(b) Close up of the needle used to apply the glue on the PCB.

Figure 3.18: The new gluing system of the wiring machine for the CDCH2's construction.

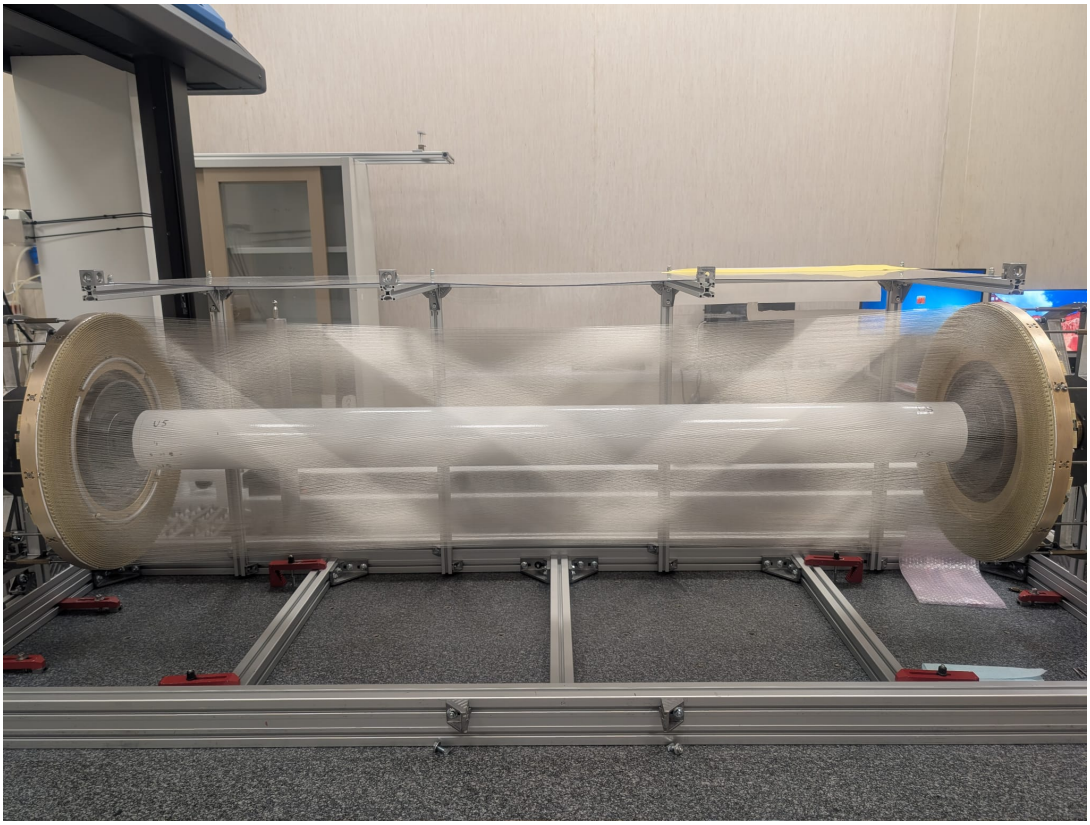

Figure 3.19: The CDCH2.

Chapter 4

CDCH calibration with Michel positrons data

This chapter deals with the CDCH calibration using e^+ data collected in 2022, following a scheme developed for the 2021 analysis. The candidate has been in charge of the CDCH calibration on the 2022 dataset, in view of the reprocessing for the 2021+'22 MEG II analysis.

With the expression "calibration of the CDCH" we refer to the set of tasks and procedures aimed at guaranteeing optimal performances of the detector, reducing biases in the different reconstruction stages, from hit reconstruction to tracking. The steps toward the full detector's calibration are summarized in the diagram of Figure 4.1.

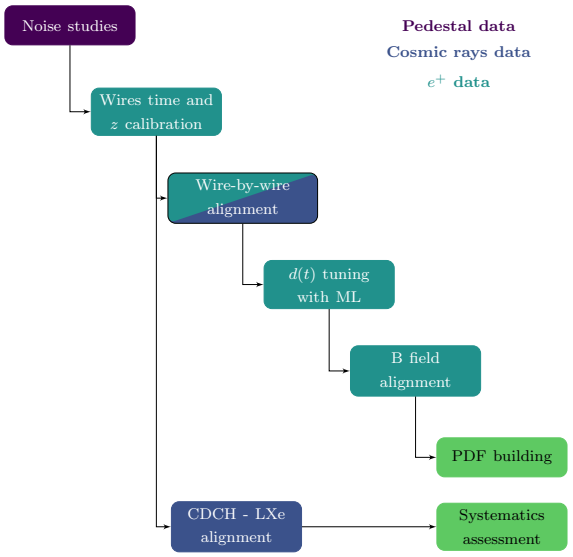

Figure 4.1: Schedule of the CDCH calibration towards the Physics analysis.

This subject is divided into two chapters, according to the type of data used in the specific calibration step: in this one, we focus on the calibration with Michel positrons data; in Chapter 5 we deal with cosmic rays data.

In order: Section 4.1 is about noise studies; Section 4.2 is dedicated to the iterative alignment procedure; Section 4.3 is about COBRA magnetic field tuning and Section 4.4 about the relative alignment between the CDCH and the target, closely related to the CDCH - COBRA alignment; Section 4.5 discusses updates of the Machine Learning algorithms; update of track selection criteria is discussed in Section 4.6; Section 4.7 reports on the stability of the performances during the whole data taking period. For the calibration with Michel positrons, we describe the procedure applied for 2022 data only. The 2021 dataset was already calibrated for the 2021 analysis [8, 90] and no issue was found which could motivate a revised calibration.

4.1 CDCH noise studies in 2022

The characteristics of the electronic signal of each readout wire end during data taking is investigated to spot deviations from the correct behavior: in general, hits' signals have an amplitude higher than 20 mV; the CDCH occupancy during physics data taking is uniform in ϕ, with more hits recorded in the innermost layers; the baseline is centered at zero (after noise removal) and its RMS is below 3 mV. We look for the following problems, visible in the data representation illustrated in Figure 4.2:

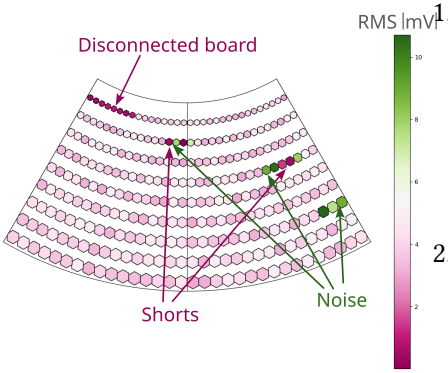

Figure 4.2: Shorts, disconnected boards and noisy wires are outliers in the distribution of the signals' RMS. In a bi-dimensional view of the CDCH like the one reported here, wires deviating from the average trend are easily spotted.

1. broken or disconnected FE boards: they have very small readout signals for all eight channels, with an RMS below 1 mV (corresponding to the WaveDREAM DRS chip noise) and no recorded hits. If the problem reguards a board distributing the HV, no signal on either side of the wire will be recorded; otherwise, one end works properly;

2. short-circuited anode wires: in this case noise levels can vary considerably. 28 known shorts were identified during the detector commissioning and isolated from the HV directly on the FE board. If a new short appears, and a hardware intervention to isolate it is not possible, the corresponding FE board must be disconnected;

3. noisy wire ends, defined by an amplitude/baseline RMS much larger than the typical value of 5/2.5 mV respectively. These wires usually record a very high number of fake hits. Anodes next to shorts are affected by these problems. For other wires instead, the noise arise from missing electric components on the FE board (resistors, capacitors) in the shaping or amplification stage: in this case, the signal/noise ratio can be improved with a moving-average low-pass filter.

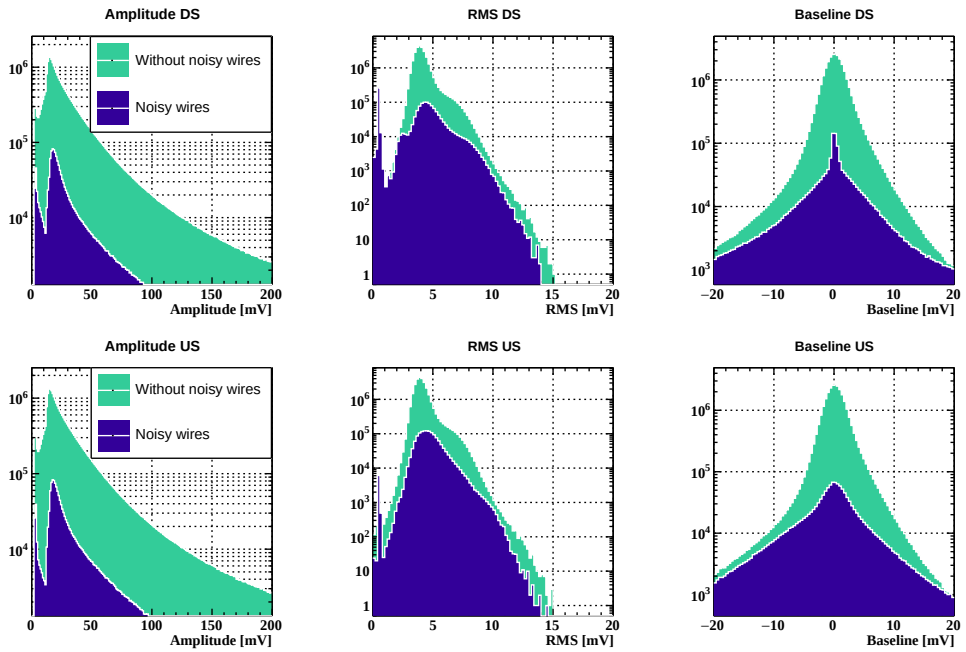

Figure 4.3: Distributions of signals' amplitude, RMS and baseline observed on 2022 data, on top for upstream signals, on bottom for downstream ones. The distributions are shown for both the noisy (blue) and the good wires (green).

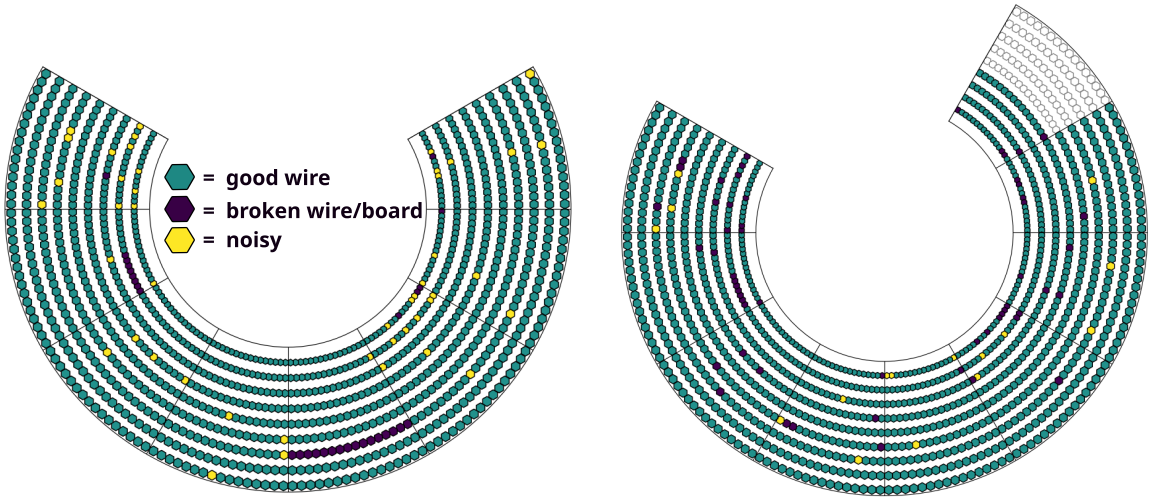

(a) Year 2021 (b) Year 2022

Figure 4.4: Map of the noisy (yellow) and broken wires and boards (dark purple).

In Figure 4.3 we plot the histograms of the signals' amplitude, RMS and baseline measured for 2022 data. The contribution of the problematic wires is shown superimposed to the distribution of good wires. Comparing the distributions of the two kinds of signals, we can notice that the wires identified as problematic have: smaller signals, never above 100 mV and more often no signal at all (higher peak around ~0 mV); peak in the RMS distribution around ~ 0 mV, which identifies shorts or disconnected boards; broader baseline fluctuations (noise).

Between the run of 2021 and 2022 the CDCH underwent a hardware intervention to mitigate the source of a high frequency noise on a few CDCH sectors [85]. This work allowed to recover the signal from 5 disconnected FE boards which were propagating noise to nearby sectors. In addition to this intervention, four CDCH sectors (layer 6-9 of sector 11) were instrumented in order to widen the acceptance.

The impact of this work on the CDCH is clearly visible comparing the two 2D plots of the CDCH in Figure 4.4. The number of bad channels during run 2021 and 2022 is reported in Table 4.1. Usually, noise levels are very stable during the data taking period; no FE board breaks or new shorts show up after the first week of beamtime.

Table 4.1: List of bad readout channels with no signal during 2021 and 2022 data taking periods, separated between US and DS when relevant.

Issue	Year 2021		Year 2022	
	US	DS	US	DS
# FE boards not readout	7	8	2	3
# noise wires with no signal	21	42	28	33
# short-circuit anodes	28		28	
Tot. bad wires	73		64	

4.1.1 Burst of noise during September 2022

During September 2022, a problem to the low voltage system of the CDCH front-end boards resulted in a high frequency noise on a few sectors of the CDCH connected to the damaged low voltage module. In Figure 4.5 we show that in that period of time some wires had much higher levels of noise which

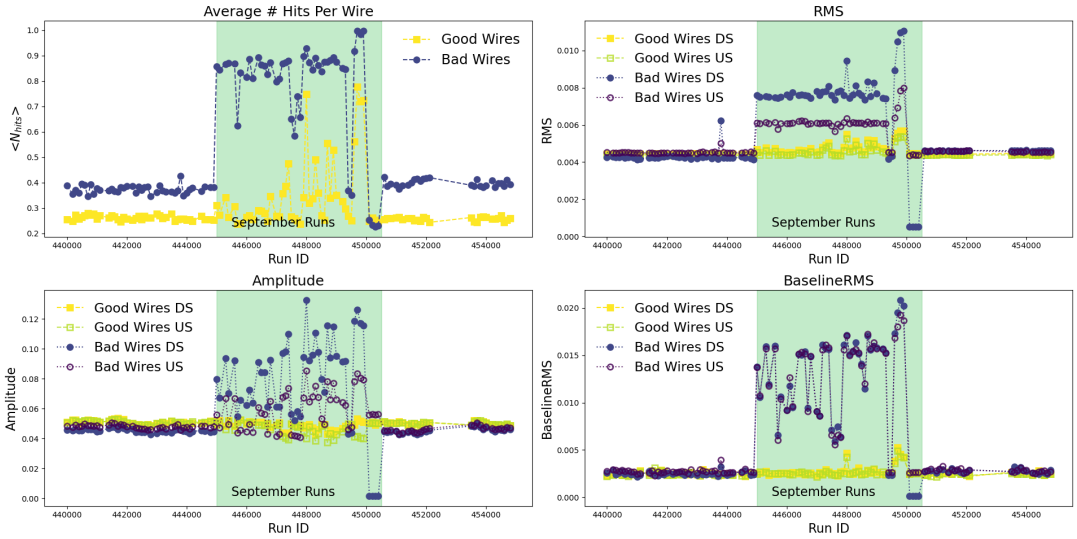

Figure 4.5: Time dependent analysis of noise levels on a set of wires affected by the problem in September (dark colors) and a set of undisturbed wires (light colors). Upstream (US) and downstream (DS) ends of the wires are separated to highlight that the noise originated from an hardware problem on the DS side of the detector.

resulted in a large occupancy causing problems to the pattern recognition algorithm, with the tracking efficiency worsening from 65% to 33%. This problem was spotted already during the data taking period and solved by repairing the low voltage module; on the analysis side, a new routine for noise filtering allowed to retrieve a good signal efficiency on all wires: we applied first the low pass filter at 225 MHz, then the low frequency noise subtraction algorithm for eliminating the coherent noise contribution[50]. The result for a single waveform example is shown in Figure 4.6.

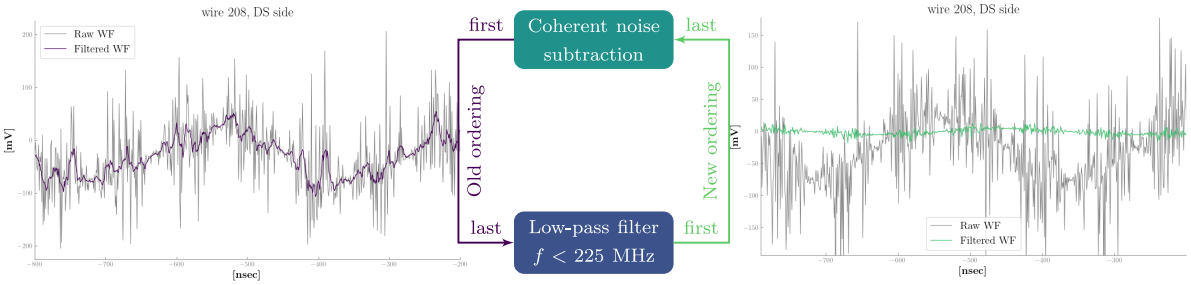

Figure 4.6: On the left: a raw waveform (grey) analyzed using the old ordering of the noise filters, as shown on the scheme at the center; on the right: the same waveform is processed with the new method (filtered waveform in green).

The new ordering of the filter algorithms allowed to completely recover signals on the wires affected by this noise, so that full tracking efficiency was recovered. As illustrated in Figure 4.7, the rate of Michel decays detected per unit time $dk_{\mu\to e\nu\overline{\nu}}/dt$ is now constant throughout the full data taking period at 3×10^7 μ^+/s. This fix allowed to recovery $\sim$ 5% of the full accumulated statistics in 2022.

4.2 The iterative alignment of the CDCH

The accurate alignment of the CDCH is a key calibration step towards the achievement of optimal detector performances. The tracker intrinsic spatial resolution is better than the alignment precision from the optical survey measurements carried out during the mounting stage (see Chapter 2, Section 3.1), therefore a software alignment strategy is used [85, 99].

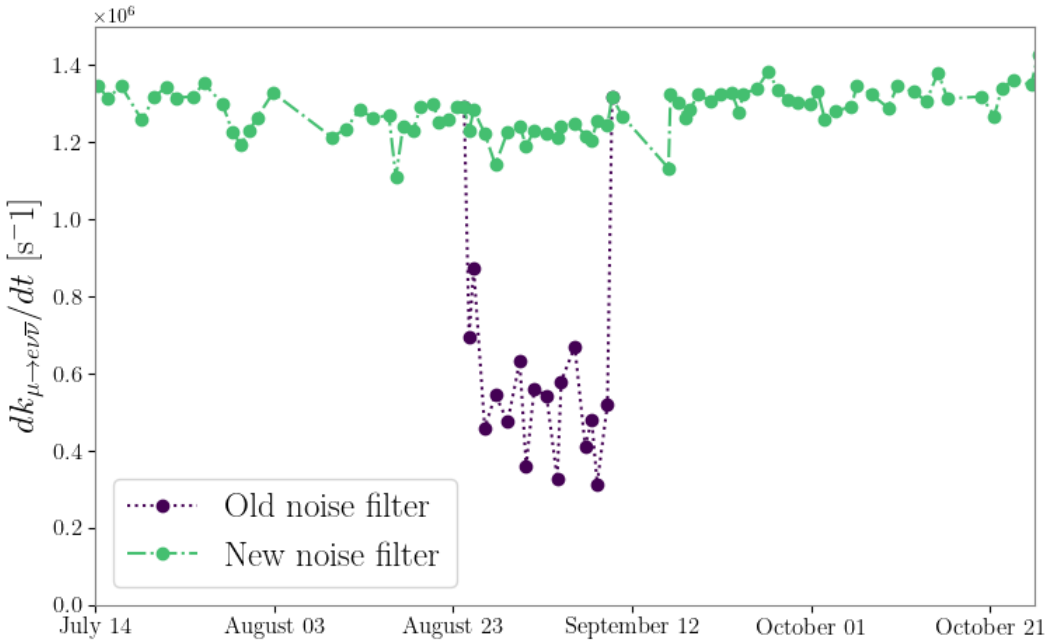

Figure 4.7: The rate of positrons from Michel decay detected in the apparatus during the data taking period is a good observable to monitor the efficiency of the TDAQ and of the spectrometer. During September, the drop in CDCH efficiency by almost 50% is clearly visible. With the application of the new noise filter algorithm though, full CDCH efficiency is recovered.

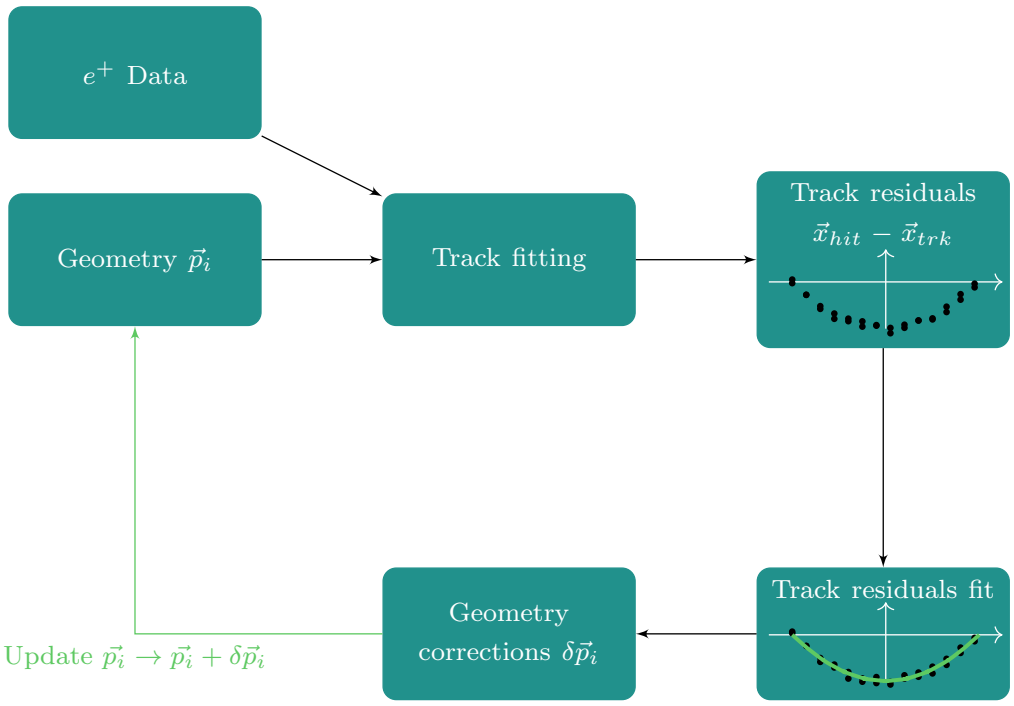

Figure 4.8: Scheme of the iterative alignment procedure.

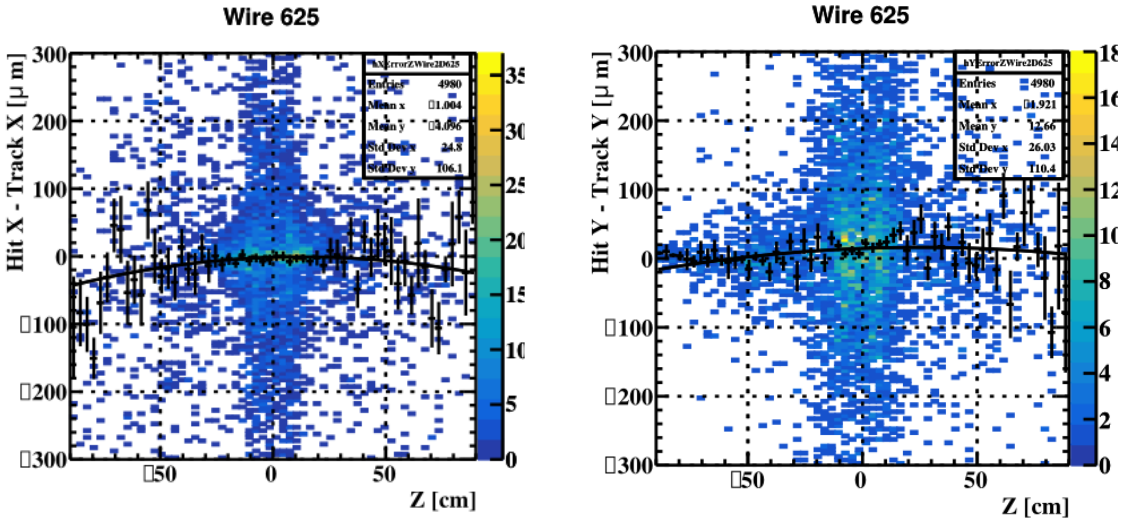

(a) $x^{meas} - x^{fit}$ VS z.

(b) $y^{meas} - y^{fit}$ VS z.

Figure 4.9: Parabolic fit to the residuals distribution for the wire 625 of the CDCH.

Software alignment algorithms use charged particle tracks to determine the optimal geometry parameters $\vec{p}$ of the tracker modules solving the following χ^2 problem:

$$\chi^2 = \sum_{i}^{tracks} \sum_{j}^{hits} \left(\vec{x}_{ij}^{meas} - \vec{x}^{fit}(\vec{p}, \vec{\tau}_i)_{ij}\right)^T V_{ij}^{-1} \left(\vec{x}_{ij}^{meas} - \vec{x}^{fit}(\vec{p}, \vec{\tau}_i)_{ij}\right) \tag{4.1}$$

where $\vec{x}_{ij}^{meas} - \vec{x}_{ij}^{fit}(\vec{p}, \vec{\tau}_j)$ are the track residuals between measured position and fit estimate of hit j on track i with track parameters $\vec{\tau}_j$. Hit coordinates $\vec{x}$ are given in the local frame of the drift cell. V_{ij} is the covariance matrix.

Currently, the CDCH geometrical parameters of each wire are determined with an *iterative* procedure [50, 90] using $\mu \rightarrow e\nu\overline{\nu}$ events summarized in the block diagram scheme of Figure 4.8: first, tracking is performed using geometry parameters $\vec{p}_i$, where $i = 0, ..., N$ is the iteration step; second, for every wire in the CDCH the distribution of track residuals as a function of the recorded hit position z along the wire is drawn and fitted with a parabolic function (one fit for the x component of the residuals and one for the y):

$$f^{x(y)}(z) = c_0^{x(y)} + c_1^{x(y)} \cdot z + c_2^{x(y)} \cdot \left(\frac{2z}{L}\right)^2 \tag{4.2}$$

finally, the best-fit values $\hat{c_0}^{x(y)}$, $\hat{c_1}^{x(y)}$, $\hat{c_2}^{x(y)}$ are used to correct the wire parameters and a new iteration starts with the updated geometry. The procedure stops when the algorithm converges, namely when the χ^2/dof distribution of fitted tracks peaks at 1 and the distribution of residuals for each wire shows no bias.

The geometrical parameters of each wire $\vec{p}$ are six (number of degrees of freedom of a parabola in three dimensions): x_0, y_0, θ , ϕ, s_0, γ (see 3.1.2). We choose to fix the z_0 parameter because we don't have enough resolution on the z coordinates of the hit to determine it more precisely than the optical survey ($\mathcal{O}$(0.5 mm)).

The update rules $\vec{p}_{i+1} = \vec{p}_i + \vec{\delta p}_i$ are derived starting from the following first-order approximation of track residuals:

$$\vec{x}_{hit} - \vec{x}_{trk} = \Delta\vec{x_0} + R(\delta\theta, \delta\phi)\begin{pmatrix}0\\0\\z\end{pmatrix} + \left(\delta s_x \hat{r} - \delta s_y \hat{t}\right) \cdot \left(\frac{4z^2}{L^2} - 1\right) \tag{4.3}$$

where we have introduced the two carthesian components of the sagitta $\vec{(s)}$, s_x and s_y as in Figure 4.10:

$$\begin{cases} s_x = s_0 \cdot \cos\gamma \\ s_y = s_0 \cdot \sin\gamma \end{cases} \rightarrow \begin{cases} s_0 \equiv \sqrt{s_x^2 + s_y^2} \\ \gamma \equiv \arctan 2\left(s_y, s_x\right) \end{cases} \tag{4.4}$$

where $\hat{r}$ is the radius unit vector between the CDCH center and wire center (x_0, y_0) and $\hat{t}$ is the orthogonal vector to $\hat{r}$ in the $x-y$ frame.

From Equation 4.3, the following update rules descend

$$\begin{cases} x_0\ (y_0) \rightarrow x_0\ (y_0) - c_0^{x(y)} - c_2^{x(y)} \\ \theta,\ \phi \rightarrow \text{polar and azimuthal angles of the vector} \\ \qquad \begin{pmatrix} x^{US} - z^{US} \cdot \hat{c}_1^x - \hat{c}_2^x \\ y^{US} - z^{US} \cdot \hat{c}_1^y - \hat{c}_2^y \\ z^{US} \end{pmatrix} - \begin{pmatrix} x^{DS} - z^{DS} \cdot \hat{c}_1^x - \hat{c}_2^x \\ y^{DS} - z^{DS} \cdot \hat{c}_1^y - \hat{c}_2^y \\ z^{DS} \end{pmatrix} \\ s_x \rightarrow s_x + c_2^x \cdot \hat{r}^x + c_2^y \cdot \hat{r}^y \\ s_y \rightarrow s_y - c_2^x \cdot \hat{t}^x - c_2^y \cdot \hat{r}^y \end{cases} \tag{4.5}$$

where $\vec{x}^{US/DS}$ are the coordinates of the wire at the end plates.

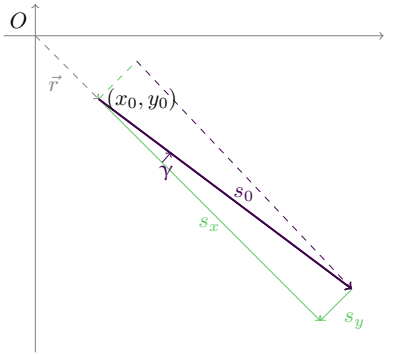

Figure 4.10: Redefinition of $\vec{s}$ using carthesian coordinates (green) instead of polar coordinates (blue).

4.2.1 Results of the iterative alignment

The wires position can change in time as a consequence of external factors altering the CDCH geometry: of course, hardware maintenance works requiring to extract the CDCH from the COBRA magnet cryostat, but also one FE board failure altering the electrostatic equilibrium of the CDCH can have a visible impact on the wire geometry. Looking at the track residuals in Figure 4.12, measured for 2022 Michel data with the geometry determined in 2021, a non-null bias is visible for the central wires in plane 2, 3 and 4: this is compatible with an electrostatic effect caused by the replacement of two broken FE boards in plane 3.

The alignment procedure is performed using Michel events collected in 2022, starting from the geometry determined with the alignment on 2021 data. The convergence is reached after 15 iterations. Comparing Figures 4.11, 4.12 with Figures 4.13, 4.14 the improvement of the residual distribution can be clearly seen for all wires. The improvement in hit spatial resolution is reflected also in an improvement in tracking efficiency and kinematic resolutions, as discussed in [85, 90]. The performances using 2022 data before and after the alignment are listed in Table 4.2.

Table 4.2: Positron tracking performances measured on 3×10^7 μ^+/s data acquired in 2022 using the CDCH geometry determined in 2021 or after the convergence of the alignment procedure. Efficiencies are evaluated without using the ML hit finding algorithm.

	σ_{y_e}	σ_{z_e}	σ_{θ_e}	σ_{ϕ_e}	σ_{p_e}	ϵ_{trk}
2021 iter. alignment	2.05 mm	0.79 mm	6.85 mrad	8.42 mrad	115.6 keV	56.0%
2022 iter. alignment	1.96 mm	0.70 mm	6.71 mrad	7.85 mrad	107.4 keV	57.8%

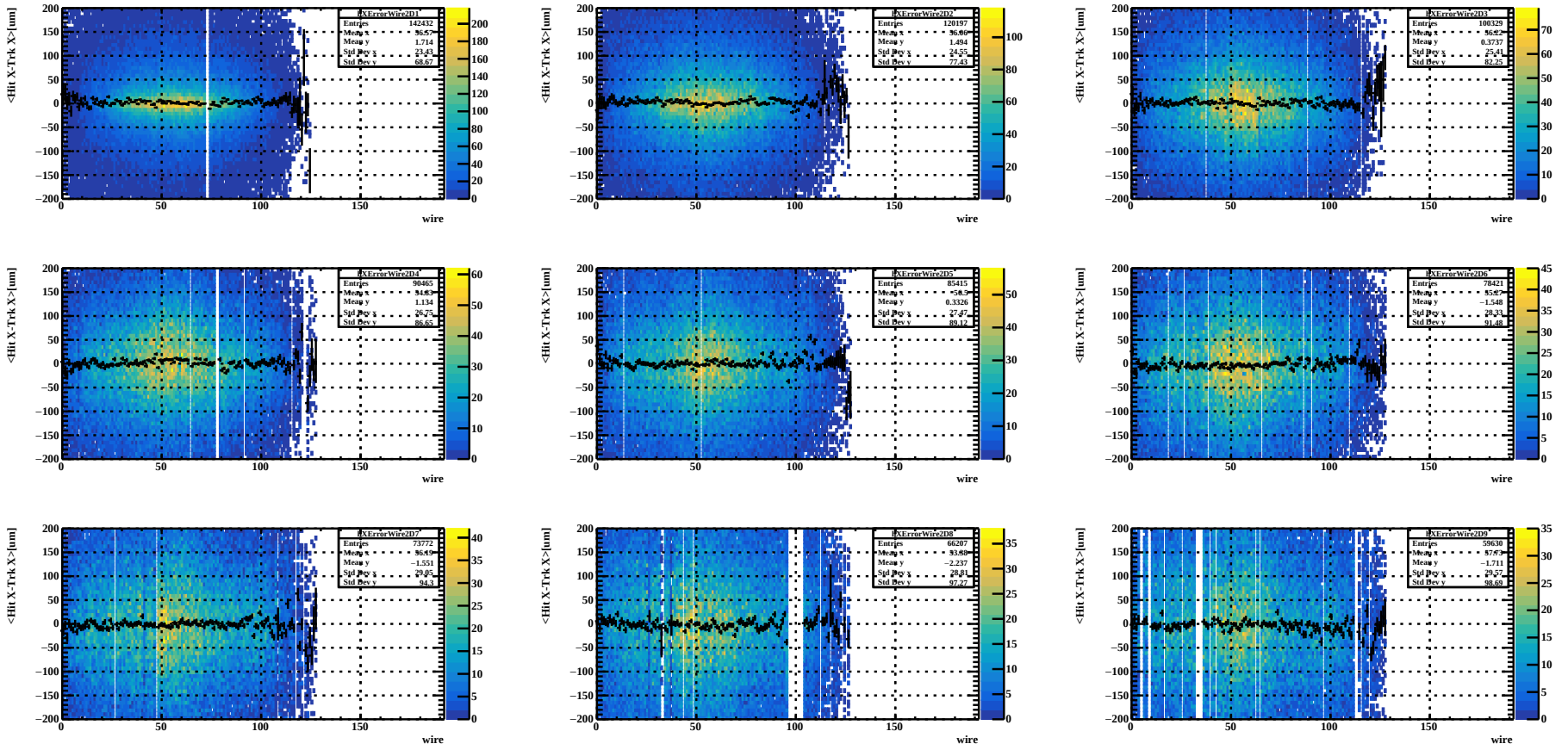

Figure 4.11: $x^{meas} - x^{fit}$ for all wires (wire ID on the $x-$axis) at the beginning of the alignment procedure, using the geometry from the alignment performed in 2021. Wires are grouped per CDCH plane.

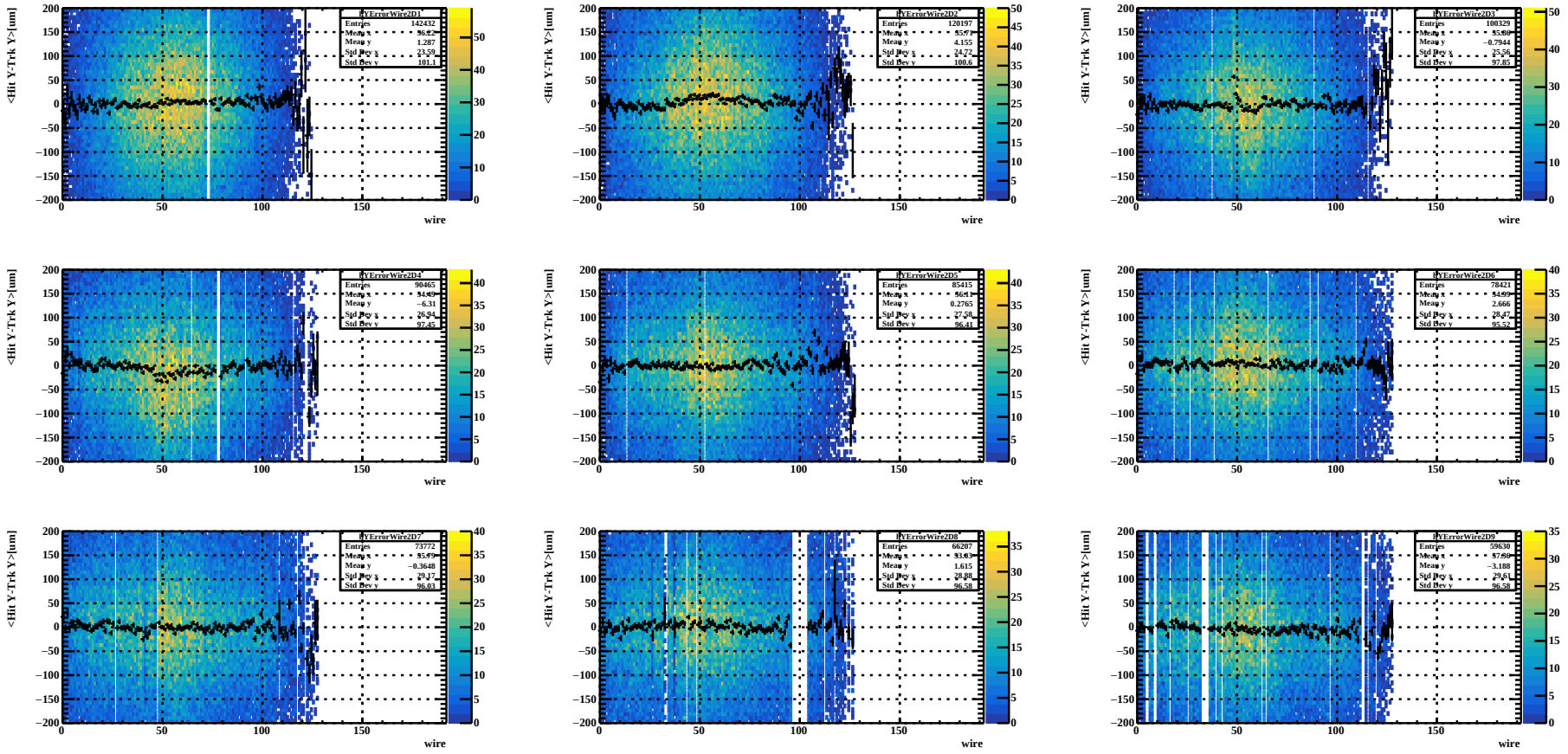

Figure 4.12: $y^{meas} - y^{fit}$ for all wires (wire ID on the $x-$axis) at the beginning of the alignment procedure, using the geometry from the alignment performed in 2021. Wires are grouped per CDCH plane.

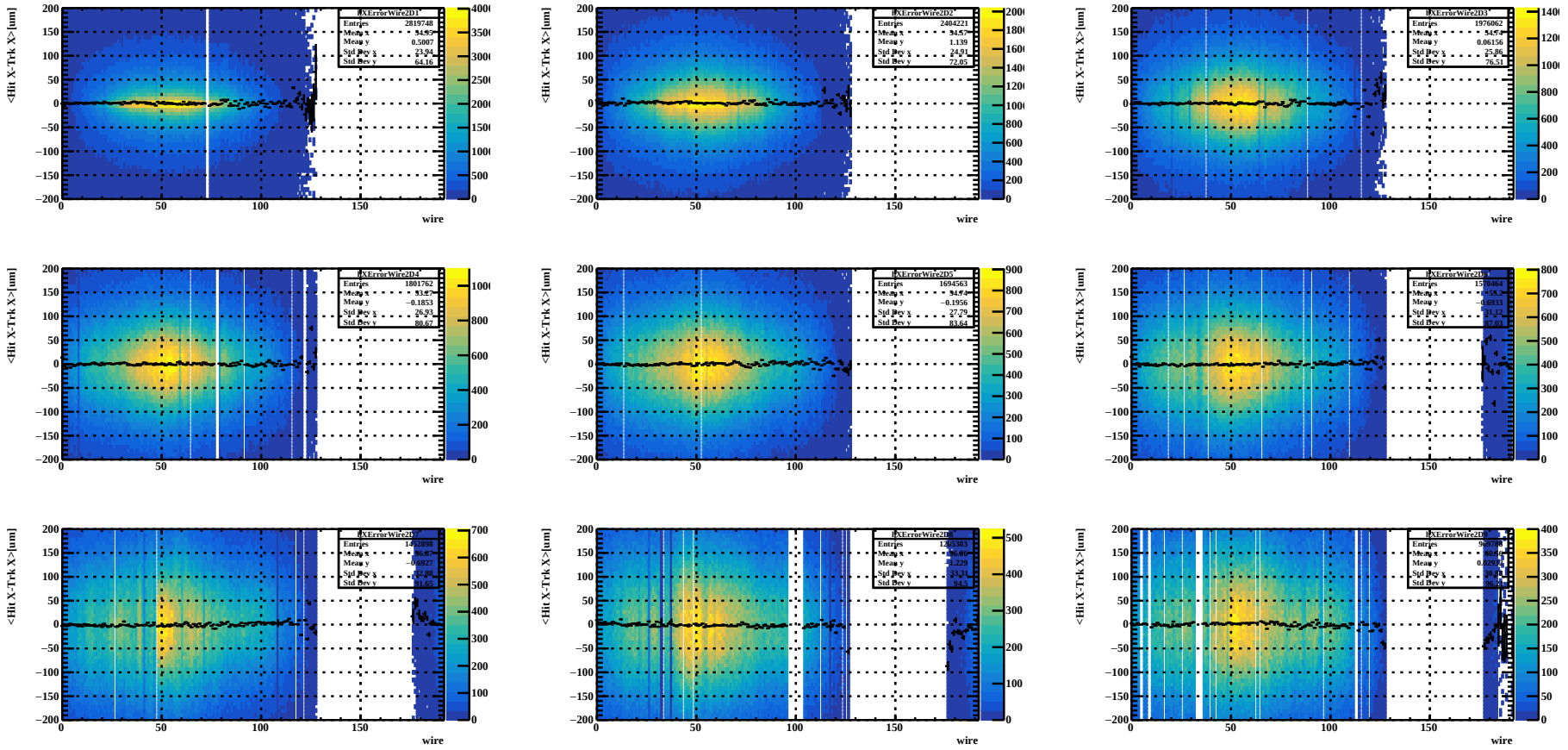

Figure 4.13: $x^{meas} - x^{fit}$ for all wires (wire ID on the $x-$axis) at the end of the alignment procedure, after 14 iterations. Wires are grouped per CDCH plane.

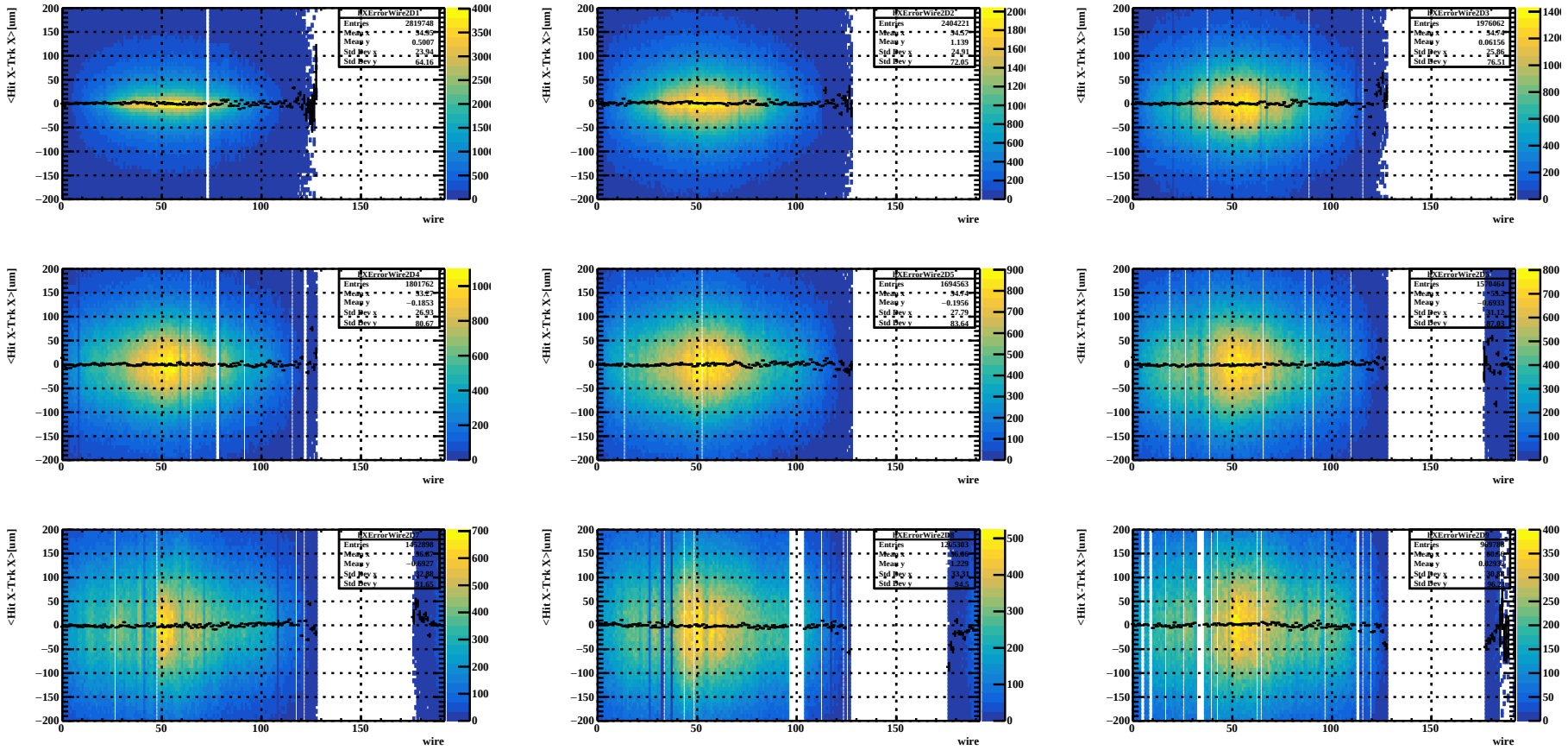

Figure 4.14: $y^{meas} - y^{fit}$ for all wires (wire ID on the $x-$axis) at the end of the alignment procedure, after 14 iterations. Wires are grouped per CDCH plane.

4.3 Magnetic field tuning

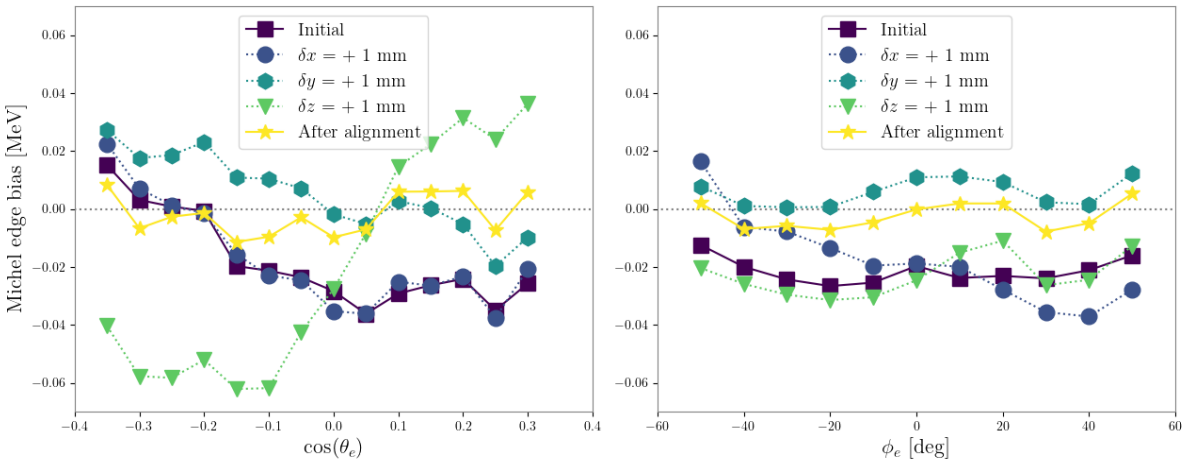

Figure 4.15: Effect of the magnetic field alignment on the angular dependence of the positron energy scale. For comparison, the effects of +1 mm shifts in x, y and z are superimposed. From [43].

Any misalignment between COBRA magnetic field and the CDCH or inconsistencies between the nominal and real field strength is a source of error in the positron reconstruction: misalignment (translations and rotations) manifests itself as a non-constant positron energy scale as a function of the emission angles θ_e and ϕ_e; instead, a discrepancy in the field strength $|\vec{B}|$ corresponds to a constant shift of the energy scale. The positron energy scale bias is measured as a deviation of the Michel edge position from the theoretical value.

The optimization of the magnetic field parameters is done testing tracking performances with different sets of parameters, until the biases are removed. Ignoring rotations, the number of parameters to test is four: x, y, z shifts and the scaling parameter. Based on survey measurements and on the specifications of the magnet, the range of possible values is bounded. Although feasible, this is a very computationally expensive and time consuming procedure, since for every set of parameters many data need to be reprocessed to have a meaningful statistics to draw conclusions.

This procedure was carried out first for the 2021 analysis [43]. The results of this study are illustrated in Figure 4.15. For 2021, the best magnetic field parameters for positron reconstruction are:

x shift	y shift	z shift	$\lvert\vec{B}\rvert$ scaling
100 µm	700 µm	300 µm	0.9991

The same studies were repeated for the combined 2021 and 2022 analysis. Since between 2021 and 2022 data taking nor the CDCH nor the magnet were moved, no misalignment is expected. Indeed, the Michel edge bias angular distribution is flat (Figure 4.16). Yet, an average deviation from zero is observed. Taking the weighted average of biases in ϕ_e and $\cos\theta_e$ angular distribution, the bias is measured to be (-10 ± 2) keV.

This shift in the positron energy scale is caused by a redefinition of the MEG II target geometry in the software which was done after the magnetic field optimization studies for the 2021 analysis. This change alters the computation of the positron energy loss during tracking and results in systematically underestimating the positron energy scale. Scaling the magnetic field intensity solves the problem: approximating the positron trajectory to a circle in the transverse plane, shift $\delta p = -10$ keV/c for positrons at the end point, with $p = 52.83$ MeV/c is equal to a bias of the magnetic field δB of

$$\frac{\delta B}{B} = -\frac{\delta p}{p} \approx 2 \times 10^{-4} \tag{4.6}$$

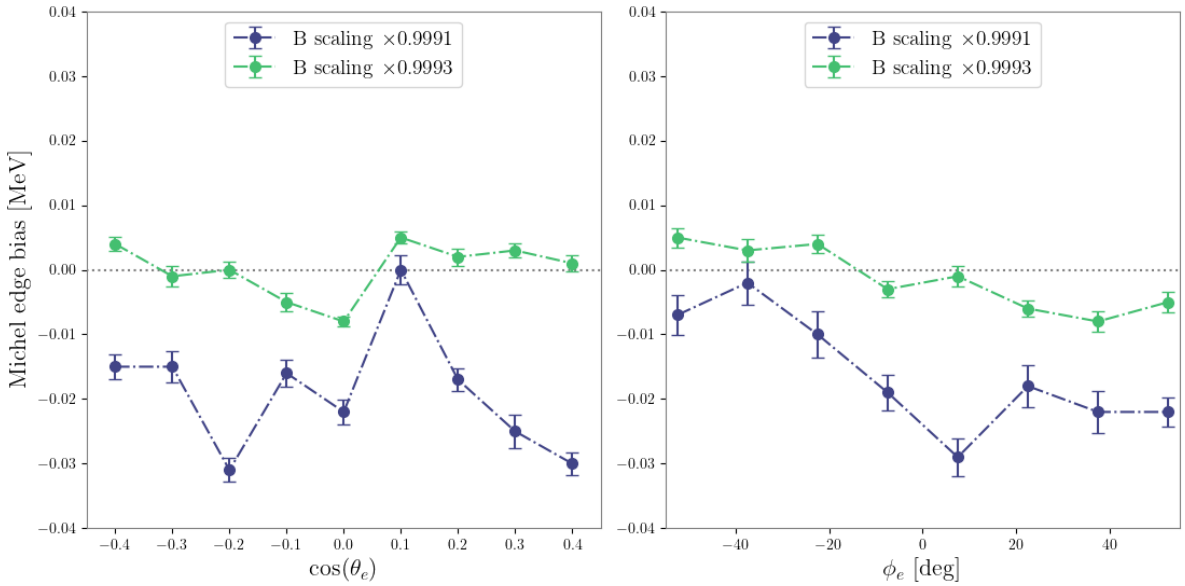

Figure 4.16: Angular dependence of the Michel edge bias with a scaling of the magnetic field intensity of 0.9991 (blue) and 0.9993 (green) which eliminates the bias in the positron reconstructed energy.

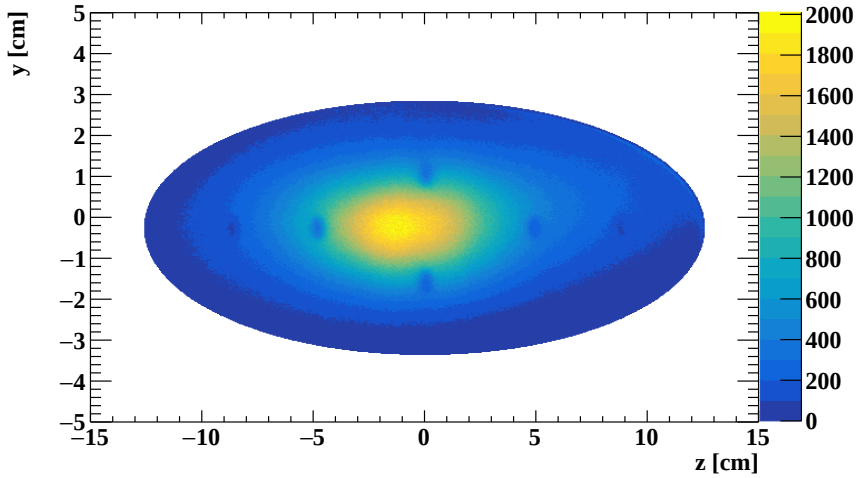

Figure 4.17: Distribution of positrons' decay vertices on the target. Figure reproduced with 2022 data.

which corresponds to a new scaling of the COBRA magnetic field from ×0.9991 to ×0.9993.

As shown in Figure 4.16, with this new scaling parameter the energy scale bias is compatible with zero: (-3 ± 2) keV. From a fit to the integrated Michel spectrum on the full 2022 dataset, the positron energy scale bias is:

$$\delta p = (-0.6 \pm 0.5) \text{ keV}$$

4.4 Target alignment with positrons

The relative alignment between the target and the CDCH is determined using fitted positrons tracks propagated back to the target. The holes drilled in the target through which muons passes undisturbed are clearly visible from the distribution of the positrons' decay vertices in Figure 4.17. The holes positions are measured from a fit to this bi-dimensional distribution. The difference between this measurement and the one obtained from the analysis of the target's pictures and the optical survey quantifies the misalignment between the CDCH and the target.

Table 4.3: Measured shifts between the CDCH and the target (TGT), and between the CDCH and COBRA, in the years 2021 and 2022.

Year	Δx [cm]		Δy [cm]		Δz [cm]	
	TGT	COBRA	TGT	COBRA	TGT	COBRA
2021	0.08 ± 0.10	0.10 ± 0.10	0.86 ± 0.10	0.70 ± 0.20	0.50 ± 0.15	0.40 ± 0.10
2022	0.08 ± 0.04	0.10 ± 0.10	0.24 ± 0.04	0.70 ± 0.20	0.57 ± 0.10	0.40 ± 0.10

The measured shifts in the x, y and z direction between the CDCH and the target in the years 2021 and 2022 are summarized in Table 4.3. In this Table, we report also the relative CDCH - COBRA shifts measured as described in Section 4.3 for the 2021 analysis: the CDCH - COBRA and CDCH - target alignment parameters are all compatible within uncertainties, hint of a possible error in the optical survey measurement of the CDCH position which can be corrected with these software alignment techniques.

4.5 Retraining of ML algorithms

The ML algorithms used in the hit recognition and in the $d(t)$ relations were retrained on 2022 data. In principle, differences in the distributions of features between 2021 and 2022 data (different noise levels, different time calibration of the wires etc.) may cause inefficiencies in the application of the model to new data.

The retrained models though didn't show any difference with the performances obtained with the previous one trained on 2021 data. This is a hint of the robustness of the architectures employed for these two tasks in MEG II.

4.6 Update of track selection criteria

For the '21+'22 analysis the final track selection criteria have been updated to improve the quality of the best ghost track. In the previous analysis of the 2021 dataset, the ghost selection criteria were the following:

1. discard tracks with less full turns reconstructed;
2. apply the ranking method of Equation 3.4, as described in Chapter 3, Section 3.2.4, privileging tracks with hits found by the conventional hit finder algorithm.

To this list, a third condition has been added between the first and second step: if some tracks successfully fit the last half turn before the pTC, discard the tracks which couldn't fit it.

This new selection cut doesn't affect the CDCH efficiency, but has a significant impact in increasing the resolutions of the selected tracks, as visible in the comparison of the E_e uncertainty in Figure 4.18.

4.7 Positron reconstruction stability in time

Under normal operation condition of the detector, spectrometer performances are expected to be constant at fixed beam intensity: this is monitored with a time dependent scan of the detector performances.

In Figure 4.19 we illustrate the time stability of resolutions obtained with the double turn analysis during the whole 2022 data taking period. Resolutions are very stable, within periods of given beam intensity, and this cross-checks the correctness of the calibration procedure of the full dataset.

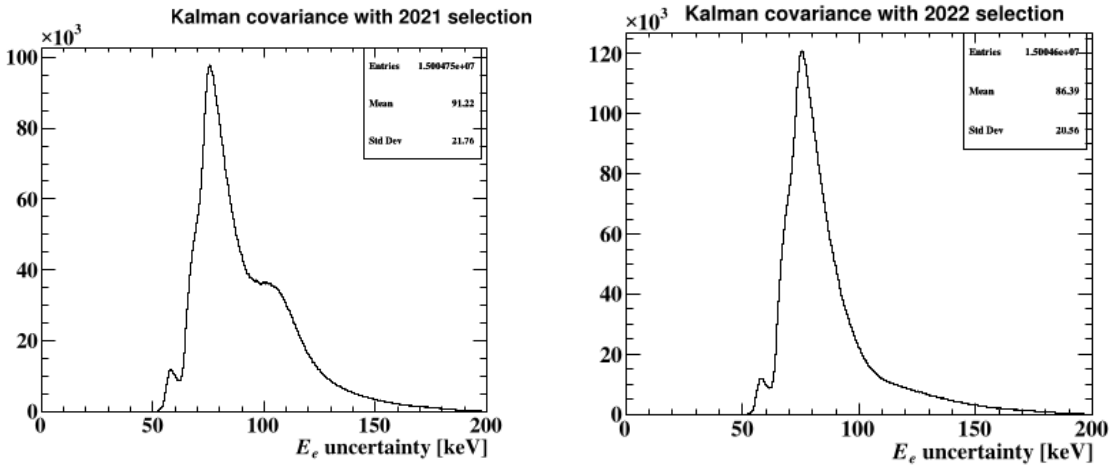

Figure 4.18: Distribution of E_e uncertainty estimated by Kalman filter for tracks selected with the 2021 criteria (left) and with the 2022 criteria (right). The shoulder at 110 keV uncertainty in 2021 is due to the preference for tracks with missing half turn.

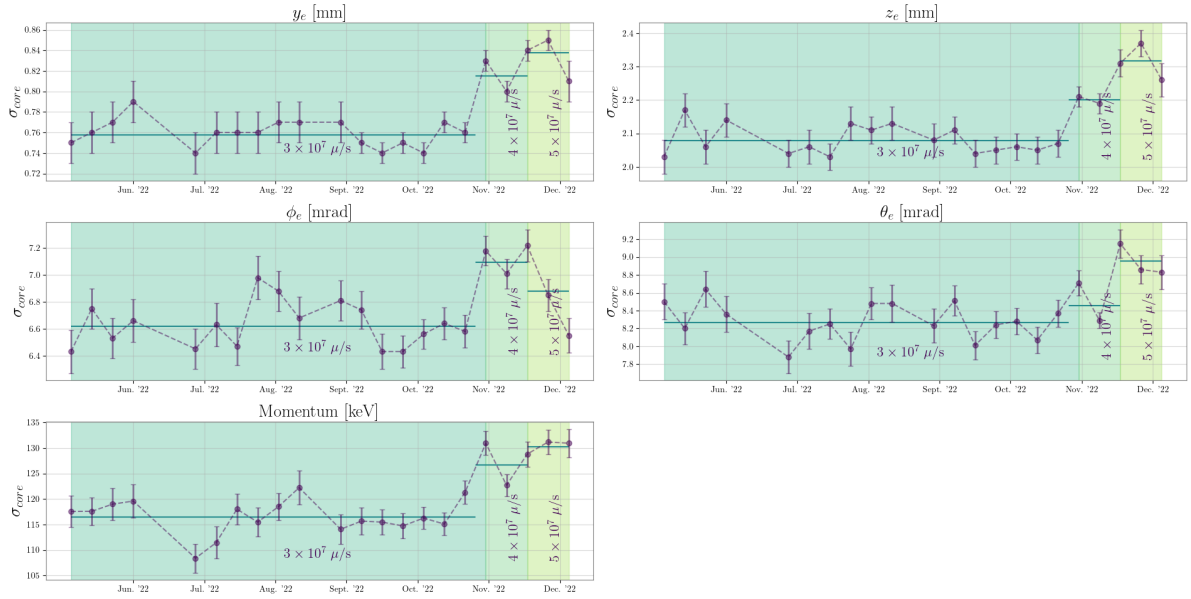

Figure 4.19: Time dependence of the resolutions of all kinematic variables on 2022 data. The color bands divide the runs for different beam intensities; the lines indicate the time average of the parameters.

Chapter 5

CDCH calibration with cosmic rays data

The candidate has developed the routine to reconstruct cosmic rays in the MEG II experiment, allowing to use extensively this dataset for the CDCH calibration. He has been in charge of the CDCH - LXe alignment, using cosmic rays data since the analysis of the 2021 dataset.

This chapter is dedicated to illustrate how cosmic rays data are employed for various calibration procedures of the spectrometer: to measure the relative alignment between the CDCH and the LXe detector (Section 5.2), and to perform the wire-by-wire alignment of the CDCH using the Millepede approach (Section 5.3). In the first Section 5.1 we discuss the development of the tracking algorithm for cosmic rays with the MEG II CDCH.

5.1 A new fitting algorithm for cosmic rays

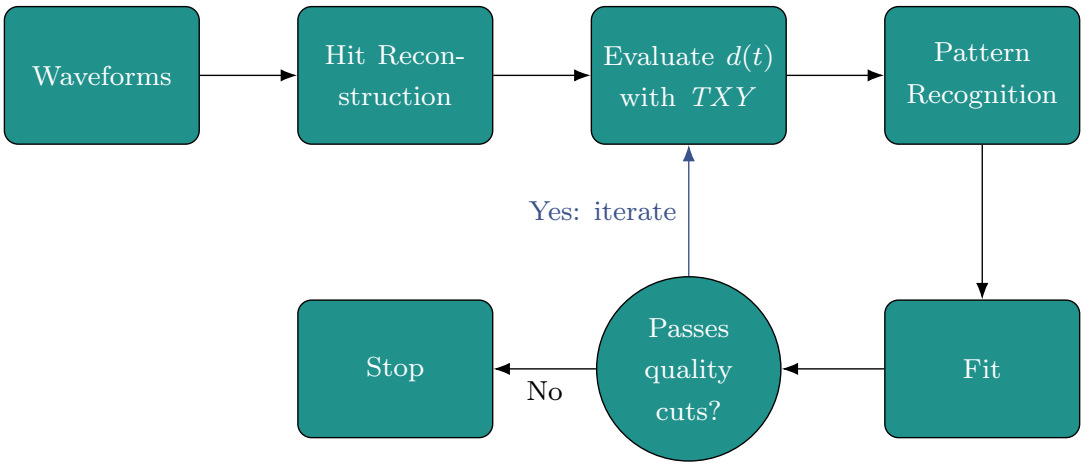

Figure 5.1: Flow-chart of the tracking algorithm for cosmic rays events.

The fitting procedure for cosmic tracks in the MEG II experiment is summarized in the flow chart of Fig. 5.1. It is much similar to the procedure described for tracking positrons, especially for the waveform analysis and hit reconstruction. The track finding and fitting algorithms though are very different and are described in the following sections.

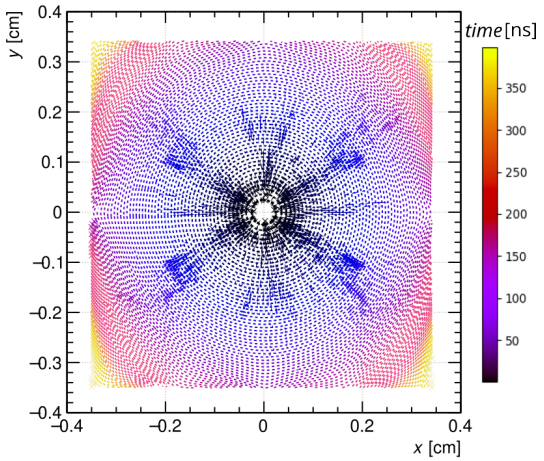

(a) Visualization of time-distance relationship inside a drift cell with no magnetic field.

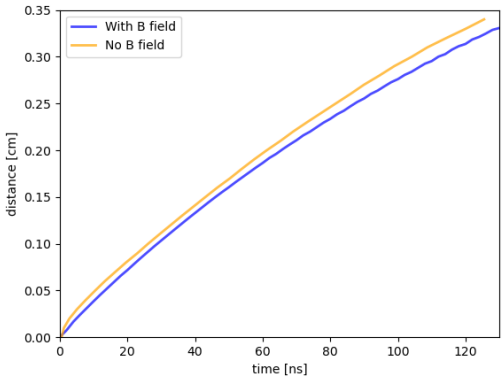

(b) Comparison between $DOCA$-time relationship with the COBRA magnetic field turned on (blue) and off (orange) respectively. Data are generated for the innermost layer, at $z = 0$.

Figure 5.2: *Garfield++* simulation of the $d(t)$ relationship without magnetic field effects.

5.1.1 New *TXY* Tables

The equations of motion for charged particles in the presence or absence of magnetic field are different, therefore a new set of *TXY* tables to track cosmic rays when COBRA is switched off has to be used.

Calling T_0 the reference time for the track, the drift time and corresponding drift distance $DOCA$ are

$$t_{drift} = t - T_0 \rightarrow DOCA = \int_0^{t_{drift}} v(t; \vec{x}) dt \tag{5.1}$$

where v is the electron's drift velocity in the gas mixture and $\vec{x}$ is the coordinate of the formation of the ionization cluster. The reference time T_0 is usually (but not always) measured by the pTC detector: in that case, from the pTC measurement T_{pTC} we can calculate T_0 as:

$$T_0 = T_{\text{pTC}} - t_{TOF} - \Delta t \tag{5.2}$$

where: t_{TOF} is the time-of-flight of the particle from the CDCH cell to the pTC, and has to be updated during the fit procedure based on the trajectory estimate; Δt is an inter-calibration factor between the time measured by CDCH and pTC boards.

As discussed also in Chapter 3, because of the gas mixture and the cell shape the relation $v(t; \vec{x})$ is not analytical and depend on the position $\vec{x}$ of the ionization inside the drift cell, therefore it has to be determined through simulations. The tables for reconstructing cosmic rays events were generated using *Garfield++* simulations, avoiding the use of the deep-learning algorithm to estimate the $DOCA$ (Chapter 3, Section 3.2), as the improvement is marginal [92].

In Figure 5.2 (a) the isochrone drift curves in the case of no magnetic field are illustrated, while in (b) the time-distance relationships in the two cases, with and without magnetic field, are compared. It is possible to appreciate that electrons drift faster in the absence of magnetic field, as expected [54].

With the new set of *TXY* tables the $DOCA$ resolution on cosmic rays improved from 250 µm to 230 µm (prior to the geometry alignment).

5.1.2 Pattern Recognition of cosmic rays events

Hit pre-selection Prior to the pattern recognition task, candidate signal and noise hits are filtered with cuts on the amplitude and integrated charge of the reconstructed cluster, requiring: single side signal amplitude $\geq$ 10 mV, and single side integrated charge $\geq 1 \times 10^{-9}$ C. The hit efficiency

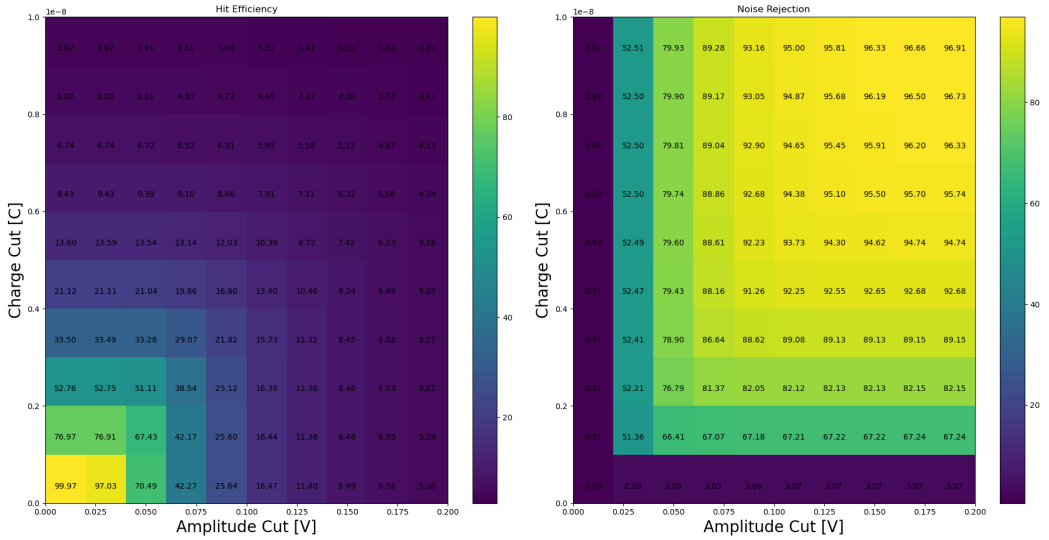

Figure 5.3: Hit efficiency and noise rejection power as a function of the applied cut in amplitude and integrated charge.

$\equiv \frac{\text{\#signal hits passing the cut}}{\text{\#all signal hits}}$ and noise rejection $\equiv \frac{\text{\#noise hits passing the cut}}{\text{\#all noise hits}}$ of these cuts estimated on $\mu \to e\nu\overline{\nu}$ data are respectively 95% and 50%. The variation of the signal hit efficiency and noise rejection efficiency with different cuts on these variables is reported in Figure 5.3. The choice of the value is made to maximize the signal hit efficiency, since cosmic rays' tracks leave less than 10 hits in the CDCH per event.

Pattern recognition strategy In the absence of magnetic field, cosmic rays travel along straight lines[i], therefore a global PR approach based on the Legendre transform [94] suits well the problem. The Legendre transform algorithm for pattern recognition is closely related to the Hough transform technique [100].

Mathematics In a plane parallel to the drift planes (i. e. the $x-y$ global plane), the cosmic track is tangent to all drift circles. The ensemble of lines tangent to a circle of radius d and center $(x_0,\ y_0)$ can be parameterized with the two parameters c and ϕ, being respectively the impact parameter (measured with respect to the origin of the coordinate system) and the incident angle of the track measured with respect to the y-axis (Figure 5.4). For each set of parameters $\{c, \phi\}$ there are two tangent lines to the drift circle which have equations:

$$c \pm d = x_0 \cdot \cos\phi + y_0 \cdot \sin\phi \qquad (5.3)$$

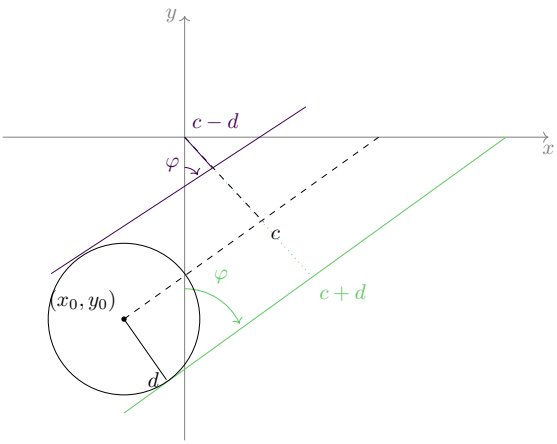

Figure 5.4: Definition of c and ϕ variables for line parameterisation in Equation 5.3.

Therefore, in what is called the *Legendre parameter space* $(c,\ \phi)$ the i-th hit defines two curves of equations

$$c = x_{0,\,i} \cdot \cos\phi + y_{0,\,i} \cdot \sin\phi \pm d_i \qquad (5.4)$$

[i]Small deviations caused by multiple scattering are negligible in the ultra-light CDCH.

Every hit in a CDCH event define two curves with the Equation 5.4. Those hits lying on a cosmic track with parameters (c_0, ϕ_0) have their relative curves in the Legendre space intersecting in a point of coordinates (c_0, ϕ_0).

A track finding algorithm based on the Legendre transform method starts building the bi-dimensional histogram in the Legendre space of the curves defined by Equation 5.4. The bin with maximum entries, which has coordinates (c_{MAX}, ϕ_{MAX}), identifies the parameters of a candidate track; the curves intersecting in that point identify the hits associated to it. In Figure 5.5 (a) we show the curves drawn in the Legendre space by a cosmic ray event. The maximum of the histogram is highlighted with a red box around it.

Since the MEG II CDCH has only stereo-layers, this method has to be applied separately to the hits in the two stereo views. After performing the search in the $(c,\ \phi)$ plane separately, candidate tracks passed on to the fitting stage are built taking all possible combinations of the hits found in the two separate searches (see Figure 5.5 (b)). The binning size of the Legendre space was tuned to obtain optimal performances: we found that a 120×120 grid was the best choice. After finding a maximum in the Legendre space, the procedure is iterated removing from the aggregation plot the hits already matched, until the maximum found has less than 3 hits. This iterative procedure allows to identify all tracks in multiple cosmic rays events and to get rid of spurious maxima which arise from noise hits or are artifacts created by the binning procedure.

This PR algorithm totally outperforms the previous one in use in the MEG II experiment for cosmic rays, which was based solely on a Determinist Annealing Filter (DAF) to reject pile-up hits:

- fake hits identification $\equiv \frac{\text{\#hits wrongly associated to the track}}{\text{\#all hits in the CDCH}}$ (measured on Monte Carlo) is less than 1%;
- signal hit efficiency $\equiv \frac{\text{\#hits correctly associated to the track}}{\text{\#all track hits}}$ (measured on Monte Carlo) is around 90%;
- Tracking efficiency increased to 50% on 2021 data (compared to 2% efficiency of the previous algorithm).

Figure 5.5 (b) features an example of a cosmic ray event reconstructed using the new track finding algorithm: the CDCH hits (white circles) belonging to the candidate track are marked in blue, and the fitted track is shown in light blue; the same event reconstructed using the Kalman filter based PR identifies in this case only five hits and fails to fit the track.

5.1.3 Track fitting

The information used to perform the fit from each hit are $\{d,\ w,\ \text{wire geometry}\}$, where d is the *DOCA* estimated from the drift time measurement using the *TXY* tables and w is the measurement of the hit coordinate along the wire described in Section 3.2.3. The *DOCA* is updated iteratively according to the particle's time-of-flight estimate. Depending on the trigger conditions, the time reference T_0 for the *DOCA* estimate is given by the pTC or the LXe detector.

Hits associated to a candidate track are fitted to a 3D line parameterized as:

$$\vec{l} = \begin{pmatrix} q_{xy} \\ 0 \\ q_{zy} \end{pmatrix} + y \cdot \begin{pmatrix} \xi \\ 1 \\ \eta \end{pmatrix} \tag{5.5}$$

The fit procedure consists of three steps:

1. track parameters are initially guessed using an analytical fit to the $x-y$ and $y-z$ projection of the hits coordinates $\{x_i, y_i, w_i\}$, where x_i and y_i are the i-th wire coordinates at the estimated w_i position along the wire;

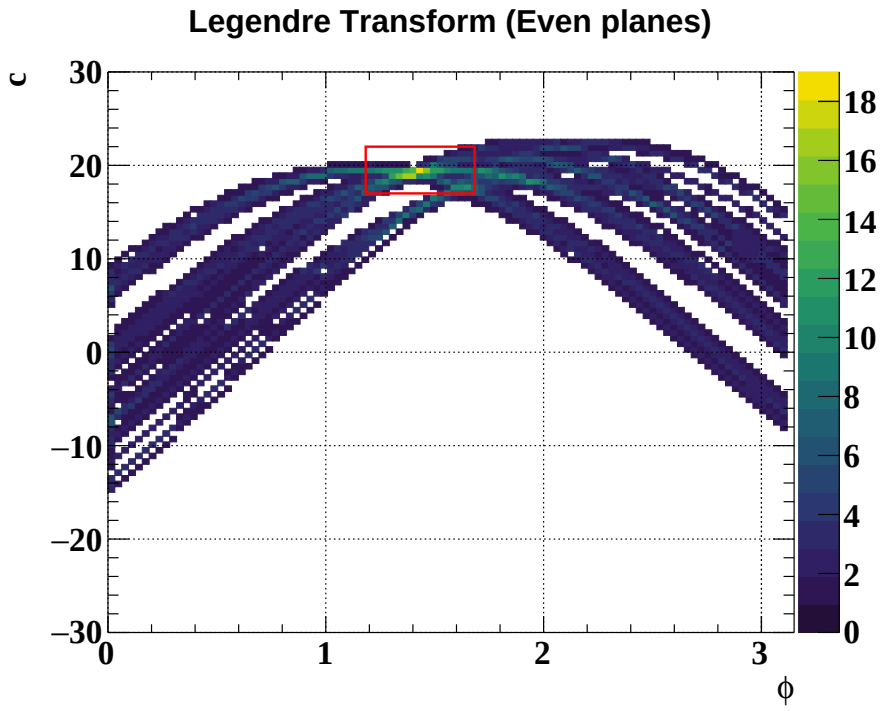

(a)

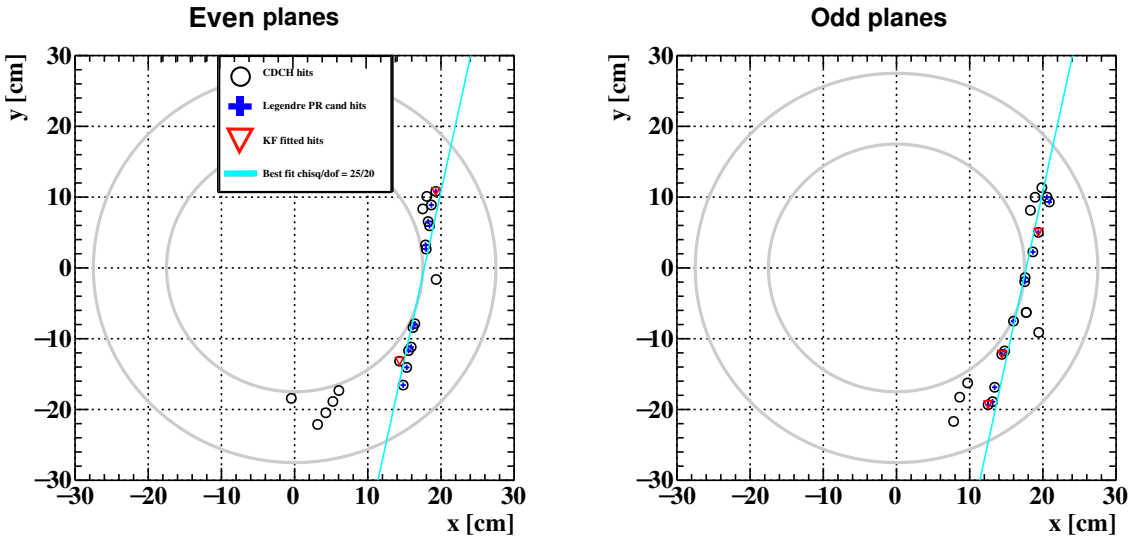

(b)

Figure 5.5: (a) Each hit in an event defines two curves, as in Equation 5.4, in the $(c,\ \phi)$ plane. Hits belonging to a common cosmic ray event intersect on the track parameters $(c_0,\ \phi_0)$ which can be identified searching for the maximum in this 2-D space (red square). (b) Event display (two separate stereo views) of a cosmic rays event on data: hits identified by the new PR algorithm based on the Legendre transform are highlighted in blue, while those (much less) identified by the old PR algorithm are in red. The fitted track is in cyan.

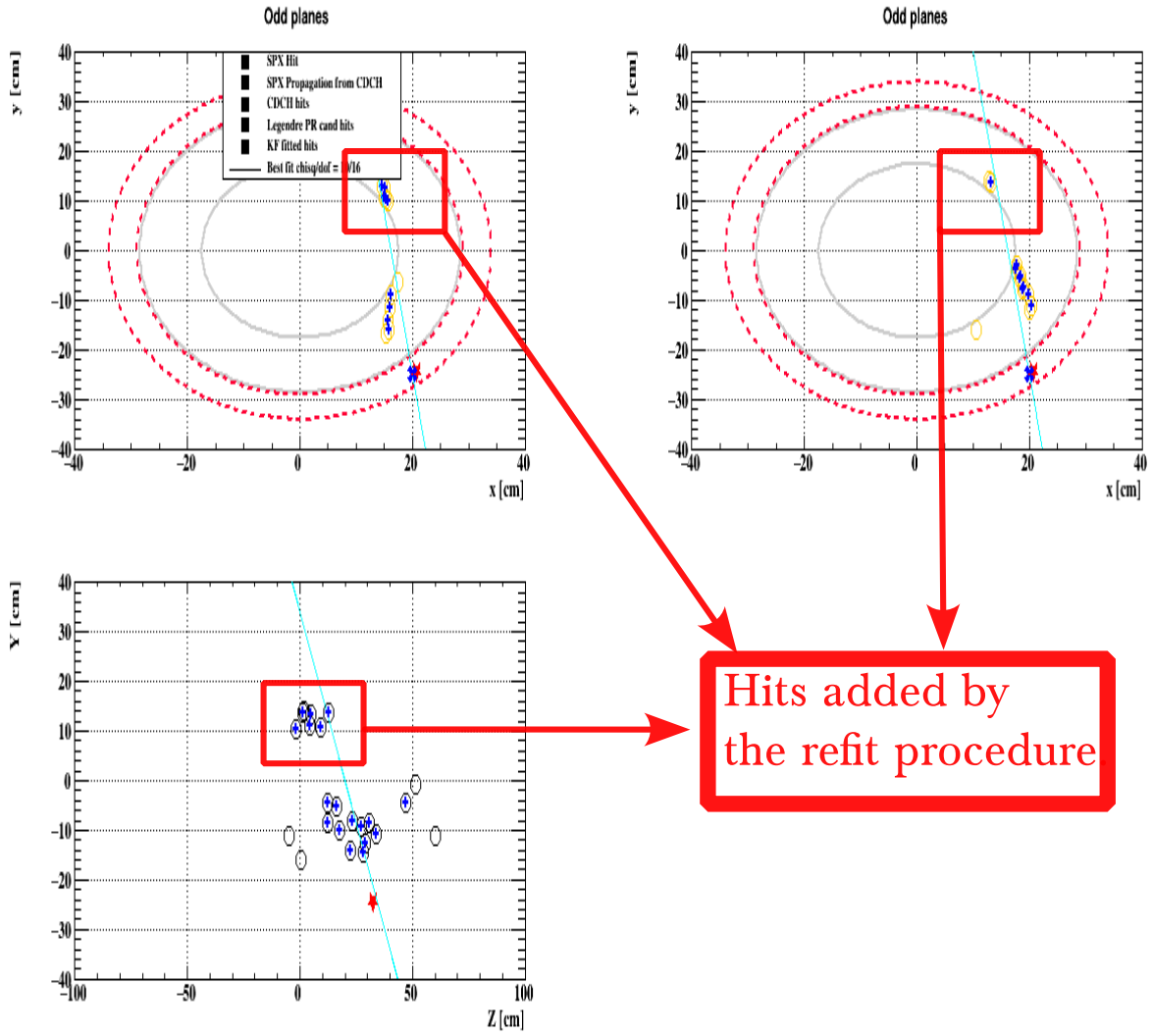

Figure 5.6: Illustration on an event display of the hits recovered with the developed *refit* method for cosmic rays.

2. starting from this guess, the best-fit parameters are determined using numerical minimization of the χ^2 function with *MINUIT* minimizer[ii]. The χ^2 function is defined as

$$\chi^2 = \sum_{i}^{N_{hit}} \left(\frac{d_i - \rho(\vec{l})}{\sigma_{d,\,i}} \right)^2 \tag{5.6}$$

where $\sigma_{d,i}$ is the uncertainty on d, $\rho(\vec{l})$ is the distance of closest approach between the straight line $\vec{l}(y, q_{xy},\ q_{zy},\ \xi,\ \eta)$ and the i-th hit wire w_i, and is determined through an analytical minimization algorithm[iii];

3. after a first fit the time-distance relationship can be refined providing an estimate of the incidence angle of the track ϕ in each drift cell allowing for a more precise determination of d. At each iteration step, outliers satisfying $\left|\frac{d_i - \rho_i}{\sigma_{d,i}}\right| > 5$ are removed. The iterative fit procedure is stopped after three loops, which we observed are enough to improve the fit results, with no significant improvements deriving from more steps;

4. a *refit* procedure searches for hits close ($\rho < 1$ cm) to the best fit track which were possibly missed by the pattern recognition algorithm. If at least a new hit is found, the fitting procedure restarts adding those hits to the measurements. This is really helpful in improving the tracking efficiency and the number of hits per track for the class of tracks traversing the center of the CDCH, leaving two distant segments of track along their path (Figure 5.6).

At the end of the fitting procedure, the best cosmic track is selected based on these criteria:

1. smallest distance between pTC hit tile (or LXe interaction point) and track projection to that position;

2. in case of two tracks propagating to the same pTC tile (LXe interaction point) within a 12 cm (10 cm) uncertainty prefer the track with more hits;

3. require $\chi^2/dof < 10$ for all tracks.

5.2 CDCH - LXe alignment with cosmics

Cosmic rays crossing both the LXe detector and the CDCH tracker (Figure 5.7) with COBRA B field turned off ($B = 0$) are used to measure the relative CDCH - LXe alignment in the z direction. [iv]

Cosmic rays passing through the CDCH are fitted to a straight line in 3-dimensions using the parametrization in Equation 5.5. The fitted line is propagated to the inner radius of the LXe detector R_{in}, and the intersection point between the track and the LXe detector's inner face is called $\vec{x}_{CDCH} = (x_{CDCH}, y_{CDCH}, z_{CDCH})$. Calling $\vec{x}_{LXe} = (x_{LXe}, y_{LXe}, z_{LXe})$ the measurement by the LXe detector of the cosmic ray interaction point (see next section), the misalignment in the z direction δz between the two detectors can be measured from the difference $z_{LXe} - z_{CDCH}$ (see Figure 5.8):

$$z_{LXe} - z_{CDCH} = \delta z + w \cdot \tan\phi \tag{5.7}$$

where $w \equiv R - R_{in}$ is the depth of the reconstructed interaction point $\vec{x}_{LXe}$ inside the LXe; $\phi \equiv -\arctan(\eta/\xi)$ is the angle of incidence of the cosmic ray track on the LXe detector in $x - z$ plane.

[ii] https://root.cern.ch/root/html534/TMinuit.html

[iii] Wires don't have a linear shape because of gravitational and electrostatic forces acting on them. See Chapter 2, Section 3.1.2.

[iv] The relative alignment in the x and y direction is not possible because the shift estimate would be strongly biased by the angular distribution of cosmic rays, therefore the MEG II Collaboration decides not to trust those results. This bias is not present when we average on z, as illustrated in the text.

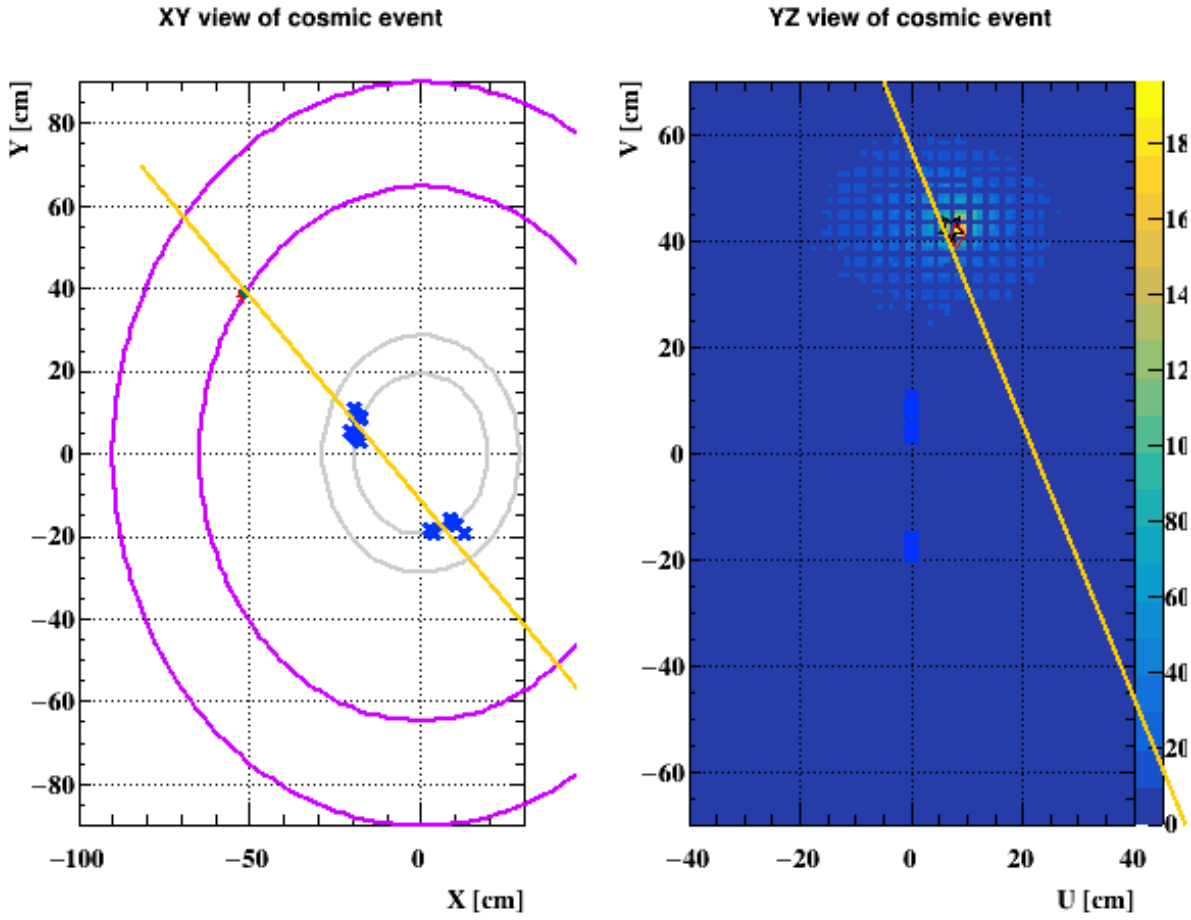

Figure 5.7: Event display in $x - y$ and $u - v$ view of a cosmic ray passing through the CDCH and the LXe detector. In the $u - v$ view the color scale is determined by the number of photons N_{pho} seen by each MPPC. The fitted track is drawn as well as the points $\vec{x}_{CDCH}$ (black star) and $\vec{x}_{MPPC}$ (red rhombus). See the text for the definitions.

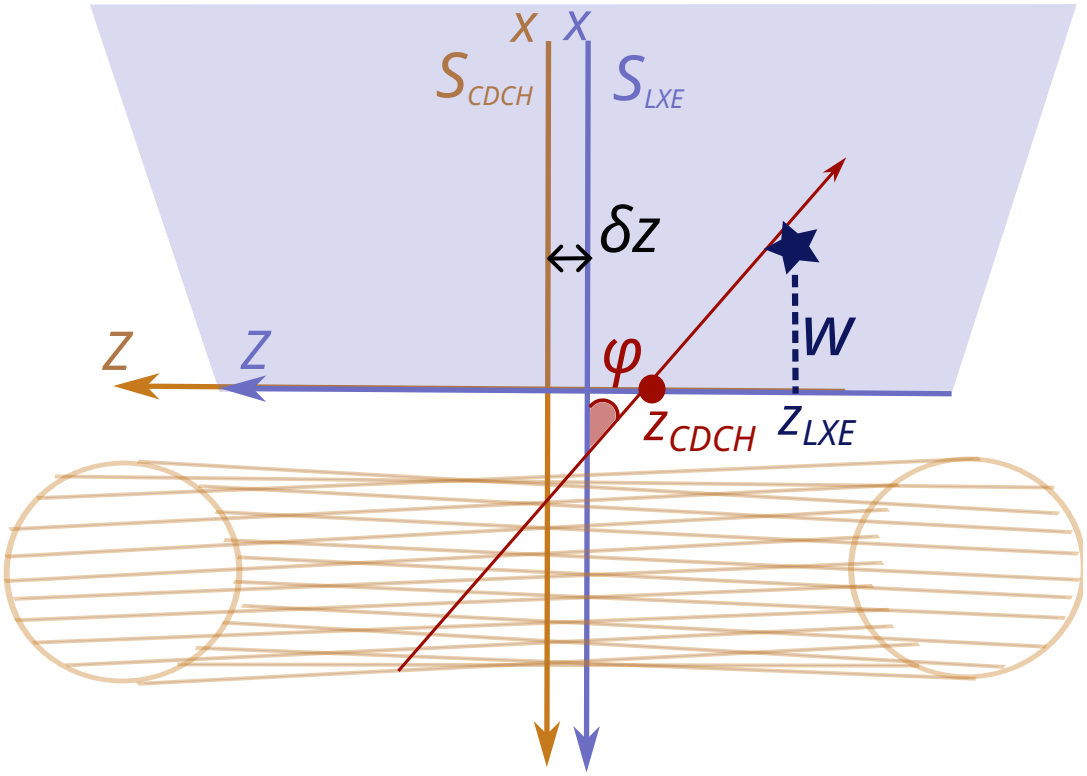

Figure 5.8: Scheme of the CDCH - LXe alignment principle.

5.2.1 How to measure the cosmic ray interaction point in the LXe detector

Since a cosmic ray leaves a continuous streak of light along its path inside the LXe, the identification of a single interaction point $\vec{x}_{LXe}$ poses many reconstruction problems which may lead to biasing the measurement.

We investigated two methods to evaluate $\vec{x}_{LXe}$:

1. The `xecposlocalfit` method: the standard photon reconstruction algorithms are used to determine through a χ^2 fit procedure a "first interaction point" of the cosmic ray inside the LXe detector [101]. This algorithm is tuned for photons coming from the target and doesn't work well in reconstructing cosmic rays which enter the LXe detector preferentially from the back or lateral faces ($v_{LXe} > 0$): in Figure 5.9 we show the bias in estimating the position in v of the cosmic ray for $v_{LXe} > 0$. Therefore with this method tracks with $v_{LXe} > 0$ can not be used for the analysis. In addition, the depth distribution w of the events reconstructed with `xecposlocalfit` method peaks at 4 cm and in virtue of the relation (5.7) this is a source of bias in z. Indeed:

$$\mathrm{E}\left[z_{LXe} - z_{CDCH}\right] = \delta z + \mathrm{E}\left[w \cdot \tan\phi\right] \neq \delta z \text{ if } \mathrm{E}\left[w \cdot \tan\phi\right] \neq 0 \tag{5.8}$$

   This dependence further causes the distribution of $z_{LXe} - z_{CDCH}$ to have a greater variance:

$$\mathrm{Var}\left[z_{LXe} - z_{CDCH}\right] = \mathrm{Var}\left[z_{LXe}\right] + \mathrm{Var}\left[z_{CDCH}\right] + \mathrm{Var}\left[w \cdot \tan\phi\right] \tag{5.9}$$

2. *max MPPC* method: we take as the best estimate of $\vec{x}_{LXe}$ the coordinates $\vec{x}_{MPPC} = (x_{MPPC}, y_{MPPC}, z_{MPPC})$ of the MPPC which detected the highest number of photons N_{pho} in the event (requiring also that the brighter face of the LXe detector in the event is the inner face, covered with MPPC). This method worked to eliminate the reconstruction error in the estimate of y_{LXe}. Further, the bias coming from the $\tan\phi$ correlation is strongly reduced, because MPPCs cover the detector inner face: as reported in Table 5.1, the bias is negligible when using the *max MPPC* method.

For these reasons, we find that the *max MPPC* method is more suited to measure the CDCH - LXe misalignment. Results are discussed in the next Sections.

Table 5.1: Biases on $z_{LXe} - z_{CDCH}$ caused by the tan ϕ dependence expected when using the `xecposlocalfit` or the *max MPPC* methods.

	2021		2022	
	`xecposlfit`	*max MPPC*	`xecposlfit`	*maxMPPC*
$\langle w_{LXe} \cdot \tan\phi \rangle$	0.83 mm	-20 µm	0.96 mm	< 10 µm

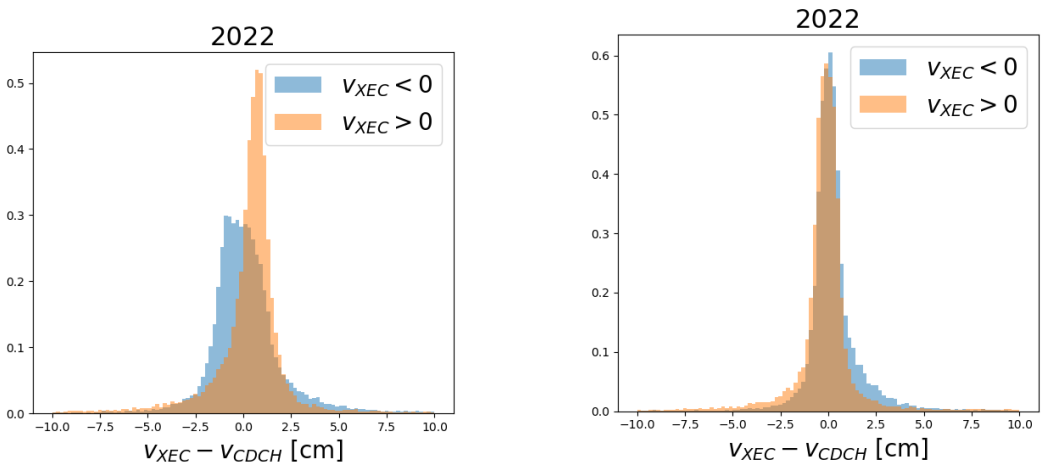

(a) `xecposlfit` method.

(b) *maxMPPC* method.

Figure 5.9: Distribution of the residual $v_{LXe} - v_{CDCH}$ for cosmic rays impinging on the upper ($v_{LXe} > 0$, in orange) or on the lower part ($v_{LXe} < 0$, in blue) of the XEC. Comparing (a) with (b) we notice the disappearence of a systematic bias when the *maxMPPC* method is used for reconstruction. The data used for the plots were collected in 2022.

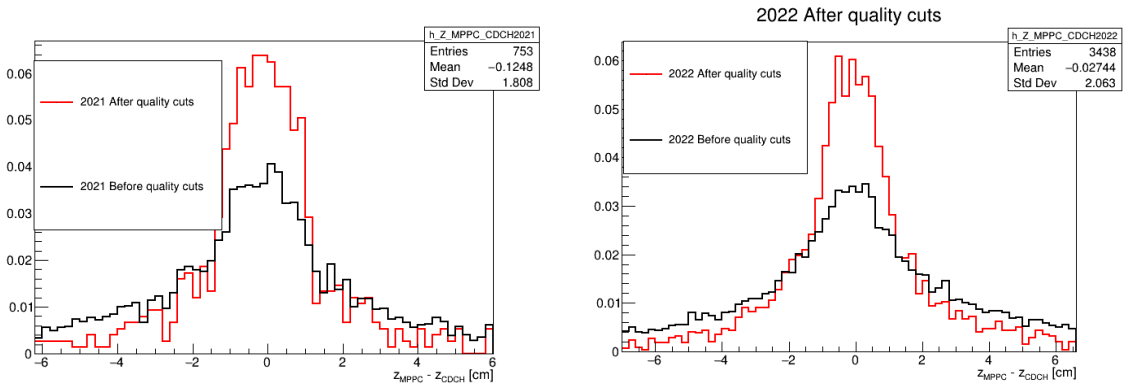

(a) Year 2021 (b) Year 2022

Figure 5.10: Effect of quality cuts on the distribution. Each histogram is normalized to itself.

5.2.2 Analysis of 2021 & 2022 datasets

Quality cuts We impose the following quality cuts to select correctly reconstructed events:

- $E_{LXe} > 100$ MeV: cosmic ray events with a lower energy deposit in the LXe detector are those that cross it next to the borders, and may be badly reconstructed;
- $|z_{LXe}| < 20$ cm: we restrict the geometrical acceptance to avoid border effects (z_{LXe} is limited by the geometry of the detector while z_{CDCH} is not because it is an extrapolation from a fit);
- $d < 10$ cm, where d is the distance between $\vec{x}_{CDCH}$ and $\vec{x}_{LXe}$;
- $\left|\frac{z_{LXe}-z_{CDCH}}{\sigma_z}\right| < 3$ to reject outliers. $\sigma_z \equiv \sqrt{\sigma^2_{z_{CDCH}} + \sigma^2_{z_{LXe}}}$. $\sigma_{z_{CDCH}}$ is evaluated from the covariance matrix of the fit results while $\sigma_{z_{LXe}} = \frac{a}{\sqrt{12}}$ where a = 12 mm is the MPPC dimension;
- Quality cuts on reconstructed tracks in the CDCH:
  - Goodness of fit: $p\text{-}value > 0.1$ (χ^2 test);
  - Number of hits on the CDCH track: $N_{hits} \geq 8$;
  - $\sigma_{z_{CDCH}} < 1.5$ cm @ R_{in}: we select only events with a precise estimate of the projected point, with the minimum precision chosen to be equal to the MPPC size;
  - $|x_0| < 27$ cm & $|z_0| < 90$ cm: these are cuts on highly slanted tracks that don't have their intercept inside the CDCH volume.

In Figure 5.10 we show for the year 2021 & 2022 the difference in the distribution of $z_{LXe} - z_{CDCH}$ with and without these quality cuts.

Dataset The dataset for the 2021 CDCH - LXe alignment consists of ≈ 400k events taken in three different periods; the 2022 CDCH - LXe alignment data are almost 1.2 milions, acquired in a few days in September 2022. Data are collected with COBRA off and triggering on a high energy signal inside the LXe detector. After the quality cuts are applied, we are left with 800 and 3400 events in 2021 and 2022 respectively.

Fit procedure We perform an unbinned maximum likelihood fit to the $z_{LXe} - z_{CDCH}$ distribution using a double gaussian distribution with five degrees of freedom:

$$\mathcal{L}(\vec{x}; f_{core}, \mu_{core}, \sigma_{core}, \mu_{tail}, \sigma_{tail}) = \prod_i f_{core} \cdot e^{-\frac{(x_i-\mu_{core})^2}{2\sigma^2_{core}}} + (1 - f_{core}) \cdot e^{-\frac{(x_i-\mu_{tail})^2}{2\sigma^2_{tail}}} \tag{5.10}$$

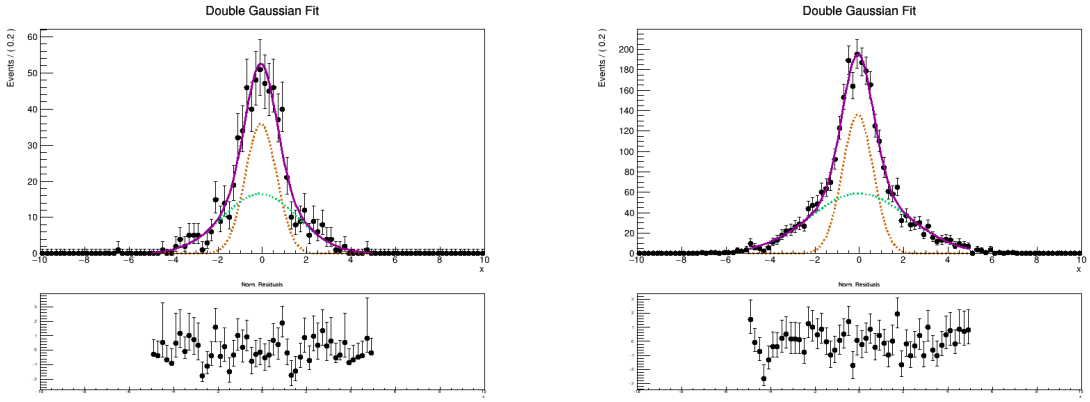

(a) Year 2021 (b) Year 2022

Figure 5.11: Plots of the fit to the $z_{LXe} - z_{CDCH}$ distribution

Table 5.2: Unbinned ML fit results. The quality cuts applied on data are the one described above.

Parameter	**2021**	**2022**
p-value (χ^2 test)	0.99	0.45
f_{core}	0.47 ± 0.07	0.42 ± 0.04
μ_{core}	-0.67 ± 0.66 mm	-0.73 ± 0.33 mm
μ_{tail}	-1.03 ± 1.00 mm	-0.02 ± 0.45 mm
σ_{core}	7.06 ± 0.65 mm	7.00 ± 0.40 mm
σ_{tail}	17.0 ± 2.0 mm	22.0 ± 1.8 mm

The best fitted value for μ_{core} is the best estimate of the misalignment δz between the two detectors. The fit range is restricted to $|z_{LXe} - z_{CDCH}| < 5$ cm, since outside that interval the number of events is almost zero.

In Figure 5.11 we plot the fit on 2021 & 2022 data. The best fit estimate of the parameters are listed in Table 5.2. We note that all fit parameters are compatible between year 2021 and year 2022, while the difference on the mean uncertainty is explained by the different number of events: $\sqrt{\frac{N_{2022}}{N_{2021}}} \approx 2$.

5.2.3 Assessing systematic uncertainties in z alignment with cosmic rays

We discuss the studies to assess the impact of two systematic uncertainties for the estimate of δz:

- Fit uncertainty;
- $\Delta z - \phi$ correlation.

Fit uncertainty The fit result may depend on the selection criteria for good events. Some of the quality cuts are strongly motivated by the cosmic ray topology (like the fiducial volume cuts) or to remove badly reconstructed events (cut on the outliers and on the χ^2 of the track and on E_{LXe}). Instead, other quality cuts (listed below) are chosen arbitrarily: we perform the same fit procedure described above selecting events passing different cuts, extract the best fit parameters and take the median[v] as the best value for the parameter and the semi-dispersion on the parameters $\Delta q = \frac{q_{MAX} - q_{min}}{2}$ as the systematic error on the fit procedure. The cuts that we varied are:

[v] Not the weighted average because we don't use independent sets of measurements to perform the different fits, therefore results are strongly correlated.

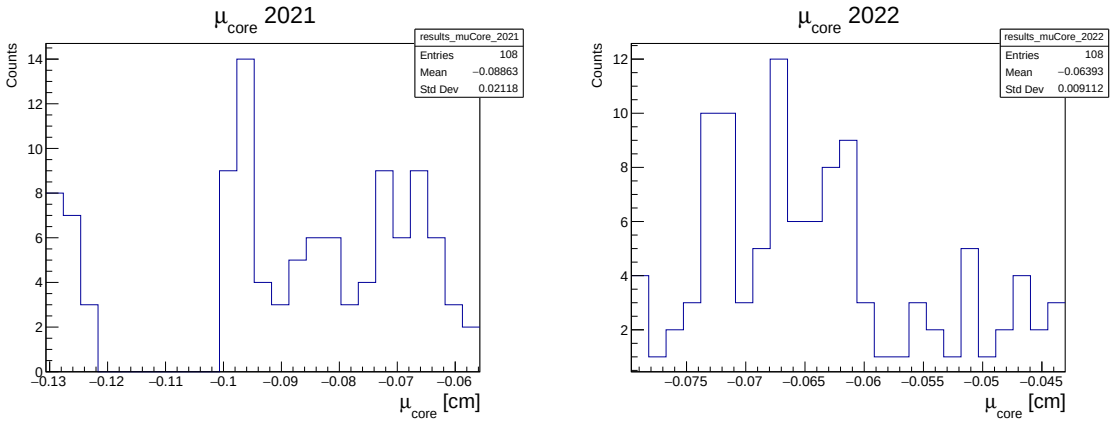

(a) Year 2021

(b) Year 2022

Figure 5.12: Distribution of the best fit estimate of μ_{core} varying the selection cuts.

Table 5.3: Final estimate of the parameters μ_{core} (estimate of δz) and μ_{tail} (to check consistency of the analysis) with included the systematic error from the choice of quality cuta. The values are reported as: (central value) ± (stat.) ± (syst.).

Parameter	2021	2022
μ_{core} [mm]	$-0.85 \pm 0.63 \pm 0.37$	$-0.65 \pm 0.33 \pm 0.18$
μ_{tail} [mm]	$-0.73 \pm 0.93 \pm 0.91$	$-0.42 \pm 0.43 \pm 0.37$

- $N_{hits} \in [8; 10]$ to impose more stringent requirements on the quality of the fitted track in the CDCH (above $nhits > 10$ there are too few events);
- $d \in [5 \text{ cm}; 10 \text{ cm}]$;
- $|\sin\phi| \in [0.5; 1]$: this is to evaluate if there is any bias coming from events with different incident angles on the LXe;
- $\sigma_{z_{CDCH}} \in [0.5 \text{ cm}; 1 \text{ cm}]$.

We consider only results from correctly converging fit (correlation matrix positive definite, $p - value$ (χ^2 test) $> 10\%$). The distributions of the μ_{core} parameter estimate are shown in Figure 5.12. The results are reported in Table 5.3.

$\Delta z - \phi$ correlation To see if the integrated distribution of $z_{LXe} - z_{CDCH}$ has a bias dependent on the incident angle ϕ, we perform different fits to the $z_{LXe} - z_{CDCH}$ in bins of ϕ: $\sin\phi < -0.5$; $-0.5 < \sin\phi < 0.5$ and $\sin\phi > 0.5$. Then, we make a line fit to the $\mu_{core} - \phi$ correlation (Figure 5.13). The line intercept at $\sin\phi = 0$, q, is an unbiased measure of δz. Indeed, for cosmic rays entering the LXe at 90° with respect to the surface ($\sin\phi = 0$), the Equation 5.7 for the misalignment simplifies to:

$$z_{LXe} - z_{CDCH} \equiv \delta z$$

Any difference between this measurement of δz, q, and the μ_{core} parameter in Table 5.3 would indicate that the method described in Section 5.2.2 was effectively biased.

The results from the line fit are:

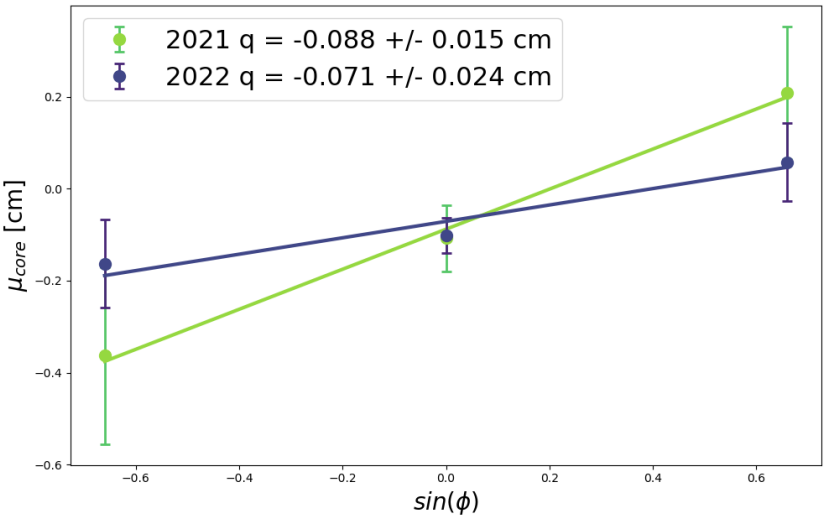

Figure 5.13: Best fitted lines to the $\mu_{core} - \sin\phi$ relation for the years 2021 and 2022.

Table 5.4: Summary of the measurements to estimate the LXe detector's shift along z, to determine its correct position.

Year	Optical survey	δz	CDCH - COBRA $z-$shift	Combined
2021	0.0 ± 0.5 mm	-0.85 ± 0.73 mm	-0.40 mm	-0.14 ± 0.41 mm
2022	0.0 ± 0.5 mm	-0.65 ± 0.37 mm	-0.40 mm	-0.16 ± 0.29 mm

2021 $q = -0.88 \pm 0.15$ mm 2022 $q = -0.71 \pm 0.24$ mm

Both results are completely compatible with the previous estimate, therefore we conclude that there is no measurable effect of the ϕ dependence on the estimate of δz with the *max MPPC* method.

5.2.4 Results

The final alignment of the LXe detector is determined by combining the results of this study on the CDCH - XEC alignment with the optical survey measurements of the LXe detector's position with respect to the COBRA cryostat (Chapter 2, Section 2.2.6).

The LXe detector position measured by the optical survey is 0.0 ± 0.5 mm, both for 2021 and 2022.

The z misalignment between the CDCH and the LXe detector measured with cosmic rays is relative to the CDCH, not the COBRA cryostat. The CDCH - COBRA shift in z was tuned with Michel positrons (Chapter 4, Section 4.3) and is equal to -400 µm. Taking this into account, the combination of the measurement is done taking the weighted average:

$$\delta z_{combined} = \frac{(\delta z_{CDCH-LXe} - \delta z_{CDCH-COBRA}) \cdot w^2_{CDCH-LXe} + \delta z_{survey} \cdot w^2_{survey}}{w^2_{CDCH-LXe} + w^2_{survey}} \quad , \quad w \equiv \frac{1}{\sigma} \tag{5.11}$$

The final estimate of the LXe detector's shift along z is given in Table 5.4. These results allow to correct a position reconstruction bias

5.3 CDCH alignment with Millepede

The iterative alignment exploited for the CDCH (see Chapter 4, Section 4.2) has proven very effective [50] for improving fit residuals and optimizing tracking performances for both 2021 and 2021+2022 analysis.

Nonetheless, there are several reasons motivating studies for a second, independent alignment algorithm of the CDCH:

- the use of solely $\mu \to e\nu\overline{\nu}$ events doesn't allow to identify possible *weak modes*[vi] of the alignment parameters, and indeed using datasets with different tracks topologies is advised for a better convergence;
- the curvature of tracks in the COBRA magnetic field is sensitive to misalignments arising from inaccuracies in the wire geometry as well as from relative displacements between the magnetic field and the CDCH. Currently, the optimization of magnetic field parameters is done after the iterative alignment (Chapter 4, Section 4.2), but the results of the iterative alignment itself may be biased by the magnetic field used for tracking. Using tracks acquired with the COBRA magnetic field turned off shall disentangle magnetic field and CDCH alignment;
- before converging, the iterative method requires several iteration steps, where tracks are refitted with the corrected values of the geometry. With 14 iterations required for convergence on 2022 data, the total computing time for 2022 alone was $\sim$ 15 CPU years (i. e. $\sim$ 1 month with 150 CPU running in average)[vii]. A similar amount of time was used for the alignment of the CDCH geometry in 2021.

For all these reasons we set up a second alignment routine using the Millepede global strategy [102] on cosmic rays data acquired with the magnetic field turned off. The Millepede alignment method, described in more detail in the next subsection, has been successfully employed in many high-energy physics experiments: CMS [103], Belle II [104], AMS [105]. The CMS [106], AMS and MEG collaborations [9] reported satisfactory results for the alignment of tracker detectors using cosmic ray events only.

5.3.1 What is Millepede?

Millepede solves the extended χ^2 problem in Equation 4.1 including both the track parameters, referred to as local parameters, and the geometry parameters, referred to as global parameters. The goal of the alignment is to determine the best corrections for the geometry. Millepede includes first-order corrections to the tracks' parameters in the evaluation of the global parameters corrections, therefore iterations are not needed (unless second-order corrections are relevant). This strategy makes the Millepede algorithm faster and more robust than the iterative procedure.

How is this achieved?

The objective function to minimize is

$$\chi^2 = \sum_{j}^{N_{tracks}} \sum_{i}^{N_{hits}} \frac{\left(m_{ij} - f(m_{ij}; \vec{\tau}_j, \vec{p})\right)^2}{\sigma_{ij}^2} \equiv \sum_{j}^{N_{tracks}} \sum_{i}^{N_{hits}} \frac{z_{ij}^2}{\sigma_{ij}^2} \tag{5.12}$$

where: m_{ij} and σ_{ij} are the position measurement and its error; $\vec{\tau}_j$ are the parameters of the track in event j; $\vec{p}$ are the global parameters. For cosmic ray data the χ^2 of a single track is the one given in Equation 5.6, with $m_{ij} \equiv d_{ij}$, the local parameters $\vec{\tau}_j = \{q_{xy},\ q_{yz},\ \xi,\ \eta\}_j$ and the global parameters those describing the geometry of each wire (Chapter 3, Section 3.1.2).

We introduce the notation

$$\delta\tau_{ij,k} = \frac{\partial z_{ij}}{\partial \tau_{j,k}} \quad \delta p_{ij,k} = \frac{\partial z_{ij}}{\partial p_k} \tag{5.13}$$

for the derivatives of residuals in the $j-$th event with respect to local and global parameters, and expand the expression 5.12 to first order to linearize the problem:

$$f(m_{ij}; \vec{\tau}_j, \vec{p}) \simeq f(m_{ij}; \vec{\tau}_{j,0}, \vec{p}_0) + (\delta\vec{\tau}_{ij})^T \Delta\vec{\tau}_j + (\delta\vec{p}_{ij})^T \Delta\vec{p} \tag{5.14}$$

[vi] *weak mode* = combination of alignment parameters that doesn't alter the computed χ^2.

[vii] The MEG II offline computing system is based on an high-performance computing cluster (HPCE) managed at PSI https://www.psi.ch/en/awi/high-performance-computing-and-emerging-technologies-group.

where $\vec{\tau}_0$ and $\vec{p}_0$ indicate the initial estimate for local and global parameters.

Following the notation in [102], we can now write the solution to the global minimization problem with respect to both global and local parameters as the solution of a single large linear system:

$$\left(\begin{array}{c|ccc} \mathbf{C} & \dots & \mathbf{G}_j & \dots \\ \hline \dots & \dots & 0 & 0 \\ \mathbf{G}_j^T & 0 & \mathbf{\Gamma}_j & 0 \\ \dots & 0 & 0 & \dots \end{array}\right)\left(\begin{array}{c} \Delta\vec{p} \\ \hline \dots \\ \Delta\vec{\tau}_j \\ \dots \end{array}\right) = \left(\begin{array}{c} \vec{b} \\ \hline \dots \\ \vec{\beta}_j \\ \dots \end{array}\right) \tag{5.15}$$

where:

$$\begin{cases} (\mathbf{\Gamma}_j)_{kl} = \sum_i \delta\tau_{ij,k}\delta\tau_{ij,l} \\ (\mathbf{G}_j)_{kl} = \sum_i \delta\tau_{ij,k}\delta p_{ij,l} \\ (\mathbf{C})_{kl} = \sum_{i,j} \delta p_{ij,k}\delta p_{ij,l} \\ (\beta_j)_k = \sum_i \delta\tau_{ij,k} z_{ij} \\ (b)_k = \sum_{i,j} \delta p_{ij,k} z_{ij} \end{cases} \tag{5.16}$$

By construction, $\mathbf{C}$ and $\mathbf{\Gamma}$ are symmetric matrices and therefore invertible as long as they are not singular. The matrix $\mathbf{C}$ has dimension $N_{align} \times N_{align}$ (N_{align} = number of alignment parameters), while $\mathbf{\Gamma}$ has dimension $N_{track} \times N_{track}$ (N_{track} = number of local parameters). The degrees of freedom of this system are equal to the number of alignment parameters N_{align} plus the number of parameters for all the tracks used — i.e., millions. Since solving the full system directly is not feasible, it can be simplified by exploiting the specific structure of the global matrix (a sparse matrix with many zero blocks), to reduce it to a smaller system corresponding to the alignment-only problem. This is done by defining the new quantities

$$\mathbf{C}' = \mathbf{C} - \sum_j \mathbf{G}_j \mathbf{\Gamma}_j^{-1} \mathbf{G}_j^T \quad \vec{b}' = \vec{b} - \sum_j \mathbf{G}_j \mathbf{\Gamma}_j^{-1} \vec{\beta}_j \tag{5.17}$$

so that the system for finding the quantities $\Delta\vec{p}$ becomes:

$$\mathbf{C}'\Delta\vec{p} = \vec{b}' \Rightarrow \Delta\vec{p} = \mathbf{C}'^{-1}\vec{b}' \tag{5.18}$$

and therefore the correct set of geometry parameters is:

$$\vec{p} = \vec{p}_0 + \Delta\vec{p} \tag{5.19}$$

Ideally Equation 5.18 solves in a single step the alignment problem if all assumptions for the linearization of the problem are satisfied. If instead the problem has some non-linearities, like outliers in data or incorrect estimate of the initial guess for $\vec{p}_0$ so that second-order terms are relevant, iteration of the procedure may be needed for a satisfactory convergence.

A software package named Millepede II [107], a revised version of the old Millepede program, provides users with the tools to solve the mathematical problem of the alignment with the Millepede technique. The program is composed of two parts:

1. The `mille` program encodes the data provided by the user after tracking in a binary file which contains residuals, derivatives, measurement errors;

2. the output binary file from `mille` is fed into the Fortran program `pede`, which runs the routine to build the linear system, solves it and outputs a text file containing the correction parameters $\Delta\vec{p}$. We can recognize in $\mathbf{C}'^{-1}$ the covariance of the solution $\Delta\vec{p}$, therefore it is possible to estimate the error of the correction parameters: the errors on correction parameters $\sigma_{\Delta p}$ are written in the output file too.

The derivatives in Equation 5.13 are evaluated from the exact analytical formula: since the equations are rather lengthy, we use the `sympy` Python library [108] to write down the extended formula for z_{ij} and subsequently use the automatic differentiation tool `clad` [109] to get derivatives with respect to the desired parameters.

5.3.2 Alignment parameters

With a total of 1098 sense wires (excluding noisy, non-working, non-connected channels), the number of degrees of freedom of the CDCH geometry is 6588 in total. This number is reduced when constraints are applied.

5.3.3 Constraints for the alignment problem

Linear constraints $\sum_i p_i = k$ on a set of parameters can be imposed on the linear system 5.15, which is then solved by the `pede` routine using the Lagrange multipliers technique.

The need to impose external constraints often arise in the alignment problem, for example to eliminate a weak mode, or to get valid physical solutions. For example:

- Although the χ^2 formula is insensitive to global translations or rotations of the CDCH, such transformations are forbidden because the CDCH is mounted inside the COBRA magnet and its absolute positioning is known with great accuracy. This is equal to imposing the following constraints on the solutions to the linear problem:

$$\begin{cases} \sum_i \delta x_{0,i} = 0 & \text{translations} \\ \sum_i \delta y_{0,i} = 0 & \\ \sum_i \delta \theta_i = 0 & \text{rotations} \\ \sum_i \delta \phi_i = 0 & \end{cases} \tag{5.20}$$

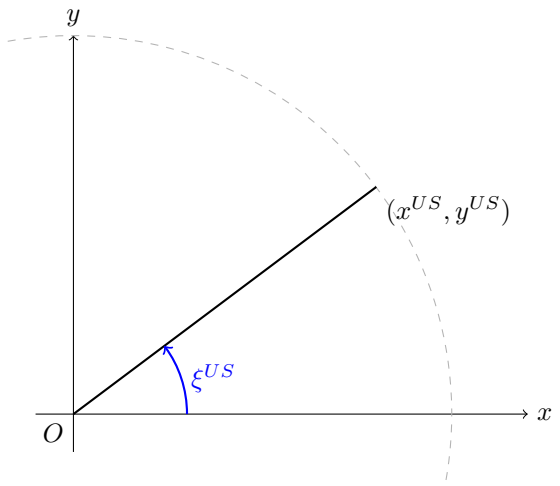

Figure 5.14: Definition of wire' coordinates at the endplate.

- The average radius R of each layer at both endcaps of the CDCH (US and DS) is well measured during the assembling procedure of the CDCH. To fix the radius the following constraints can be applied:

$$\begin{cases} \sum_{i \in layer} \cos \xi_i^{US} \cdot \delta x_i^{US} + \sin \xi_i^{US} \cdot \delta y_i^{US} = 0 \\ \sum_{i \in layer} \cos \xi_i^{DS} \cdot \delta x_i^{DS} + \sin \xi_i^{DS} \cdot \delta y_i^{DS} = 0 \end{cases} \tag{5.21}$$

  where $x_i^{US(DS)}$, $y_i^{US(DS)}$ are the coordinates of the i–th wire evaluated at the US (DS) endcap and $\xi_i^{US(DS)}$ is the angle between the wire vector $(x_i^{US(DS)}, y_i^{US(DS)})$ and the x global axis (Figure 5.14);

- Similarly, a global rotation of each layer at the end-caps is forbidden and the constraint on this deformation is:

$$\begin{cases} \sum_{i \in layer} -\sin \xi_i^{US} \cdot \delta x_i^{US} + \cos \xi_i^{US} \cdot \delta y_i^{US} = 0 \\ \sum_{i \in layer} -\sin \xi_i^{DS} \cdot \delta x_i^{DS} + \cos \xi_i^{DS} \cdot \delta y_i^{DS} = 0 \end{cases} \tag{5.22}$$

  using the same notation of the radial constraint formula.

(a) Scheme of the PCB deformation.

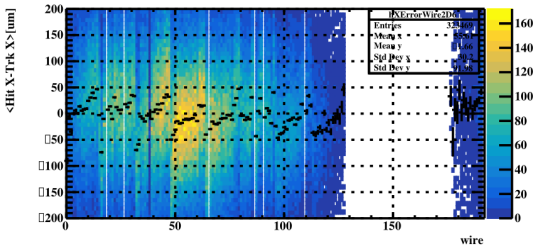

(b) Track residuals (x coordinate) in each wire in layer 6 of the CDCH. Tracking is done using the geometry of the CDCH derived from the optical survey measurements. A 16-wires-periodic trend in the average track residuals is clear.

Figure 5.15: Movement of wires at the end of each PCB.

Apart linear constraints, it is also possible to implement *Gaussian constraints* for the global parameters $\vec{p}$: the optical survey measured the geometry parameters $\vec{p}_0$ with a precision σ_p. We can use these measurements modifying the χ^2 formula in 4.1 by adding a gaussian term to the χ^2 for each parameter p_i:

$$\chi^{2\prime} = \chi^2 + \sum_i \left(\frac{\delta p_i}{\sigma_{p,i}} \right)^2 \tag{5.23}$$

These gaussian terms put a penalty on solutions too distant from the initial measurements. Since the optical survey measures the wires' positions at the end plates, not at the wire center $z = 0$, we don't have a direct measurements for σ_p in Equation 5.23. To have a reasonable estimate of σ_p, the average misalignment expected, we take it to be the RMS of the corrections on wires parameters from the iterative alignment conducted in 2021, which started from the geometry determined from the survey measurements:

$$\sigma_{x_0} = \sigma_{y_0} \approx 50\ \mu\text{m}; \quad \sigma_\theta = 0.1\ \text{mrad}; \quad \sigma_\phi = 1\ \text{mrad}; \quad \sigma_{s_x} = \sigma_{s_y} \approx 50\ \mu\text{m} \tag{5.24}$$

We find that gaussian constraints grant the best results in our case: any result shown in the following uses these constraints in the solution of the alignment problem (see also Appendix D).

One final "constraint" worth mentioning is the practice of fixing some wires to their default geometry, under the consideration that the initial position of these wires is well known. Fixed wires prevent nearby wires from moving too far away from their initial position, since the χ^2 of tracks passing through these wires would increase. This technique is particularly helpful to prevent global transformations of wires not compatible with the position determined by the survey conducted on the detector position.

For each sector of the CDCH, made of a single PCB with 16 anode wires soldered to it, we expect the position of the central wires of each sector to be known more precisely with respect to the outer wires. This is a consequence of the CDCH modular construction: as shown in Figure 5.15 (a), PCBs tend to return to a flat shape if the glue under them relaxes and the PEEK layer on top of them is not ultra-tight. This phenomenon is actually observed in the periodic pattern of track residuals bias obtained using the survey geometry for the fit (Figure 5.15 (b)). Displacements of the wires at the edge of the PCBs are of the order of ≈ 50 µm, while for wires at the PCB's center the displacemente is $\lesssim 10$ µm.

For this reason, unless specified in the text, we fix the position of the two central wires for each CDCH sector.

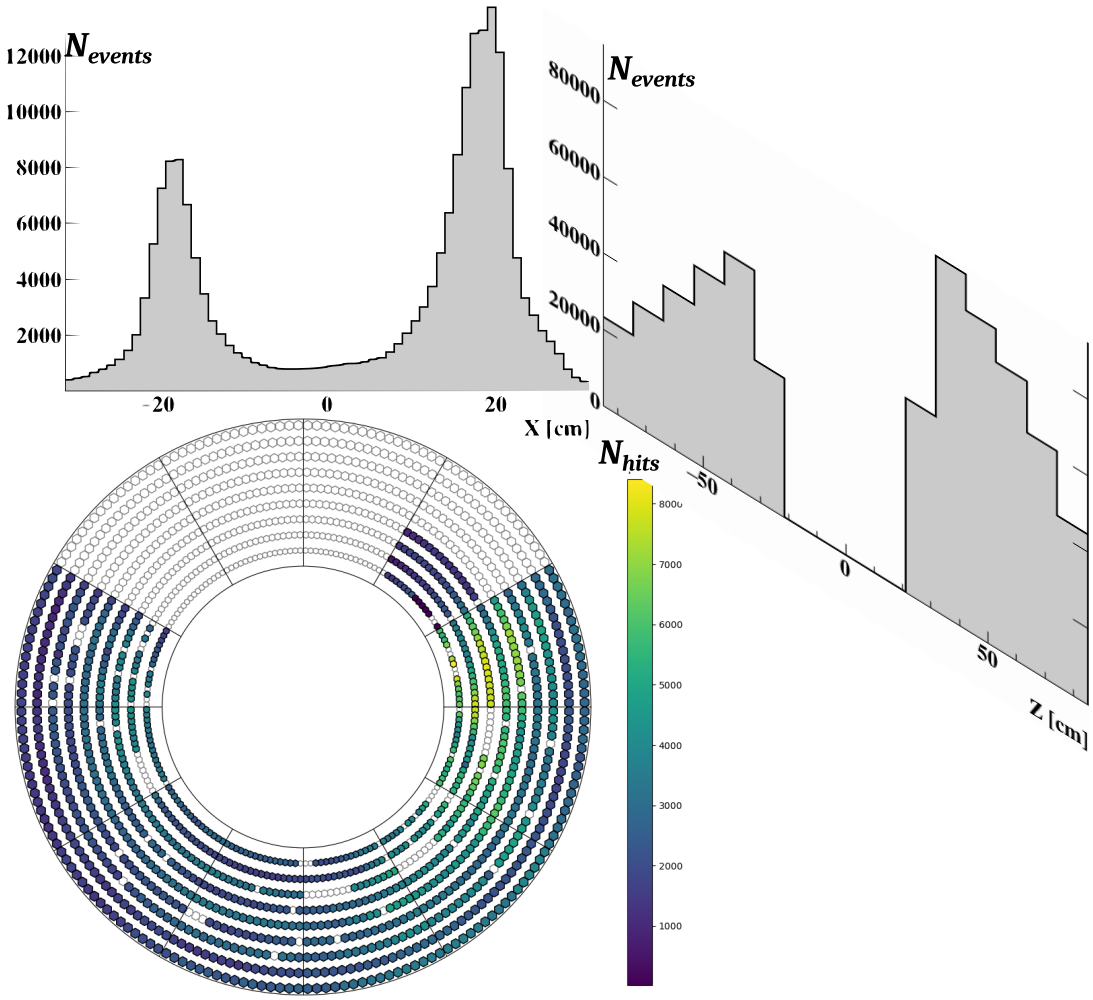

Figure 5.16: Spatial distribution of cosmic ray recorded events in 2022 that have been successfully reconstructed, as described in the text. The N_{hits} for each wire is shown in the 2D view of the CDCH. The cumulative histogram of the crossing position of cosmic rays with the x-axis at $y = 0$ (i.e. the q_{xy} parameter) is plotted on top of the figure. On the right, the distribution along the longitudinal z coordinate of the hit of the cosmic rays on the pTC detector is shown.

5.3.4 Cosmic rays dataset

A set of ≈ 150k cosmic events have been recorded during the Summer of 2022 (≈ 5 days of data taking in a period of beam stop) for the purpose of the alignment studies of the CDCH with Millepede. Cosmic events are recorded by triggering on the coincidence between a hit inside the pTC and an event in the CDCH (requiring 2 hits on the US and 2 hits on the DS side of the CDCH exceed a threshold of 60 mV).

Cosmic rays tracks are reconstructed using the procedure described in Section 5.1, using the time of the hit on the pTC tile as reference time T_0 (Equation 5.1). The following quality cuts are applied:

- $\chi^2/dof < 25$ and $|\frac{z_{ij}}{\sigma_{ij}}| < 5$ for all hits: to reject outliers for the fit but with a loose cut to avoid cutting hits on poorly placed wires;
- The best-fit track should be propagated successfully to the pTC tile triggering the event;
- Tracks striking less than four different layers are rejected to mitigate a peculiar weak mode resulting in a *squeezing* of the CDCH. See the discussion in Appendix D and in [110].

The spatial distribution of cosmic rays events on the CDCH is displayed in Figure 5.16, where we can notice that:

- the part at $x > 0$ of the CDCH is struck more often than the part at $x < 0$ because the LXe detector is acting as an absorber of soft cosmic rays in that region of space;
- the number of fitted tracks passing through the center of the CDCH is much lower than those passing at the sides. The reason is that vertical tracks passing through the CDCH center pose a problem to the track finding task: due to the absence of part of the CDCH readout channels, they have less hits (less than 10 in average per track), causing the PR to be inefficient; in addition, many bad wires are concentrated in that region of space (white spots in the 2D plot), increasing the probability to have tracks with too few hits to be identified or fitted;
- the distribution of cosmic rays hits on the pTC along the longitudinal z coordinate is not uniform; this effect is present on raw data and unaltered by the analysis procedure. While the fewer hits at $|z| < 30$ cm depends on detector acceptance for inclined cosmic rays, the asymmetry between $z > 0$ and $z < 0$ events is most probably an artifact from the data taking conditions, possibly caused by noisy wire ends on one side of the CDCH.

5.3.5 Results on Monte Carlo

The alignment algorithm is tested on Monte Carlo (MC) simulations of cosmic rays events: the MC generated cosmic rays strike wires which have a given geometry, the *goal* geometry of the alignment problem, while at the reconstruction stage the tracking is performed starting from a *misaligned* geometry. The performance of the Millepede alignment algorithm is evaluated based on its ability to retrieve the correct corrections to the wire parameters and converge to the target geometry.

The spatial distribution of cosmic rays in the simulation was generated from the experimental one (reported in Figure 5.16), in order to study the effects of track topology on the alignment procedure. Further, to simulate a realistic misalignments of wires parameters, we set as the goal geometry the one determined in 2022 through the iterative alignment procedure, while the misaligned geometry is the one used for the 2021 analysis (the starting point for the alignment in 2022 with the iterative method).

We tested Millepede on a MC generation with 700k cosmic events. Studies of the quality of the convergence varying the statistics are conducted later and described in the Section 5.3.6.

A good convergence of the alignment is observed:

- the correlation between the Millepede corrections and the true misalignments is almost one for all parameters. See Figure 5.17;

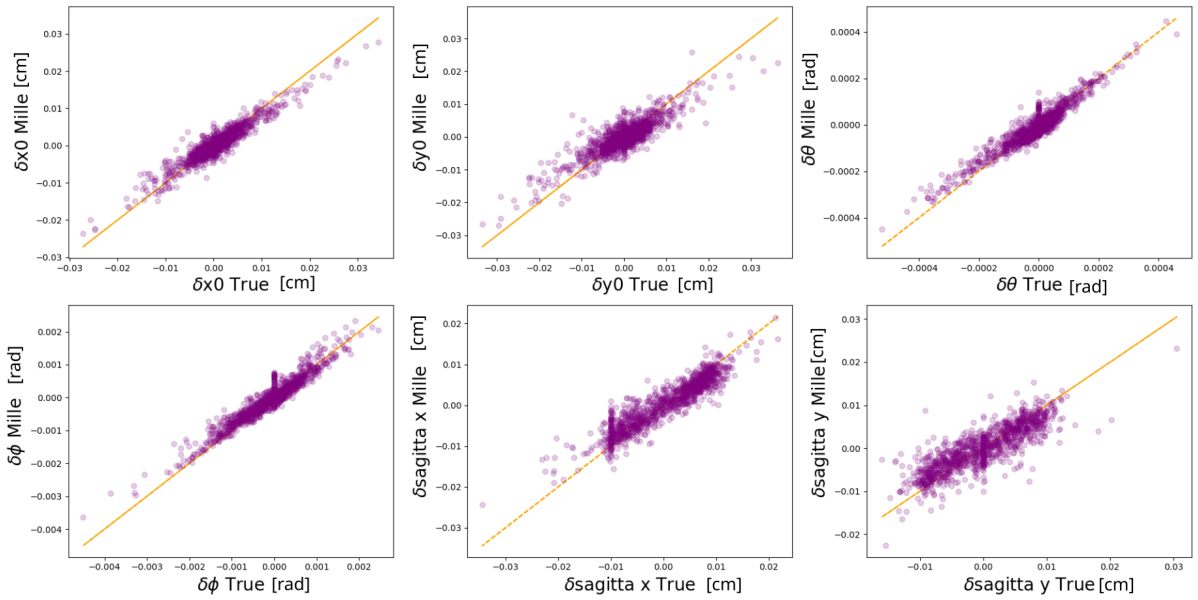

Figure 5.17: Correlation between Millepede corrections after the first iteration and the MC true displacement of the wires parameters. Some wires have the same parameters between ideal and misaligned geometries, and they can be seen as clusters of vertically aligned points. The orange line is the line of equation $x = y$.

- The convergence of the alignment procedure can be monitored evaluating the trend of *residual misalignment* at various iterations. We define the *residual misalignment* Δp^i of one parameter p at the i-th iteration as:

$$\Delta p^i \equiv \sqrt{\frac{1}{N_{wires}} \sum_{j \in wires} \left(p_j - \hat{p}_j^i\right)^2} \tag{5.25}$$

  where p_j is the true value of the parameter p for wire j and $\hat{p}_j^i$ is the geometry parameter determined after the i-th iteration. Ideally, Δp has a minimum corresponding to the precision of the method, where the precision depends on the covariance matrix of the global χ^2.

  In Figure 5.18 we plot the trend of Δp^i for all parameters[viii] through three iterations of the Millepede procedure, after which no significant improvement is observed. In Table 5.5 we list the precision obtained in the alignment of the geometry parameters with this simulation and this alignment procedure.

5.3.6 Results on 2022 data

The starting point for the alignment with Millepede is the geometry determined through the geometrical survey. This guarantees that the Millepede results are independent from those obtained with the iterative alignment procedure. In addition, imposing constraints on global shifts and rotations of the CDCH ensures that the Millepede solutions don't move the CDCH position in the global reference frame, which was determined through direct measurements. Also, as discussed above in the constraints section 5.3.3, we have a strong motivation for fixing central wires of each PCB to boost the convergence.

We performed three iterations of the Millepede algorithm before reaching convergence. For each iteration, the `Mille` routine runs in $\approx$ 30 minutes on the full dataset while the `pede` program solves the linear system with the inversion methods in $\approx$ 1 minute. Considering the time needed for data reprocessing between iterations, the procedure takes around 30 hours (on this dataset) for each iteration.

[viii] To condense all parameters in a single plot, the single Δp are normalized to the initial misalignment of the parameters Δp_0.

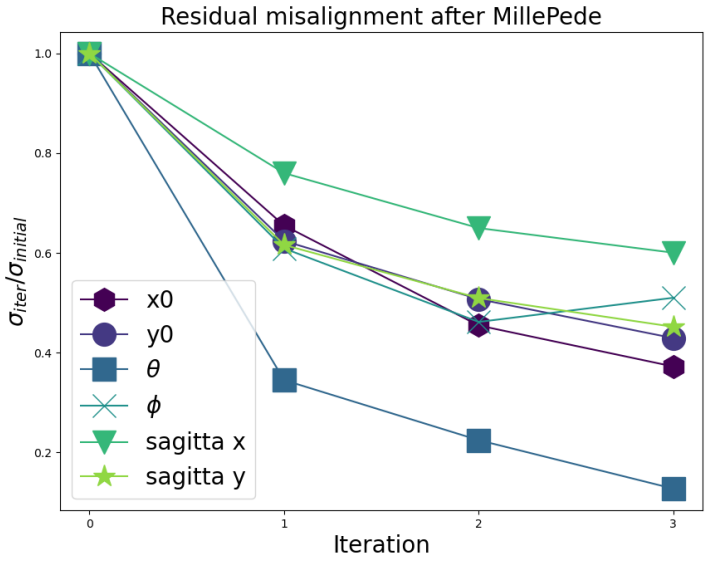

Figure 5.18: Residual misalignment for all parameters trend after each iteration of the algorithm. The alignment for the ϕ parameter reached its precision limit, as is visible from the trend of the curve.

Table 5.5: Achieved precision on the determination of geometry parameters with Millepede.

Parameter	Resolution
x_0	30 µm
y_0	35 µm
θ	20 µrad
ϕ	200 µrad
s_x	30 µm
s_y	30 µm

Between each iteration, the Millepede procedure is ran several times with different configurations: applying different sets of constraints, like radial and rotational constraints on each layer (see Section 5.3.3), varying the variance of the gaussian constraints in Equation 5.23, removing any fixed wire. We find the following choices to be the most performing at each iteration:

1. apply global shift constraints and gaussian constraints on all parameters as described in Section 5.3.3; fix two wires per PCB;

2. as step 1, but fix only one wire per PCB to find the optimal geometry for more wires;

3. as step 2, but don't impose the constraints on global shifts: as is visible in Figure 5.21, layers 1 and 2, the most external ones, have an average bias of $\sim$ 30 µm, different from that in any other layer. It is possible that the measurements for those layers in the survey geometry were systematically incorrect: therefore the assumptions $\sum_i y_{i,0} = k$ and $\sum_i x_{i,0} = k$ are not valid.

The improvement in wire-by-wire residuals can be seen comparing Figure 5.20 and 5.21, where tracking is performed with the geometry from the survey, and Figure 5.22 and 5.23, with the geometry determined after the third iteration of Millepede. This improvement on residuals is also visible comparing the χ^2/dof distribution of e^+ tracks with different geometries (Figure 5.19 (a)). Residuals are evaluated using $\mu \to e\nu\overline{\nu}$ data taken in 2022 with 3×10^7 μ^+/s data, a dataset completely different from the one used for the alignment.

Tracking performances (measured on the same sample of Michel positrons) improve as well, although they don't reach the same level obtained with the iterative alignment procedure:

- the tracking efficiency raises from 55.0% to 57.0% (Figure 5.19 (b));

- the resolution on the positron's kinematic parameters also improves (Table 5.6).

Table 5.6: Comparison of tracking performances with different geometries.

Variable	Survey Geo	Millepede iter#3	Iter. align.
σ_z	2.05 mm	2.14 mm	1.96 mm
σ_y	0.79 mm	0.79 mm	0.70 mm
σ_ϕ	6.85 mrad	6.81 mrad	6.71 mrad
σ_θ	8.42 mrad	7.80 mrad	7.85 mrad
σ_p	115.6 keV	112.0 keV	107.4 keV
ϵ_{trk}	55.0%	57.0%	57.8%

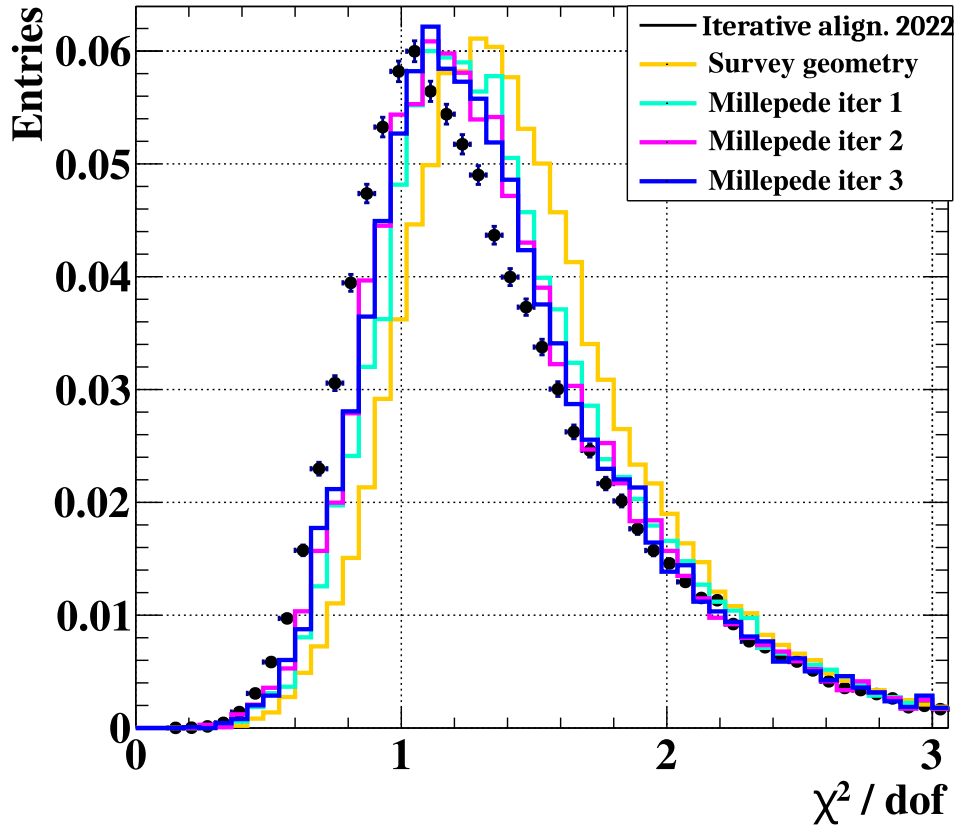

(a) Comparison of χ^2/dof distribution of positron tracks with different geometries. The geometry obtained with the iterative alignment is shown with black markers.

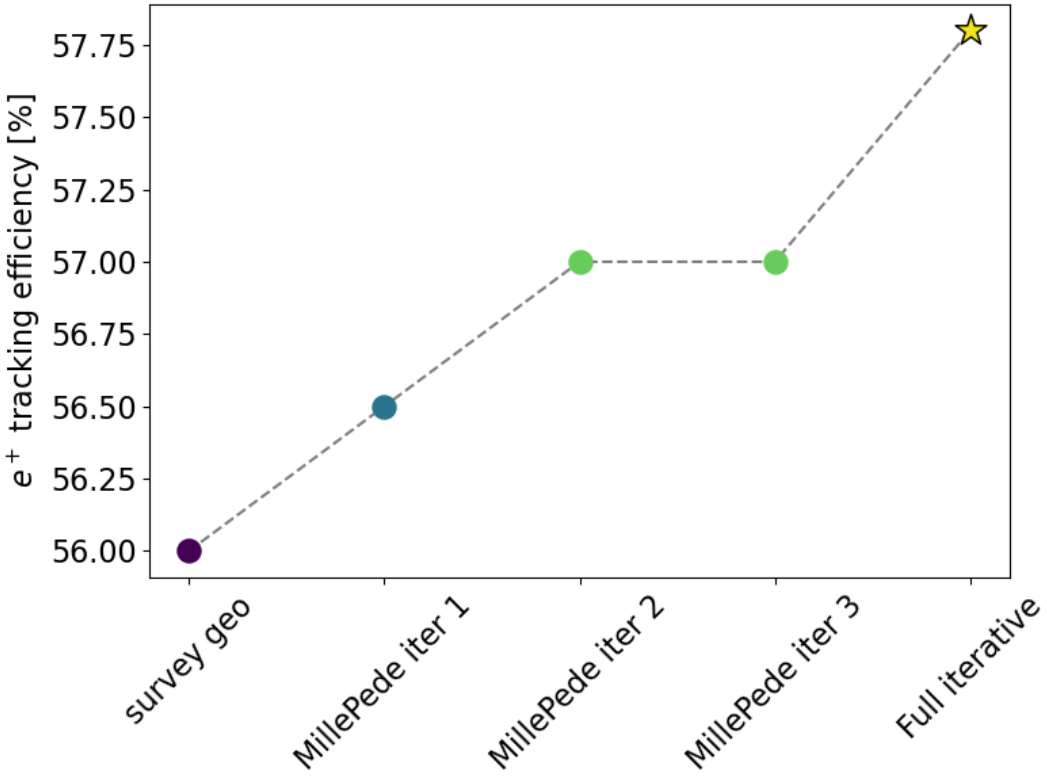

(b) Comparison of tracking efficiency with different geometries.

Figure 5.19: Comparison between different geometries: geometrical survey, Millepede at different iterations (1, 2 and 3) and the geometry from the iterative alignment in 2022.

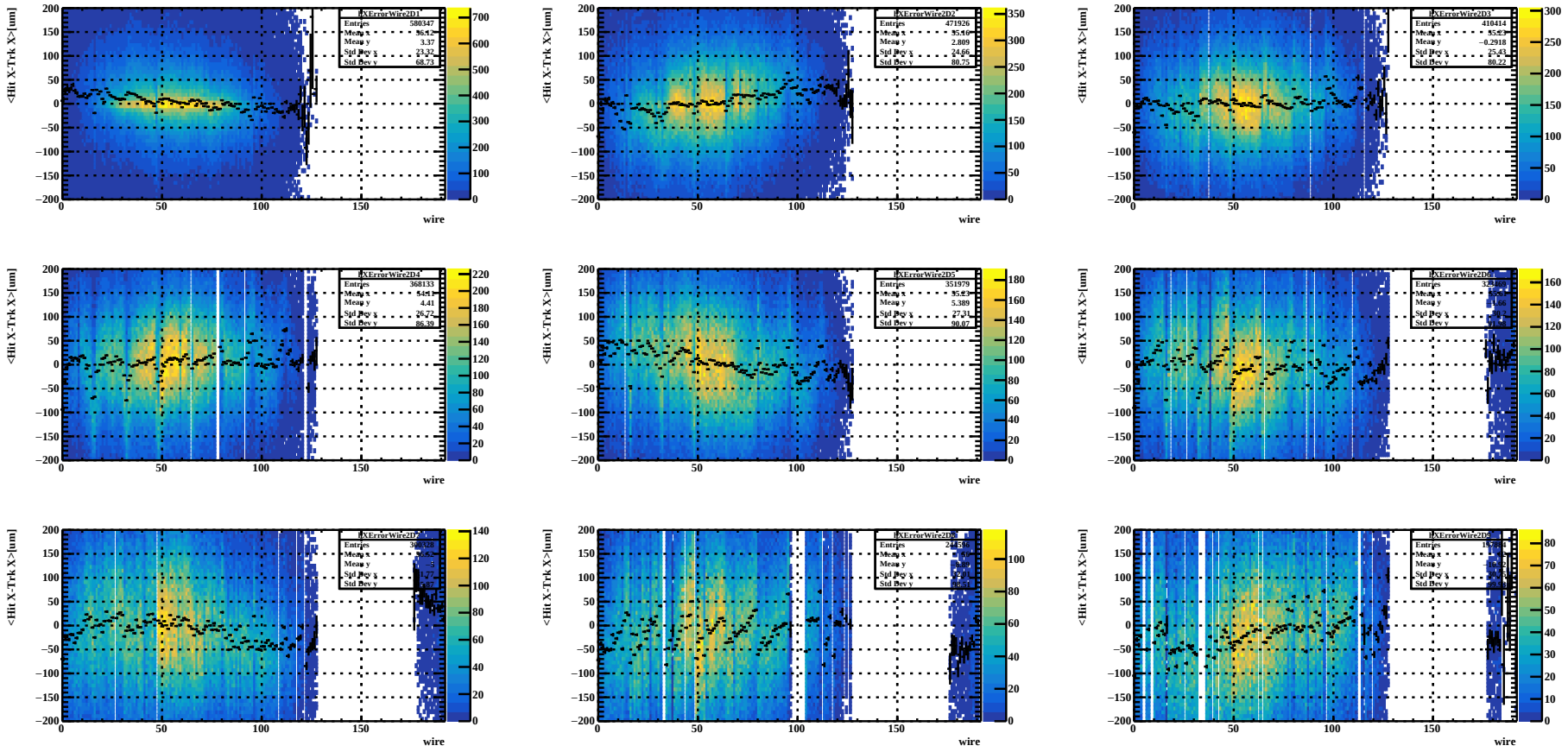

Figure 5.20: $x^{meas} - x^{fit}$ for all wires (wire ID on the x axis) measured on a sample of Michel positrons data acquired in 2022 with 3×10^7 μ^+/s beam intensity. The geometry used for reconstruction is the one determined from the optical survey.

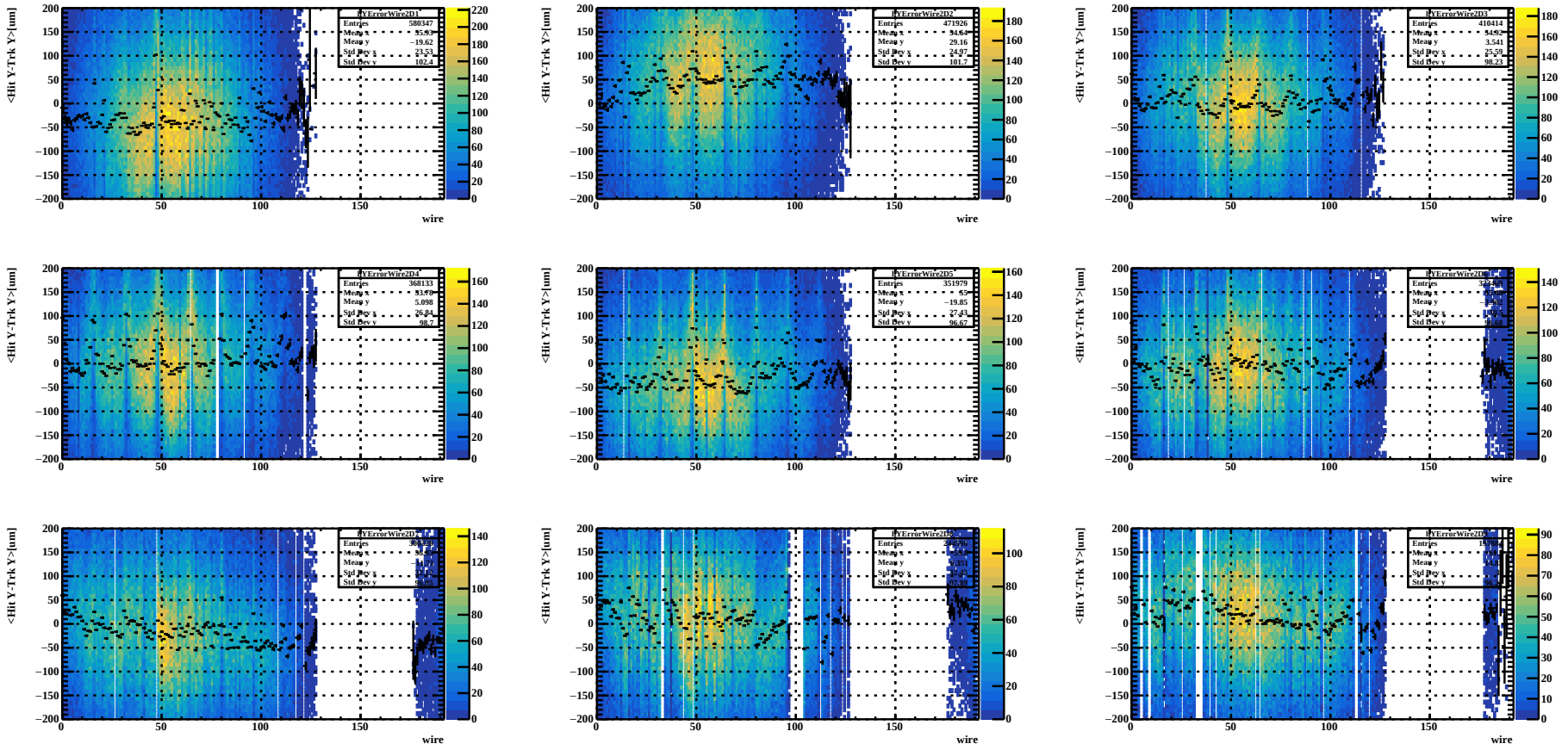

Figure 5.21: $y^{meas} - y^{fit}$ for all wires (wire ID on the x axis) measured on a sample of Michel positrons data acquired in 2022 with 3×10^7 μ^+/s beam intensity. The geometry used for reconstruction is the one determined from the optical survey.

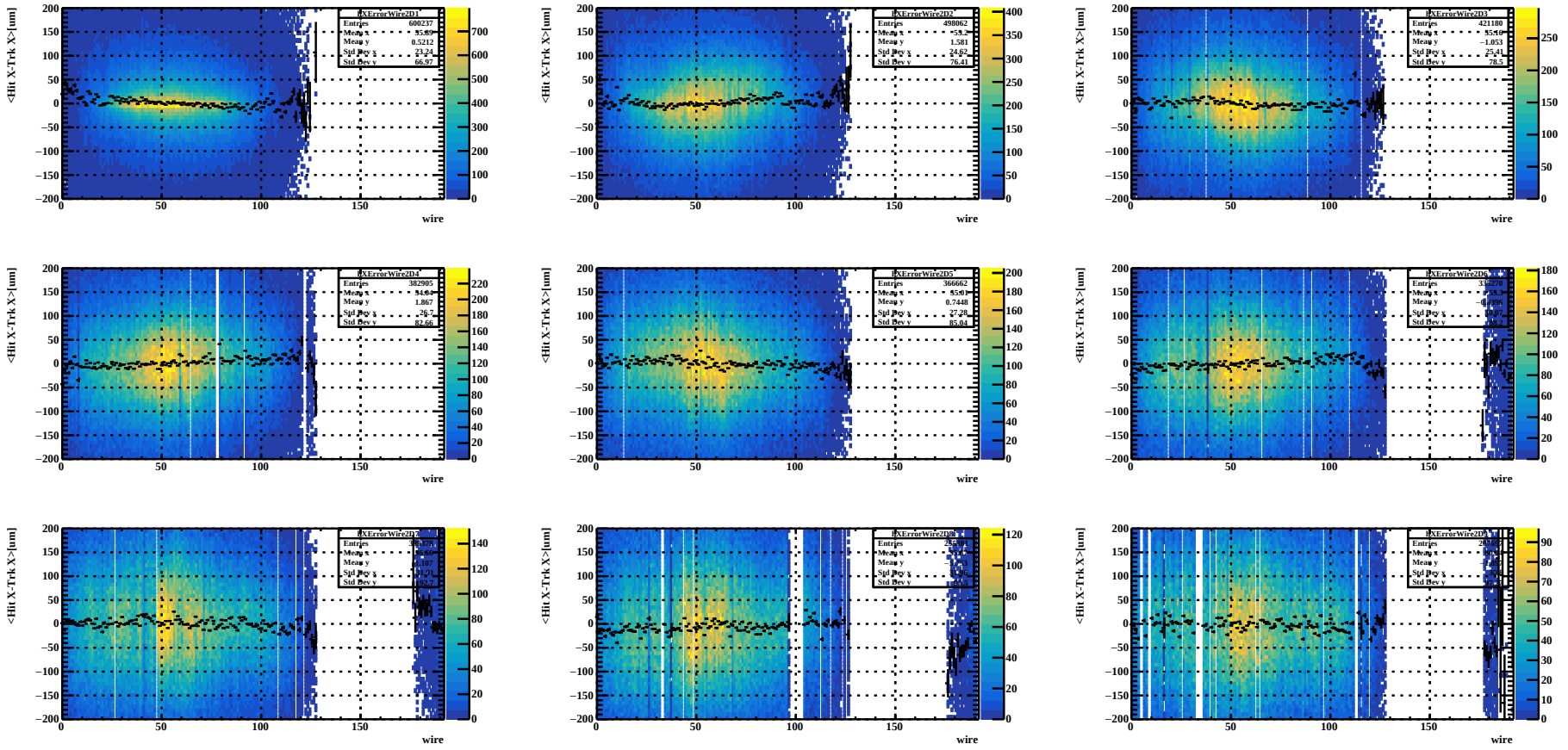

Figure 5.22: $x^{meas} - x^{fit}$ for all wires (wire ID on the x axis) measured on a sample of Michel positrons data acquired in 2022 with 3×10^7 μ^+/s beam intensity. The geometry is the result of three iterations of the Millepede algorithm on data, as described in the text.

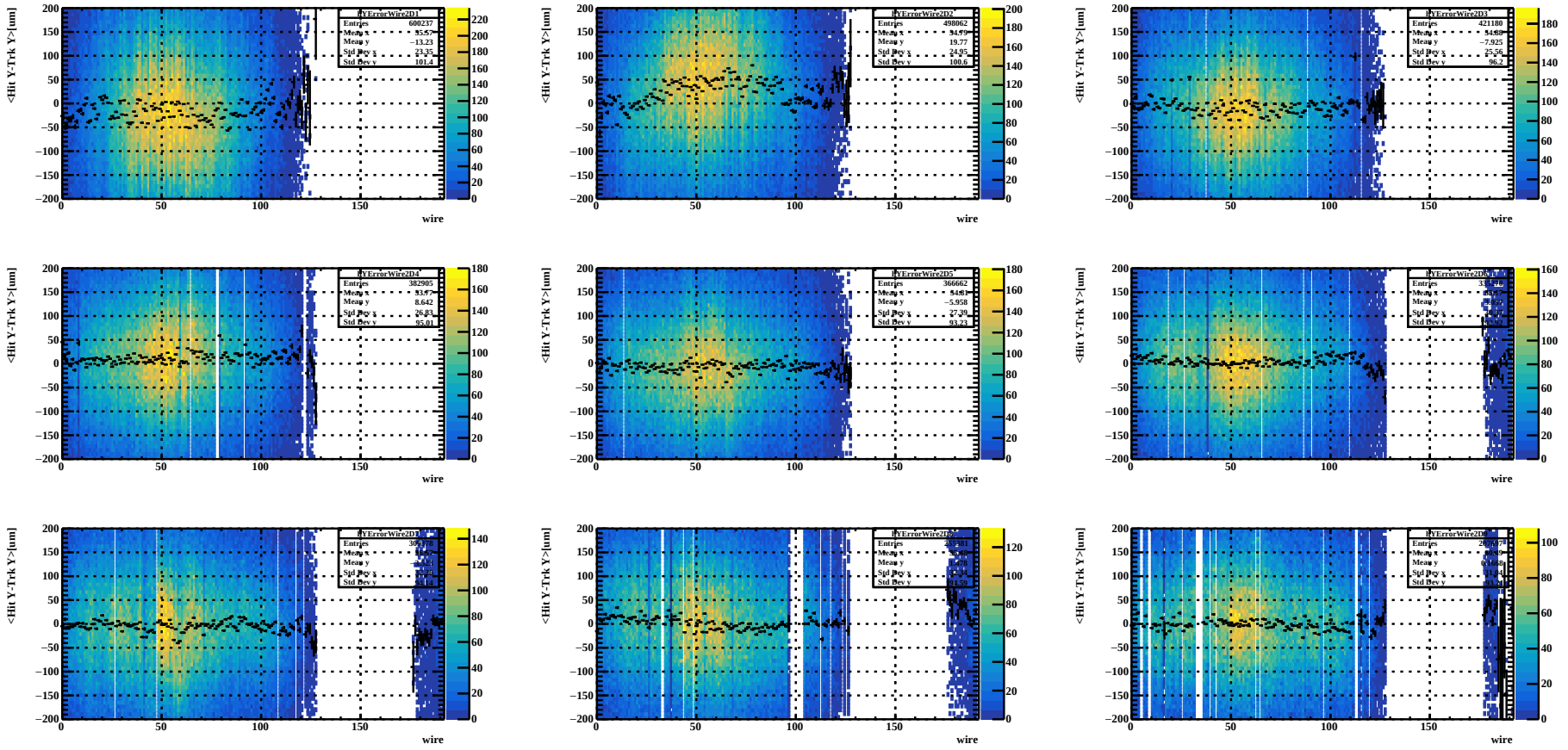

Figure 5.23: $y^{meas} - y^{fit}$ for all wires (wire ID on the x axis) measured on a sample of Michel positrons data acquired in 2022 with 3×10^7 μ^+/s beam intensity. The geometry is the result of three iterations of the Millepede algorithm on data, as described in the text.

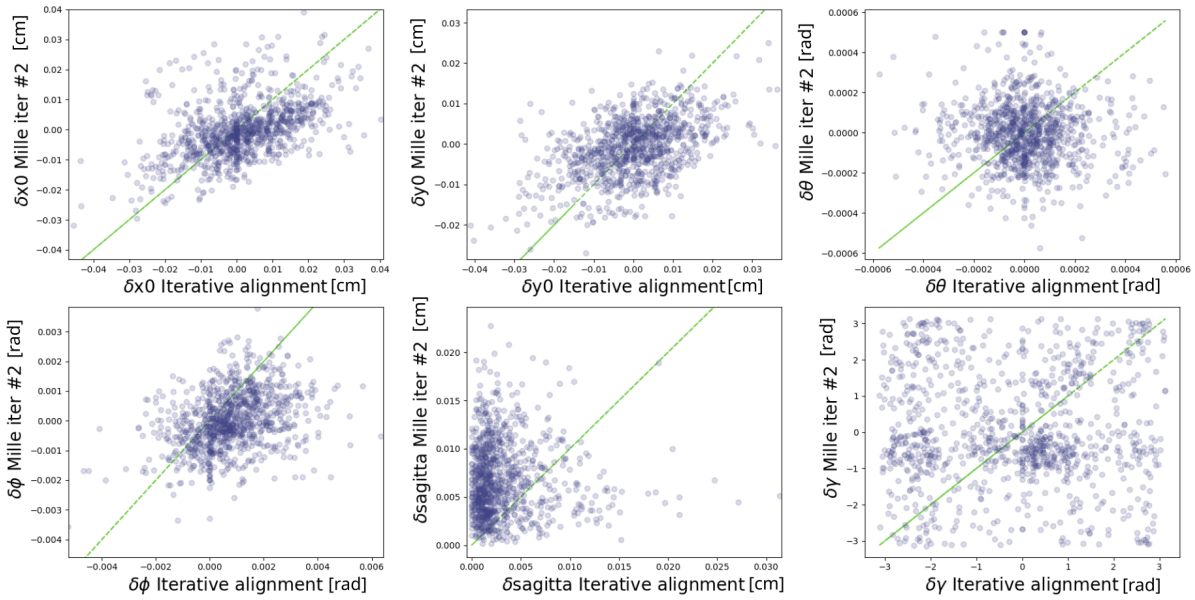

Figure 5.24: Correlation between geometry parameters correction from Millepede and from the iterative alignment procedure. The green line is the line of equation $x = y$.

Comparing the correction of Millepede to the geometrical survey and those of the iterative alignment (Figure 5.24) we observe a positive correlation between all parameters, except for those related to the sagitta, s_0 and γ.

The correlation between corrections is not full and especially the dispersion for θ and ϕ is quite large: this might be due to a different precision in the determination of correction parameters. In the next Section we investigate these problems to better understand the limitations of Millepede.

Instead, the difference in sagitta parameters between the two geometries means that one of the methods converged to a wrong geometry. Therefore, either cosmic rays, being vertical tracks, don't allow to determine correctly the wires' sagitta, or the iterative alignment on positrons tracks has a weak mode which is insensitive to the size of the sagitta. The first hypothesis is ruled out by the validation of Millepede on MC simulations described in the previous Section; the second one instead is supported by preliminary studies described in [85], where it is showed how changing sagitta parameters up to 1 mm deflection of the wires has little effect in the track residuals, which don't show the same significant bias.

5.3.7 Limitations of the alignment with Millepede on 2022 data

As afore mentioned, we try to investigate the reasons for poorer performances of Millepede compared to the iterative alignment.

Although a misalignment of some wires parameters is clearly visible as a bias in the track residuals (Figure 5.22 and 5.23), after the third iteration the algorithm reaches a minimum, i.e. the size of the error on each correction parameters is of the same size (or bigger) than the correction itself. The error on each correction parameter $\sigma_{\Delta p}$ depends on the covariance matrix of the global χ^2 problem, therefore it roughly scales as $1/\sqrt{N_{hits}}$, where N_{hits} is the number of hits on the wire that we try to align. This trend is visible in Figure 5.25 (a). Figure 5.25 (b) instead shows the average number of hits per wire belonging to a certain plane: because of acceptance effects, the outermost layers are those with less hits. The precision on the alignment parameters attainable with Millepede with the 2022 data is limited by the collected statistics, which is not sufficient to reach the precision of the iterative alignment method.

Using MC simulations, we further investigated how the convergence of Millepede depends on the available statistics by running a single iteration of the algorithm on three sets of simulated cosmic rays containing 700k, 300k, and 100k events. Figure 5.26 shows the residual misalignment for all parameters

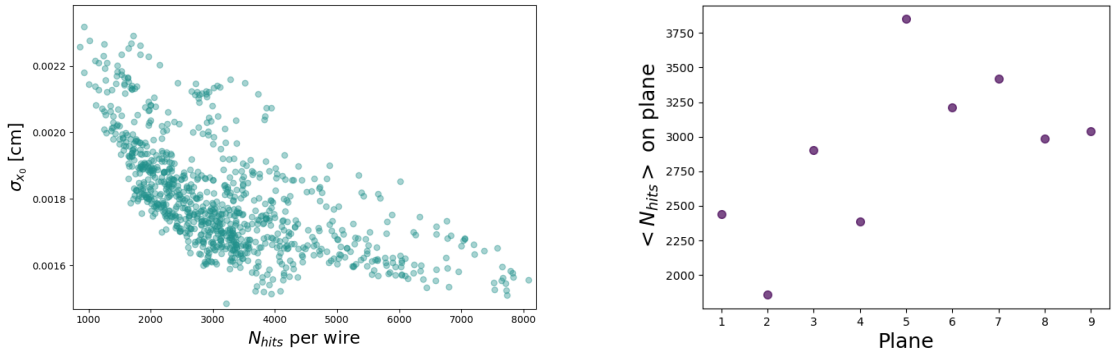

(a) Resolution on the δx_0 parameter for each wire as a function of the number of hits N_{hits}. The parameter σ_{x_0} is taken from the pede output as described in the text.

(b) Average number of hits N_{hits} per CDCH plane with the 2022 cosmics dataset.

Figure 5.25: The impact of statistics on the precision for the determination of alignment parameters.

in the three cases: the difference in the achieved precision after one iteration of Millepede is clearly visible, particularly between the 100k and 300k samples. From these studies we conclude that the statistical error saturates with a data sample of $\approx$ 1 M cosmic rays events.

During the 2023, 2024 and 2025 data taking campaigns, almost 2 M cosmic rays events have been collected each year, in order to perform these alignment studies extensively and overcoming this limitation.

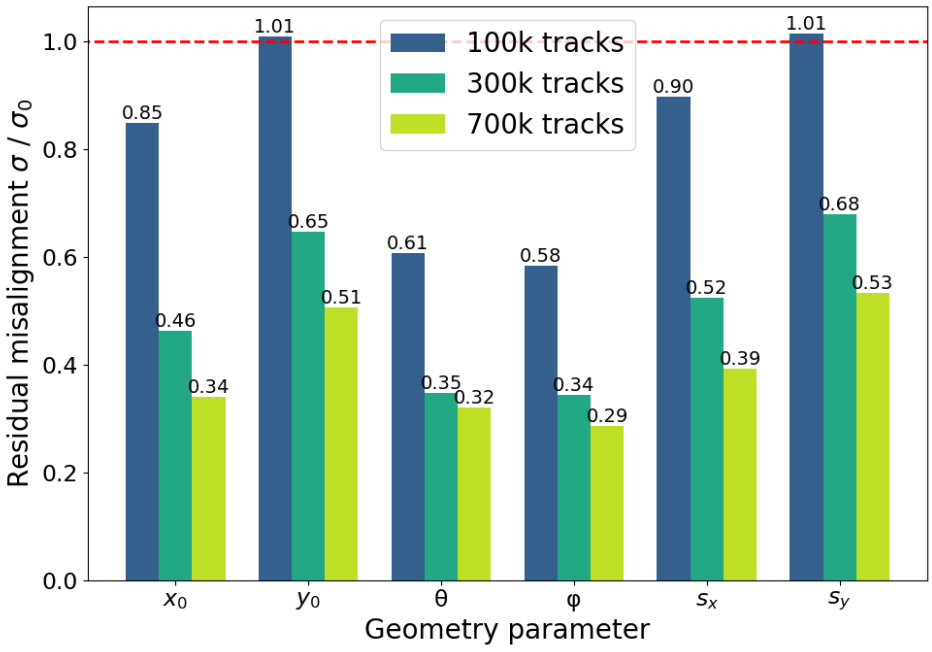

Figure 5.26: Residual misalignment measured on MC simulations with different statistic (100k, 300k, 700k tracks) for each variable.

In Figure 5.27 the residual misalignment of each parameter for each plane is calculated. Indeed, as shown in Figure 5.25 (b), the number of hits vary much in each layer, and consequently in some CDCH layers the convergence of the algorithm is poorer. In the case of layers 1 and 2, which had the

largest initial misalignment, as visible from the first two plots of Figure 5.21, the issue of the lack of statistics is preventing a better determination of the geometry parameters and therefore those layers' track residuals can not improve any further (Figure 5.23).

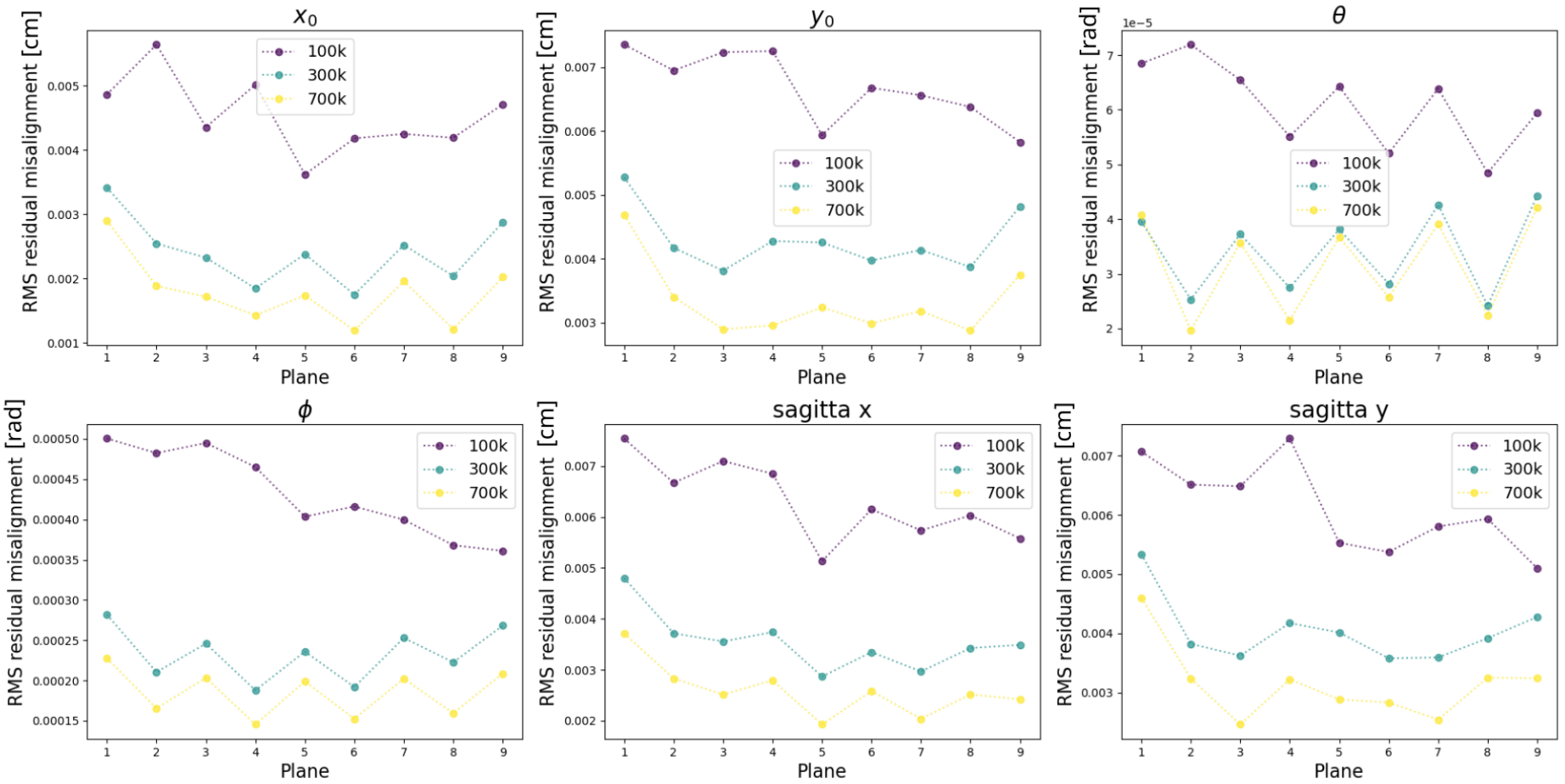

Figure 5.27: Residual misalignment measured on MC simulations with different statistic (100k, 300k, 700k tracks) for each variable, grouped by CDCH plane.

Part III

MEG II results on the 2021+'22 dataset

Chapter 6

Positron Analysis

In this chapter, the construction of the positron probability density functions, following the full calibration of the spectrometer, is presented. This is the primary contribution of the candidate to the MEG II analysis of the 2021+'22 dataset, effectively summarizing the calibration procedures discussed in the previous chapters.

In this Chapter, we introduce the MEG II analysis strategy (Section 6.1), we report the results of the Positron Analysis on the 2021+'22 dataset, i.e. the measurement of the spectrometer's performances at the end of the calibration procedures (Section 6.2), and the determination of the parameters to build the positron's probability density functions (PDFs) for the final analysis.

6.1 The MEG II analysis technique

The number of observed $\mu^+ \to e^+\gamma$ events N_{sig} is determined through an unbinned maximum likelihood analysis of the data [9] falling inside the "analysis" region defined by: 48 MeV $< E_\gamma <$ 58 MeV, 52.2 MeV $< E_{e^+} <$ 53.5 MeV; $|t_{e^+\gamma}| < 0.5$ ns; $|\phi_{e^+\gamma}| < 40$ mrad; $|\theta_{e^+\gamma}| < 40$ mrad [8].

The analysis is performed adopting a blind approach: the events inside a "blinding box" defined by 48.0 MeV $< E_\gamma <$ 58.0 MeV ("energy side-band") and $|t_{e^+\gamma}| < 1$ ns ("time side-band") are initially hidden to Collaboration members. Note that the analysis region is a subset the blinding box. Only once the probability density functions (PDFs) of observables used to discriminate signal from background are ready to build the likelihood function $\mathcal{L}(N_{sig})$, the hidden data are unblinded and used to extract a confidence interval for the expected number of signal events.

The branching ratio BR($\mu^+ \to e^+\gamma$) is derived from N_{sig} by the following equation [9]:

$$\mathrm{BR}(\mu^+ \to e^+\gamma) \equiv \frac{\Gamma(\mu^+ \to e^+\gamma)}{\Gamma_{tot}} = \frac{N_{sig}}{N_\mu} \tag{6.1}$$

where N_μ is the number of muon decays detected in the detector's acceptance during data taking, called the *normalisation factor*.

The blinding box for the '21+'22 analysis is shown in Figure 6.1. All necessary studies on the background, including the construction of the PDFs, are done in side-bands outside the analysis region. Data in the time side-bands are used to study the accidental background, while the energy side-bands around the $t_{e^+\gamma}$ coincidence peak are used to determine the PDFs of RMD events as well as signal's PDFs.

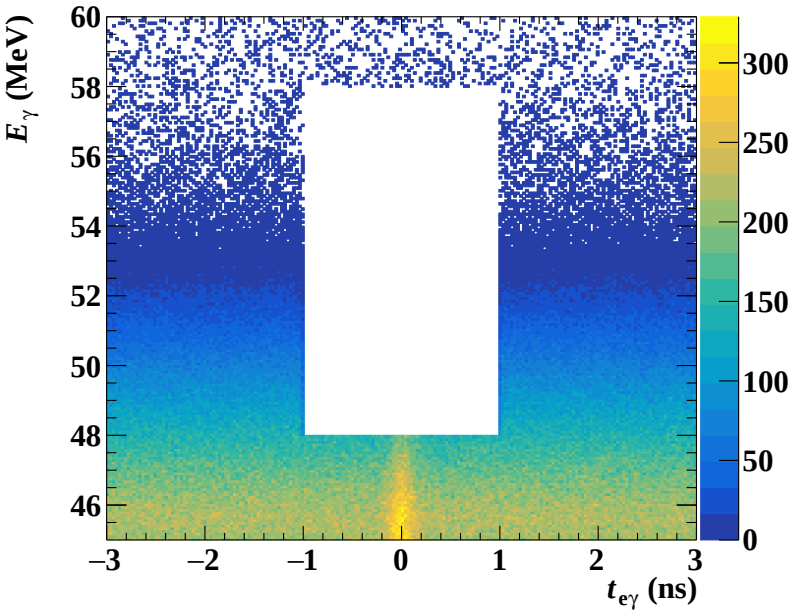

Figure 6.1: E_γ - $t_{e^+\gamma}$ bi-dimensional distribution of MEG II data collected during the '21 and '22 data taking campaigns. The area with missing data corresponds to the blinding box.

6.1.1 The likelihood function

The likelihood function contains four fit parameters with respect to which it is minimized: N_{sig}, N_{RMD}, N_{ACC}, the number of measured signal, RMD and accidental events respectively, and x_{TGT}, a parameter accounting for misalignments of the muon stopping target.

The extended likelihood function is the following:

$$\begin{aligned}
&\mathcal{L}(N_{sig}, N_{RMD}, N_{ACC}, x_{TGT}) = \\
&= \exp\left\{-\frac{x_{TGT}^2}{2\sigma_{TGT}^2}\right\} \cdot \exp\left\{-\frac{\left(N_{RMD} - \overline{N_{RMD}}\right)^2}{2\sigma_{RMD}^2}\right\} \cdot \exp\left\{-\frac{\left(N_{ACC} - \overline{N_{ACC}}\right)^2}{2\sigma_{ACC}^2}\right\} \times \\
&\times \frac{\exp\left\{-N_{sig} - N_{RMD} - N_{ACC}\right\}}{N_{obs}!} \prod_{i=1}^{N_{obs}} \left(N_{sig}\mathcal{S}\left(\vec{x}_i | x_{TGT}\right) + N_{RMD}\mathcal{R}\left(\vec{x}_i\right) + N_{ACC}\mathcal{A}\left(\vec{x}_i\right)\right)
\end{aligned} \tag{6.2}$$

where $\vec{x}_i$ are the observables of each event (used to discriminate signal and background). The parameters N_{RMD}, N_{ACC} and x_{TGT} are *nuisance parameters* in this analysis, with their values constrained to fluctuate with a gaussian distribution of variance σ_N^2 around the mean value $\overline{N}$ determined on data.

In order to cross-check the results, two independent likelihood analyses with different types of PDFs are performed: one with per-event PDFs and one with constant PDFs.

Per-event PDFs Detector resolutions vary for each event because of different detector conditions, event topology and reconstruction performances. The per-event likelihood analysis aims at preserving every relevant information for each event, like the full covariance matrix of the Kalman filter tracking algorithm for positrons, including also correlations between observables. In total, eight observables $\vec{x}$ for each event are used in the fit procedure:

- the kinematics observables E_{e^+}, E_γ, $t_{e^+\gamma}$, $\theta_{e^+\gamma}$, $\phi_{e^+\gamma}$;
- the number of pixels hit inside the pTC, n_{pTC}, which affects the $t_{e^+\gamma}$ resolution as discussed in Chapter 2 Section 2.2.3, and has a very different distribution for signal and background;
- the RDC observables (in case of a signal in the RDC), $t_{e^+}^{RDC} - t_\gamma^{LXe}$ and $E_{e^+}^{RDC}$, used to identify candidate background events.

The per-event PDFs depend also on other observables, which are correlated with $\vec{x}_i$. Correlations are implemented using conditional PDFs. Photon observables depend in general on the photon energy and its interaction point coordinates v_γ and w_γ [i]; the positron PDFs instead depend on the positron energy, the reconstructed decay vertex position and of course the beam intensity R_μ.

The signal $\mathcal{S}(\vec{x}_i)$, RMD $\mathcal{R}(\vec{x}_i)$ and accidental $\mathcal{A}(\vec{x}_i)$ PDFs are obtained combining the one-dimensional PDFs of the observables $\vec{x}_i$.

This is the signal PDF decomposition into its one-dimensional terms for every observable in $\vec{x}_i$:

$$\begin{aligned}\mathcal{S}(\vec{x}_i) &= \\ &= \mathcal{S}_0(R_\mu) \times \\ &\quad \mathcal{S}_1(E_\gamma|R_\mu, v_\gamma, w_\gamma) \times \\ &\quad \mathcal{S}_2(E_e|R_\mu, \vec{\sigma}_e) \times \\ &\quad \mathcal{S}_3(t_{e^+\gamma}, n_{\mathrm{pTC}}|E_\gamma, E_e) \times \\ &\quad \mathcal{S}_4(\theta_{e\gamma}|R_\mu, E_e, v_\gamma, w_\gamma, \vec{\sigma}_e, x_{TGT}) \times \\ &\quad \mathcal{S}_5(\phi_{e\gamma}|R_\mu, E_e, \theta_{e\gamma}, \phi_e, v_\gamma, w_\gamma, \vec{\sigma}_e, x_{TGT}) \times \\ &\quad \mathcal{S}_6(t^{RDC}_{e\gamma}, E^{RDC}_{e^+}|R_\mu)\end{aligned} \tag{6.3}$$

For energies, angles and time, the signal PDFs are modelled as Gaussian functions reflecting the measured resolutions, with the possible addition of tails, according to the results of calibrations described in the next Sections.

This is the decomposition of the RMD PDF:

$$\begin{aligned}\mathcal{R}(\vec{x}_i) &= \\ &= \mathcal{R}_0(R_\mu) \times \\ &\quad \mathcal{R}_1(E_\gamma|R_\mu, E_e, \phi_{e\gamma}, \theta_{e\gamma}, v_\gamma, w_\gamma) \times \\ &\quad \mathcal{R}_2(E_e|R_\mu, \theta_{e\gamma}, \phi_{e\gamma}\vec{\sigma}_e) \times \\ &\quad \mathcal{R}_3(t_{e^+\gamma}, n_{\mathrm{pTC}}|E_\gamma, E_e) \times \\ &\quad \mathcal{R}_4(\theta_{e\gamma}|R_\mu, v_\gamma, w_\gamma, \vec{\sigma}_e) \times \\ &\quad \mathcal{R}_5(\phi_{e\gamma}|R_\mu, \theta_{e\gamma}, v_\gamma, w_\gamma, \vec{\sigma}_e) \times \\ &\quad \mathcal{R}_6(t^{RDC}_{e\gamma}, E^{RDC}_{e^+}|R_\mu)\end{aligned} \tag{6.4}$$

The RMD PDFs for E_γ, E_e, $\theta_{e\gamma}$, $\phi_{e\gamma}$ are obtained convoluting the theoretical spectra with the experimental resolutions; $\mathcal{R}_6(t^{RDC}_{e\gamma}, E^{RDC}_{e^+}|R_\mu)$ is the same function used in the signal PDF, $\mathcal{S}_6$; $\mathcal{R}_3(t_{e^+\gamma}, n_{\mathrm{pTC}}|E_\gamma, E_e)$ is obtained from a fit to the energy-sideband.

The accidental background PDF is the following:

$$\begin{aligned}\mathcal{A}(\vec{x}_i) &= \\ &= \mathcal{A}_0(R_\mu) \times \\ &\quad \mathcal{A}_1(E_\gamma|R_\mu, v_\gamma, w_\gamma) \times \\ &\quad \mathcal{A}_2(E_e|R_\mu, \vec{\sigma}_e) \times \\ &\quad \mathcal{A}_3(t_{e^+\gamma}, n_{\mathrm{pTC}}|R_\mu, E_e, w_\gamma) \times \\ &\quad \mathcal{A}_4(\theta_{e\gamma}) \times \\ &\quad \mathcal{A}_5(\phi_{e\gamma}|v_\gamma) \times \\ &\quad \mathcal{A}_6(t^{RDC}_{e\gamma}, E^{RDC}_{e^+}|R_\mu, E_\gamma)\end{aligned} \tag{6.5}$$

The accidental E_e PDF is obtained from the Michel spectrum fit in the side-band region. In this sense, it is identical to the signal E_e PDF when correlations are not taken into account. The accidental E_γ PDF

[i] u_γ and θ_e dependencies are not included because they would give rise to results on the $\mu \to e\gamma$ decay dependent on assumptions to the underlying New Physics model.

is taken from the Monte Carlo spectrum with an additional smearing, fitted to data to match the data distribution in the side-bands. The angular, $t_{e\gamma}$, n_{pTC} and RDC PDFs instead are fitted directly from data using polynomial functions.

The PDFs depend on the beam intensity R_μ: not only many observables are strongly dependent on R_μ, but also the ratio between signal and background events depend on it. Therefore, different PDFs for these observables are built for each beam period and $\mathcal{S}_0(R_\mu)$, $\mathcal{R}_0(R_\mu)$ and $\mathcal{A}_0(R_\mu)$ are weights for the relative contribution of each term.

Constant PDFs Another approach for the PDFs' construction uses "constant PDFs". They are built with constant parameters by averaging out the temporal variations (within a period of fixed beam intensity), the position dependence of the detector response (with the only exception of the conversion depth inside the calorimeter, with different PDFs for $w_\gamma < 2$ cm and $w_\gamma > 2$ cm) and the correlations between the observables.

The total number of observables $\vec{x}_i$ used for this analysis are six:

- the positron and photon energy, E_{e^+} and E_γ;
- the relative angle between positron and photon, $\Theta_{e^+\gamma}$, is used in place of its two projections;
- the relative time, $t_{e^+\gamma}$;
- the two RDC observables, $t_{e\gamma}^{RDC}, E_{e^+}^{RDC}$.

The PDFs decomposition for signal and background is the same as for the per-event analysis discussed above. Correlations are included in this analysis through a rescaling of the observables' resolutions [43].

This approach shows worse sensitivity ($\approx 15\%$) compared to the per-event one, while it's less prone to systematic uncertainties. This method is hence used as a cross-check of the per-event analysis.

6.1.2 Confidence interval

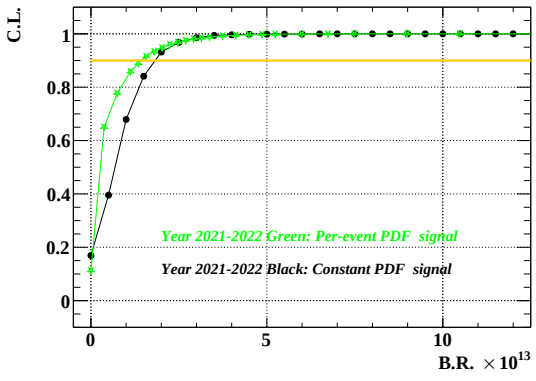

Figure 6.2: Confidence interval on BR($\mu^+ \to e^+\gamma$) calculated from a pseudo-experiment generated with a null signal hypothesis. In green is the result for the "per-event PDFs" analysis, in black for the "constant PDFs" analysis. The point where the curves crosses the 90% C.L. line (yellow) represents the 90% C.L. upper limit on BR($\mu^+ \to e^+\gamma$) from this simulation.

The construction of the confidence interval for the number of signal N_{sig} events is based on the Feldman–Cousins prescription [111], with the profile likelihood ratio ordering. The profile likelihood ratio λ_p is defined as

$$\lambda_p(N_{sig}) = \begin{cases} \dfrac{\mathcal{L}(N_{sig}, \hat{\hat{\theta}}(N_{sig}))}{\mathcal{L}(0, \hat{\hat{\theta}}(0))} & \text{if } \hat{N}_{sig} < 0 \\ \dfrac{\mathcal{L}(N_{sig}, \hat{\hat{\theta}}(N_{sig}))}{\mathcal{L}(\hat{N}_{sig}, \hat{\theta})} & \text{if } \hat{N}_{sig} \geq 0 \end{cases} \tag{6.6}$$

where θ is a vector of nuisance parameters, $\hat{N}_{sig}$ and $\hat{\theta}$ are the parameters values maximizing the likelihood function, $\hat{\hat{\theta}}(N_{sig})$ are the values for θ which maximize the likelihood function at fixed N_{sig}. In Figure 6.2 we illustrate an example of a confidence interval calculated on a pseudo-experiment with zero signal. The 90% C.L. upper limit is shown for both analysis techniques, to illustrate the difference between them.

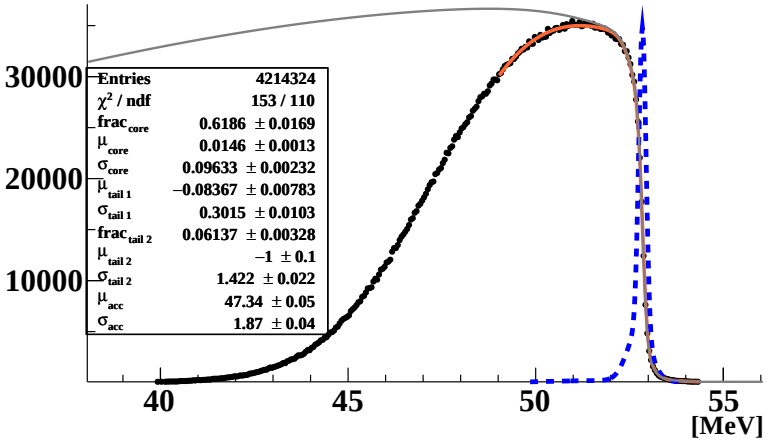

Figure 6.3: Fit to the Michel spectrum of positrons collected at 5×10^7 μ^+/s beam intensity in 2022. Data points are in black; the theoretical spectrum (with radiative corrections to NLO) is in gray; the resolution function (sum of three gaussian distributions) is in blue; the fitted function of Equation 3.5 is in orange.

6.2 Positron's reconstruction performances

After detector calibration is terminated and reconstruction parameters are optimized on data, we can proceed towards the measurement of the resolution functions of the kinematic variables and the correlations between them, used to build the PDFs for the analysis. In this section we describe in detail the spectrometer performances and the investigation of the correlations, while in the following Sections we will summarize the resolutions of the other detectors.

6.2.1 Momentum resolution

Table 6.1: Core positron's momentum resolution measured on the full dataset at different beam intensities.

	Beam intensity [$\times 10^7$ μ^+/s]						
	2021				**2022**		
	2	3	4	5	3	4	5
σ_{p_e} [keV]	85	89	94	97	89	95	95

The positron momentum resolution is measured on data with a fit to the Michel spectrum (Chapter 3, Section 3.3). The average core resolution for different beam intensities is reported in Table 6.1. For reference, the fit to data collected at 5×10^7 μ^+/s beam intensity is shown in FIgure 6.3.

From the best fit parameters of the resolution function (Equation 3.5), which is a sum of three gaussian shapes, the positron momentum PDF is determined:

- the accidental background E_e PDF is parameterized as the full Michel spectrum fit function;
- the RMD E_e PDF is built convolving the full resolution function with the theoretical shape of the momentum spectrum from the radiative decay;
- instead, the signal E_e PDF is parameterized using the two main main gaussian shapes in the resolution function fitting the Michel spectrum. The third component, the long tail, is dropped since this term accounts for events with a poor angular resolution, which are outside the $|\phi_{e\gamma}| <$ 40 mrad requirement. The two gaussian terms are re-normalized to integrate to one, with an increase of the core component of $5 - 10\%$ with respect to the background PDF.

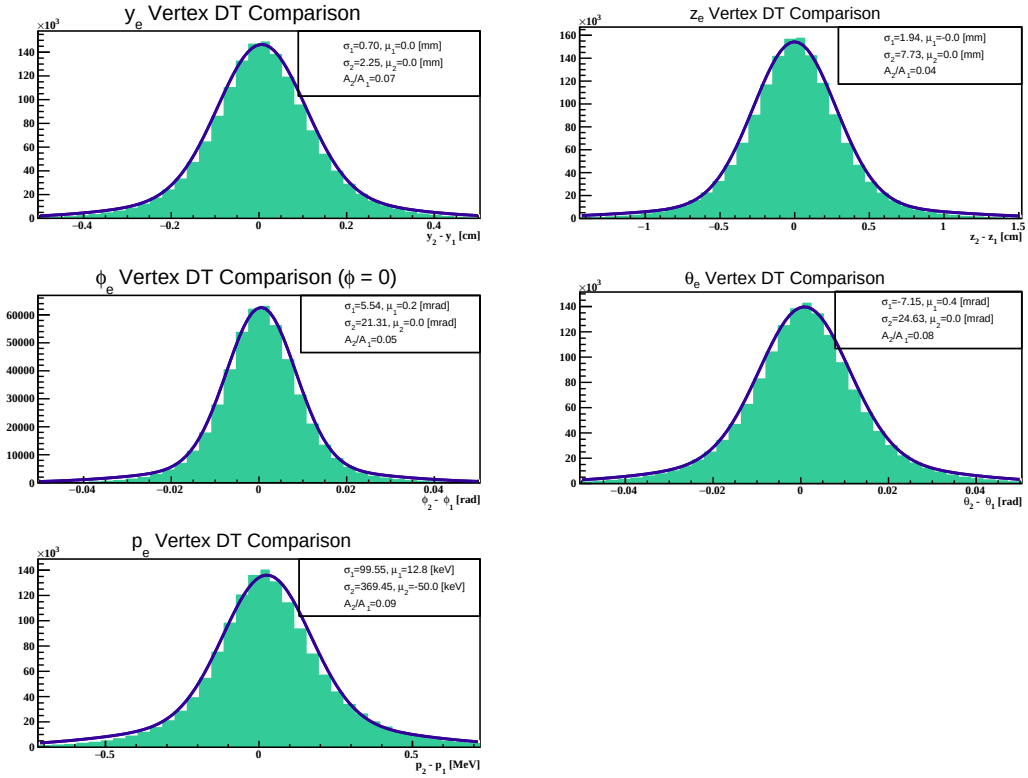

Figure 6.4: Histograms of double turn residuals. Dataset: 2022 data collected at 3×10^7 μ^+/s.

6.2.2 Results of double turn analysis

The double turn method has been explained in Chapter 3, Section 3.3.2. With this method, we can extract the resolution functions for signal like events of the variables:

- y_e and z_e, the reconstructed position at the target. x_e is fixed with good precision by the target shape and therefore it's not a free parameter;
- the angles θ_e and ϕ_e to describe the direction of the positron at the exit from the target. The uncertainty on ϕ_e has a minimum at $\phi_e = 0$ (positron exiting in direction opposite to the LXe detector), both because this is the condition in which most wires are hit along the trajectory and because of purely geometrical effects described in [112]. Therefore, we usually evaluate the ϕ_e resolution for tracks with $\phi_e = 0$, and correct for the $\sigma_{\phi_e} - \phi_e$ correlation afterwards (see below);
- the momentum p_e. The actual momentum resolution is determined by the Michel fit, with this method offering a consistency check.

The fit function of Equation 3.6 has four free parameters: the resolution of the first gaussian, the most abundant in proportion, σ_{core}; its mean μ_{core}; the resolution of the second gaussian, σ_{tail}; the relative fraction between the size A of the tail and core gaussians, $f \equiv \frac{A_{tail}}{A_{core}}$. The mean of the tail gaussian is fixed to zero to stabilize the fit procedure. Only in the case of the fit to the momentum distribution μ_{tail} is set as a free parameter.

The fitted histograms for the case of 2022 dataset at 3×10^7 μ^+/s is shown for reference in Figure 6.4.

The results of the double turn analysis for the full 2021+'22 dataset, split in years and beam intensities, is summarized in Table 6.2. We note explicitly that:

- at fixed beam intensity, the resolutions measured on data collected in 2021 and 2022 are well compatible within error (the error on the best fit parameter for σ_{core} is $\approx 1\%$);

Table 6.2: Best fit parameters for the two gaussian convolution function for the '21+'22 analysis. ϕ_e refers to a selection of data around $\phi_e = 0$.

Fit parameter	Variable	Beam intensity [$\times 10^7$ μ^+/s]						
		2021				**2022**		
		2	3	4	5	3	4	5
σ_{core}	y_e [mm]	0.70	0.69	0.74	0.74	0.69	0.73	0.74
	z_e [mm]	1.95	2.01	2.08	2.16	1.94	2.08	2.12
	ϕ_e [mrad]	5.29	5.86	5.82	6.22	5.09	5.38	5.48
	θ_e [mrad]	7.15	7.24	7.50	7.46	7.15	7.42	7.63
	p_e [keV]	98	102	105	111	99	104	108
σ_{tail}	y_e [mm]	2.32	2.10	2.20	2.17	2.25	2.16	2.12
	z_e [mm] 7.54	7.93	7.93	8.02	7.92	7.41	7.31	7.31
	ϕ_e [mrad]	18.47	22.60	21.75	22.77	19.66	20.37	20.53
	θ_e [mrad]	23.69	23.72	25.27	25.34	24.40	23.98	25.16
	p_e [keV]	373	372	370	390	362	367	378
μ_{core}	y_e [mm]	0.10	0.08	0.09	0.08	0.00	0.00	0.00
	z_e [mm]	-0.18	-0.16	-0.17	-0.16	0.00	0.00	0.00
	ϕ_e [mrad]	-0.25	-0.14	-0.24	-0.23	0.00	0.00	0.10
	θ_e [mrad]	0.48	0.51	0.54	0.30	0.40	0.40	0.40
	p_e [keV]	12.88	13.78	13.06	13.09	13.3	12.9	12.4
f_{tail}	y_e [mm]	0.06	0.10	0.08	0.10	0.07	0.09	0.10
	z_e [mm]	0.04	0.04	0.05	0.06	0.04	0.05	0.06
	ϕ_e [mrad]	0.06	0.04	0.05	0.05	0.09	0.09	0.09
	θ_e [mrad]	0.07	0.09	0.08	0.10	0.07	0.09	0.08
	p_e [keV]	0.08	0.09	0.10	0.10	0.08	0.10	0.10

- resolutions worsen with higher beam intensities, but the difference is not drastic: all resolutions differ by less than 10%;
- the bias of the distribution (μ_{core}) is almost null, especially for 2022 data. This is a strong evidence of the correctness of the alignment procedures on the CDCH, the target and the magnetic field.

The resolution σ_{core} obtained from the double turn analysis has to be corrected with inputs from Monte Carlo simulations to get the right estimate of the kinematics resolution for signal like events, since candidate $\mu \to e\gamma$ events have longer tracks with more hits and slightly different topology with respect to the background positrons used for this study.

This procedure is not necessary for the momentum resolution estimate from the Michel fit procedure since we are fitting the resolution function at the edge of the spectrum, where positrons have a momentum very close to that of a signal positron.

Calling $\sigma_{q,\,DT}$ the core resolution of the variable q obtained through the double turn method, we can compute $\sigma_{q,\,signal}$ using the formula:

$$\sigma^{data}_{q,\,signal} = \sigma^{data}_{q,\,DT} \times \frac{\sigma^{MC}_{q,\,signal}}{\sigma^{MC}_{q,\,DT}} \tag{6.7}$$

where $\sigma_{MC,\,signal}$ is the width of the gaussian distribution of $q_{rec} - q_{true}$ evaluated on MC samples of signal only events (Figure 6.5), while $\sigma_{MC,\,DT}$ is the resolution from the double turn analysis performed on MC simulations of Michel positrons only. For every nominal beam intensity, a different simulation is run to take into account the pile-up effects.

The resolutions of all kinematic variables are listed in Table 6.3, where they are compared with the resolutions quoted for the analysis of the 2021 dataset. All variables have a resolution $\approx$ 10% better

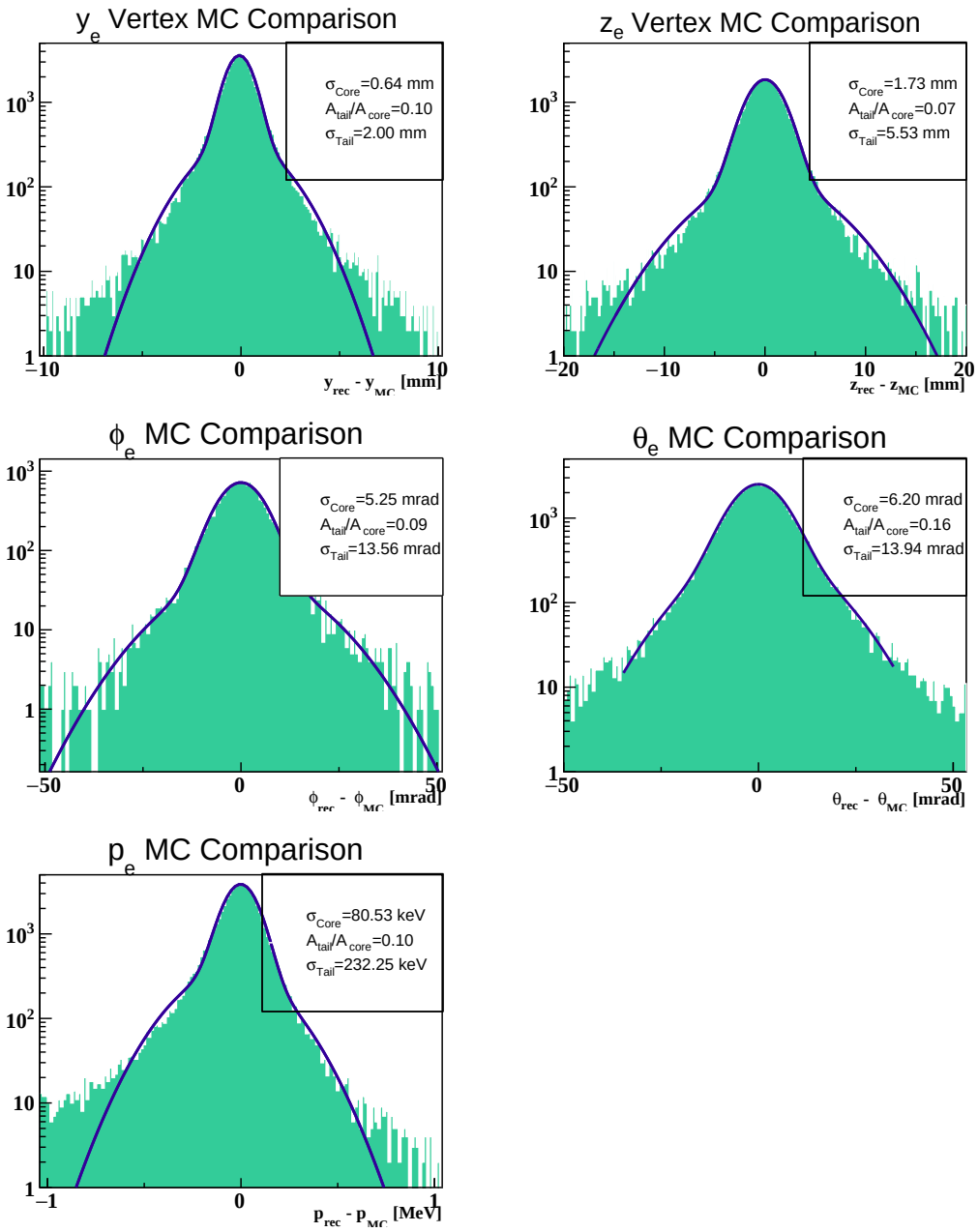

Figure 6.5: Double gaussian fit to the distribution of $q_{e,\,rec} - q_{e,\,MC}$ on MC simulations of signal events at 3×10^7 μ^+/s beam intensity.

Table 6.3: Summary of positron's kinematics resolutions for the 2021 + '22 analysis.

	Variable	2×10^7	3×10^7	4×10^7	5×10^7	**Average**	Analysis 2021 [8]
2021	y [mm]	0.64	0.60	0.67	0.67	0.65	0.83
	z [mm]	1.76	1.80	1.89	1.97	1.85	2.00
	ϕ ($\phi = 0$) [mrad]	4.83	5.28	5.12	5.43	5.18	5.75
	θ [mrad]	6.17	6.27	6.23	6.30	6.30	7.20
	p [keV]	76.11	81.26	87.83	90.08	83.51	98.50
2022	y [mm]	-	0.61	0.67	0.67	0.65	-
	z [mm]	-	1.76	1.89	1.93	1.86	-
	ϕ ($\phi = 0$) [mrad]	-	5.22	5.34	5.43	5.33	-
	θ [mrad]	-	6.20	6.16	6.50	6.29	-
	p [keV]	-	78.60	87.60	87.35	84.52	-

than that quoted for the previous analysis, thanks to the upgrade in the reconstruction software and more refined calibration procedures, which benefited from all the work done already prior to the 2021 result.

Distribution of pulls The above resolutions are used to build the constant PDFs likelihood. The per-event positron PDFs uses pull parameters of the variables $s_q \equiv \frac{q^{rec} - q^{true}}{\sigma_q}$, where σ_q is the error on the variable q estimated by the Kalman filter, which replaces the average resolution used in the constant PFDs method. In the double turn analysis, the pull parameter of a variable is calculated as:

$$s_q \equiv \frac{q_2 - q_1}{\sigma_{1\times2}}, \qquad \text{where } \sigma_{1\times2} \equiv \sqrt{\sigma_1^2 + \sigma_2^2} \tag{6.8}$$

where $\sigma_{1(2)}$ is the uncertainty (from the Kalman filter covariance matrix) for turn 1 (or 2).

On Monte Carlo instead, we can compute the pull of a variable also as:

$$\frac{q_{rec} - q_{MC}}{\sigma_{rec}} \tag{6.9}$$

where σ_{rec} is the fitting error. As already discussed, double turn parameters extracted from data are corrected with the parameters extracted from the double turn analysis on MC Michel positrons samples and from the $rec - MC$ distributions on MC signal events.

For the sake of simplicity, the plots illustrating the double turn and MC analysis on the pulls distributions, as well as all parameters used in the final analysis, are described in Appendix E. We preferred to show the detector's resolutions as they give a better understanding of its performances. The same has been done also for the study of correlations.

6.2.3 Correlations

The physical assumption that a signal positron must originate from inside the thin MEG II target causes many kinematic variables to be correlated with the (y_e, z_e, ϕ_e, θ_e) variables. For example, a mismeasurement of the positron energy δE_e may move the positron origin on the target and change its direction of flight. Correlations between variables, if not taken into account, introduce biases in the probability density functions for the final analysis and spoil resolutions. Therefore, they have to be carefully studied on data and simulations, and need to be implemented into the final analysis. All correlations were already studied in MEG for the first physics analysis and the same correlations are observed also in MEG II. A complete description is given in two Technical Reports internal to the MEG Collaboration [112, 113].

In the double turn analysis, the following correlations can be observed:

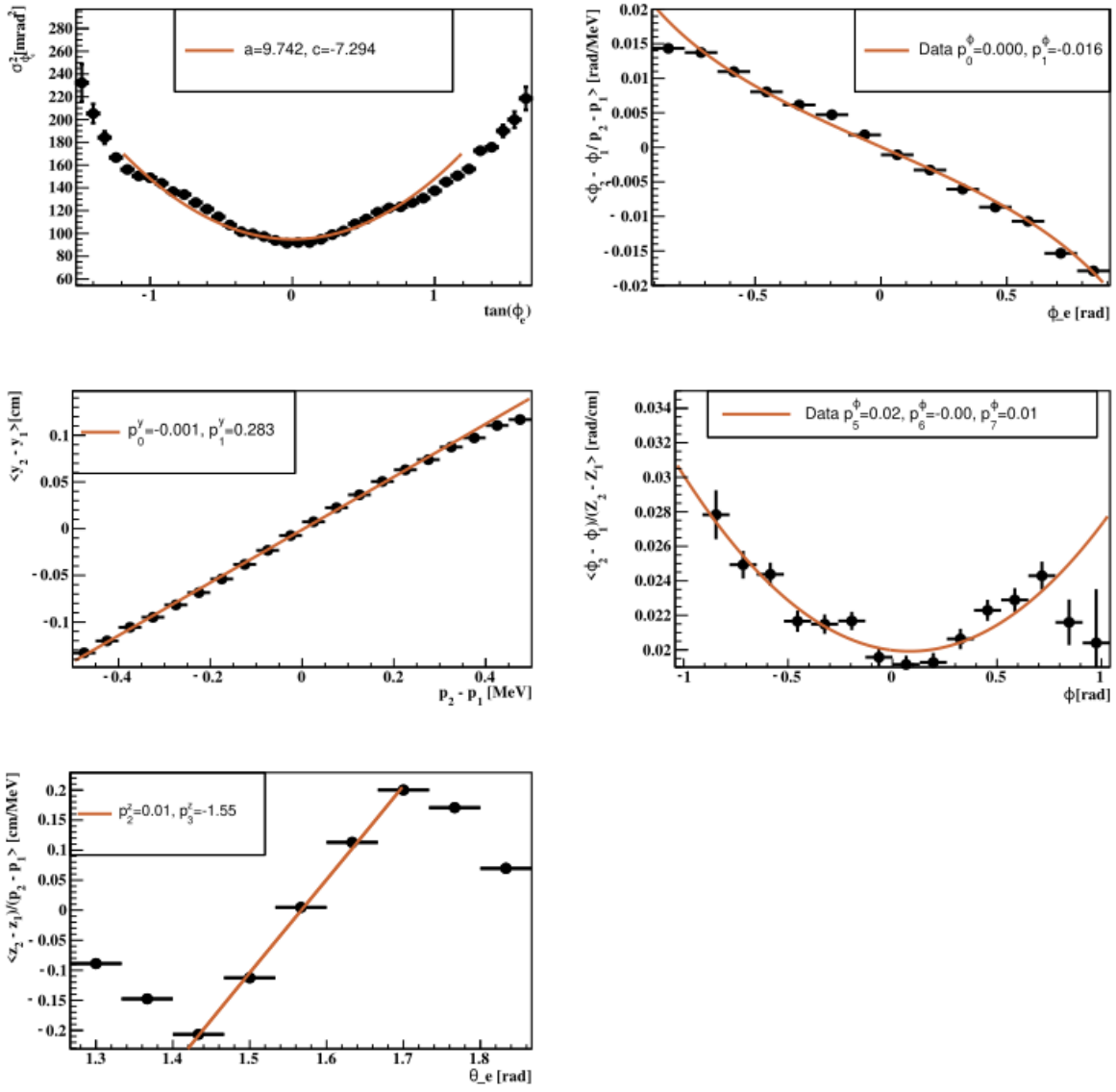

Figure 6.6: Correlations measured on 3×10^7 μ^+/s data from the double turn analysis.

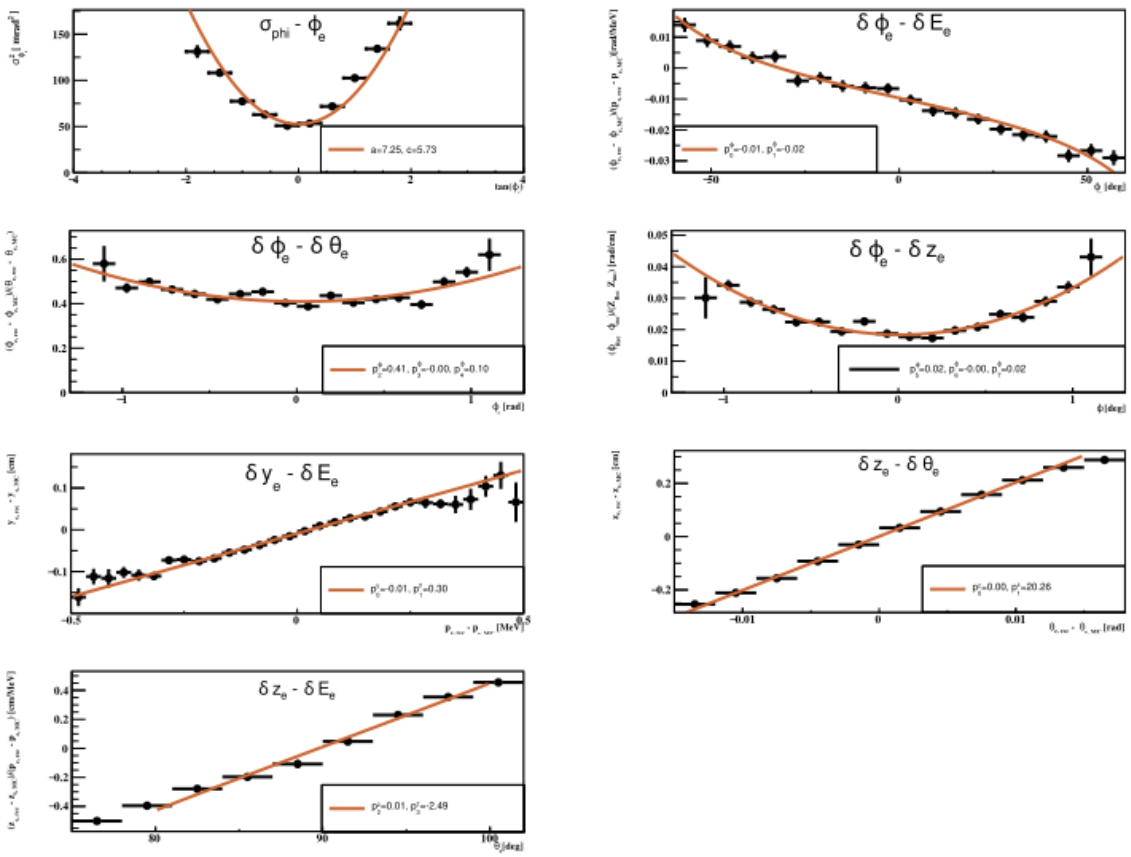

Figure 6.7: Correlations measured on MC simulations of signal positrons at 3×10^7 μ^+/s.

- $\delta\phi_e = \left[p_0^\phi + p_1^\phi \cdot \tan\phi_e\right] \cdot \delta E_e$
- $\delta y_e = p_0^y + p_1^y \cdot \delta E_e$
- $\delta z_e = \left[p_2^z + p_3^z \cdot \cot\theta_e\right] \cdot \delta E_e$
- $\delta\phi_e = \left[p_5^\phi + p_6^\phi \cdot \phi_e + p_7^\phi \cdot \phi_e^2\right] \cdot \delta z_e$

In the above formulas, δq is the bias in the double turn $q_2 - q_1$ distribution, and the parameters p^q are the correlation coefficients.

In addition to these correlations, the already mentioned quadratic dependence $\sigma_{\phi_e} = \sigma_\phi(\phi = 0) + c \cdot \phi_e^2$ is observed in the double turn analysis. In Figure 6.6 we illustrate these correlations as measured in 2022 3×10^7 μ^+/s data.

Not all correlations can be observed with double turn studies since these involve Michel positrons. Other correlations emerge by looking at Monte Carlo distributions of the difference between reconstructed and true values for signal positrons. As in the case of resolutions, correlations measured with data are corrected with the measurements obtained by Monte Carlo simulations to obtain the final correlation parameter for signal positrons. The formula to be used is:

$$p_{q,\ signal} = p_{q,\ DT}^{data} \times \frac{p_{q,\ signal}^{MC}}{p_{q,DT}^{MC}} \tag{6.10}$$

The correlations that can be observed only on MC are:

- $\delta z_e = p_0^z + p_1^z \cdot \delta\theta_e$

Table 6.4: Correlation coefficients of positron kinematic variables for the '21+'22 analysis. The definition of the parameters is given in the text.

Parameter	Beam intensity [$\times 10^7$ μ^+/s]						
	2021				**2022**		
	2	3	4	5	3	4	5
c [mrad]	5.74	5.72	5.25	5.73	5.81	5.60	
p_0^ϕ	compatible with zero						
p_1^ϕ	$-2 \cdot 10^{-2}$	$-2 \cdot 10^{-2}$	$-2 \cdot 10^{-2}$	$-1 \cdot 10^{-1}$	$-2 \cdot 10^{-2}$	$-2 \cdot 10^{-2}$	$-1 \cdot 10^{-2}$
p_2^ϕ	$3 \cdot 10^{-1}$	$4 \cdot 10^{-1}$	$5 \cdot 10^{-1}$	$5 \cdot 10^{-1}$	$4 \cdot 10^{-1}$	$5 \cdot 10^{-1}$	$4 \cdot 10^{-1}$
p_3^ϕ	compatible with 0						
p_4^ϕ	$1 \cdot 10^{-1}$	$2 \cdot 10^{-1}$	$4 \cdot 10^{-1}$	zero	$2 \cdot 10^{-1}$	zero	$4 \cdot 10^{-1}$
p_5^ϕ	compatible with 0						
p_6^ϕ	$-3 \cdot 10^{-2}$	$4 \cdot 10^{-3}$	$-2 \cdot 10^{-2}$	$-1 \cdot 10^{-3}$	$1 \cdot 10^{-2}$	$-9 \cdot 10^{-3}$	$7 \cdot 10^{-3}$
p_7^ϕ	compatible with 0						
p_0^y	compatible with 0						
p_1^y	0.33	0.32	0.30	0.31	0.30	0.30	0.29
p_0^z	compatible with 0						
p_1^z	20.0	20.3	20.5	20.6	20.2	20.5	20.6
p_2^z	compatible with 0						
p_3^z	-1.95	-1.71	-1.71	-1.58	-1.37	-1.53	- 1.54

Table 6.5: The positron efficiency for the 2021+'22 analysis.

	Beam intensity [$\times 10^7$ μ^+/s]			
	2	3	4	5
ϵ_{e^+}	$(70 \pm 4)\%$	$(67 \pm 4)\%$	$(64 \pm 4)\%$	$(60 \pm 4)\%$

- $\delta\phi_e = \left[p_2^\phi + p_3^\phi \cdot \phi_e + p_4^\phi \cdot \phi_e^2\right] \cdot \delta\theta_e$

The correlations observed with MC simulations of signal positrons at 3×10^7 μ^+/s are illustrated in Figure 6.7 .

In Table 6.4 all correlations parameter for the '21 + '22 analysis are summarized, already corrected with MC inputs. They are all very similar to those determined for the analysis of the '21 dataset.

6.2.4 Positron efficiency

The positron reconstruction efficiency (combination of pTC's and CDCH's efficiencies) for 2022 data is similar to the one obtained with 2021 data. The results, separated for beam intensity, are summarized in Table 6.5.

6.2.5 Timing performances

The positron time resolution depends on the variable n_{pTC}, the number of pTC tiles hit by the positron, according to the formula 2.3:

$$\sigma_{t_e}(n_{\mathrm{pTC}}) = \frac{\sigma t_e^{single}}{\sqrt{n_{\mathrm{pTC}}}} = \frac{\sigma t_e^{counter} \oplus \sigma t_e^{off} \oplus \sigma t_e^{elec}}{\sqrt{n_{\mathrm{pTC}}}}$$

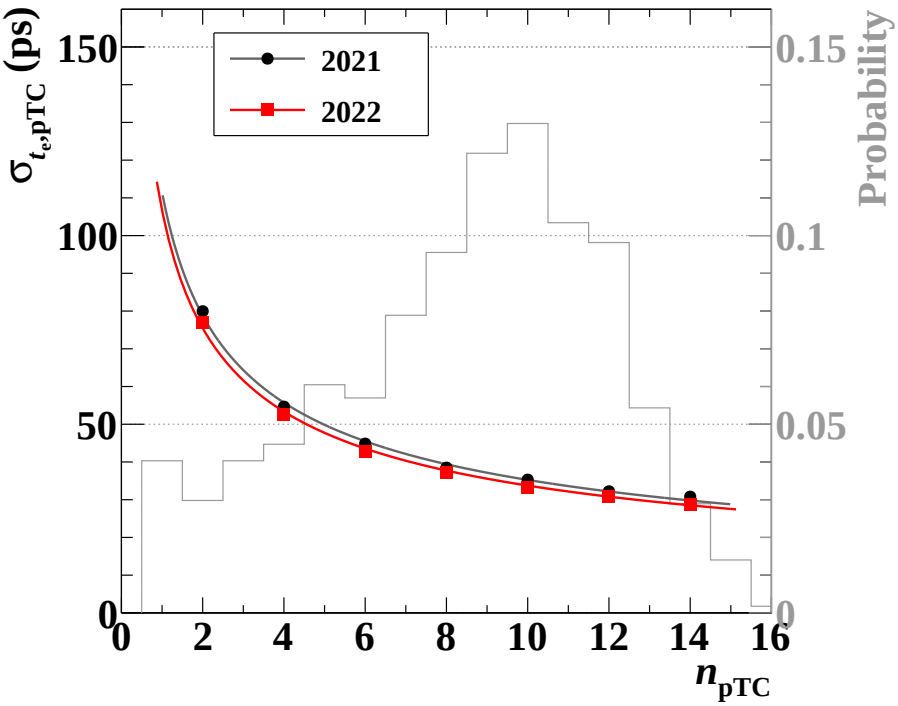

Figure 6.8: Positron time uncertainty as a function of n_{pTC} measured on 2021 (black) and 2022 (red) data. The distribution of n_{pTC} is shown in grey.

The measured trend of σ_{t_e} as a function of n_{pTC} is shown in Figure 6.8. The measurements are done with Michel positrons data, and results for both 2021 and 2022 are illustrated. In both years, the curves have a plateau for $n_{\mathrm{pTC}} \geq 16$: above this value there is no improvement in σ_{t_e}. The distribution $p(n_{\mathrm{pTC}})$ for signal positrons, is superimposed to the Figure. This distribution is obtained through MC simulations of signal-like events.

Since in average a signal positron strikes 9 different tiles, the average time uncertainty is $\langle \sigma_{t_e} \rangle \approx 40$ ps: 43 ps and 42 ps respectively in 2021 and 2022.

Chapter 7

Final results

Having previously introduced (Chapter 6, Section 6.1) the MEG II analysis technique, and described in detail the positron's PDFs, in the Sections 7.1.1, 7.1.2, 7.1.3, 7.1.4 we summarize the performances and PDFs of the other detectors, which crucial to build the full likelihood functions.

Section 7.2 illustrates the properties of the 2021-'22 dataset, in particular the accumulated statistics needed to convert the number of observed signal events N_{sig} into the branching ratio of $\mu^+ \to e^+\gamma$.

Section 7.3 illustrates the experimental sensitivity obtainable for the measurement of BR($\mu^+ \to e^+\gamma$) with the 2021 + '22 dataset. The effect of systematic uncertainties is also reported there.

The last Section 7.4 is dedicated to illustrating the results after unblinding of the data.

7.1 Detectors performances and PDFs

In this Section we revise the performances of the other MEG II detectors not covered in Chapter 6. We also describe the remaining one-dimensional PDFs needed to write the final likelihood function for the analysis.

7.1.1 Photon reconstruction performances & E_γ PDFs

All details about the Photon Analysis can be found in [55, 101].

Resolutions The resolutions of photon's kinematic variables are summarized in the following list:

- the achieved precision on the photon conversion point coordinates are: $\sigma_{u,v} = 2.5/4.0$ mm for photons converting at depths smaller/larger than 2 cm, and $\sigma_w = 5.0$ mm. This marks an improvement of a factor 2 and 1.2 respectively with respect to the MEG detector. The $\sigma_{u,v}$ resolutions are estimated imaging a lead collimator positioned in front of the LXe detector with 17.6 MeV photons [43]. Instead, σ_w is derived from MC simulations;

- the time resolution, driven by the PMTs precision, is:

$$\sigma_{t_\gamma} = (65 \pm 5) \text{ ps for } E_\gamma = 55 \text{ MeV} \tag{7.1}$$

  This is measured by using $\pi^0 \to \gamma\gamma$ events. It is derived from the width of the time difference between the two photons, one detected in the LXe detector and one in the pre-shower counter (made of plastic scintillators coupled with SiPMs) in front of the BGO calorimeter (see Chapter 2, Section 2.2.4).

  The resolution on t_γ depends on the number of detected photons, which varies with E_γ. This correlation is measured with CEX data and applied in the per-event analysis;

- the measured energy resolution on signal photons is also similar to that measured in MEG: for the 2021 and 2022 analysis $\sigma_{E_\gamma}/E_\gamma = 2.0\%/1.8\%$ (2021) and $2.4\%/1.9\%$ (2022) depending on the conversion depth. See Figure 7.1.

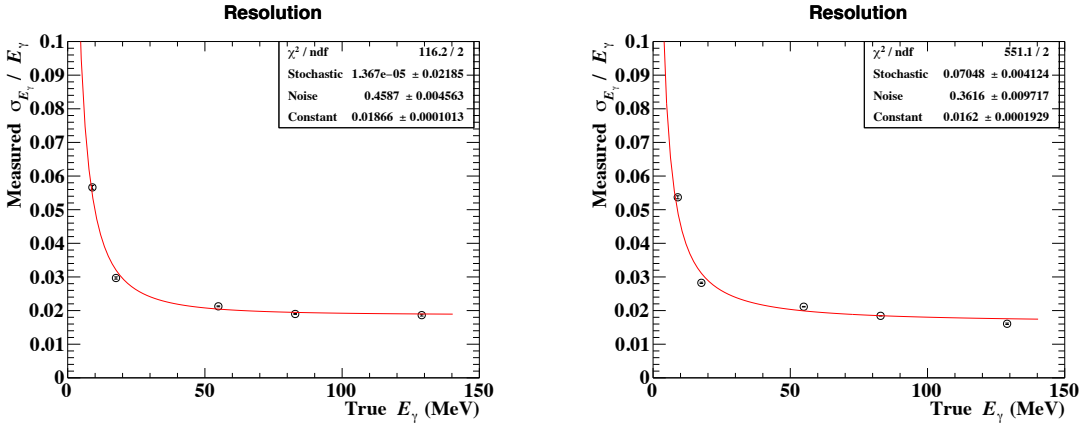

(a) Year 2021. (b) Year 2022.

Figure 7.1: Energy resolution of the LXe detector as a function of the photon measured energy.

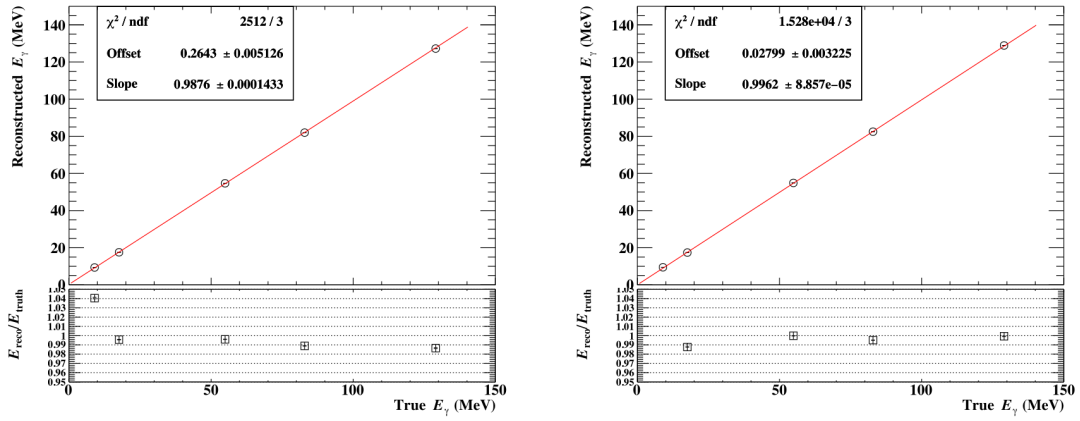

(a) 2021. (b) 2022.

Figure 7.2: Linearity of the reconstructed energy.

Linearity of the LXe detector response The energy scale S_E of Equation 2.6 for 52.83 MeV photons is extrapolated from the fit to the 55 MeV peak from the CEX reaction (Chapter 2, Section 2.2.4), simply multiplying the energy scale best-fit parameter by $\frac{52.83}{55}$. With the LXe detector fully calibrated, it is possible to check the linearity of the response. This is evaluated by fitting to a straight line the reconstructed energies E_{rec} of the calibration lines described in Chapter 2, Section 2.2.4, ranging from 9 MeV to 129 MeV with their true energy E_{true}. The best fit lines for 2021 and 2022 are shown in Figure 7.2.

The linearity is within 1.5% in the range 17.6-129 MeV, and since the energy scale for 52.8 MeV signal photons is derived from that of 55 MeV photons, non-linearity effects are completely negligible in the analysis.

Photon reconstruction efficiency Using The signal-photon efficiency is measured to be: $\epsilon_\gamma = (62 \pm 3)\%$.

E_γ PDFs The signal E_γ PDF is modeled as a sum of two asymmetric gaussian functions with an exponential tail, which parametrizes the detector response at 52.8 MeV:

$$f(x) = \begin{cases} C \cdot \exp\left\{\left[-\frac{(x-\mu)}{2\sigma^2}\right]\right\} & \text{if } x > \mu + \tau \\ C \cdot \exp\left\{\left[\tau \cdot \frac{(\tau/2 - x + \mu)}{\sigma^2}\right]\right\} & \text{if } x \leq \mu + \tau \end{cases} \tag{7.2}$$

where C is the normalisation parameter, the energy peak position with respect to 52.83 MeV is μ, and σ is the energy resolution, determined with data. The parameter τ characterizes the energy leak of the LXe detector.

The RMD E_γ PDF is obtained by convoluting the detector response function described above with the theoretical spectrum.

The E_γ PDF for accidental background events is obtained from a fit to the data spectrum in the time side-bands, with the shape of the fit function determined from MC simulations of background events including high-energy photons originating from positrons' annihilation-in-flight, RMD, bremsstrahlung, cosmic rays. The detector response derived from the data are convoluted with the simulated spectrum. The accidental background spectrum is shown in Figure 7.3.

The correlation terms in the E_γ PDFs with the photon conversion point's coordinates (v, w) are obtained from data, studying the detector response in different (v, w) segments.

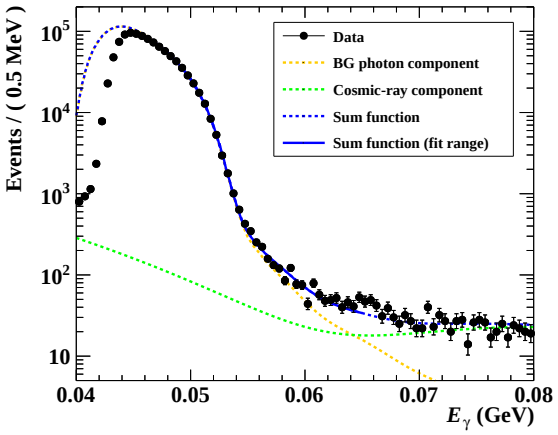

Figure 7.3: Accidental background spectrum fitting for the full 2022 side-band data (black markers). The photon component is in yellow, the cosmic rays's one is highlighted in green; the sum function is in blue.

7.1.2 Photon - Positron combined performances

Angular performances & $\phi_{e\gamma}$, $\theta_{e\gamma}$ PDFs The $(\phi_{e\gamma}, \theta_{e\gamma})$ emission angles between the positron and the photon are derived from the spectrometer measurements of (ϕ_e, θ_e) at the target, which defines the positron flight direction. The photon emission angle is measured in the MEG II reference frame connecting with a straight line the first interaction point in the LXe detector $(u_\gamma, v_\gamma, w_\gamma)$ with the positron's origin coordinates at the target (x_e, y_e, z_e). In Figure 7.4 we plot the distribution of the angular resolution.

The $\theta_{e\gamma}, \phi_{e\gamma}$ response functions are analytically described, starting from the single variable PDFs, as a sum of two gaussians. As visible in the bumpy distributions of the angular resolutions, correlation effects with many other variables $(\phi_e, \sigma_{\phi_e}, w_\gamma, E_e)$ have to be taken into account: this is done with the Double Turn analysis method highlighted in Chapter 6.

The signal angle PDFs are parameterized as the response function, while the RMD function is obtained convoluting it with the theoretical angular distributions. The accidental background angular PDFs are instead built by fitting the observed angular distribution in the time side-bands to a polynomial function.

Time performances & $t_{e\gamma}$ PDF The $t_{e\gamma}$ resolution, $\sigma_{t_{e\gamma}}$, is simply the sum of the spectrometer's and LXe detector's resolutions:

$$\sigma_{t_{e\gamma}} = \sqrt{\sigma_{t_e}^2 + \sigma_{t_\gamma}^2} \equiv \frac{\sigma_{t_e}^{single}}{\sqrt{n_{\text{pTC}}}} \oplus \sigma_{t_\gamma} \tag{7.3}$$

according to Equation 2.3. The σ_{t_γ} resolution depends on E_γ, since the more scintillation light is observed by the photosensors, the more precise the estimate of the time is.

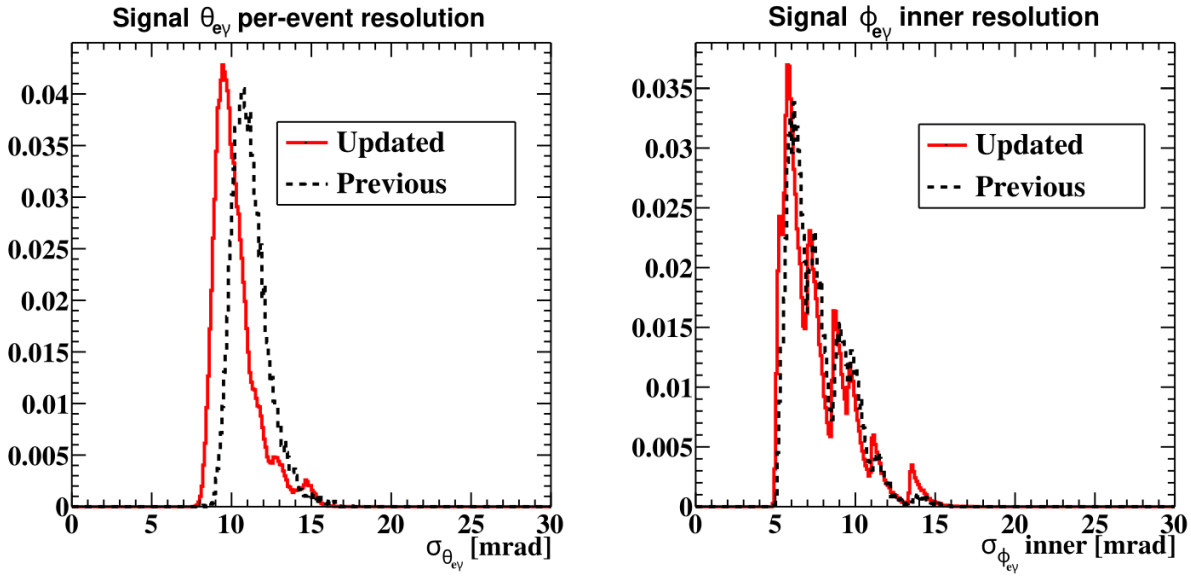

Figure 7.4: Distribution of the signal angular resolution event-by-event. In red, with the updated Positron Analysis illustrated in Chapter 4, Section 4.6; in black for the old analysis [8]. The bumps in the distributions are due to the strong dependence of the LXe detector angle resolution on the photon conversion point, as well as the $\sigma_{\phi_e} - \phi_e$ correlation discussed in Chapter 6, Section 6.2.

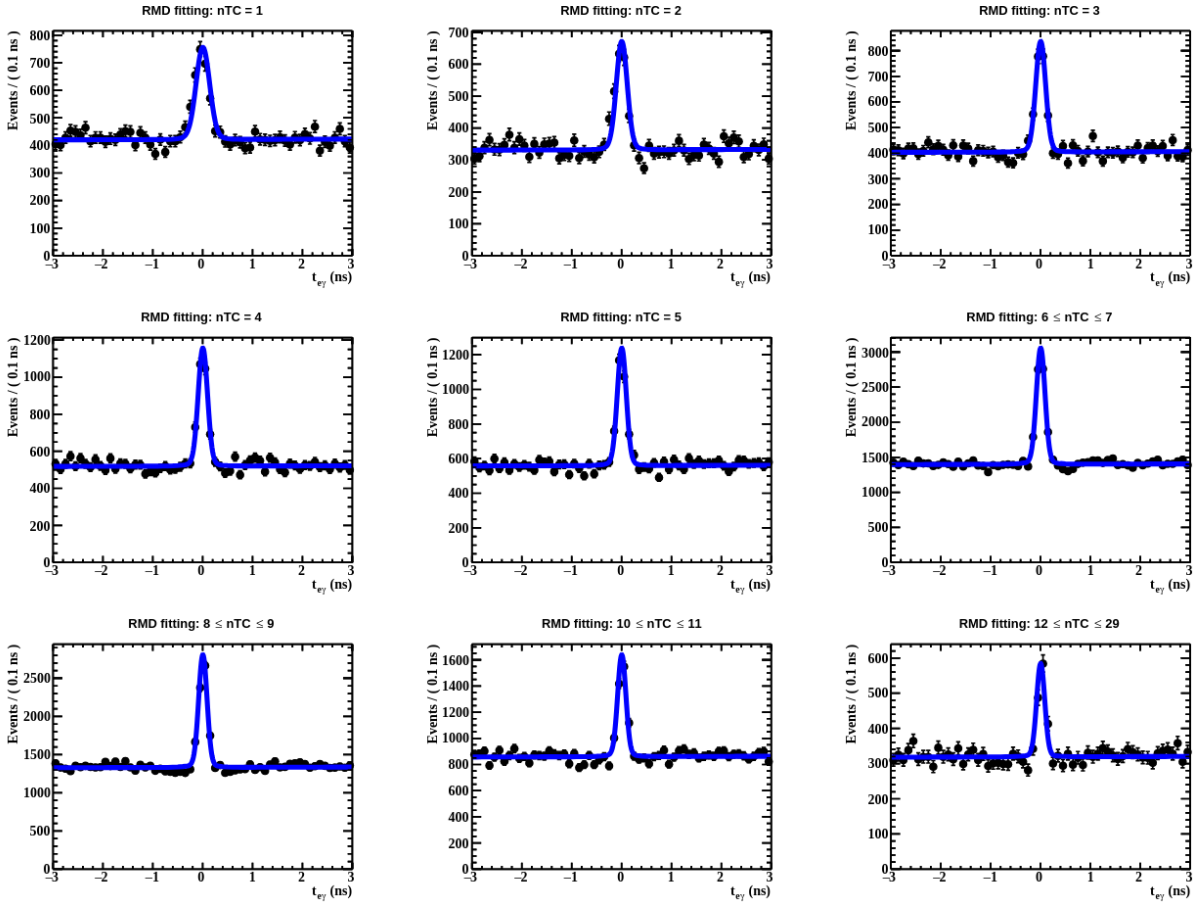

Figure 7.5: Fit to the $t_{e\gamma}$ distribution in the energy side-band for different values of n_{pTC}, the number of pTC tiles hit by the positron.

Because of the n_{pTC} dependence of the resolution, the $t_{e\gamma}$ PDF has two components:

$$p(t_{e\gamma}, n_{\text{pTC}}|E_\gamma, E_e) = p_a(t_{e\gamma}|n_{\text{pTC}}, E_\gamma, E_e) \times p_b(n_{\text{pTC}}|E_e) \tag{7.4}$$

where the first term parametrizes the response function of the detector at fixed n_{pTC}, while the second term describes the n_{pTC} distribution in a class of events. Signal and background events, having different ranges for E_e, which imply different positrons trajectories, have different distributions of $p_b(n_{\text{pTC}}|E_e)$[i]. The p_b distribution absorbs most of the dependence of p_a on E_e: a little correlation with E_e remains however in p_a since errors in E_e cause errors in the time-of-flight calculation, which results in a small $t_{e\gamma}$ bias of $\approx$ 15 ps.

The term $p_a(t_{e\gamma}|n_{\text{pTC}}, E_\gamma, E_e)$ is the same for signal and RMD events[ii] and is determined through a fit to the RMD peaks in the energy side-bands region, slicing data at fixed n_{pTC}, as shown in Figure 7.5. The functional form of the accidental background PDF is determined through a polynomial fit to data in the time side-band. The distribution of accidental background events is flat, as visible also in Figure 7.5 in the range 1 ns $< |t_{e\gamma}| <$ 3 ns.

The term $p_b(n_{\text{pTC}}|E_e)$ (see also Chapter 6, Section 6.2.5) is evaluated with MC simulations for the signal PDF, with fits to time-sidebands data for both the accidental and RMD background PDFs.

7.1.3 RDC performances

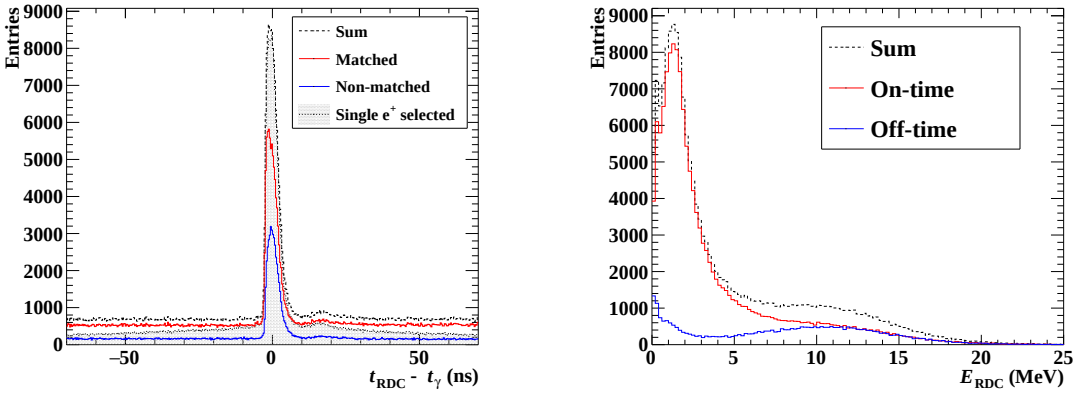

(a) Time difference $t_{RDC} - t_\gamma$ distribution.

(b) E_{RDC} distribution.

Figure 7.6: RDC variables distribution measured on 3×10^7 μ^+/s data. In red for matched events, in blue for non-matched events. From [55].

By detecting low-energy positrons in time with a signal in the LXe detector, the RDC helps tagging background events. The measured time resolution is:

$$\sigma_{t_{RDC}} = 90 \text{ ps} \tag{7.5}$$

while the energy resolution is:

$$\frac{\sigma_{E_{RDC}}}{E_{RDC}} = (7.5 \pm 0.3)\% \quad @1 \text{ MeV} \tag{7.6}$$

The RMD tagging efficiency of the detector, namely the fraction of events with a high energetic photon ($E_\gamma > 48$ MeV) matched in time ($|t_{RDC} - t_\gamma| < 8$ ns) to a positron signal in the RDC, was improved from $\approx$17% (2021 analysis) to $\approx$23% for this analysis. Details of these studies are reported in [55]. In Figure 7.6 we show the distribution of $t_{RDC} - t_\gamma$ and E_{RDC} for matched and non-matched events.

[i] For the signal, there is no E_e dependence since signal positrons are monochromatic.

[ii] Except that the E_e dependence is removed from the signal PDF.

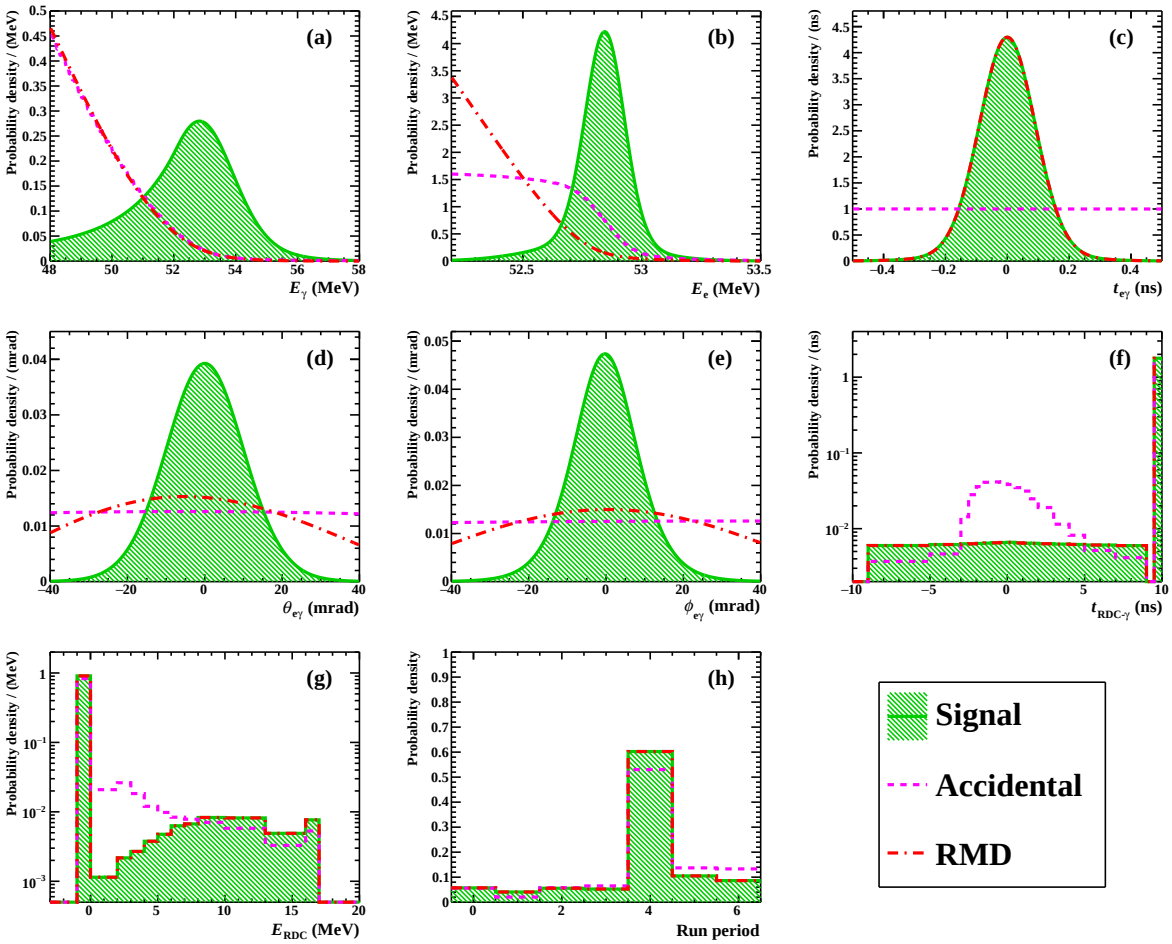

Figure 7.7: One-dimensional projection of the average signal (green), RMD (red) and accidental (magenta) PDFs: a) E_γ, b) E_e, c) $t_{e\gamma}$, d) $\theta_{e\gamma}$, e) $\phi_{e\gamma}$, f) $t_{RDC-\gamma}$, g) E_{RDC}, h) run periods. The run period statistical weights are categorized assigning an integer to each different period: in 2021, from 0 to 3, in 2022 from 4 to 6.

7.1.4 Summary of PDFs

From the detectors' resolutions discussed in the previous sections, the final PDFs described in Sections 6.1.1, 7.1.1, 7.1.2, 7.1.3 are built. In Figure 7.7 we show the shapes of the one-dimensional PDFs in Equations 6.3~6.5, grouped per observable.

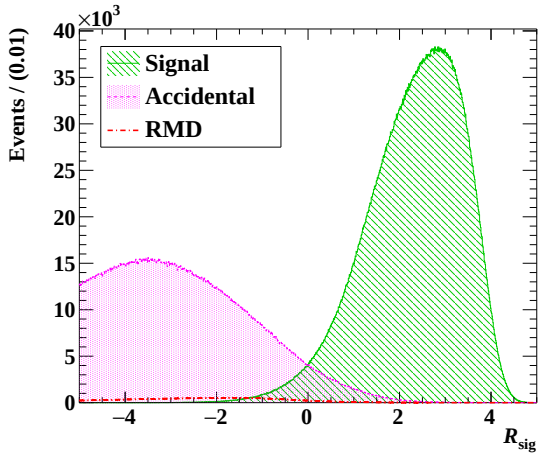

Figure 7.8: R_{sig} distribution for signal (green), RMD (red) and accidental (magenta) events.

The likeliness R_{sig} of an event to be a signal event compared to the background hypothesis is defined as:

$$R_{sig} = \log_{10}\left(\frac{\mathcal{S}(\vec{x}_1)}{f_{RMD}\mathcal{R}(\vec{x}_i) + f_{ACC}\mathcal{A}(\vec{x}_i)}\right) \quad (7.7)$$

where f_{RMD} and f_{ACC} are the fraction of RMD and accidental events expected in the data from the sideband fit.

The R_{sig} distribution of the data is used to cross-check at a single glance the result of the likelihood analysis.

7.2 Dataset for the '21+'22 analysis

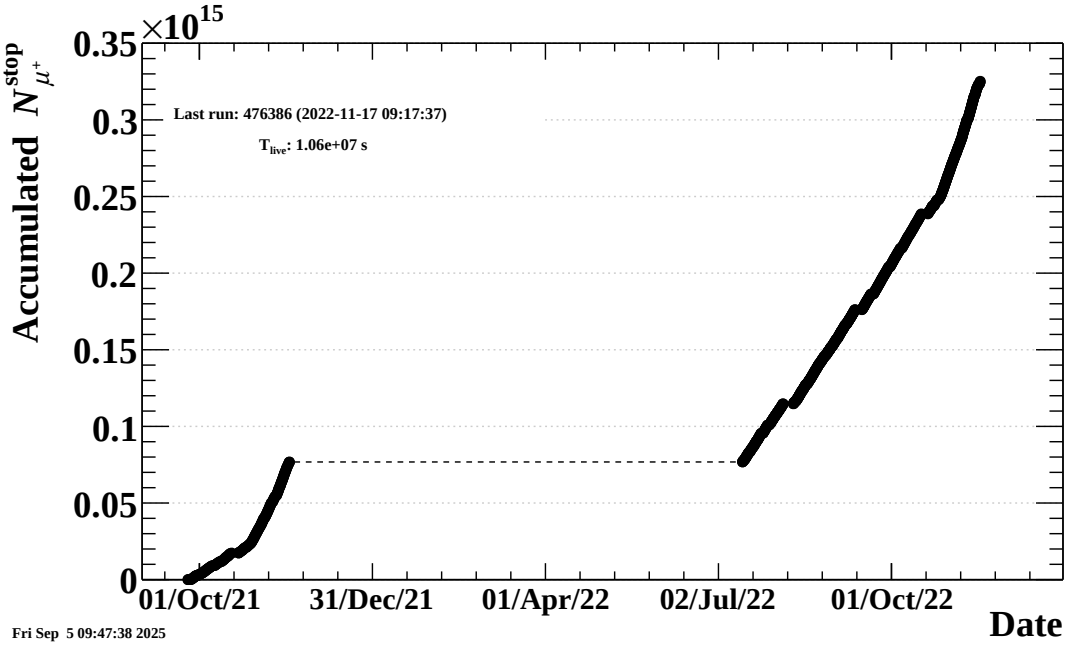

(a) Cumulated statistics.

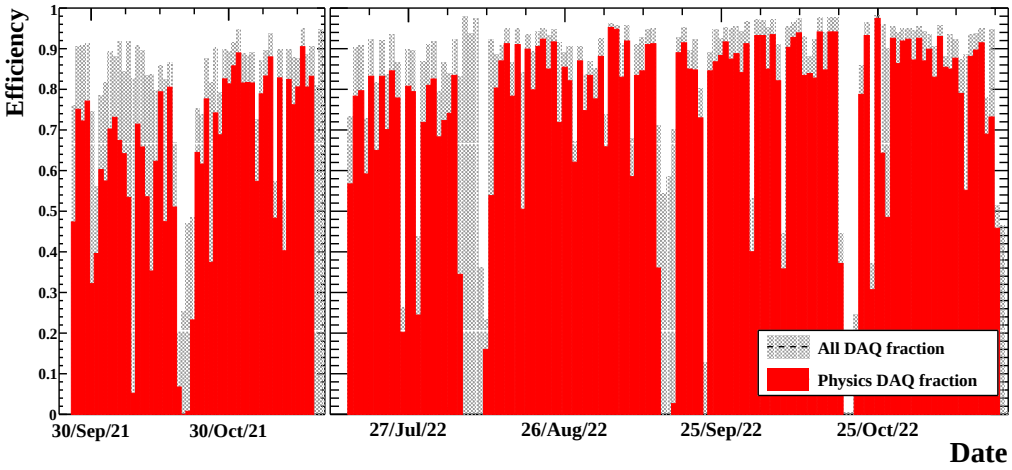

(b) DAQ efficiency as a function of time between 2021 (left subplot) and 2022 (right subplot). The different type of data acquired are highlighted: in red for physics run, in grey for calibrations.

Figure 7.9: Characteristics of the 2021+'22 dataset.

This analysis uses data collected between 2021 and 2022 (Figure 7.9 (a)). The 2022 dataset which is included for the first time in this analysis contains almost thrice the cumulated 2021 statistics. In this period, the beam intensity was varied between $(2-5)\times 10^7$ μ^+/s: in 2021 the intensity variation was motivated by the interest in investigating detector performances under different conditions to find the optimal one; in 2022, most of the dataset was collected with 3×10^7 μ^+/s beam intensity.

Most of the beam time allocated for the MEG II experiment is used for the physics run. The calibration procedures accounts for 20% of the total DAQ time in 2021 and 10% in 2022, with most of the time allocated for the CEX calibration of the LXe detector. The DAQ efficiency was in average 82% in 2021 and 96% in 2022, thanks to a significant upgrade of the DAQ server. See Figure 7.9 (b) for the detailed trend of DAQ time and efficiency.

Table 7.1: Parameters to estimate the normalisation factor N_μ for the '21+'22 analysis.

Parameter	**2021**	**2022**
$P^{e\nu\overline{\nu}}$	$2\times10^6 - 7\times10^6$	$3\times10^6 - 1.6\times10^7$
$\epsilon^{e\gamma}_{TRG}/\epsilon^{e\nu\overline{\nu}}_{TRG}$	≈ 0.80 depending on R_μ	0.88 - 0.90 depending on R_μ
$\epsilon^{e\gamma}_{e}/\epsilon^{e\nu\overline{\nu}}_{e}$	1.07	1.04
$\epsilon^{e\gamma}_{\gamma}$	0.62	0.63
$\epsilon^{e\gamma}_{sel}$	0.93	0.93

7.2.1 Normalisation

Since$\text{BR}(\mu^+ \to e^+\nu\overline{\nu}) \approx 1$, the normalisation factor N_μ (Chapter 6, Section 6.1) can be calculated with the following formula:

$$N_\mu = \frac{N^{e\nu\overline{\nu}}}{f^{e\nu\overline{\nu}}_{E_e}} \times P^{e\nu\overline{\nu}} \times \frac{\epsilon^{e\gamma}_{TRG}}{\epsilon^{e\nu\overline{\nu}}_{TRG}} \times \frac{\epsilon^{e\gamma}_{e}}{\epsilon^{e\nu\overline{\nu}}_{e}} \times \mathcal{A}^{e\gamma}_{\gamma} \times \epsilon^{e\gamma}_{\gamma} \times \epsilon^{e\gamma}_{sel} \tag{7.8}$$

where:

- $N^{e\nu\overline{\nu}}$ is the number of Michel positron detected with 50.0 MeV $< E_e <$ 56.0 MeV in a sample of Michel positrons-rich data collected in parallel to the physics data taking using a pre-scaled trigger based on pTC signals, with pre-scaling factor $P^{e\nu\overline{\nu}}$;
- $f^{e\nu\overline{\nu}}_{E_e} = 0.101$ is the fraction of the Michel spectrum falling in the above energy range;
- $\frac{\epsilon^{e\gamma}_{TRG}}{\epsilon^{e\nu\overline{\nu}}_{TRG}}$ is a correction factor for the different trigger efficiencies of Michel positrons events and $e^+\gamma$ pairs;
- $\frac{\epsilon^{e\gamma}_{e}}{\epsilon^{e\nu\overline{\nu}}_{e}}$ is a correction factor for the different positron reconstruction efficiencies of the two event categories;
- $\mathcal{A}^{e\gamma}_{\gamma} = 0.985 \pm 0.005$ is the geometrical acceptance for a signal photon given an accepted signal positron, computed with MC simulations;
- $\epsilon^{e\gamma}_{\gamma}$ is the photon detection efficiency for signal photons;
- $\epsilon^{e\gamma}_{sel}$ is the selection efficiency for $e^+ - \gamma$ pairs.

The values of the different terms in Equation 7.8 for the two data taking periods are reported in Table 7.1. The details of how each term is calculated is given in [8].

The normalisation factors for 2021 and 2022 are:

2021 $N^{2021}_\mu = (0.28 \pm 0.01)\times10^{13}$

2022 $N^{2022}_\mu = (1.05 \pm 0.05)\times10^{13}$

The error on N_μ mostly comes from the error on $\epsilon^{e\gamma}_{sel}$ and $\epsilon^{e\gamma}_{\gamma}$. The total normalisation factor for this analysis is:

$$N^{'21+'22}_\mu = (1.33 \pm 0.05)\times10^{13} \tag{7.9}$$

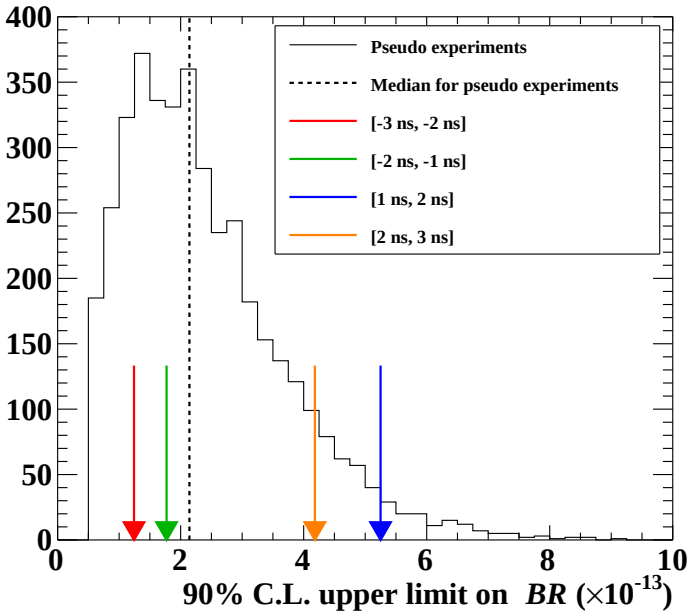

Figure 7.10: Distribution of the 90% C.L. upper limits on BR($\mu^+ \to e^+\gamma$) from a set of pseudo-experiments. The median of the distribution, which we call the experimental sensitivity, is shown as a dashed line. The colored arrows are the results of the analysis conducted in four different analysis region falling inside the time side-band (see the legend), and serve as a consistency check. All four results are compatible with the null hypothesis, as expected.

7.3 Sensitivity

The sensitivity of the experiment is evaluated as the median of the distribution of upper limits (90% C.L.) on the branching ratio, obtained from a set of pseudo-experiments generated under the null signal hypothesis (*toy MC*). The toy datasets are produced with an expected background yield consistent with that derived from the side-band studies:

N_{ACC} The number of accidental background events in the signal region is extrapolated from the count of events in the time sideband (1 ns $< |t_{e\gamma}| <$ 3 ns):

$$\langle N_{ACC} \rangle \pm \sigma_{ACC} = 364.0 \pm 9.5 \tag{7.10}$$

N_{RMD} The number of RMD events in the signal region is estimated by extrapolating the number of RMD events fitted in the energy side-band ($E_e > 49$ MeV; $\Theta_{e\gamma} > 176^\circ$; 46.5 MeV $< E_\gamma <$ 48 MeV) time distribution:

$$\langle N_{RMD} \rangle \pm \sigma_{RMD} = 10.1 \pm 1.7 \tag{7.11}$$

The kinematic variables for the simulated events are sampled according to the experimental PDFs.

The following uncertainties remain as a source of systematic error, and are included in the sensitivity's calculation:

- misalignment of the target and the LXe detector with respect to the CDCH;
- uncertainty in the normalisation;
- uncertainty in the E_γ and E_e energy scale;
- timing misalignment between the pTC and the LXe detector;

Systematic errors are taken into account either with the profile likelihood method, including a nuisance parameter in the likelihood function, or randomly fluctuating the PDFs according to the uncertainties of the parameters. The first method is more robust but is also more CPU-expensive; for this reason, only the most relevant systematic effects are included with the profile method. This is the case for

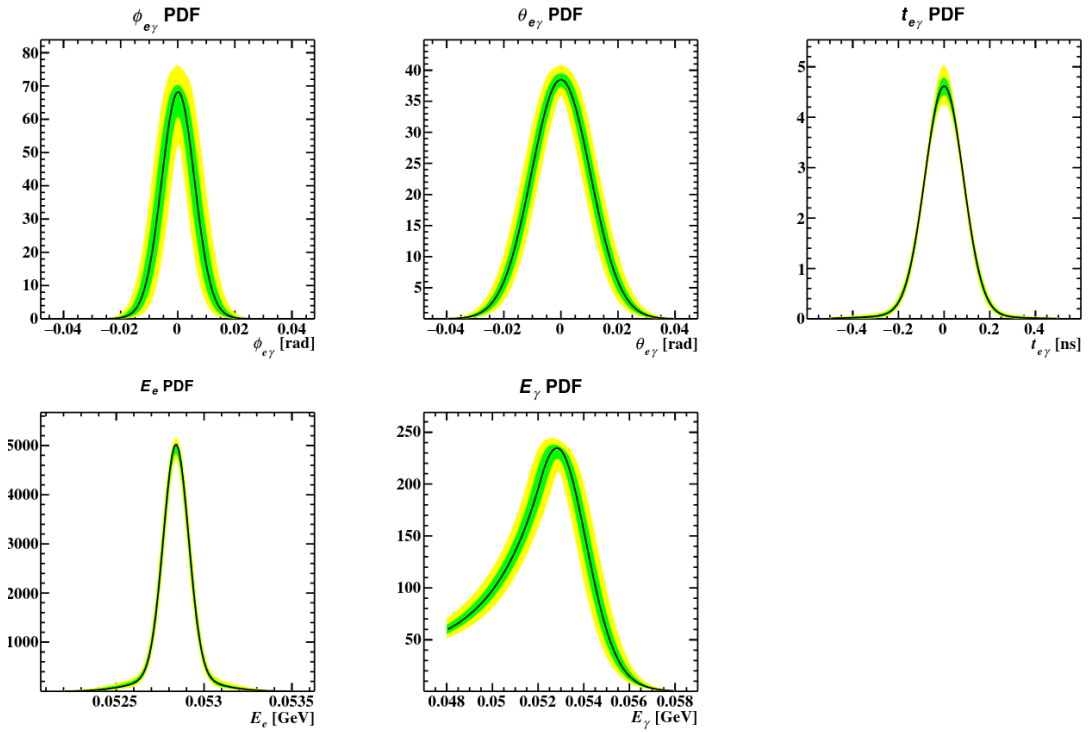

Figure 7.11: PDFs with the inclusion of systematic errors at 1σ (green) and 2σ (yellow) level.

the target misalignment, included with the x_{TGT} parameter of Equation 6.2. All other uncertainties are accounted for using the random sampling technique: event-by-event the PDFs' shapes are altered changing the parameters according to their associated errors.

For the 2021+'22 dataset, the sensitivity evaluated with the "per-event PDFs" method is:

$$\mathcal{S}_{90} = 2.2 \times 10^{-13} \tag{7.12}$$

including all systematics. This sensitivity is better by $\approx$ 15% than the one returned by the "constant PDFs" method: $\mathcal{S}_{90} = 2.5 \times 10^{-13}$. The distribution of the toy MCs upper limits is shown in Figure 7.10. In this Figure, the results of the analysis applied in four fictitious analysis regions inside the time side-bands are also shown: the null results of these fits are a consistency check of the analysis.

7.3.1 Breakdown of systematics

Systematics effects reduce the sensitivity by 3%. This represents an important improvement with respect to the 2021 analysis, when their impact was estimated to be 5% [8].

The average contribution of each systematic uncertainty, evaluated by calculating the sensitivity without including it, is reported in Table 7.2, while Figure 7.11 shows the variation of the PDFs shapes when systematic errors are included. The biggest improvement in the reduction of systematics comes from the revised analysis of detectors' alignment: the target alignment in 2022 was improved by the increased statistics of Michel positrons which could be employed for the hole analysis; the uncertainty on the CDCH - LXe alignment was improved by employing the analysis strategy detailed in Chapter 5, Section 5.2.

7.4 Results

After data unblinding, a total of 357 events were observed within the analysis region. The (E_e, E_γ) and $(\cos\Theta_{e\gamma}, t_{e\gamma})$ distribution of the 10 best ranked events, according to the R_{sig} score, are shown in Figure 7.12. The contours of the average signal PDF are superimposed on the plots. No excess of events is

Table 7.2: Breakdown of systematic uncertainties for the 2021+'22 analysis (when different uncertainties are applied to each year, both values are reported). The results are compared with those obtained in the 2021 analysis [8].

Syst.	Analysis 2021 Uncertainty	Analysis 2021 $\mathcal{S}_{90}$ effect	Analysis 2021+'22 Uncertainty	Analysis 2021+'22 $\mathcal{S}_{90}$ effect
$\phi_{e\gamma}$ / $\theta_{e\gamma}$	Target align.: 100 µm LXe shift: 1 mm	2.0%	Target align.: 100/50 µm LXe shift: 400/300 µm	1.4%
N_μ	5%	0.6%	5%	0.4%
E_γ scale	0.3%	1%	0.3%/0.2%	1%
E_e scale	6 keV	0.1%	6 / $<$ 1 keV	0.1%
$t_{e\gamma}$ bias	4 ps	0.1%	4 / 3 ps	$<$ 0.1%

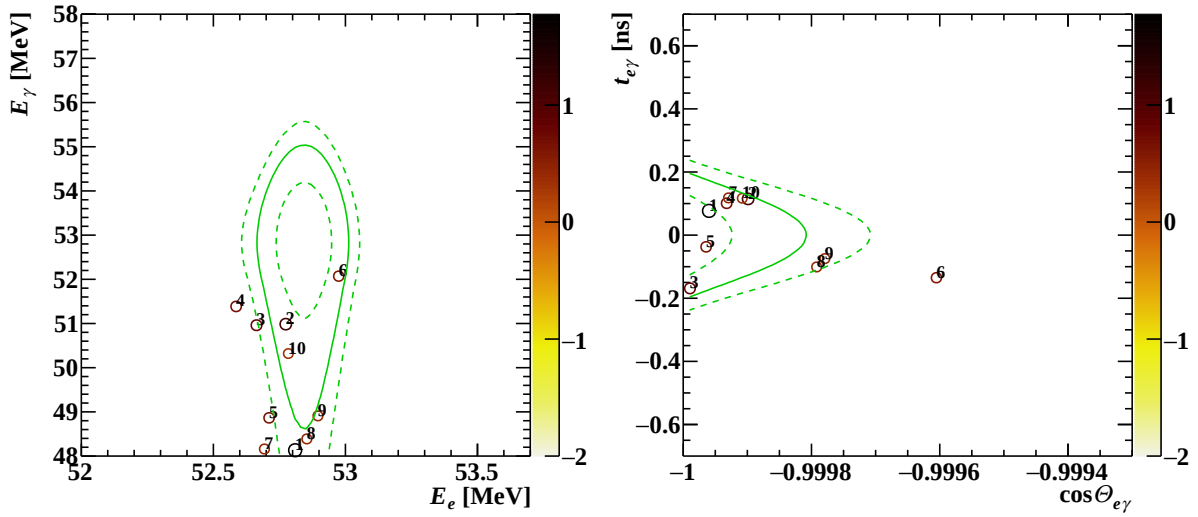

Figure 7.12: Event distributions on the (E_e, E_γ) (left) and $(\cos\Theta_{e\gamma}, t_{e\gamma})$ planes. Only the 10 best ranked events are plotted as markers with a color code based on their R_{sig} score. The average signal PDF contours (1σ, 1.64σ, 2σ) are drawn.

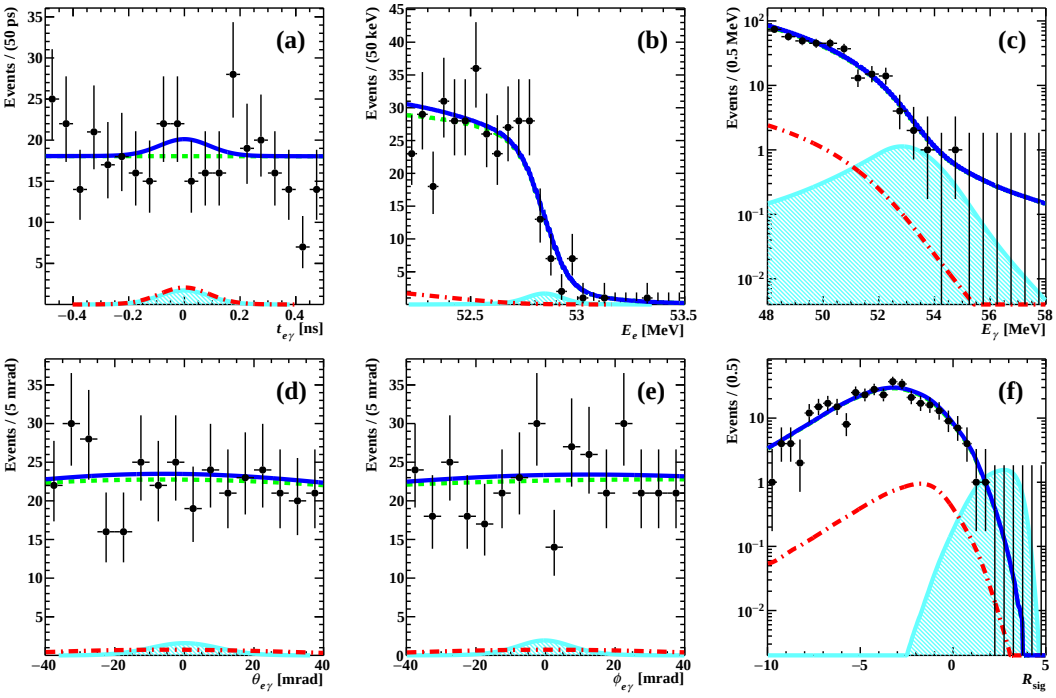

Figure 7.13: One-dimensional projection of the data on each observable with the fitted per event PDFs shapes plotted. The signal shape is enlarged by a factor ×10 so that it can be visible.

observed in the signal region. The one-dimensional projection of data to the fitted per-event PDFs is shown in Figure 7.13.

The best-fit estimate of $\mathrm{BR}(\mu^+ \to e^+\gamma)$ with the "per-event PDFs" method (when the fit is performed not constraining N_{sig} to be positive) is:

$$\mathrm{BR}_{fit} = -3.8 \times 10^{-13} \tag{7.13}$$

which translates to an upper limit on the branching ratio of:

$$\mathrm{BR}_{90} = 1.5 \times 10^{-13} \quad (90\%\ \mathrm{C.\,L.}) \tag{7.14}$$

7.4.1 Consistency checks on the result for $\mathrm{BR}(\mu^+ \to e^+\gamma)$

Unconstrained fit The likelihood fit in the analysis region was repeated releasing the constraints on N_{RMD} and N_{ACC}. This fit yields the following best-fit estimates of these parameters:

$$\hat{N}_{RMD} = 0 \pm 8 \quad \hat{N}_{ACC} = 357 \pm 19 \tag{7.15}$$

both consistent with the estimates from the side-bands' fits (Section 7.3).

Comparison with the "constant PDFs" analysis The best-fit estimate of $\mathrm{BR}(\mu^+ \to e^+\gamma)$ with the "contant PDFs" method (when the fit is performed not constraining N_{sig} to be positive) is:

$$\mathrm{BR}_{fit} = -5.0 \times 10^{-13} \tag{7.16}$$

and the corresponding upper limit is:

$$\mathrm{BR}_{90} = 1.9 \times 10^{-13} \quad (90\%\ \mathrm{C.\,L.}) \tag{7.17}$$

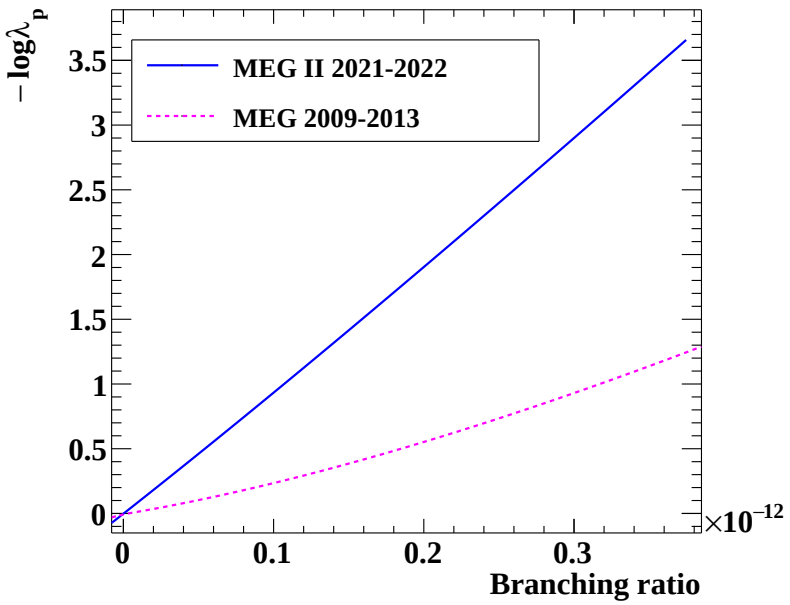

Figure 7.15: Profile of the negative log-likelihood ratio $-\log\lambda_p$ as a function of the branching ratio. The blue curve corresponds to the MEG II 2021+'22 data, while the magenta one is computed on the full MEG dataset [9].

This result is compatible with the one obtained with the "per-event PDFs" analysis, with the probability of having a difference in the BR upper limit measured by the two analysis greater than 0.4×10^{-13} equal to 68%. Also, the slightly worse upper limit obtained from the "constant PDFs" analysis is compatible with the sensitivity being $\approx$ 15% smaller. The consistency between the two results is well represented in the plot of Figure 7.14: there, the 90% C.L. upper limits of an ensemble of 10^3 pseudo-experiments (null signal hypothesis) computed with the two analysis frameworks are compared. The distribution is linear, with an angular coefficient different from one, as expected from the different sensitivity of the two analysis. The results of the analysis in the signal region is shown as a black star marker, while the results of the analysis on the four time side-band regions (Section 7.3) are shown as blue markers, and they all lay in the bulk of the distribution.

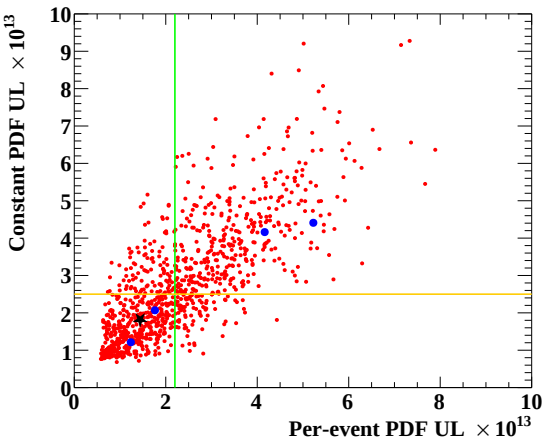

Figure 7.14: Scatter plot of the 90% C.L. upper limits (red marks) calculated on a set of pseudo-experiments (null signal hypothesis) with the two analysis' strategies. The green line indicates the sensitivity of the "per-event PDFs" method, while the yellow line is for the "constant PDFs" one. The black star is the upper limit measured in the signal region, while the blue circles are the upper limits computed on the time side-band regions for cross-check purposes.

7.4.2 Combination with MEG results

In the past analysis the results from the 2021 dataset alone of the MEG II experiment were combined with those from the MEG experiment to improve the sensitivity on the branching ratio [8]. The sensitivity of this analysis with the full 2021+'22 MEG II dataset is a factor 2.4 better than the final MEG sensitivity [9], as clearly visible from the steeper profile likelihood function in Figure 7.15. Since the improvements from the combination with MEG results would be a few % only this time, we didn't investigate this possibility and do not quote a combined result.

Chapter 8

Conclusions & Future prospects

The candidate has been actively involved in all activities regarding MEG II data taking and the CDCH maintenance works in the period 2022-'25. He is collaborating to the Positron Analysis for the analysis of the 2023+'24 dataset and is developing the Graph Neural Network Pattern Recognition algorithm.

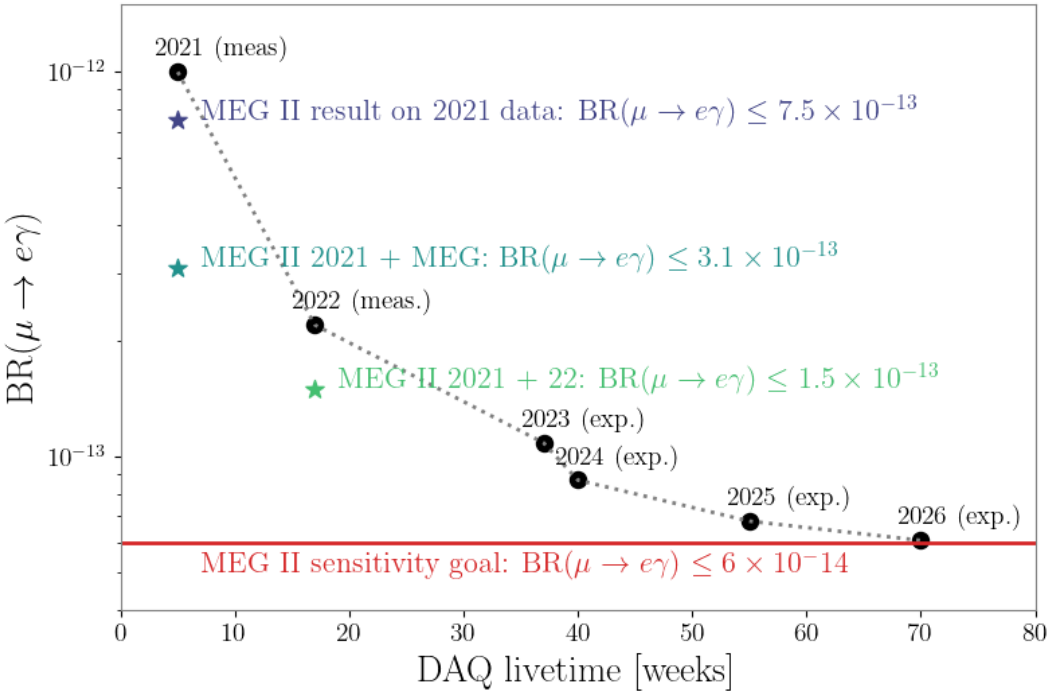

Figure 8.1: Updated projections of the MEG II sensitivity on BR($\mu \to e\gamma$) until the end of data taking, expressed as a function of the DAQ time. The upper limits set through the analysis of the first data samples are indicated with star markers.

The result of the analysis of the 2021+'22 dataset by the MEG II experiment, presented in all the above chapters of this thesis and in a recent article [114], allowed to set a new upper limit on the branching ratio for the cLFV decay $\mu \to e\gamma$:

$$\mathrm{BR}(\mu \to e\gamma) \leq 1.5 \times 10^{-13}$$

This represents an improvement of a factor two with respect to the past limit determined com-

bining the results from MEG's full statistics and MEG II's 2021 dataset only. Thanks to the improved performances of the MEG II detectors system, it has been possible to perform a much more sensitive search with respect to the MEG experiment (by a factor ×3) despite having collected around half the number of stopped muons ($N_\mu^{stop} \approx 7.5 \times 10^{14}$ for MEG, 3.5×10^{14} for MEG II in the 2021+'22 sample). In addition, this high number of muons was collected in less time, because the detectors and TDAQ are stable at higher beam intensities.

The relevance of this result to New Physics observables, which have been introduced in Chapter 1, can be found in [115–123].

This achievement is but a first step of the MEG II experiment. As shown in Figure 2.20, since 2022 the cumulated statistics has tripled, and presently the data taking campaign is ongoing (2025) and is foreseen to continue also in 2026 (Figure 8.1). Considering the current analysis status and the expected statistics which will be cumulated before the shut down of the experiment, the sensitivity goal of $\mathrm{BR}(\mu \to e\gamma) \leq 6 \times 10^{-14}$ of experiment is in reach.

In the next years, the expected MEG II sensitivity could be further improved thanks to improvements in the analysis.

For a brief overview of ongoing studies on the LXe detector performances, see [55].

On the tracker side:

- systematic effects linked to the CDCH - COBRA alignment will be better understood and controlled thanks to the application of the Millepede software alignment algorithm presented in Chapter 5, Section 5.3. While these studies could not produce significant results for the 2021+'22 analysis because of a lack of statistics in the cosmic ray dataset (Chapter 5, Section 5.3.6), for the years 2023, '24, '25 the situation is different, with more than one million cosmic rays events collected to complete these alignment studies;

- novel track finder algorithms using Deep Neural Network techniques have been developed inside the MEG II Collaboration with the two-fold aim of improving the computing time of tracking algorithms and the tracking efficiency. One of the newly proposed algorithms uses Graph Neural Networks, and is discussed in detail in Appendix F. Another one, using a Transformer architecture is described in [124]. These methods proved already highly successful in augmenting the positron reconstruction efficiency beyond the MEG II design value ($\varepsilon_{e^+}^{CDCH} \approx 82\%$), overcoming the performance degradation induced by pile-up effects. The combination of these two algorithms will be the cornerstone of the positron reconstruction in the future MEG II analysis.

The successful deployment of both these tools would result in a significant improvement to MEG II's sensitivity, the first one reducing systematic uncertainties, the second one improving the detection efficiency, boosting the normalization factor N_μ up to $\approx$ 15% for 5×10^7 μ^+/s data: depending on the statistics which will be accumulated in the last year of data taking, this achievement could push MEG II sensitivity even beyond its goal.

Appendix A

Calibration of the CDCH for the ALP search

We report the positron reconstruction performances for data acquired during low intensity runs, with $R_\mu \approx 1 \times 10^6$ μ^+/s. These data are used for the ALP search (Chapter 2, Section 2.3).

Spectrometer's performances are measured on low-intensity data as described in Chapter 3, Section 3.3. The results are listed in Table A.1.

Table A.1: Resolution and positron detection efficiency at low intensity. The results are compared with the performances at a beam intensity of 3×10^7 μ^+/s to highlight the difference.

Variable	@ 3×10^7 μ^+/s	@ 1×10^6 μ^+/s
σ_{p_e}	87 ± 6 keV (f = 0.67)	74 ±6 keV (f = 0.68)
σ_{θ_e}	7.34 mrad	7.05 mrad
σ_{ϕ_e}	6.24 mrad	6.35 mrad
σ_{y_e}	0.69 mm	0.67 mrad
σ_{z_e}	1.81 mm	1.67 mrad
$\epsilon_{e,\mathrm{CDCH}}$	67%	81%

Appendix B

An event display for the X17 data taking

Online reconstruction of tracks is not possible currently with MEG II software since it is a very time consuming task. We developed an event display tool based on the Legendre transform algorithm to visualize curved tracks online. This tool was deployed for the X17 data taking campaign of February 2023 and was helpful in the first stages of this measurement to understand the acquired data.

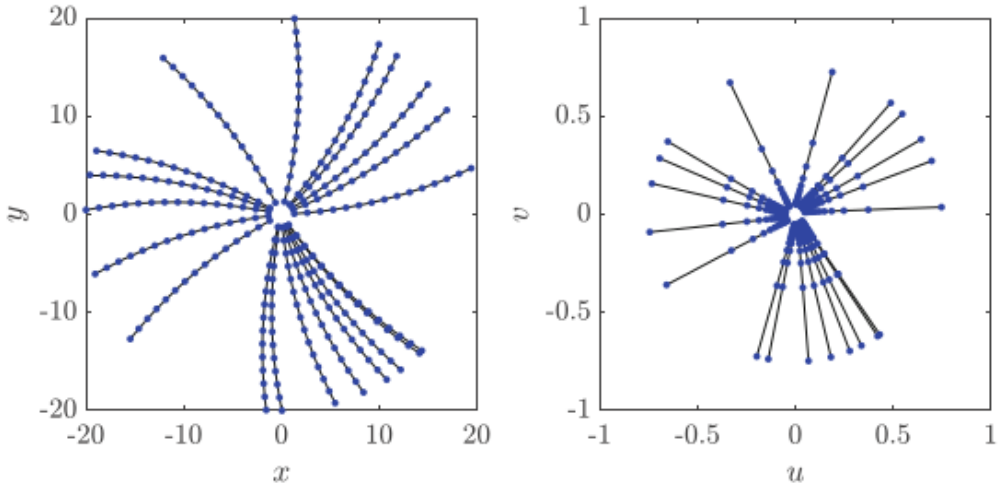

Figure B.1: Representation of curved tracks in the $x - y$ space mapped to lines passing through the center in the parametric $u - v$ space. From [94].

The same Legendre transform algorithm used to identify line patterns (Chapter 5, Section 5.1) can identify circles, once the following mapping of the hit coordinates $\{x, y\}$ is made:

$$\begin{cases} u = \frac{-2x}{x^2+y^2} \\ v = \frac{-2y}{x^2+y^2} \end{cases} \tag{B.1}$$

If all circles pass through the origin (which can be identified as the target), then substituting u and v in the circle equation (radius R and origin (x_0, y_0)):

$$(x - x_0)^2 + (y - y_0)^2 = R^2 \rightarrow u \cdot x_0 + v \cdot y_0 = 0 \tag{B.2}$$

which is the equation of a line passing through the origin (Figure B.1). Once the wire coordinates $\{x_i, y_i\}$ at $z = 0$ are transformed in this way to the set of values $\{u_i, v_i\}$, we can search for maximum in the Legendre space In the case of MEG II CDCH however tracks don't follow an helicoidal path, therefore the trajectory projection in the $x - y$ plane is only approximately a circle. In particular, the approximation is good only for tracks close to the target region ($z \approx 0$). Despite this, the algorithm is

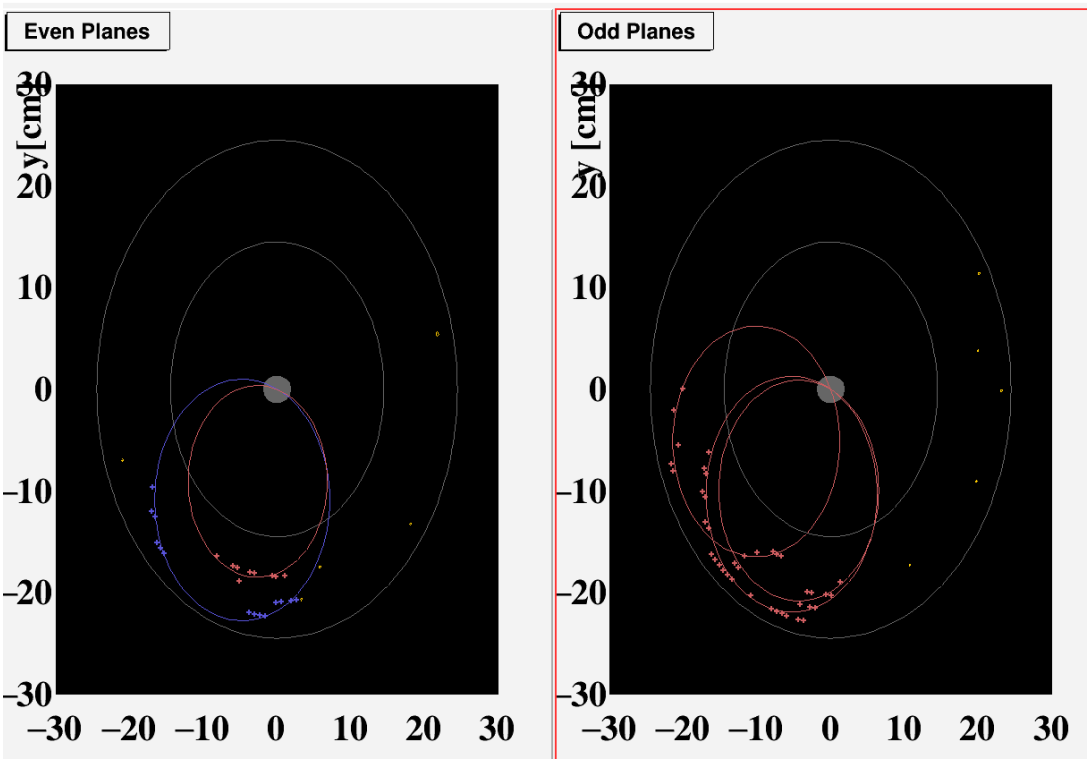

Figure B.2: A recorded event in the CDCH during the X17 run in February 2023. Candidate positron tracks are highlighted in red, electrons are in blue.

able to identify curved tracks well enough to point out for shifters the existence of charged particles in the recorded data. In addition, the longitudinal coordinate measurements w_i of the hits (Chapter 3, Section 3.2.3), combined with their angular coordinate $\phi_i \equiv \arctan\left(\frac{y_i}{x_i}\right)$, can be used to identify candidate positrons (moving clock wise) or electrons (counter-clock wise). An event display is reported in Figure B.2.

Appendix C

Measurement of the attachment parameter of MEG II gas mixture

Stable operations of the CDCH have been achieved employing a quaternary gas mixture with He - Isobutane 90:10 + 1.5% Isopropanol + 0.5% Oxygen, as described in Chapter 3.

Historically, the use of oxygen in gas mixtures for tracking detectors has been strongly discouraged: the probability of loosing ionized electrons on their drift path (*attachment* phenomena) depends on the electronegativity of the gas mixture components, and being oxygen very electronegative it is believed that detection efficiency would be severely compromised. In addition, the common sense is supported by *Garfield++* software, a standard tool for the simulation of gas response in tracking detectors, which confirms this worry of experimentalists because it reports a very high attachment parameter for oxygen mixtures.

Yet, in literature [125] the existence of a discrepancy between *Garfield++* simulations of oxygen attachment parameter η and measurements has already been pinpointed (Figure C.1), and the successful operation of the MEG II CDCH further suggests a need to review the belief of the community on this matter.

In this Appendix, I will resume the recent work done by the MEG II Collaboration to solve the software problem in *Garfield++* and I will show the comparison between MEG II data with Monte Carlo simulations that validate this revision of *Garfield++* code. This topic is further investigated in this article [126].

Garfield++ simulation of Attachment

The electron attachment in the presence of oxygen is described in *Garfield++* by a two-stage mechanism:

$$e^- + O_2 \rightarrow (O_2^-)^* \quad \text{(excited ion formation)} \tag{C.1}$$

followed by de-excitation of the oxygen ion through collision with another oxygen molecule or another molecule X in the mixture:

$$(O_2^-)^* + O_2 \rightarrow O_2^- + O_2 + \gamma \quad \text{(single process)} \tag{C.2}$$

$$(O_2^-)^* + X \rightarrow O_2^- + X + \gamma \quad \text{(three-body process)} \tag{C.3}$$

This latter mechanism is called three-body because it involves three particles: the electron, oxygen ion, and the molecule X.

The attachment rate R in a given mixture is proportional to the capture cross-section of oxygen σ_C, multiplied by the oxygen density in the mixture n_{O_2} and the de-excitation rate. The de-excitation

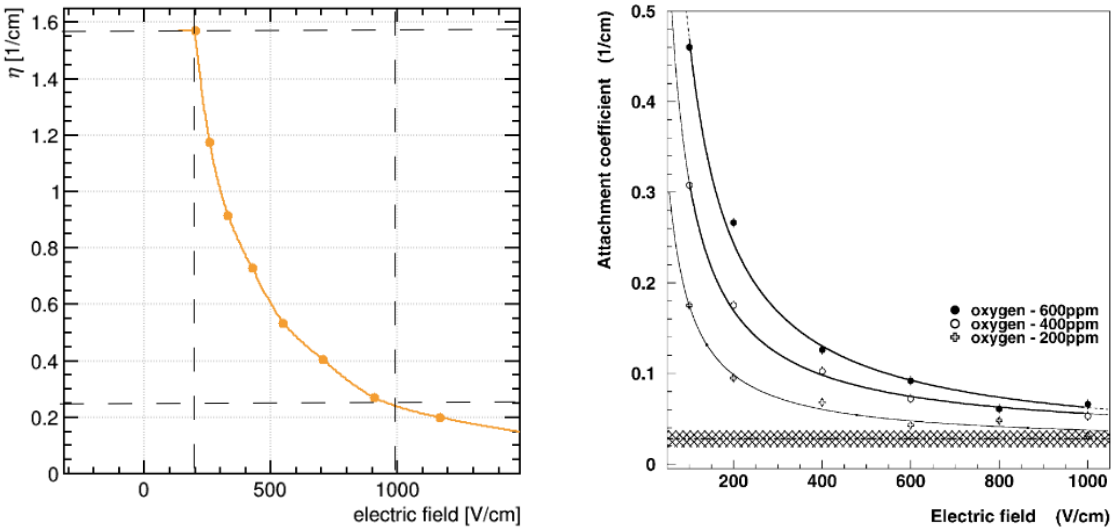

(a) Garfield++ (version 2023.4) calculated attachment coefficient as a function of electric field for a mixture 90:10 He - isobutane + 600 ppm O_2.

(b) Direct measurements of the attachment coefficient in a 90:10 He - isobutane mixture with O_2 addition in different amounts.

Figure C.1: Simulations (left) and measurements from [125] (right) of the attachment coefficient of a 90:10 He - isobutane gas mixture with O_2 addition disagree by a factor ≈ 6.

rate is obtained by summing the de-excitation cross-sections σ_{d,X_i} for each of the components X_i in the mixture:

$$R \propto \sigma_C \times n_{O_2} \times \sum_{i=1}^{N} \sigma_{d,X_i} \times n_{X_i} \tag{C.4}$$

The density of element X_i can also be written as the density n of the gas mixture multiplied by the mass fraction f_{X_i} of component X_i, and the de-excitation cross-section for each molecule X_i can be normalized to the one for oxygen:

$$R \propto \sigma_C \times n_{O_2} \times n \times \sigma_{d,O_2} \times \sum_{i=1}^{N} \frac{\sigma_{d,X_i}}{\sigma_{d,O_2}} \times f_{X_i} \tag{C.5}$$

The behavior of each gas usable in *Garfield++* is encoded in individual subroutines in the FORTRAN program `magboltz`. The capture and de-excitation rates for oxygen are correctly calculated using the specified oxygen density for the mixture, while the three-body process rate is calculated internally in the subroutine describing oxygen, assuming the mixture is entirely composed of oxygen. In fact, the parameter $T3B$, defined as:

$$T3B = \sum_{i=1}^{N} \frac{\sigma_{d,X_i}}{\sigma_{d,O_2}} \times f_{X_i}$$

is normally set to one and must be modified by hand depending on the type of mixture used to obtain meaningful results. De-excitation cross-sections as a function of energy are known only for a limited set of gases [127]. While there are measurements for Isobutane (with large uncertainties $\approx 25\%$), those for Isopropanol are absent, which is an ingredient of the MEG II mixture. Using as de-excitation cross-section for Isopropanol the average of those for ethyl alcohol and methanol, the estimated attachment coefficient is $\times 5.4$ smaller than the one returned by *Garfield++* without this code modification. The uncertainty on this estimate of η is $\approx 20\%$ due to the large uncertainty on the Isobutane cross-section measurement and the unknown value for the Isopropanol.

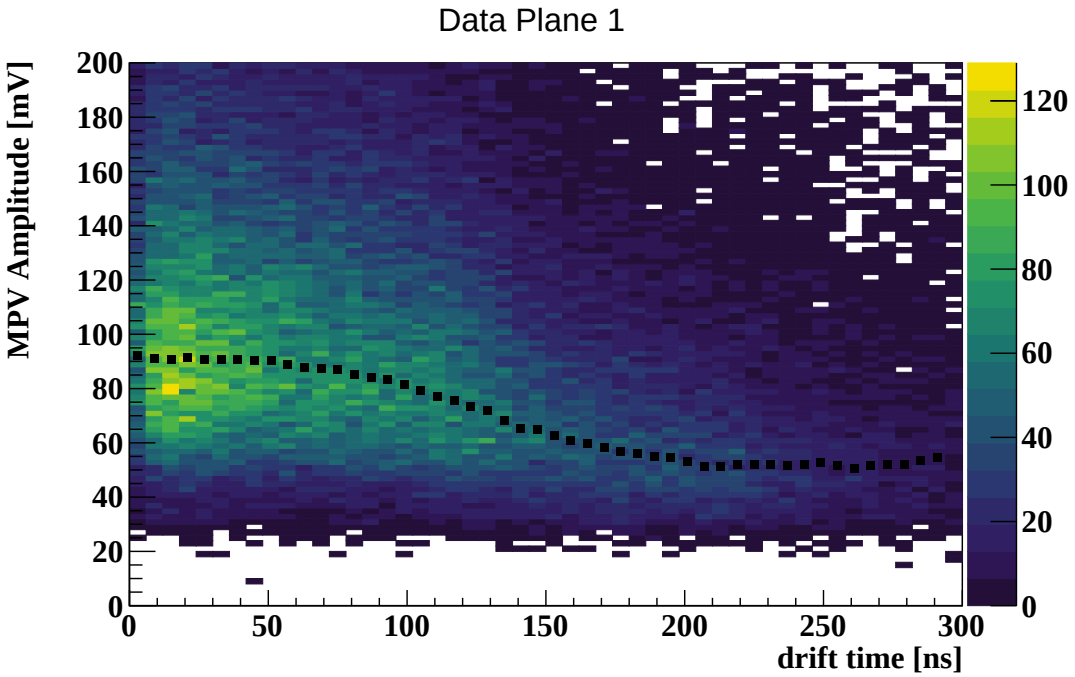

Figure C.2: Bi-dimensional distribution of amplitude and drift time for signal hits. The black markers indicate the most probable value of the amplitude. This is measured from a fit to the distribution of amplitudes at fixed drift time using a Landau function as described in the text.

Comparison between Garfield++ predictions and MEG II measurements

We try to estimate the attachment parameter for the MEG II CDCH gas mixture from the distribution of the signal amplitude for the first cluster as a function of drift time.

When a particle traverses a drift cell, $N_{clusters}$ clusters each with $n_{el,i}$ electrons are produced from the primary ionization; these electrons' clusters drift towards the anode and form a signal unless along their path they are lost because of attachment effects. The probability of an electron getting attached to an ion is larger the longer the drift path is. If less clusters and electrons contribute to the formation of the hit signal, its amplitude will be smaller and therefore we expect to observe smaller signal amplitudes for longer drift times because of attachment effects.

The bi-dimensional distribution of amplitude VS drift time is shown in Figure C.2 for Michel positrons data with a beam intensity of 3×10^7 μ^+/s. The black markers in the plot are the most probable value of the amplitude within a drift time window, extracted from the fit to a Landau distribution. Since the drift time depends slightly on the cell size, for this analysis we restrict ourselves to hits on cells belonging to the first layer of the CDCH and around the center, $|z_{hit}| < 10$ cm. The curve shows a monotone decreasing trend from large amplitudes at small drift times to smaller signal amplitudes, eventually flattening to the average amplitude of a single ionization cluster ($\lesssim 60$ mV).

The agreement of the data with a certain value of the attachment parameter have been investigated using Monte Carlo simulations, since the amplitude-drift time shape may depend on various effects not easy to evaluate through an analytic formula, such as the pile-up of multiple clusters, for example.

The attachment effect is introduced in the Monte Carlo simulation of the CDCH in the following way:

- in an ionization event of a cell, n electrons are generated at distance d from the anode and it takes a time t_{drift} for them to reach the anode;
- each of the n electrons reaches the anode with probability $1 - p_{attachment}(t_{drift}; \eta)$;
- the signal amplitude is simulated based on the number of survived electrons.

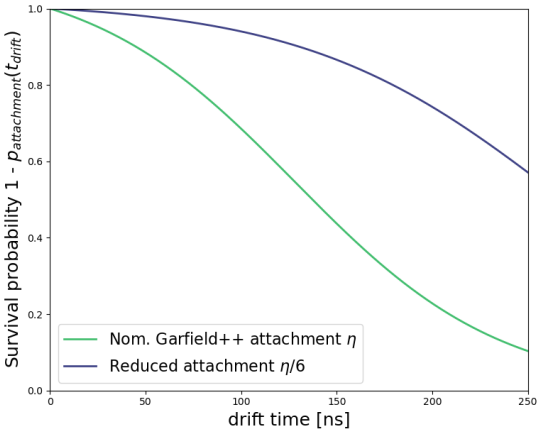

(a) Survival probability of electrons in Monte Carlo simulations.

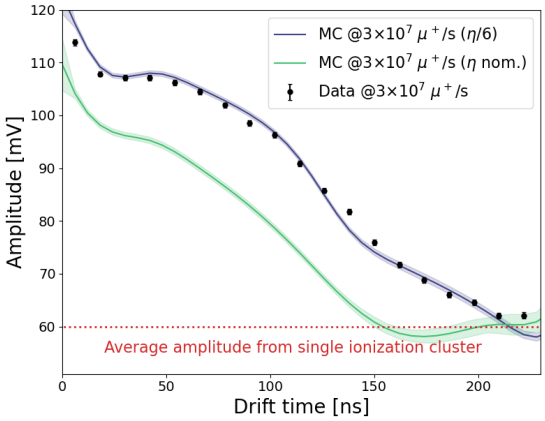

(b) Comparison of the amplitude VS drift time between data and Monte Carlo simulations. The band around the MC curves correspond to $\pm 1\sigma$ area, where σ is the error from the Landau fit procedure.

Figure C.3: Comparison of Monte Carlo simulations with different attachment coefficients.

Since the attachment probability depends on the value of the electric field, and this in turns depend on the distance d from the anode, the attachment probability $p_{attachment}(t_{drift}; \eta)$ is calculated using simulations with the *Garfield++* software integrating the differential attachment probability along the drift path corresponding to t_{drift}. The survival probability $1 - p_{attachment}$ is shown in Figure C.3 (a) for two sets of Monte Carlo simulations (at 3×10^7 μ^+/s beam intensity) with different attachment parameters:

- one simulation uses the *Garfield++* default attachment parameter η (green line);
- the other one is the MEG II official simulation implementing a reduced attachment parameter with respect to the *Garfield++* standard: $\eta/6$ (blue line). This value for the attachment was obtained empirically and is close to the theoretical one calculated above: $\eta \to \eta/5.4$.

In Figure C.3 (b) we plot the amplitude vs drift time curves for these two simulations with superimposed as black error markers the experimental data, showing the good agreement with the revised value for the attachment coefficient.

Appendix D

A weak mode of Millepede alignment with cosmics

In the MillePede algorithm only constraints on global shifts of the CDCH are imposed, following Equation 5.20 in Chapter 5, Section 5.3.3. We performed two iterations of the MillePede routine after which we saw no improvement, as it is evident from the χ^2/dof comparison in Figure D.1. Indeed from Figure D.1 it seems that no improvement on the χ^2 minimization can be expected, since the χ^2/dof distribution after the second iteration is superimposed to the one with optimal geometry.

Yet, looking at the distribution of residual misalignment between the ideal geometry parameters and the ones determined from MillePede (i.e. $q_{true} - q_{Mille}$), a systematic deformation of the CDCH with respect to the true geometry is detected: as shown in Figure D.2, a correlation between the residual misalignment in x_0 and x_0 is observed, which results in a *squeezing* of the CDCH.

This deformation is a so called *weak mode* of our alignment problem: a solution which minimizes

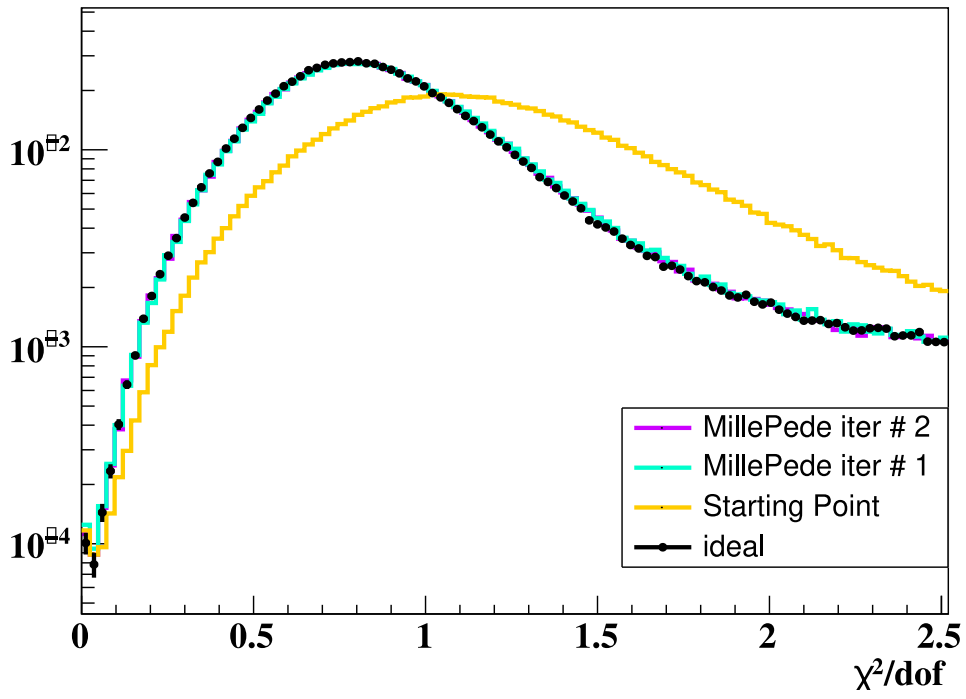

Figure D.1: Comparison of χ^2/dof of MC cosmic rays tracks with different geometries: before applying MillePede corrections, after the first and second iteration and with the ideal geometry. The distributions for Millepede iter 1 and 2 superimpose almost ideally.

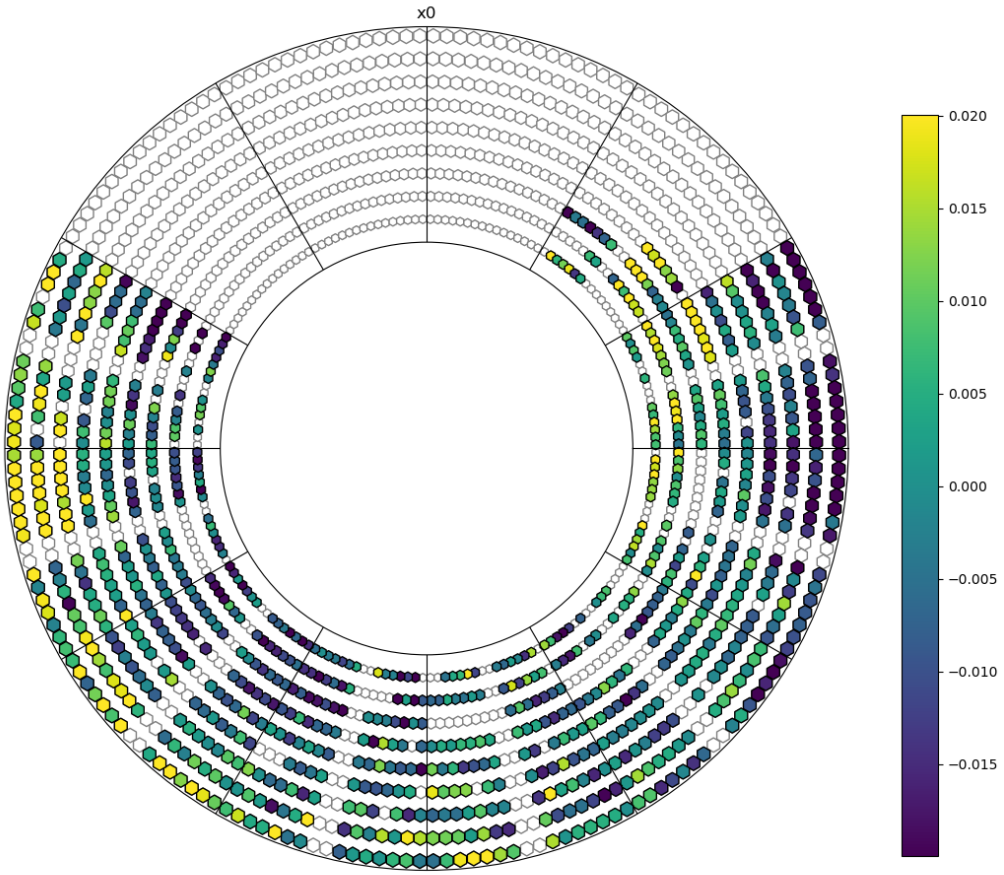

(a) xy view of the corrections δx_0 on all wires. The gradient of colors clearly shows the deformation of the CDCH that resembles a *squeezing*.

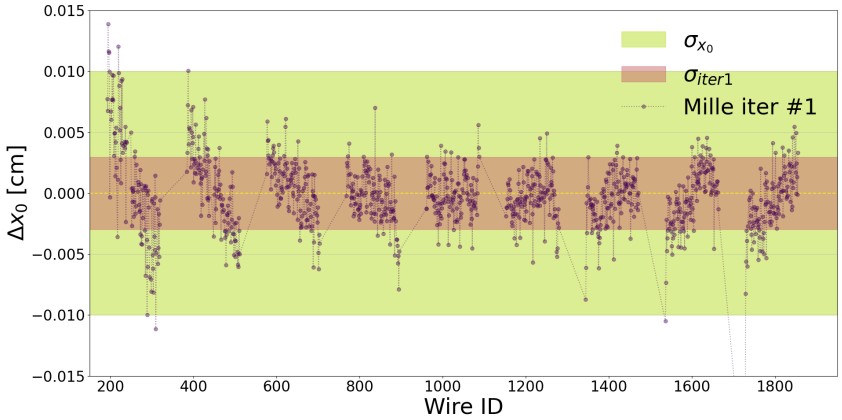

(b) Wire-by-wire residual misalignment of the x_0 parameter. Dots are the wire-by-wire residual misalignment and the pink band is the RMS of the distribution; the green band is the initial applied misalignment to the x_0 parameter. The squeezing deformation of all layers along the x axis appears clearly as a correlation between position of the wire and residual misalignment.

(c) Scheme explaining how the squeezing deformation can be caused by the topology of cosmic tracks.

Figure D.2: Visualization of the *squeezing* deformation in the CDCH after one iteration of the MillePede algorithm.

the χ^2 but returns an altered geometry. In our case, where only cosmic rays are used for the alignment procedure, the track topology is responsible for the appearance of this weak mode: as represented schematically in Figure D.2 (c), vertical tracks passing through few external layers only may be brought closer to wires (meaning that the χ^2 is reduced) either moving the track itself or moving wires in the outer direction towards the track. Such a sample of tracks biases the solution for the most external layers and have some effect also on the most internal ones, while the layers in the middle of the CDCH aren't affected at all. This effect was reproduced with MC simulations.

The successful alignment strategy that eliminates this weak mode involves: a cut on data to select only tracks hitting a wire on at least four layers, increasing the correlation between wires on external and inner layers; using gaussian constraints on all wire parameters. These techniques are used for the alignment on 2022 data, as reported in Chapter 5, Section 5.3.

Appendix E

Analysis of positrons pulls distributions

Pulls distributions

In the double turn analysis, the pull parameter of a variable is calculated as:

$$\frac{q_2 - q_1}{\sigma_{1\times2}}, \quad \text{where } \sigma_{1\times2} \equiv \sqrt{\sigma_1^2 + \sigma_2^2} \tag{E.1}$$

using the fitting uncertainty σ from the Kalman filter algorithm. The pull distributions of positron observables for 3×10^7 μ^+/s data are illustrated in Figure E.1.

On Monte Carlo instead, we can compute the pull of a variable also as:

$$\frac{q_{rec} - q_{MC}}{\sigma_{rec}} \tag{E.2}$$

where σ_{rec} is the fitting error. As already discussed, double turn parameters extracted from data will be corrected with the parameters extracted from the double turn analysis on MC Michel positrons samples and from the $rec - MC$ distributions on MC signal events. The pull distributions for signal MC events simulated at 3×10^7 μ^+/s beam intensity are shown in Figure E.2.

The pull distributions are fitted with a linear sum of two gaussian terms. If the fit estimate of the parameters error is correct, the core gaussian variance should be close to one. A second gaussian term is added to account for a tail component of events with systematically larger errors (from geometrical effects, for example).

The best fit parameters from the double turn analysis on '21 + '22 are reported in Table E.1. We note that the core variances after corrections with MC inputs are all close to 1, except for z_e. This fact was already observed during the '21 analysis [90] and is not understood yet. No significant difference between 2021 and 2022 data is observed, except for the mean of the pull distributions, as was already noticed above, and is probably linked to upgrades in the software analysis and in the calibration procedure.

Correlations

The six correlations[i] between kinematic variables are estimated also using the pull distributions, for the per-event analysis. In Figure E.3 the correlations observed on data through the double turn analysis are shown, while the MC correlations measured on simulated signal events at 3×10^7 μ^+/s beam intensity are illustrated for reference in Figure E.4

[i] In the per-event analysis the $\phi_e - \sigma_\phi$ trend is taken into account automatically

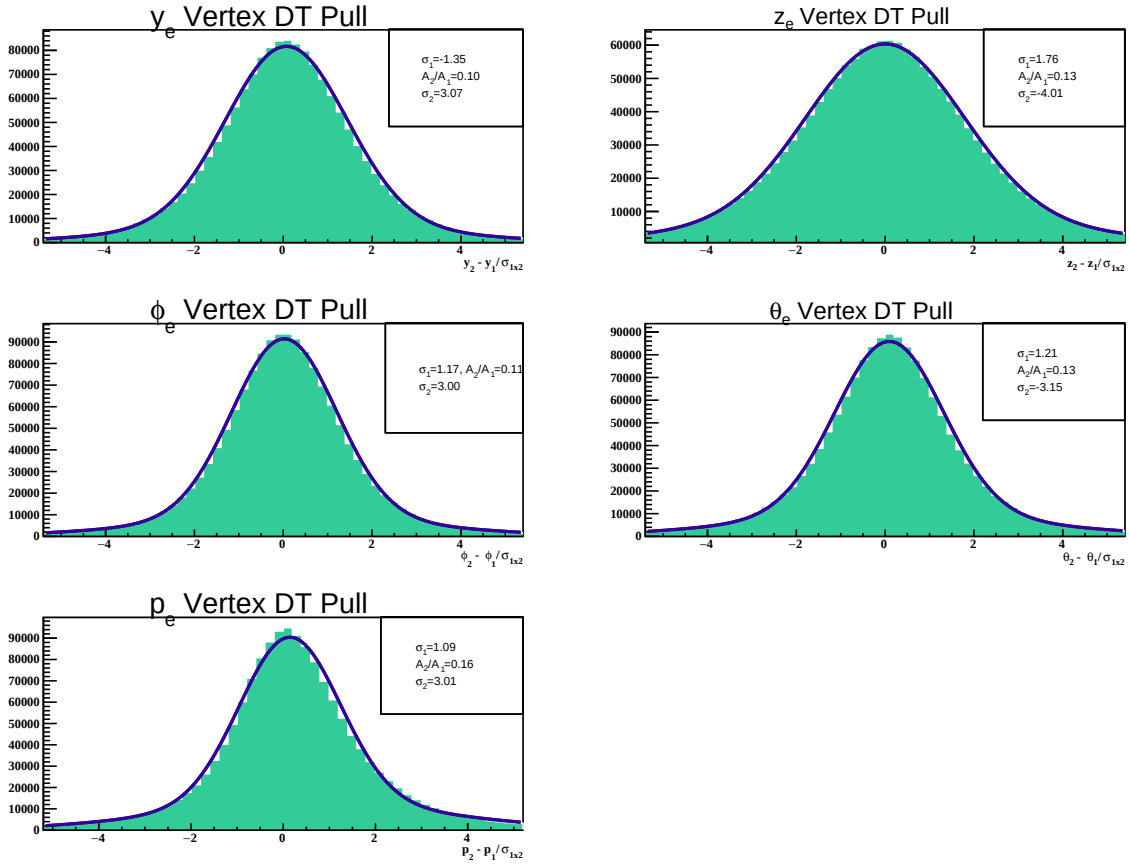

Figure E.1: Double turn pull distributions measured on 2022 3×10^7 μ^+/s data.

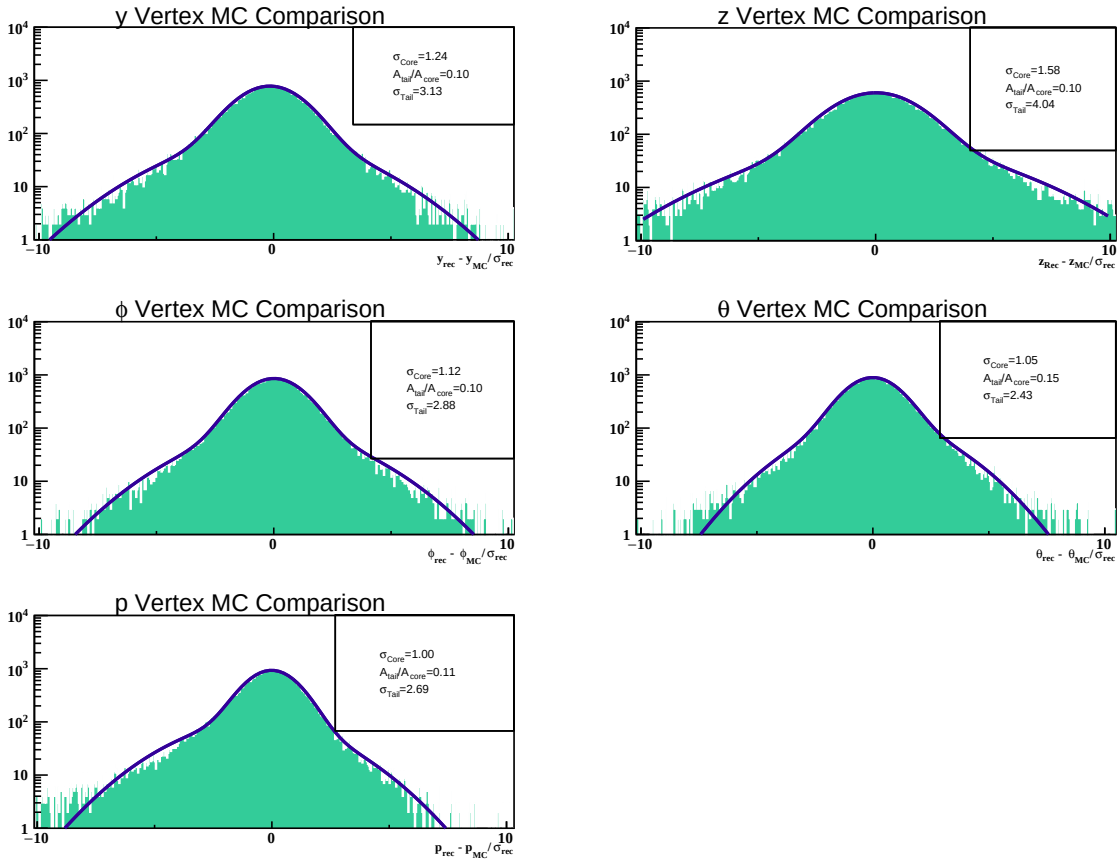

Figure E.2: MC pull distributions $rec - MC$ measured on simulations of signal events at 3×10^7 μ^+/s beam intensity.

Table E.1: Best fit parameters for the two gaussian sum for the '21+'22 analysis with per-event PDFs. σ^{pull}_{signal} is the core resolution corrected with MC inputs to evaluate the signal resolution. Data in 2021 were collected at beam intensities ranging from $2-5\ \times 10^7\ \mu^+$/s.

Fit parameter	Variable	Beam intensity [$\times 10^7\ \mu^+$/s]						
		2021				2022		
		2	3	4	5	3	4	5
σ^{pull}_{core}	y_e	1.32	1.38	1.44	1.47	1.35	1.42	1.47
	z_e	1.77	1.77	1.84	1.93	1.81	1.94	1.99
	ϕ_e	1.14	1.18	1.18	1.23	1.17	1.22	1.24
	θ_e	1.26	1.21	1.25	1.29	1.21	1.27	1.30
	p_e	1.05	1.10	1.11	1.18	1.09	1.15	1.18
σ^{pull}_{tail}	y_e	2.97	3.04	3.06	3.14	3.07	3.16	3.23
	z_e	3.83	3.83	3.96	4.09	4.36	4.61	4.74
	ϕ_e	2.68	2.85	2.91	2.95	3.00	3.09	3.09
	θ_e	3.12	2.95	3.12	3.28	3.15	3.23	3.32
	p_e	2.85	2.89	2.91	3.06	3.01	3.12	3.19
μ^{pull}_{core}	y_e	0.23	0.20	0.22	0.19	0.07	0.07	0.05
	z_e	-0.25	-0.21	-0.23	-0.21	0.00	-0.02	-0.03
	ϕ_e	-0.09	-0.07	-0.09	-0.09	0.02	0.01	0.02
	θ_e	0.13	0.13	0.12	0.07	0.09	0.08	0.08
	p_e	0.13	0.14	0.13	0.13	0.14	0.14	0.13
μ^{pull}_{tail}	y_e	0.41	0.19	0.20	0.25	0.09	0.06	0.03
	z_e	-0.07	-0.06	-0.08	-0.17	-0.03	-0.06	0.02
	ϕ_e	-0.02	-0.09	-0.03	-0.05	0.11	0.09	0.09
	θ_e	0.00	0.05	0.14	0.06	0.11	0.11	0.08
	p_e	0.59	0.57	0.51	0.50	0.50	0.46	0.43
f^{pull}_{tail}	y_e	0.10	0.10	0.10	0.10	0.10	0.10	0.10
	z_e	0.12	0.15	0.15	0.17	0.10	0.10	0.10
	ϕ_e	0.12	0.13	0.13	0.15	0.11	0.11	0.12
	θ_e	0.09	0.15	0.15	0.15	0.13	0.15	0.15
	p_e	0.15	0.17	0.21	0.21	0.16	0.18	0.19
σ^{pull}_{signal}	y_e	1.11	1.15	1.20	1.21	1.09	1.18	1.21
	z_e	1.63	1.61	1.68	1.70	1.63	1.70	1.75
	ϕ_e	1.08	1.10	1.12	1.13	1.09	1.16	1.14
	θ_e	1.07	1.04	1.04	1.08	0.99	1.00	0.97
	p_e	0.86	0.92	0.95	0.98	0.92	0.99	0.98

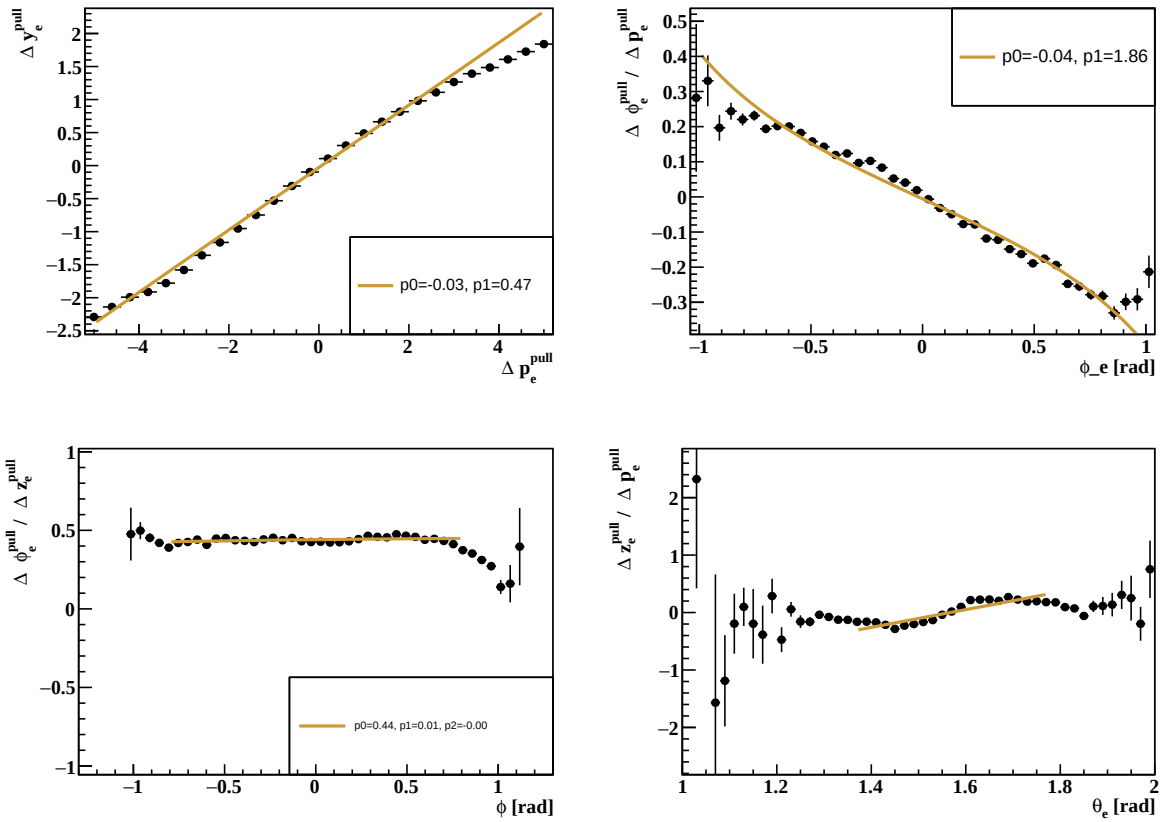

Figure E.3: Double turn correlations between the positron observables quantified using the pull distributions. The data were recorded at 3×10^7 μ^+/s beam intensity.

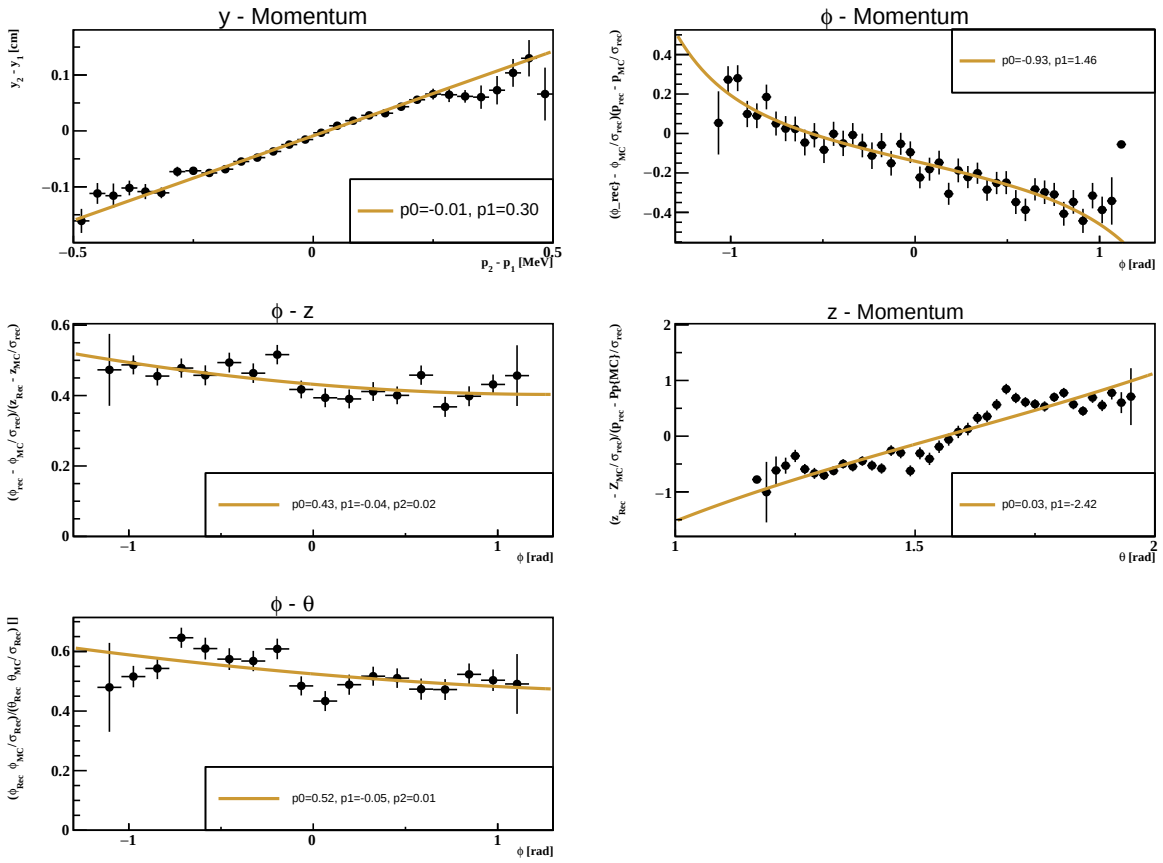

Figure E.4: MC correlations between the positron observables quantified using the pull distributions. This MC simulations includes signal events at 3×10^7 μ^+/s nominal beam intensity.

Appendix F

Studies on a Graph Neural Network-based Pattern Recognition

The present track finder algorithm employed in the MEG II analysis framework is based on the Kalman Filter technique (Chapter 3, Section 3.2). Notoriously, Pattern Recognition (PR) tasks relying on this method are computationally expensive and struggle in high pile-up environments because of the exponential complexity that characterizes similar local and iterative approaches.

At present, tracking takes 15-30 seconds to perform reconstruction of a single event on the MEG II cluster, for events collected at $3{-}5{\times}10^7$ μ^+/s beam intensity. The complete reconstruction of all recorded events by the MEG II experiment takes $\approx 3-5$ months per year of collected data. Since around 70% - 80% of the total time employed for the full event reconstruction is devoted to tracking tasks, the present PR algorithm makes it difficult to investigate efficiently the optimization of the tracker and is slowing MEG II analysis: studies are slow and time consuming, and the cost of reprocessing to apply some changes is not negligible.

Apart from computing time performances, the degradation of the tracking efficiency at high beam intensities is clearly visible on MEG II data (Chapter 3, Section 3.3.3). A novel, faster PR algorithm insensitive to pile-up could overcome this issue too, increasing also the positron reconstruction efficiency and boosting the overall experimental sensitivity, since $N_\mu \propto \epsilon_{e^+}$ (Equation 7.8).

With these two main objectives in mind, MEG II Collaboration started to investigate the possibility of developing a track finder using Deep Neural Network techniques, which are intrinsically fast and have proven very effective in similar tasks [128, 129]. Here, the first results of a PR algorithm using a Graph Neural Network (GNN) [130] architecture are presented.

What is a graph?

A *graph* $\mathcal{G}$ is a mathematical object defined as a pair $(\mathcal{V},\ \mathcal{E})$, where $\mathcal{V} = \{v_i\}$ is set of *nodes* (or *vertices*) and $\mathcal{E} = \{e_i\}$ is a set of *edges* connecting pairs of adjacent nodes (all nodes can be connected or just some of them based on some relationship between them).

Many data structures emerging in physical problems can be organized in graphs. In the particular case of particle tracking we can identify the set $\mathcal{V}$ as the ensemble of hits inside a detector and $\mathcal{E}$ as the set of segments connecting these hits. Particle tracking is the problem of identifying the subset of $\mathcal{V}$ and $\mathcal{E}$ corresponding to hits left by a particle along its track and the track segments connecting them using a suitable function ϕ operating on the elements of $\mathcal{G}$. In general, ϕ will be a function of node, edge and/or graph features.

In recent years many studies pointed out that Graph Neural Networks are suited to solve tracking problems [129, 131]. Graph Neural Networks (GNN) are deep learning algorithms exploiting the strong relation features of graphs to learn functions operating on them, allowing to calculate sophisticated edge-, node- and graph-level outputs. A comprehensive introduction to GNN formalism useful for applications in Particle Physics can be found in [130, 132].

For the seek of simplicity, I will describe the underlying concept only of the GNN architectures built to address the problem for a new MEG II PR algorithm (Section F).

The architecture & training

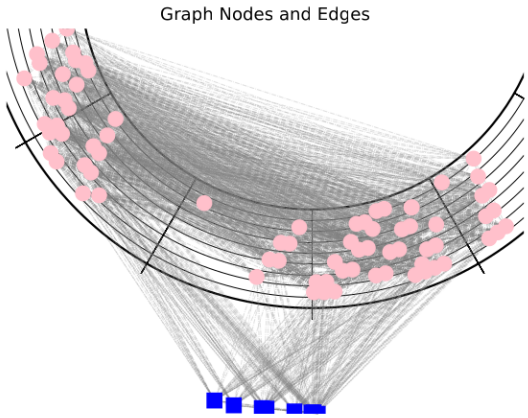

(a) Event graph before the inference stage displayed in the $x - y$ view of the CDCH. CDCH hits are in pink, pTC hits are in blue.

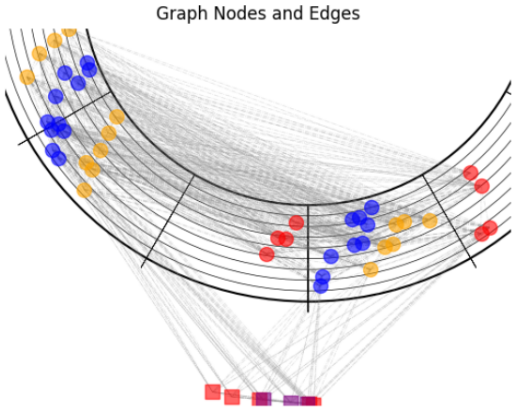

(b) Event graph after the inference stage. The code color is: blue for the hits belonging to the first track turn, orange for the second, red for the third.

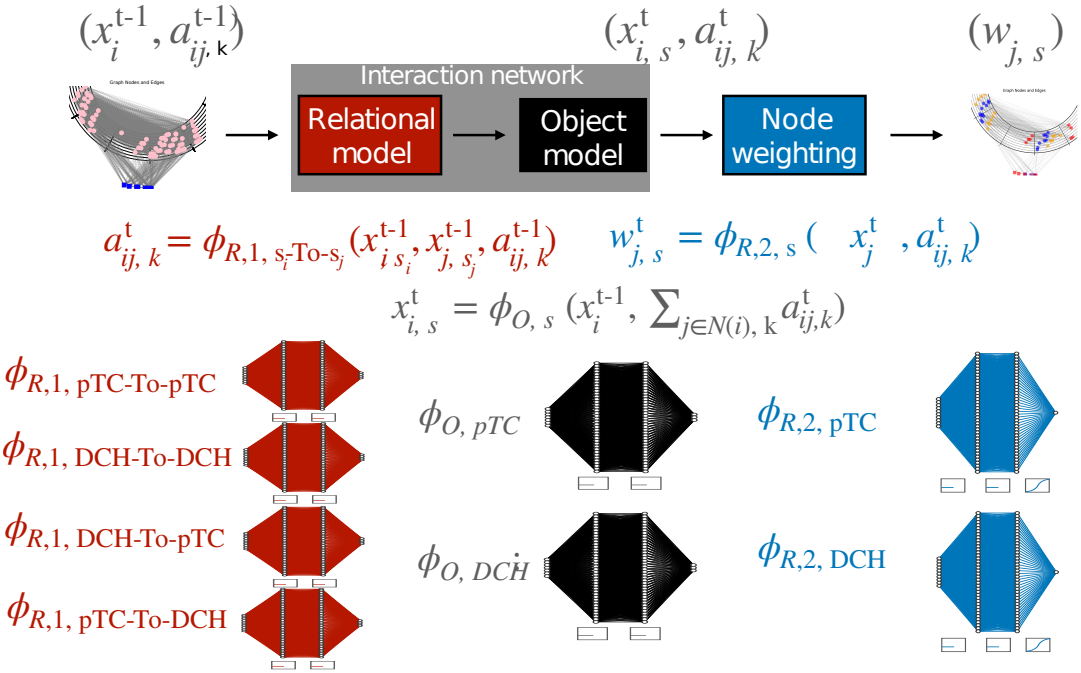

(c) GNN heterogeneous architecture. Modified from [131].

Figure F.1: The GNN classifier implemented for MEG II.

Architecture We implemented a GNN model based on the one in [131]: our PR task will reduce to a *node-classification* algorithm on a graph built from detector hits.

The first step towards the realization of the algorithm is building a graph from an event in MEG II tracker. Hits from the CDCH and the pTC are considered as the nodes of the graph and are connected based on proximity criteria:

- $\Delta\phi_{ij} \equiv$ distance between the anodes of the $i-$th and $j-$th hit in the CDCH (expressed in units of 16 wires, i.e. a CDCH azimuthal sector)< 1 if the hits lay in the same layer; < 3 if the hits are from different layers;
- $\Delta l_{ij} \equiv$ numbers of layers between the i-th and the $j-$th hit in the CDCH ≤ 2;
- All pTC hits are connected between them and to the hits in the three outermost CDCH layers.

The result is a representation of the event like the one displayed in Figure F.1 (a): a set of nodes connected with edges.

The goal of the proposed architecture is to classify detectors' hits, distinguishing between signal hits and noise. Because the positrons along their trajectory leave hits in peculiar patterns, characteristic of the number of turns of the track inside the CDCH, we built a multi-classifier to separate between noise and the different turns. The result of an inference step is visible in Figure F.1 (b).

The architecture (Figure F.1 (c)) is composed of three different Multi Layer Perceptron (MLP) networks $\phi_{R_1}, \phi_{R_2}, \phi_O$ with respectively seven, seven and five fully connected layers with 150 nodes each and ReLU activation function [i]. The MLPs ϕ_{R_1} and ϕ_O act on the graph elements (edges and nodes respectively) to update the space of features based on the relationship between connected nodes and edges (a strategy known as *message passing*): calling $\vec{a}_{ij}^{\,t_0}$ the set of initial (t_0) features of the edge between nodes i and j, and $\vec{x}_i^{\,t_0}$ the set of initial features of the i-th node, then the set of features are updated iteratively with the following Equations:

$$\vec{a}_{ij}^{\,\prime\, t} = \phi_{R_1}\left(\vec{x}_i^{\,t_0}, \vec{x}_j^{\,t_0}, \vec{a}_{ij}^{\,t_0}\right) \tag{F.1}$$

$$\vec{x}_i^{\,\prime\, t} = \phi_O\left(\vec{x}_i^{\,t_0}, \sum_j \vec{a}_{ij}^{\,\prime\, t}\right) \tag{F.2}$$

where the sum $\sum_j$ runs over all neighbors of node i. After evaluating new features at time t, this procedure can be iterated.

The starting nodes' and edges' features are based on hits information available after the hit reconstruction procedure (Chapter 3, Section 3.2). Those used currently in the model are:

$$\begin{cases} \vec{x}_i = \{x_{0,i}, y_{0,i}, \phi_i, \theta_i, z_i, t_i, ampl_i\} \text{ for CDCH hits} \\ \qquad\quad = \{x_i, y_i, z_i, t_i, ampl_i\} \text{ for pTC hits} \\ \vec{a}_{ij} = \{\Delta x_{ij}, \Delta y_{ij}, \Delta t_{ij}\} \end{cases} \tag{F.3}$$

where $x_{0,i}, y_{0,i}, \phi_i, \theta_i, z_i$ are the CDCH wire coordinates at the center, its orientation angles and the measured position along the wire of the hit; x_i, y_i, z_i for the pTC are the hit coordinates as reconstructed in the pTC tile.

ϕ_{R_2} returns the score of the multi-classification problem for each hit i and acts like:

$$s_i = \phi_{R_2}\left(\vec{x}_i^{\,t}, \vec{x}_j^{\,t}, \vec{a}_{ij}^{\,t}\right) \tag{F.4}$$

Since the pTC and the CDCH are different detectors, with very different features characterizing nodes and edges, we built an heterogeneous GNN: depending on whether the nodes represent CDCH or pTC hits, a different NN is used. Therefore, we have two different NN for pTC and CDCH hits for both ϕ_O and ϕ_{R_2} (illustrated in Figure F.1 (c)), and four different ϕ_{R_1} NNs acting on edges, depending on the kind of nodes which are connected: $\phi_{R_1,\, pTC-CDCH}$, $\phi_{R_1,\, CDCH-pTC}$, $\phi_{R_1,\, pTC-pTC}$, $\phi_{R_1,\, CDCH-CDCH}$.

The GNN was built using PyTorch [133] framework with `pytorch-geometric` [134] library.

[i] *ReLU* = Rectified Linear Units https://pytorch.org/docs/stable/generated/torch.nn.ReLU.html.

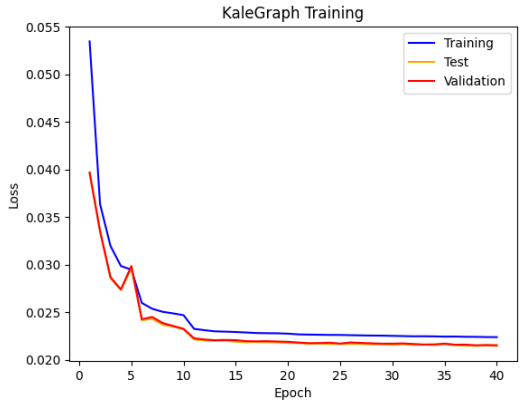

Figure F.2: Loss descent during the training of the GNN model.

Training The GNN was trained on $\approx$ $100k$ events containing positron tracks from Michel decay, collected in 2022 at 5×10^7 μ^+/s beam intensity. The truth content of nodes' labels (noise hits, first, second, third turn etc...) is assessed by the standard track finder algorithm based on the track following strategy with Kalman Filter. Events with no reconstructed positron are not used for training, since they may bias the output with misleading labels.

The loss function optimized during the training stage is a *categorical cross entropy*, as defined in [135]. A typical learning curve is shown in Figure F.2.

Performances

At 5×10^7 μ^+/s beam intensity, most of the hits identified by the hit finder algorithms are actually noise, or effects of cross-talk. This GNN model achieves 85% accuracy in classifying them (Figure F.3 (a) and (b)), while maintaining an accuracy in assigning correctly signal hits to the track turn above 95% for turns 1 and 2, which are also the more frequent cases.

These results were obtained without a thorough search in the space of hyper-parameters, but the reasonable results achieved by this classifier pushed us towards the implementation of this GNN-based PR inside the MEG II software, to test its performances on the full tracking chain (improvements on the architecture are left for the future).

The GNN output is used as a *filter*: instead of feeding all CDCH and pTC hits to the Kalman Filter track finding algorithm, we exploit the labels from the GNN output to discard noise and group hits in classes of supposed track turns to ease the standard track finding algorithm with less and more consistent hits to match in a track.

This simple workflow is represented in Figure F.4. More sophisticated strategies not based on the Kalman Filter at all [136] could be investigated in the future.

The model was exported to the ONNX format and subsequently deployed using the ONNX Runtime [137] to enable efficient inference within the MEG II software environment (C++-based).

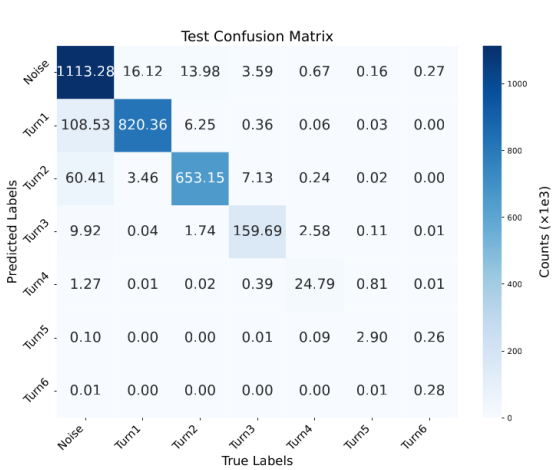

(a) Confusion matrix with the total number of hits classified in each way indicated in the table.

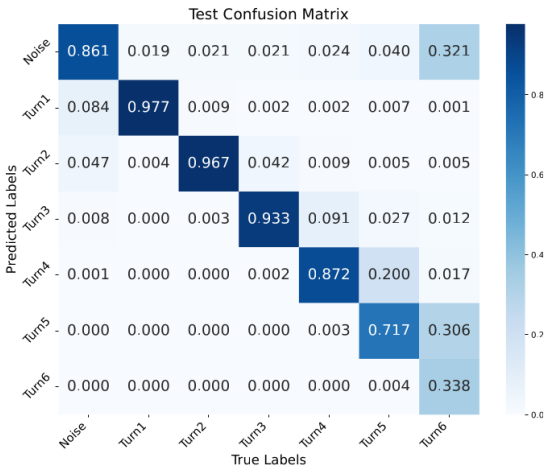

(b) Here, the content of each column is normalized to one.

Figure F.3: Confusion matrix of the GNN model evaluated on a test sample of Michel positrons data at 5×10^7 μ^+/s.

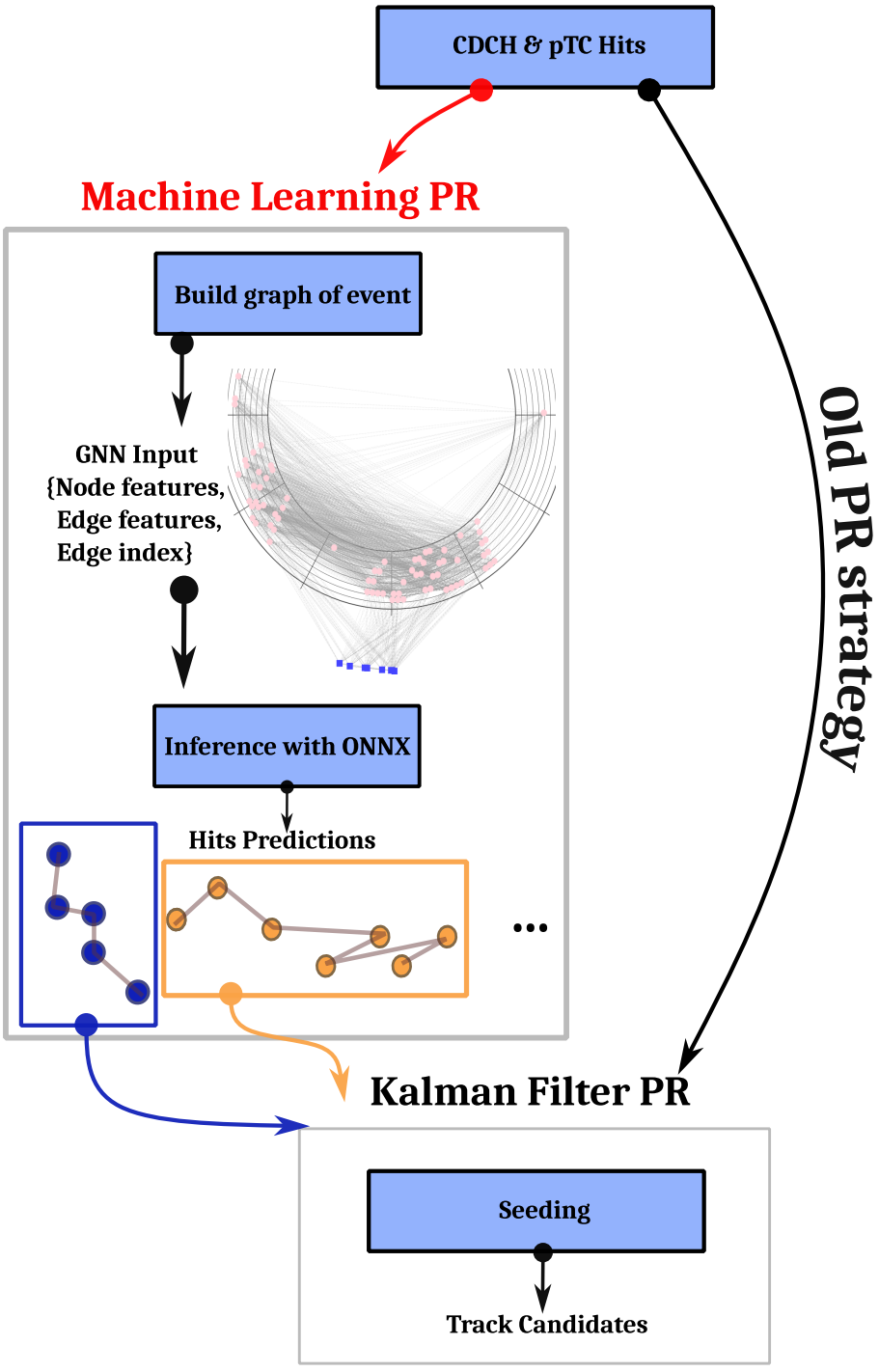

Figure F.4: Scheme of the GNN track finder task for MEG II. First, CDCH and pTC hits are fed into the GNN model; second, this classifier makes inference about the probability of hits to belong to certain track segments, as described in the text; third, CDCH and pTC hits are passed to the standard Kalman Filter PR according to the GNN labels. Conversely, the standard PR feeds all hits directly to the Kalman Filter PR.

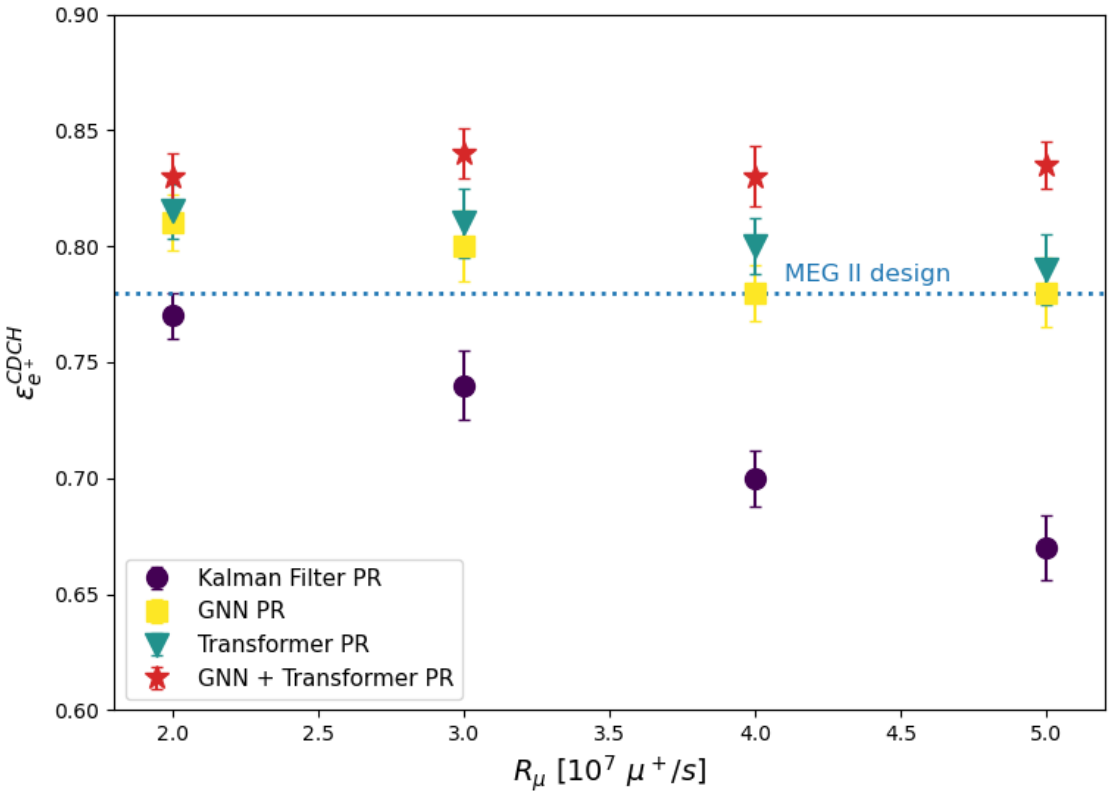

Figure F.5: Comparison of the tracking efficiency at different beam intensities between the standard PR task, the new GNN-based and Transformer-based PR and both DNN algorithms combined.

Positron reconstruction performances As shown in Figure F.5, the GNN-based track finder consistently outperforms the conventional PR algorithm across all beam rates, yielding an efficiency improvement of approximately 10%.

In parallel with the GNN approach, an alternative deep neural network architecture based on a Transformer model [138], which is described in [124, 139], has been developed. This model achieves an enhancement in tracking performance similar (or slightly better) to the one obtained with the GNN PR, as indicated by the green markers in Figure F.5.

The two approaches though are not equivalent and exploit complementary features of the data: when applied sequentially, they provide an additional gain in performance, resulting in a tracking efficiency of $\varepsilon_{e^+}^{CDCH} \approx 82\%$, independent of the pile-up conditions.

The adoption of DNN-based algorithms for the track finding problem in MEG II has enabled a tracking efficiency that surpasses the original design specifications, effectively mitigating the pile-up limitations that affected the conventional PR algorithm.

In addition to the efficiency gain, a modest but consistent improvement is also observed in the resolution of the reconstructed kinematic observables. Importantly, these resolutions exhibit no significant dependence on the beam rate, confirming the robustness of the neural network-based reconstruction against pile-up effects (see Table F.1).

Analysis speed-up The improvements in computing time are significant, with a speed-up of the new track finder with the GNN classifier by a factor 30%-40% depending on the pile-up condition (Figure F.6), which would improve by almost 30% the reprocessing time of MEG II data.

The time performances of the Transformer PR are comparable with that of the GNN algorithm, and when the two algorithms are run in combination they match the computing time of the conventional PR. Although the reprocessing time for the MEG II final analysis is not boosted by this new track finder

Table F.1: Comparison of the resolutions on e^+ observables between the conventional Kalman Filter based PR and the new PR using the GNN and Transformer classifier. The resolutions are measured on data of Michel positrons collected at 5×10^7 μ^+/s in 2022.

Variable	Kalman PR	GNN + Transformer
y_e [mm]	0.71 ± 0.01	0.71 ± 0.01
z_e [mm]	2.04 ± 0.02	2.02 ± 0.02
ϕ_e [mrad]	6.40 ± 0.07	6.32 ± 0.06
θ_e [mrad]	7.55 ± 0.07	7.48 ± 0.09
p_e [keV]	92	89

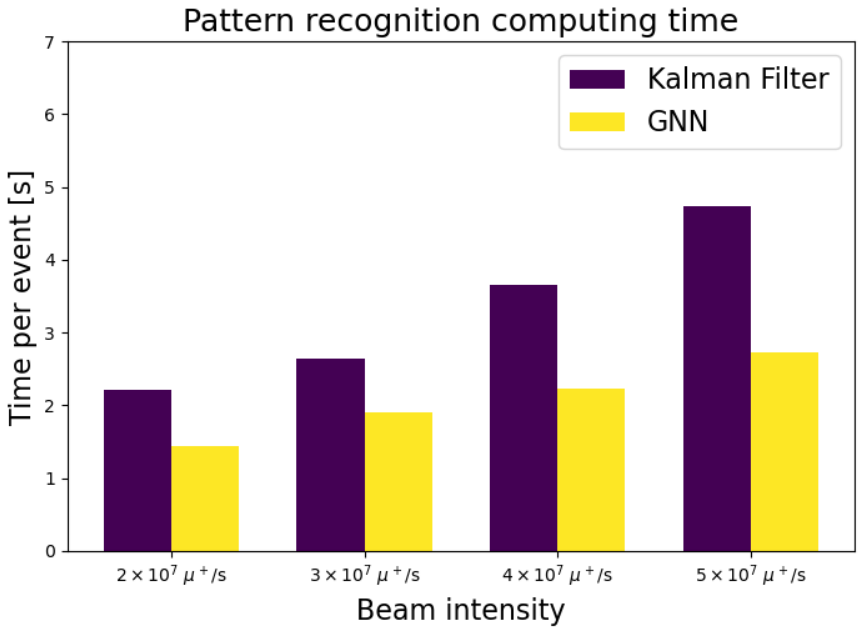

Figure F.6: Comparison between the computing time for the Kalman-based PR (purple) or the GNN-based PR (yellow).

approach, most calibration tasks for the tracker can profit of the speed-up offered by the GNN PR, when the full reconstruction chain is not needed (for example, for the iterative alignment procedure or B Field alignment studies).

Implications for MEG II experiment The increase in tracking efficiency, achieved without any degradation (and in fact with a slight improvement) of the tracker's resolutions, has a direct impact on the experimental sensitivity to the $\mu^+ \to e^+\gamma$ decay. In a quasi background-free experiment such as MEG II, the sensitivity scales approximately linearly with the overall detection efficiency. Consequently, the observed improvement translates into an expected gain in sensitivity of nearly 10%.

Furthermore, the robustness of the tracking performances against pile-up indicates that the detector is not intrinsically limited by high-rate conditions. This finding has allowed to identify a new optimal operating point for the 2025 and 2026 data-taking campaigns, with a beam intensity of 5×10^7 μ^+/s, compared to the previously adopted 4×10^7 μ^+/s, thereby maximizing the data acquisition rate.

Bibliography

[1] A. Pais. *Inward bound: of matter and forces in the physical world.* New York: Oxford University Press, 1986.

[2] S. H. Neddermeyer and C. D. Anderson. "Note on the Nature of Cosmic-Ray Particles". In: *Phys. Rev.* 51.10 (1937), pp. 884–886.

[3] C. M. G. Lattes, G. P. S. Occhialini, and C. F. Powell. "Observations on the Tracks of Slow Mesons in Photographic Emulsions". In: *Nature* 160.4067 (1947), pp. 486–492.

[4] J. C. Street and E. C. Stevenson. "New Evidence for the Existence of a Particle of Mass Intermediate Between the Proton and Electron". In: *Phys. Rev.* 52.9 (1937), pp. 1003–1004.

[5] M. Conversi, E. Pancini, and O. Piccioni. "On the Disintegration of Negative Mesons". In: *Phys. Rev.* 71.3 (1947), pp. 209–210.

[6] B. Pontecorvo. "Nuclear capture of mesons and the meson decay". In: *Phys. Rev.* 72.3 (1947), p. 246.

[7] G. Danby et al. "Observation of high-energy neutrino reactions and the existence of two kinds of neutrinos". In: *Phys. Rev. Lett.* 9.1 (1962), p. 36.

[8] MEG II Collaboration. "A search for $\mu^+ \to e^+ \gamma$ with the first dataset of the MEG II experiment". In: *Eur. Phys. J. C* 84.3 (2024), p. 216.

[9] MEG Collaboration. "Search for the lepton flavour violating decay $\mu^+ \to e^+\gamma$ with the full dataset of the MEG experiment". In: *Eur. Phys. J. C* 76 (2016), p. 434.

[10] L. Calibbi and G. Signorelli. "Charged lepton flavour violation: an experimental and theoretical introduction". In: *Riv. Nuovo Cim.* 41 (2018), pp. 71–174.

[11] S. Mihara et al. "Charged Lepton Flavor–Violation Experiments". In: *Annu. Rev. Nucl. Part. Sci.* 63.1 (2013), pp. 531–552.

[12] P. Minkowski. "$\mu \to e\gamma$ at a Rate of One Out of 10^9 Muon Decays?" In: *Phys. Lett. B* 67 (1977), pp. 421–428.

[13] M. Fukugita and T. Yanagida. *Physics of Neutrinos and Application to Astrophysics.* Springer Science & Business Media, 2013.

[14] B. Pontecorvo. "Mesonium and Antimesonium". In: *Sov. Phys. JETP* 6 (1958), pp. 429–431.

[15] Z. Maki, M. Nakagawa, and S. Sakata. "Remarks on the unified model of elementary particles". In: *Progress of Theoretical Physics* 28.5 (1962), pp. 870–880.

[16] H. Georgi and S. L. Glashow. "Unity of all elementary-particle forces". In: *Phys. Rev. Lett.* 32.8 (1974), p. 438.

[17] Particle Data Group. "Review of particle physics". In: *Phys. Rev. D* 110.3 (2024), p. 030001.

[18] R. K. Ellis et al. "Physics Briefing Book: Input for the European Strategy for Particle Physics Update 2020". In: (2019). arXiv: 1910.11775 [hep-ex].

[19] E. J. Konopinski and H. M. Mahmoud. "The Universal Fermi Interaction". In: *Phys. Rev.* 92.4 (1953), pp. 1045–1049.

[20] S. M. Bilenky, S.T. Petcov, and B. Pontecorvo. "Lepton mixing, $\mu^+ \to e^+ \gamma$ decay and neutrino oscillations". In: *Phys. Lett. B* 67.3 (1977), pp. 309–312.

[21] S.T. Petcov. In: *Sov. J. Nucl. Phys.* 25 (1977), p. 340.

[22] S. P. Martin. "A Supersymmetry primer". In: *Adv. Ser. Direct. High Energy Phys.* 18 (1998), pp. 1–98. arXiv: hep-ph/9709356.

[23] H. Baer, V. Barger, and H. Serce. "Lepton flavor violation from SUSY with nonuniversal scalars". In: *Physical Review Research* 1.3 (2019), p. 033022.

[24] A. M. Sirunyan et al. "Search for supersymmetry in multijet events with missing transverse momentum in proton-proton collisions at 13 TeV". In: *Phys. Rev. D* 96.3 (2017), p. 032003.

[25] M. Aaboud et al. "Search for supersymmetry in events with four or more leptons in $\sqrt{s}$=13 TeV pp collisions with ATLAS". In: *Phys. Rev. D* 98.3 (2018), p. 032009.

[26] L. Calibbi et al. "Status of supersymmetric type-I seesaw in SO (10) inspired models". In: *J. High Energy Phys.* 2012.11 (2012), pp. 1–19.

[27] M. Hirsch, F.R. Joaquim, and A. Vicente. "Constrained SUSY seesaws with a 125 GeV Higgs". In: *J. High Energy Phys.* 2012.11 (2012), pp. 1–33.

[28] T. Fukuyama, K. Ichikawa, and Y. Mimura. "Revisiting fermion mass and mixing fits in the minimal SUSY SO(10) GUT model". In: *Phys. Rev. D* 94.7 (2016), p. 075018.

[29] J. Ellis and D. V. Nanopoulos. "Flavour-changing neutral interactions in broken supersymmetric theories". In: *Phys. Lett. B* 110.1 (1982), pp. 44–48.

[30] H. Baer et al. "Status of weak scale supersymmetry after LHC Run 2 and ton-scale noble liquid WIMP searches". In: *Eur. Phys. J. Special Topics* 229.21 (2020), pp. 3085–3141.

[31] H. Baer et al. "Radiative Natural Supersymmetry with a 125 GeV Higgs Boson". In: *Phys. Rev. Lett.* 109.16 (2012), p. 161802.

[32] A. De Gouvêa and P. Vogel. "Lepton flavor and number conservation, and physics beyond the Standard Model". In: *Prog. Part. Nucl. Phys.* 71 (2013), pp. 75–92.

[33] K. Arndt et al. "Technical design of the phase I Mu3e experiment". In: *Nucl. Instrum. Methods A* 1014 (2021), p. 165679.

[34] R. Donghia. "The Mu2e experiment at Fermilab: Design and status". In: *Il Nuovo Cimento. C* 40.FERMILAB-CONF-17-653-E (2017).

[35] Y. Kuno. "A search for muon-to-electron conversion at J-PARC: The COMET experiment". In: *Progress of Theoretical and Experimental Physics* 2013.2 (2013), p. 022C01.

[36] E. P. Hincks and B. Pontecorvo. "On the absence of photons among the decay products of the 2.2 microsecond meson". In: *Can. J. Res.* 28.1 (1950), pp. 29–43.

[37] R. Eichler et al. *IMPACT conceptual design report.* PSI Bericht 22-01. 2022.

[38] G. Dal Maso et al. "Future facilities at PSI, the high-intensity muon beams (HIMB) project". In: *EPJ Web of Conferences.* Vol. 282. EDP Sciences. 2023, p. 01012.

[39] G Cavoto et al. "The quest for $\mu \to e\gamma$ and its experimental limiting factors at future high intensity muon beams". In: *Eur. Phys. J. C* 78 (2018), pp. 1–15.

[40] Study Group for Future $\mu \to e\gamma$ Searches. "Future $\mu \to e\gamma$ experiments". In: *PoS* Muon4Future2023 (2024), p. 025.

[41] Y. Kuno and Y. Okada. "Muon decay and physics beyond the Standard Model". In: *Rev. Mod. Phys.* 73.1 (2001), pp. 151–202.

[42] MEG II Collaboration. "The design of the MEG II experiment". In: *Eur. Phys. J. C* 78 (2018), pp. 1–60.

[43] MEG II Collaboration. "Operation and performance of MEG II detector". In: *Eur. Phys. J. C* 84.2 (2024), p. 190.

[44] MEG Collaboration. "The MEG detector for $\mu^+ \to e^+\gamma$ decay search". In: *Eur. Phys. J. C* 73 (2013), pp. 1–59.

[45] J. Grillenberger, C. Baumgarten, and M. Seidel. "The High Intensity Proton Accelerator Facility". In: *SciPost Phys. Proc.* (2021), p. 002.

[46] F. A. Berg. "CMBL - A High-Intensity Muon Beam Line & Scintillation Target with Monitoring System for Next-Generation Charged Lepton Flavour Violation Experiments". PhD thesis. Zurich, ETH, 2017.

[47] G. Cavoto et al. "A photogrammetric method for target monitoring inside the MEG II detector". In: *Rev. Sci. Instrum.* 92.4 (2021), p. 043707.

[48] D. Palo et al. "Precise photographic monitoring of MEG II thin-film muon stopping target position and shape". In: *Nucl. Instrum. Methods A* 944 (2019), p. 162511.

[49] W. Ootani et al. "Development of a thin-wall superconducting magnet for the positron spectrometer in the MEG experiment". In: *IEEE Trans. Appl. Supercond.* 14.2 (2004), pp. 568–571.

[50] A.M. Baldini et al. "Performances of a new generation tracking detector: the MEG II cylindrical drift chamber". In: *Eur. Phys. J. C* 84.5 (2024), pp. 1–28.

[51] A. Ferrari et al. "The KLOE drift chamber". In: *Nucl. Instrum. Methods A* 494.1-3 (2002), pp. 163–172.

[52] M. De Gerone et al. "Design and test of an extremely high resolution Timing Counter for the MEG II experiment: preliminary results". In: *J. Instrum.* 9.02 (2014), p. C02035.

[53] G. Boca et al. "The laser-based time calibration system for the MEG II pixelated Timing Counter". In: *Nucl. Instrum. Methods A* 947 (2019), p. 162672.

[54] H. Kolanoski and N. Wermes. *Particle Detectors: Fundamentals and Applications*. Oxford University Press, USA, 2020.

[55] K. Yamamoto. "A search for $\mu^+ \to e^+\gamma$ with the highest sensitivity beyond the MEG experiment". PhD thesis. The University of Tokyo, 2025.

[56] B. Vitali et al. "A liquid hydrogen target to fully characterize the new MEG II liquid xenon calorimeter". In: *Nucl. Instrum. Methods A* 1049 (2023), p. 168020.

[57] M. Takahashi et al. "Development of a high-rate capable DLC-RPC based on a current evacuation pattern". In: *J. Instr.* 20.06 (2025), p. C06007. arXiv: 2501.05128 [physics.ins-det].

[58] L. Galli et al. "WaveDAQ: An highly integrated trigger and data acquisition system". In: *Nucl. Instrum. Methods A* 936 (2019), pp. 399–400.

[59] M. Francesconi et al. "The WaveDAQ integrated Trigger and Data Acquisition System for the MEG II experiment". In: *Nucl. Instrum. Methods A* 1045 (2023), p. 167542. ISSN: 0168-9002.

[60] S. Ritt, R. Dinapoli, and U. Hartmann. "Application of the DRS chip for fast waveform digitizing". In: *Nucl. Instrum. Methods A* 623.1 (2010), pp. 486–488. ISSN: 0168-9002.

[61] E. G. Grandoni. "Studio di sensibilità del decadimento cLFV $\mu \to$ eaγ nell'esperimento MEG II". MA thesis. Università di Pisa, 2023.

[62] R. D. Peccei and H. R. Quinn. "CP conservation in the presence of pseudoparticles". In: *Phys. Rev. Lett.* 38.25 (1977), p. 1440.

[63] L. Calibbi et al. "Looking forward to lepton-flavor-violating *ALP*s". In: *J. High Energy Phys.* 2021.173 (2021).

[64] MEG Collaboration. "Search for lepton flavour violating muon decay mediated by a new light particle in the MEG experiment". In: *Eur. Phys. J. C* 80.9 (2020), p. 858. arXiv: 2005.00339 [hep-ex].

[65] M. Francesconi. "The new trigger and data acquisition system for LFV searches in the MEG II experiment". PhD thesis. Università degli Studi di Pisa, 2020.

[66] Y. Jho, S. Knapen, and D. Redigolo. "Lepton-flavor violating axions at MEG II". In: *J. High Energy Phys.* 2022.29 (2022).

[67] R. Bayes et al. "Search for two body muon decay signals". In: *Phys. Rev. D* 91.5 (2015), p. 052020.

[68] MEG II Collaboration. "Search for the X17 particle in ^{7}Li(p, e^{+}e^{-})^{8}Be processes with the MEG II detector". In: *Eur. Phys. J. C* 85.7 (2025), p. 763. arXiv: 2411.07994 [nucl-ex].

[69] A. J. Krasznahorkay et al. "Observation of anomalous internal pair creation in ^{8}Be: A possible indication of a light, neutral boson". In: *Phys. Rev. Lett.* 116.4 (2016), p. 042501.

[70] A. J. Krasznahorkay et al. "New anomaly observed in ^{12}C supports the existence and the vector character of the hypothetical X17 boson". In: *Phys. Rev. C* 106.6 (2022), p. L061601.

[71] A.J. Krasznahorkay et al. "New anomaly observed in ^{4}He supports the existence of the hypothetical X17 particle". In: *Phys. Rev. C* 104.4 (2021), p. 044003.

[72] T. T. Anh et al. "Checking the 8Be Anomaly with a Two-Arm Electron Positron Pair Spectrometer". In: *Universe* 10.4 (2024), p. 168.

[73] J. L. Feng et al. "Protophobic fifth-force interpretation of the observed anomaly in ^{8}Be nuclear transitions". In: *Phys. Rev. Lett.* 117.7 (2016), p. 071803.

[74] D. S. M. Alves et al. "Shedding light on X17: community report". In: *Eur. Phys. J. C* 83.230 (2023).

[75] E. Di Meco. "Looking for X_{17} at PADME". In: *Nuovo Cim. C* 47.3 (2024), p. 115.

[76] B. G. Servin et al. "Searching for internal pair creation anomalies and the X17 boson at LNL". In: *Nuovo Cim. C* 48.1 (2024), p. 23.

[77] C. J. G. Mommers and M. Vanderhaeghen. "X17 discovery potential in $\gamma d \to e^{+}e^{-}$pn at MAGIX@MESA". In: *EPJ Web Conf.* 303 (2024), p. 05004.

[78] G. Azuelos et al. "Status of the X17 search in Montreal". In: *J. Phys. Conf. Ser.* 2391.1 (2022), p. 012008. arXiv: 2211.11900 [physics.ins-det].

[79] F. Bossi et al. "Search for a new 17 MeV resonance via $e^{+}e^{-}$ annihilation with the PADME Experiment". In: (2025). arXiv: 2505.24797 [hep-ex].

[80] M. Chiappini. "The new drift chamber of the MEG-II experiment, in search for lepton flavor violations". MA thesis. Università di Pisa, 2016.

[81] M. Chiappini. "The construction and commissioning of the ultra low mass MEG II drift chamber for the search of the $\mu^{+} \to e^{+}\gamma$ decay at branching ratios below 10^{-13}". PhD thesis. Università degli Studi di Siena, 2019.

[82] M. Chiappini et al. "Commissioning and preliminary performance of the MEG II drift chamber". In: *Nucl. Instrum. Methods A* 1041 (2022), p. 167314.

[83] G. Chiarello et al. "An automatic system for the wiring of Drift Chambers for modern high intensity and high precision particle physics experiments". In: *J. Instrum.* 15.07 (2020), p. C07034.

[84] *Hexagon CMM DEA Ghibli*. Last accessed: 2025-10-23. URL: https://www.metrologyshare.com/cmm-fisso/hexagon-cmm-dea-ghibli/.

[85] A. Venturini. "Ricerca di Nuova Fisica con l'esperimento MEGII: prestazioni e ottimizzazione della nuova camera a deriva ultra-leggera". MA thesis. Università degli Studi di Pisa, 2022.

[86] A.M. Baldini et al. "Gas distribution and monitoring for the drift chamber of the MEG II experiment". In: *J. Instrum.* 13.06 (2018), P06018.

[87] M. Venturini. "Ageing and performance studies of drift chamber prototypes for the MEG experiment upgrade." PhD thesis. Università degli Studi di Pisa, 2013.

[88] M. Panareo et al. "The front end electronics for the drift chamber readout in MEG experiment upgrade". In: *J. Instrum.* 15.07 (2020), p. C07009.

[89] G. Signorelli, A. D'Onofrio, and M. Venturini. "A novel method to estimate the impact parameter on a drift cell by using the information of single ionization clusters". In: *Nucl. Instrum. Methods A* 824 (2016), pp. 581–583.

[90] D. Palo. "Search for the decay of a muon resulting in a positron-photon pair in the MEG II Experiment's First Physics Dataset and Analysis of the MEG II Drift Chamber Data". PhD thesis. UC Irvine, 2023.

[91] *Garfield++*. Last accessed: 2025-10-23. URL: https://garfieldpp.web.cern.ch/garfieldpp/.

[92] D. Palo and W. Molzon. "Neural network applications to improve drift chamber track position measurements". In: *Nucl. Instrum. Methods A* 1064 (2024), p. 169404.

[93] N. Taniguchi. "Central drift chamber for Belle-II". In: *J. Instrum.* 12.06 (2017), p. C06014.

[94] R. Frühwirth and A. Strandlie. *Pattern Recognition, Tracking and Vertex Reconstruction in Particle Detectors*. Springer Cham, 2021.

[95] C. Höppner et al. "A novel generic framework for track fitting in complex detector systems". In: *Nucl. Instrum. Methods A* 620.2 (2010), pp. 518–525.

[96] R. Frühwirth and A. Strandlie. "Track fitting with ambiguities and noise: A study of elastic tracking and nonlinear filters". In: *Comput. Phys. Commun.* 120.2 (1999), pp. 197–214. ISSN: 0010-4655.

[97] A. M. Baldini et al. "Detailed analysis of chemical corrosion of ultra-thin wires used in drift chamber detectors". In: *J. Instr.* 16.12 (2021), T12003. arXiv: 2108.13948 [physics.ins-det].

[98] G. Chiarello et al. "Analysis and study of the problems on the wires used in the MEG CDCH and the construction of the new drift chamber". In: *Nucl. Instrum. Methods A* 1046 (2023), p. 167735.

[99] *Proceedings of the first LHC Detector AlignmentWorkshop: CERN, Geneva, Switzerland 4 - 6 Sep 2006. 1st LHC Detector Alignment Workshop*. CERN. Geneva: CERN, 2007.

[100] R. O. Duda and P. E. Hart. "Use of the Hough transformation to detect lines and curves in pictures". In: *Commun. ACM* 15.1 (1972), pp. 11–15.

[101] S. Kobayashi. "Full Commissioning of Liquid Xenon Scintillation Detector to Search for $\mu^+ \to e^+\gamma$ with the Highest Sensitivity in MEG II Experiment". PhD thesis. The University of Tokyo, 2022.

[102] V. Blobel. "Software alignment for tracking detectors". In: *Nucl. Instrum. Methods A* 566.1 (2006), pp. 5–13.

[103] CMS Collaboration. "Alignment of the CMS tracker with LHC and cosmic ray data". In: *J. Instrum.* 9.06 (2014), P06009.

[104] T. Bilka et al. "Simultaneous Global and Local Alignment of the Belle II Tracking Detectors". In: *EPJ Web Conf.* 251 (2021), p. 03028.

[105] Q. Yan and V. Choutko. "Alignment of the Alpha Magnetic Spectrometer (AMS) in space". In: *Eur. Phys. J. C* 83.3 (2023), p. 245.

[106] CMS Collaboration. "Alignment of the CMS silicon tracker during commissioning with cosmic rays". In: *J. Instrum.* 5.03 (2010), T03009.

[107] *Millepede II*. Last accessed: 2025-10-02. URL: https://www.desy.de/~kleinwrt/MP2/doc/html/draftman_page.html.

[108] A. Meurer et al. "SymPy: symbolic computing in Python". In: *PeerJ Comput. Sci.* 3 (2017), e103.

[109] V. Vassilev et al. “Clad – Automatic Differentiation Using Clang and LLVM”. In: vol. 608. 1. IOP Publishing, 2015, p. 012055.

[110] A. Venturini et al. “Alignment of the MEG II cylindrical drift chamber”. In: *Nucl. Instrum. Methods A* 1067 (2024), p. 169680.

[111] G. J. Feldman and R. D. Cousins. “Unified approach to the classical statistical analysis of small signals”. In: *Phys. Rev. D* 57.7 (1998), pp. 3873–3889.

[112] E. Baracchini and F. Renga. *Positron variables correlations and resolutions and how to extract them from data*. Technical Report internal at the MEG Collaboration. 2011. URL: https://elog.psi.ch/elogs/Technical+Notes/78.

[113] Y. Fujii et al. *Likelihood Analysis on MEG data 2009-2011*. Technical Report internal at the MEG Collaboration. 2013. URL: https://elog.psi.ch/elogs/Technical+Notes/95.

[114] MEG II Collaboration. “New limit on the $\mu+\to$ e+ γ decay with the MEG II experiment”. In: *Eur. Phys. J. C* 85.10 (2025), p. 1177.

[115] S. Guo and M. Zhao. *Probing the Scotogenic Dirac Model with FIMP Dark Matter and N_{eff}*. 2025. arXiv: 2508.16362 [hep-ph].

[116] A. Liu et al. *Coscattering Dark Matter in Scotogenic Models*. 2025. arXiv: 2510.13231 [hep-ph].

[117] I. M. Ávila et al. *Dark matter as the source of neutrino mass: theory overview and experimental prospects*. 2025. arXiv: 2506.24027 [hep-ph].

[118] J. Leite, J. Perez-Soler, and A. Vicente. “Scotogenic mechanism from an extended $SU(2)_1 \times SU(2)_2 \times U(1)_Y$ electroweak symmetry”. In: *JHEP* 10 (2025), p. 129. arXiv: 2507.21223 [hep-ph].

[119] V. M. Lozano, G. Sanchez Garcia, and J. W. F. Valle. “Collider signatures of fermionic scotogenic dark matter”. In: *Phys. Rev. D* 112.5 (2025), p. 055007. arXiv: 2502.05270 [hep-ph].

[120] A. AbuSiam and A. Ahriche. “The scotogenic model with two inert doublets: Parameter space and electroweak precision tests”. In: *Int. J. Mod. Phys. A* 40.31 (2025), p. 2550157. arXiv: 2506.18051 [hep-ph].

[121] A. Darricau et al. *Flavour and precision probes of a class of scotogenic models*. 2025. arXiv: 2506.23383 [hep-ph].

[122] B. Dirgantara and J. Julio. *Constraining the new contributions to electron $g-2$ in a radiative neutrino mass model*. 2025. arXiv: 2510.08504 [hep-ph].

[123] A. E. Cárcamo Hernández et al. “Strongly coupled inert scalar sector with radiative neutrino masses”. In: *JHEP* 10 (2025), p. 061. arXiv: 2504.07193 [hep-ph].

[124] L. Dispoto et al. *Transformer-Based Approach to Enhance Positron Tracking Performance in MEG II*. Dec. 2025. arXiv: 2512.19482 [hep-ex].

[125] V. Golovatyuk, F. Grancagnolo, and R. Perrino. “Influence of oxygen and moisture content on electron life time in helium–isobutane gas mixtures”. In: *Nucl. Instrum. Methods A* 461.1 (2001). 8th Pisa Meeting on Advanced Detectors, pp. 77–79.

[126] A. M. Baldini et al. *The Use of O2 in Gas Mixtures for Drift Chambers*. Nov. 2025. arXiv: 2511.07082 [physics.ins-det].

[127] H. Shimamori and H. Hatano. “Electron attachment in gas mixtures”. In: *Chem. Phys.* 21.1077 (1977), p. 187.

[128] A. Tsaris et al. “The HEP. TrkX project: deep learning for particle tracking”. In: *J. Phys.: Conference Series*. Vol. 1085. IOP Publishing. 2018, p. 042023.

[129] R. Liu et al. “Hierarchical Graph Neural Networks for Particle Track Reconstruction”. In: *21th International Workshop on Advanced Computing and Analysis Techniques in Physics Research: AI meets Reality*. 2023. arXiv: 2303.01640 [hep-ex].

[130] J. Duarte and J. Vlimant. "Graph neural networks for particle tracking and reconstruction". In: *Artificial intelligence for high energy physics*. World Scientific, 2022, pp. 387–436.

[131] G. DeZoort et al. "Charged particle tracking via edge-classifying interaction networks". In: *Computing and Software for Big Science* 5 (2021), pp. 1–13.

[132] J. Shlomi, P. Battaglia, and J. Vlimant. "Graph neural networks in particle physics". In: *Machine Learning: Science and Technology* 2.2 (2020), p. 021001.

[133] A. Paszke et al. *PyTorch: An Imperative Style, High-Performance Deep Learning Library*. 2019. arXiv: 1912.01703 [cs.LG].

[134] M. Fey and J. E. Lenssen. *Fast Graph Representation Learning with PyTorch Geometric*. 2019. arXiv: 1903.02428 [cs.LG].

[135] *Cross Entropy Loss*. Last accessed: 2025-10-29. URL: https://docs.pytorch.org/docs/stable/generated/torch.nn.CrossEntropyLoss.html.

[136] L. Reuter et al. "End-to-End Multi-track Reconstruction Using Graph Neural Networks at Belle II". In: *Comput. Softw. Big Sci.* 9.1 (2025), p. 6. arXiv: 2411.13596 [physics.ins-det].

[137] *ONNX Runtime*. Last accessed: 2025-10-23. URL: https://onnxruntime.ai/.

[138] T. Lin et al. "A survey of transformers". In: *AI open* 3 (2022), pp. 111–132.

[139] A. Oya. *Transformer-based pattern recognition for positron tracking*. Technical Report internal at the MEG II Collaboration. 2025. URL: https://elog.psi.ch/elogs/Technical+Notes/132.

Acknowledgments

Sono stanco morto, capo!

John Coffey in *Il Miglio Verde* di S. King

Fortunately, the efforts underlying this research, which culminated in this PhD thesis, were not carried out alone. For this reason, these last pages are filled with a lot of ink and even more gratitude to all the people with whom I shared these past years: the last of my student career, the first of my life as a physicist.

The first person I want to thank is Alessandro Baldini, who has encouraged me and supported me on a daily basis during this four years of experience in MEG II. I always felt like you gave me many opportunities, which I hope I made the most of. You taught me much about the world of physics in a broader sense, and although Millepede will taunt me to my grave, you passed down to me the relevance of perseverance to reach the bottom of every question.

I owe much to others for their lessons and teaching: I want to thank in particular the MEG II Collaboration members (present and past) part of the Positron Analysis group: Fedor Ignatov, Atsushi Oya, Dylan Palo, Francesco Renga, Yusuke Uchiyama. I entered the MEG II Collaboration as a master's student with no experience, and thanks to your advices, your answers to my questions, your attention and interest in my original contribution, I could finally take an active part in a very successful experiment. I also wish to thank all other members of the MEG II Collaboration who contributed to the $\mu^+ \to e^+\gamma$ search. Your dedication and the moments of camaraderie we shared in PSI and in Japan during karaoke nights made this experience truly special.

Many thanks to all the members of the MEG II group in Pisa, whose constant presence made these years in Pisa both productive and enjoyable: Fabrizio Cei, my co-supervisor, who also patiently endured the revision of this thesis; Lapo Dispoto, perhaps my first student and certainly an outstanding colleague, whose enthusiasm reshaped the perspective on the GNN track finder during our collaboration; Giovanni Gallucci; Marco Grassi; Francesco Leonetti, with whom I shared an unforgettable month in Tokyo; Donato Nicolò, despite our disagreements on questions even more fundamental than $\mathrm{SU(3)}\times\mathrm{SU(2)}_L\times\mathrm{U(1)}_Y$; Angela Papa, especially for giving me the opportunity to contribute to a different experiment; and Giovanni Signorelli, whom I thank for first introducing me to this collaboration.

I wish to retail a special place in this list of MEG II Pisa group members to the "capi", because they have made every day and every moment of these years magical. Nothing would have been the same without your friendship, and I am most grateful for this. Thank you deeply, Hicham, MarcoC, MarcoF, Luca, Elia.

The final part of these acknowledgments is dedicated to the people in my life who supported me long before the challenges of this PhD, and who I know will continue to do so well beyond the end of this journey.

To my friends from Pistoia: after all these years, it is still the best feeling in the world to spend time with you. You literally fill the air with joy, love to live and much more wine and music that I can stand!

To Alice: thank you for showing me a new way of loving myself and others, for igniting the will to build the person I want to be, the life I want to live, and for being a part in it. Thank you for making

me part of your life! I think we are still in debt with each other over a well deserved vacation: now it's time we begin to live... travel... live.

To my Canadian family: thank you for having always supported with love and excitement my life path although the distance made it not easy.

Grazie alla mia famiglia "italiana", per la quale le parole di gratitudine non basterebbero mai e quindi qui mi fermo.